Synthesis and Self-Assembly of Bottlebrush Block Polymers: Molecular Architecture and Materials Design

Thesis by

Alice B. Chang

In Partial Fulfillment of the Requirements
for the Degree of
Doctor of Philosophy

Caltech

CALIFORNIA INSTITUTE OF TECHNOLOGY
Pasadena, California

2018
Defended May 25, 2018

Alice B. Chang
ORCID: 0000-0001-5036-2681

ACKNOWLEDGMENTS

This thesis represents contributions from many people, including mentors, colleagues, family, and friends. Our interactions have shaped me into the scientist and person I am today, and I would like to thank everyone for their support over the years.

I would first like to thank my advisor, **Prof. Bob Grubbs**. Bob has been a great mentor, and it has been a great privilege to work in his group. One of the lessons Bob teaches is simple but empowering: *don't be afraid to learn new things*. Bob communicates this through his diverse interests and generous support, which have enabled us to pursue the work described in this thesis at the intersection of polymer chemistry and polymer physics. The tremendous depths of Bob's creativity, curiosity, and kindness are truly inspiring. Moving forward, I can only do my best to live up to his support and his example.

I would also like to thank the members of my committee: **Profs. Dave Tirrell**, **Dennis Dougherty**, and **Zhen-Gang Wang.** Our conversations and committee meetings have been wonderful opportunities to discuss research directions and explore new ideas. I greatly appreciate their support and insight.

I would next like to thank other members of the Caltech community, starting with the Grubbs group. Thank you for being awesome friends and labmates! Whether we're sharing ideas, chemicals, or memes, you've made the lab a fun and inspiring place to work. I would especially like to thank three former colleagues with whom I worked closely: **Drs. Garret Miyake**, **Chris Bates**, and **Tzu-Pin Lin**. Their creativity, expertise, and encouragement have deeply influenced the way I do and think about science.

Garret was my mentor when I first joined the group as a summer (SURF) student, and he introduced me to polymer chemistry and the potential of polymer-based materials. We wrote a review together after I joined the group as a grad student, and I included an overview of the challenges in the field. Garret returned that section unmarked — all discussion of present limitations intact — except he crossed out *challenges* and replaced *opportunities*. I rolled my eyes! However, Garret's edit and enthusiasm echo now when I think about new research directions.

I started to work with Chris during my first year as a grad student, shortly after Chris joined the group as a postdoc. Chris introduced me to polymer physics, and we worked together on several aspects of this thesis, including the phase behavior of low-χ block polymers (Chapter 4) and brush polymer electrolytes (Chapter 6-2). Working with Chris taught me many valuable skills, including how to finish a project and how to write a paper, as well as the value of building diverse interests. At any point, Chris may be reading a textbook on X-ray diffraction or statistical thermodynamics or organic reaction mechanisms, and his creativity in connecting different ideas was inspiring.

TP and I started to work together during my third year as a grad student and TP's first year as a postdoc. TP brought a new perspective and energy to the group, and bouncing ideas back and forth with him was such a fun and rewarding experience. Our backgrounds were different but complementary, enabling us to explore shared interests from multiple angles. Our work together comprises Chapters 2 and 3 of this thesis, describing the synthesis of graft polymers (Chapter 2) and some physical consequences of varying the grafting density and graft distribution (Chapter 3). We once spent several days straight together (including driving 10+ hours to/from a conference) and emerged with new ideas and without hating each other — a real testament to our collaboration!

I was also fortunate to work closely with an exceptional undergrad student, **Shi En Kim**, during her last summer and part of her last year at Caltech. Working with Kim was a real joy — she learned quickly and dug deeply into our work together, and her enthusiasm was inspiring. U Chicago is lucky to have her as a grad student, and I look forward to seeing her accomplish great things.

I have been fortunate to work with several other members of the Grubbs group, and I appreciate their contributions to the work described in this thesis. **Shao-Xiong (Lennon) Luo** was a very talented undergrad who contributed to the monomer synthesis and copolymerization kinetics described in Chapter 2. **Drs. Crystal Chu**, **Pablo Guzmán**, **Allegra Liberman-Martin**, **Rob Macfarlane**, and I explored various approaches to block polymer photonic crystals (Chapter 6-1). **Brendon McNicholas** and **Nebo Momčilović** played important roles in the brush polymer electrolyte studies described in Chapter 6-2.

The work presented in this thesis has benefited from the contributions of many other members of the Caltech community. **Dr. Hsiang-Yun Chen** and **Niklas Thompson** have made key contributions to our studies of ROMP kinetics: Hsiang-Yun wrote the code to fit our copolymerization data and calculate reactivity ratios (Chapter 2-4), and Nik performed density functional theory (DFT) calculations to provide insight into the ROMP mechanism (Chapter 2-9). I would like to thank **Prof. Jonas Peters** for providing access to computational resources. I would also like to thank **Prof. Julie Kornfield** and her student, **Joey Kim**, for access to their rheometer and for valuable discussions. In addition, I would like to thank **Prof. Zhen-Gang Wang** and members of his group, including **Prof. Liquan Wang**, **Dr. Pengfei Zhang**, and **Dr. Jian Jiang**, for their patience in discussing self-consistent field theory (SCFT) and polymer phase behavior with me. Liquan, with input from Pengfei and JJ, built SCFT up from scratch in his explanations, and our conversations helped me gain a deeper appreciation for the theory.

The Caltech instrument facilities have been great resources. **Dr. Dave VanderVelde** keeps the NMR facility in shipshape, and I have learned a lot from him (and his coffee and beer posters!). **Dr. Mona Shahgholi** has helped me answer tough questions about polymer composition by mass spectrometry. **Dr. Chi Ma** trained me to operate the scanning electron microscope and has helped troubleshoot many samples since. **Mark Ladinsky** and **Dr. Alasdair McDowall** trained me to use to cryomicrotome in the bio-imaging facility; in addition, Mark microtomed several of the brush triblock samples discussed in Appendix C. I would especially like to thank **Carol Garland** for teaching me and working with me to image samples by transmission electron microscopy (TEM). Her help was invaluable in obtaining the TEM images in Chapter 4, which first alerted us to the unusual mesoscopic domain connectivity in these low-χ materials.

We have been tremendously fortunate to collaborate with members of the scientific community outside Caltech. Their contributions have crucially enabled the work presented in this thesis. I would like to express my deep appreciation for their expertise and insight, as well as my sincere hope that we will continue to find opportunities to collaborate. I will thank our collaborators in the approximate order of the first appearance of their contributions in this thesis.

My first acknowledgment must be to **Dr. Byeongdu Lee**, a beamline scientist at Argonne National Laboratory's Advanced Photon Source and a leader in the X-ray scattering community. We started to work together during my second year of grad school, and I have since learned everything I know about scattering — and most of what I know about polymer physics — from Byeongdu. In addition to providing technical support at the beamline, Byeongdu has played a key role in our work to interpret the influences of the graft polymer architecture on block polymer phase behavior. His contributions are reflected in almost every chapter of this thesis, including our models for the scaling of the lamellar period with grafting density (Chapter 3-2), the role of screening in low-χ materials (Chapter 4), and crystallization in brush block polymers (Chapter 5-3).

I would also like to thank our collaborators at the University of Minnesota: **Ingrid Haugan, Dr. Michael Maher**, **Prof. Marc Hillmyer**, and **Prof. Frank Bates**. They performed the studies described in Chapter 3-3 to explore the effects of grafting density on linear rheological properties. I greatly appreciate the opportunity to learn more about rheology and these materials through their efforts. I would additionally like to thank Frank for his valuable suggestions regarding partial mixing in our low-χ brush block polymers (Chapter 4), as well as **Drs. Sid Chanpuriya**, **Matt Irwin**, and **Tuoqi Li** for their assistance with microtomy.

Dr. Simon Jones at the Jet Propulsion Laboratory, in addition to **Prof. Christina Bauer** and her student **Matt Voegtle** at Whittier College, helped us obtain differential scanning calorimetry (DSC) data. DSC data was an important part of our studies of various systems, including the graft copolymers in Chapter 2-3, the brush LSO and LSL' triblocks in Chapter 4, and the solid polymer electrolytes in Chapter 6-2.

Prof. Mark Matsen at the University of Waterloo played a key role in our work studying the effects of low-χ block polymer design (Chapter 4). His SCFT calculations helped guide our molecular interpretation of the unusual phase behavior. In this and several other contexts, Mark was immediately ready with a compelling explanation — and not only an explanation, but a relevant reference from his previous work! I appreciate his insight and, through our work together, the opportunity to see how simulations can help build physical models.

I would next like to thank our collaborators at the National Institute of Standards and Technology (NIST): **Drs. Adam Burns**, **Dean DeLongchamp**, **Chris Soles**, and **Dan Sunday**. Adam and Chris are studying the dynamics and conformations of our graft polymers via neutron scattering (not included in this thesis). Chris, Dean, and Dan performed the resonant soft X-ray reflectivity (RSoXR) measurements and interpretation described in Chapter 4-10, which provided new insights into the LAM$_P$ structure and its demands on the bottlebrush architecture. We started to work together after Chris and I met at a conference and Chris suggested reflectivity measurements. I had never heard of the technique, and I certainly could not have imagined how powerful it can be! Working with Adam, Dean, Chris, and Dan has been great fun and a great introduction to new characterization techniques. I greatly appreciate the opportunities to collaborate.

Lastly, I would like to thank my friends and family. **Alexis Kurmis** and I were roommates during our first two years at Caltech, as well as friends from college. Sunday dinners with Alexis really helped Caltech feel like home, and they are among my favorite parts of grad school. The Grubbs group has been full of some of the greatest people and friends I have ever met. In addition to being wonderful collaborators, Garret, Chris, TP, Kim, and Pablo are good friends. **Crystal Chu** knows all the best Asian food in the LA area, and late-night boba or noodle runs were great de-stressors. Exploring Pasadena and hanging out with Crystal, **Jae Engle**, **Keary Engle**, **Natalie Khuen**, **Rob Macfarlane, Hans Renata**, and **Zach Wickens** are among my best memories of the first years of grad school. Looking forward to a reunion fried chicken crawl someday! I still listen to **Ray Weitekamp's** ingMob album sometimes. Coffee and conversations with **Julian Edwards**, **Sankar Krishnamoorthy, Allegra Liberman-Martin**, **Karthish Manthiram**, **Chris Marotta**, and **Willie Wolf** have been a lot of fun. Thanks for the cheese danishes, Julian!

Mom, **Dad**, and **Oliver** — thank you for all your love and support. Gumshoe adventures and library trips are some of the earliest things I remember, and everything since has been inspired by you. Thank you to the **Cialdella family** for welcoming me, and for all your warmth (and wine!). Last but not least, **Louis** — thank you for being here for it all. Thank you for making first New York and now LA home. Thank you for making me coffee and making me laugh. I'm looking forward to the next adventure.

ABSTRACT

Bottlebrush polymers represent a unique molecular architecture and a modular platform for materials design. However, the properties and self-assembly of bottlebrush polymers remain relatively unexplored, in large part due to the synthetic challenges imposed by the sterically demanding architecture. This thesis describes our work to close this gap, connecting (1) the synthesis of polymers with precisely tailored molecular architectures, (2) the study of fundamental structure-property relationships, and (3) the design of functional materials.

Chapter 1 introduces key concepts related to polymer architecture and block polymer phase behavior. Recent developments in the synthesis and self-assembly of bottlebrush block polymers are highlighted in order to frame the work presented in Chapters 2–6.

Chapter 2 introduces a versatile strategy to design polymer architectures with arbitrary side chain chemistry and connectivity. Simultaneous control over the molecular weight, grafting density, and graft distribution can be achieved via living ring-opening metathesis polymerization (ROMP). Copolymerizing a macromonomer and a small-molecule co-monomer provides access to well-defined polymers spanning the linear, comb, and bottlebrush regimes. This design strategy creates new opportunities for molecular and materials design.

Chapter 3 explores the physical consequences of varying the grafting density and graft distribution in two contexts: block polymer self-assembly and linear rheological properties. The molecular architecture strongly influences packing demands and therefore the conformations of the backbone and side chains. Collectively, these studies represent progress toward a universal model connecting the chemistry and conformations of graft polymers.

Chapter 4 discusses the phase behavior of ABA' and ABC bottlebrush triblock terpolymers. Low-χ interactions between the end blocks promote organization into a unique mixed-domain lamellar morphology, LAM$_{\mathrm{P}}$. X-ray scattering experiments reveal an unusual trend: the domain spacing strongly *decreases* with increasing total molecular weight. Insights

into this behavior provide new opportunities for block polymer design with potential consequences spanning all self-assembling soft materials.

Chapter 5 describes other physical consequences of low-χ block polymer design. The ternary phase diagrams for ABC, ACB, and BAC bottlebrush triblock terpolymers reveal the influences of low-χ A/C interactions, frustration, and the molecular architecture. Potential non-equilibrium effects and crystallization in these bottlebrush polymers will also be discussed.

Chapter 6 describes applications of bottlebrush polymers as functional materials. Self-assembly enables mesoscale structural control over many materials properties, such as reflectivity, conductivity, and modulus. The synthetic methods (Chapter 2) and physical insights (Chapters 3−5) provided in previous chapters illustrate opportunities for materials design. We will discuss AB brush diblock polymers that self-assemble to photonic crystals and ABA brush triblock copolymers in solid polymer electrolytes.

PUBLISHED CONTENT AND CONTRIBUTIONS

The work in this thesis includes content from the following published or submitted manuscripts. This work was enabled by the contributions of all authors, which are described in the acknowledgments and reflected throughout the thesis. In the interest of brevity, only contributions by A.B.C. have been identified below, except where appropriate to acknowledge other authors in the same role.

Chapter 2: Control over the Graft Polymer Architecture via Ring-Opening Metathesis Polymerization

1. Lin, T.-P.; Chang, A. B.; Chen, H.-Y.; Liberman-Martin, A. L.; Bates, C. M.; Voegtle, M. J.; Bauer, C. A.; Grubbs, R. H. Control of Grafting Density and Distribution in Graft Polymers by Living Ring-Opening Metathesis Copolymerization. *J. Am. Chem. Soc.* **2017**, *139*, 3896–3903. doi: 10.1021/jacs.7b00791.

   A.B.C. designed the study (with T.-P.L. and C.M.B.), performed some of the macromonomer synthesis and homo- and copolymerization experiments, interpreted data, and contributed to manuscript preparation.

2. Chang, A. B.;+ Lin, T.-P.;+ Thompson, N. B.; Luo, S.-X.; Liberman-Martin, A. L.; Chen, H.-Y.; Grubbs, R. H. Design, Synthesis, and Self-Assembly of Polymers with Tailored Graft Distributions. *J. Am. Chem. Soc.* **2017**, *139*, 17683–17693. doi: 10.1021/jacs.7b10525. (+*Equal contributions.*)

   A.B.C. designed the study, performed some of the macromonomer synthesis and homo- and copolymerization experiments, collected and analyzed X-ray scattering data, interpreted data, and wrote the paper.

Chapter 3: Impacts of the Graft Polymer Architecture on Physical Properties

3. Lin, T.-P.;+ Chang, A. B.;+ Luo, S.-X.; Chen, H.-Y.; Lee, B.; Grubbs, R. H. Effects of Grafting Density on Block Polymer Self-Assembly: From Linear to Bottlebrush. *ACS Nano* **2017**, *11*, 11632–11641. doi: 10.1021/acsnano.7b06664. (+*Equal contributions.*)

   A.B.C. designed the study, collected and analyzed X-ray scattering data, imaged materials by scanning electron microscopy, proposed a model for the observed scaling of the block polymer lamellar period (with B.L.), and wrote the paper (with T.-P.L.).

4. Haugan, I. N.; Maher, M. J.; Chang, A. B.; Lin, T.-P.; Grubbs, R. H.; Hillmyer, M. A.; Bates, F. S. Consequences of Grafting Density on the Linear Viscoelastic Behavior of Graft Polymers. *ACS Macro Lett.* **2018**, *7*, 525–530. doi: 10.1021/acsmacrolett.8b00116.

   A.B.C. contributed to the conception of the project (with all other authors), synthesized all graft polymer samples, and contributed to manuscript preparation.

Chapter 4: Manipulating the ABCs of Self-Assembly via Low-χ Block Polymer Design

5. Chang, A. B.; Bates, C. M.; Lee, B.; Garland, C. M.; Jones, S. C.; Spencer, R. K.; Matsen, M. W.; Grubbs, R. H. Manipulating the ABCs of Self-Assembly via Low-χ Block Polymer Design. *Proc. Natl. Acad. Sci.* **2017**, *114*, 6462–6467. doi: 10.1073/pnas.1701386114.

   A.B.C. designed the study, coordinated with all collaborators, synthesized all polymers, collected and analyzed X-ray scattering data (with B.L.), imaged materials by transmission electron microscopy, interpreted data, proposed a model for the unusual domain spacing trends (with C.M.B., B.L., and M.W.M.), and wrote the paper (with C.M.B.).

6. Sunday, D. F.;* Chang, A. B.;* Liman, C. D.; Gann, E.; DeLongchamp, D. M.; Matsen, M. W.; Grubbs, R. H.; Soles, C. L. Evidence for Backbone Flexibility of Bottlebrush Block Copolymers Driven by Low-χ Assembly. **2018**. *submitted.* (**Corresponding authors.*)

   A.B.C. contributed to the conception of the project (with C.L.S.), synthesized all polymers, prepared thin films for reflectivity measurements, imaged materials by atomic force microscopy, proposed a model for the observed relative domain thicknesses (with D.F.S. and M.W.M.), contributed to manuscript preparation, and serves as co-corresponding author (with D.F.S.).

Chapter 6: Applications of Bottlebrush Polymers in Functional Materials

7. Macfarlane, R. J.; Kim, B.; Lee, B.; Weitekamp, R. A.; Bates, C. M.; Lee, S. F.; Chang, A. B.; Delaney, K. T.; Fredrickson, G. H.; Atwater, H. A.; Grubbs, R. H. Improving Brush Polymer Infrared One-Dimensional Photonic Crystals via Linear Polymer Additives. *J. Am. Chem. Soc.* **2014**, *136*, 17374–17377. doi: 10.1021/ja5093562.

   A.B.C. imaged all samples by scanning electron microscopy and provided edits to the manuscript.

8. Bates, C. M.; Chang, A. B.; Momčilović, N.; Jones, S. C.; Grubbs, R. H. ABA Triblock Brush Polymers: Synthesis, Self-Assembly, Conductivity, and Rheological Properties. *Macromolecules* **2015**, *48*, 4967–4973. doi: 10.1021/acs.macromol.5b00880.

    A.B.C. synthesized some of the macromonomers and brush polymers, collected and analyzed some of the rheology and X-ray scattering data, and contributed to manuscript preparation.

9. Bates, C. M.; Chang, A. B.; Schulze, M. W.; Momčilović, N.; Jones, S. C.; Grubbs, R. H. Brush Polymer Ion Gels. *J. Polym. Sci., Part B* **2016**, *54*, 292–300. doi: 10.1002/polb.23927.

    A.B.C. synthesized some of the macromonomers and brush polymers, collected and analyzed some of the rheology and X-ray scattering data, and contributed to manuscript preparation.

10. McNicholas, B. J.; Blakemore, J. D.; Chang, A. B.; Bates, C. M.; Kramer, W. W.; Grubbs, R. H.; Gray, H. B. Electrocatalysis of CO_2 Reduction in Brush Polymer Ion Gels. *J. Am. Chem. Soc.* **2016**, *138*, 11160–11163. doi: 10.1021/jacs.6b08795.

    A.B.C. synthesized the polymers, collected and analyzed X-ray scattering data, and provided edits to the manuscript.

TABLE OF CONTENTS

Chapter 1: Introduction

Chapter 2: Control over the Graft Polymer Architecture via Ring-Opening Metathesis Polymerization

Chapter 3: Impact of the Graft Polymer Architecture on Physical Properties

Chapter 4: Manipulating the ABCs of Self-Assembly via Low-χ Block Polymer Design

Chapter 5: Consequences of Low-χ Block Polymer Design: Phase Behavior, Equilibrium, and Crystallization

Chapter 6: Applications of Bottlebrush Block Polymers in Functional Materials

Appendix A: Appendix to Chapter 2

Appendix B: Appendix to Chapter 3

Appendix C: Appendix to Chapter 4

LIST OF FIGURES AND SCHEMES

LIST OF TABLES

Chapter 1

Introduction

Table of Contents

1-1 Molecular Architecture

The molecular architecture impacts the chemical and physical properties of all polymers. In principle, there are infinitely many possible polymer architectures — that is, infinitely many ways to connect polymer chains. In practice however, long-standing synthetic challenges limit the scope of architectural design. These limitations preclude studies of fundamental physical phenomena as well as potential applications in functional materials. This thesis presents our work to close the design, synthesis, and characterization gaps for bottlebrush polymers, a unique molecular architecture.

This chapter will first introduce the bottlebrush architecture (Section 1-1). The need for improved synthetic methods and systematic structure-property studies will be emphasized. We will then review existing synthetic routes and highlight our approach: living grafting-through ring-opening metathesis polymerization (ROMP) (Section 1-2). Section 1-3 will build complexity by introducing bottlebrush block polymers and discussing the impacts of architecture on self-assembly. Lastly, Section 1-4 will outline the structure of this thesis by connecting these themes of molecular architecture and materials design.

Bottlebrush polymers are a class of graft polymers, which feature a polymer backbone bearing grafted polymer side chains. Compared to linear homopolymers (the simplest possible architecture), bottlebrush polymers display unique properties and introduce new opportunities for molecular shaping. For a fixed monomer chemistry, linear homopolymers feature only one independent structural parameter: the total degree of polymerization, N (Figure 1.1). In comparison, bottlebrush polymers feature *four* independent parameters: (1) the backbone degree of polymerization, N_{bb}; (2) the side chain degree of polymerization, N_{sc}; (3) the grafting density, z (defined as the average number of grafts per backbone repeat unit); and (4) the distribution of grafts along the backbone (uniform, tapered, etc.) (Figure 1.1). Bottlebrush polymers are primarily distinguished from other graft polymers by high z.

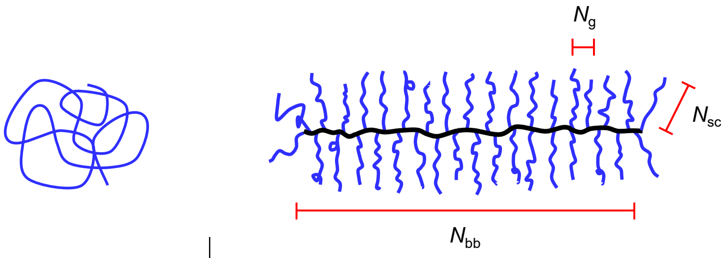

Architecture	linear	bottlebrush
Structural Parameters	N	N_{bb}, N_{sc}, z, graft distribution

Figure 1.1: Comparison of linear (*left*) and bottlebrush (*right*) polymer architectures. For a fixed monomer chemistry, the linear polymers feature one independent structural parameter: the total degree of polymerization, N. In contrast, bottlebrush polymers must be described by multiple parameters, including the backbone length (N_{bb}), side chain length (N_g), grafting density ($z = 1/N_g$), and graft distribution.

Whereas the conformation of a linear homopolymer can be largely anticipated based on N, the conformation of a bottlebrush polymer depends on the complex interplay of N_{bb}, N_{sc}, z, and the graft distribution. Polymer conformations represent the molecular basis for predicting and controlling all of the physical properties of polymers: therefore, understanding the connections between molecular architecture and polymer conformation is crucial from the perspectives of both fundamental theory and materials design.

In bottlebrush polymers, strong steric repulsion between the side chains imparts a certain bending rigidity to the backbone, causing the brush to adopt an extended, wormlike conformation.[1-2] Due to their extended conformations, bottlebrush polymers display different physical properties than linear analogues. For example, the bottlebrush architecture suppresses entanglements in the melt and lowers the melt viscosity,[3-5] thereby introducing processing advantages and new opportunities for materials design. Recent reports have exploited these unique properties in the context of supersoft elastomers, [6-8] leading to solvent-free materials with moduli as low as 100 Pa and tensile strains-at-break up to 800%.[9] These properties are direct consequences of the bottlebrush architecture. (In comparison, linear polymers of the same chemical composition have moduli greater than 10^6 Pa and strains-at-break only up to 200%.[9]) In addition to supersoft elastomers, bottlebrush polymers have been developed as rheological modifiers,[10] nanoporous materials,[11-12] solid electrolytes,[13-15] and photonic bandgap materials.[16-18]

Despite the importance of polymer conformation and the rich potential of bottlebrush materials, there is a current lack of consensus regarding many key structure-property relationships. This lack of consensus is due in large part to the challenges associated with capturing the complex interplay of all structural parameters. Table 1.1 provides one example. The influence of N_{sc} on the stiffness of the backbone (expressed as the backbone persistence length, λ_b) is considered. Even for this fundamental relationship, experiments, theory, and computer simulations have proposed many conflicting expressions. Considering the general expression $\lambda_b \sim N_{sc}^{\nu}$, the proposed scaling exponents vary over a wide range: $3/4 \leq \nu \leq 2$.

Table 1.1: Expressions for the relationship between the backbone stiffness (λ_b) and side chain degree of polymerization (N_{sc}). All expressions are provided for densely grafted bottlebrush polymers in a good solvent for the side chains. Note that expressions for the side chain length differ across the references (M, n, N_s, L); N_{sc} is used here to maintain consistency with the terminology in this thesis.

Expression	Methods	References	Eq.
$\lambda_b \sim N_{sc}^{3/4}$	Scaling theory, Monte Carlo simulations	19–21	1-1
$\lambda_b \sim N_{sc}^{1}$	Static light scattering, Small-angle X-ray scattering	22–23	1-2
$\lambda_b \sim N_{sc}^{15/8}$	Scaling theory	1	1-3
$\lambda_b \sim N_{sc}^{2} / \ln N_{sc}$	Perturbation theory, Monte Carlo simulations	24	1-4
$\lambda_b \sim N_{sc}^{2}$	Perturbation theory, Static light scattering	25–28	1-5

Initial reports attributed the wide variation in v to the limitations of certain methods. However, later insights indicate that the apparent conflicts are not consequences of calculation or measurement errors: instead, the disparities reflect the existence of multiple conformational regimes in the bottlebrush parameter space.[9,29-30] In other words, the conformation (and therefore the physical properties) of a bottlebrush polymer depends on its unique combination of N_{bb}, N_{sc}, z, etc. Recent studies have proposed *universal* models for graft polymer conformation based on scaling analyses.[9,29-30] In one example, four distinct conformational regimes were proposed based on predicted relationships between the molecular structure and the plateau modulus, then mapped in terms of N_{sc} and the average backbone length between adjacent grafts ($N_{\mathrm{g}} = 1 / z$) (Figure 1.2A). Below a critical grafting density ($N_{\mathrm{g}} > N_{\mathrm{g}}^{**}$), loose comb (LC), dense comb (DC), and loose brush (LB) regimes are anticipated as functions of N_{sc}. The comb regimes exhibit unperturbed Gaussian backbones and side chains, whereas LB marks the onset of backbone stretching due to side chain crowding. Above the critical grafting density ($N_{\mathrm{g}} < N_{\mathrm{g}}^{**}$), a dense brush (DB) regime is anticipated regardless of N_{sc}, in which both the backbones and side chains are extended. Figure 1.2B provides the corresponding scaling predictions for the entanglement plateau modulus ($G_{\mathrm{e,graft}}$) of graft polymer melts relative to linear melts ($G_{\mathrm{e,linear}}$) as a function of N_{sc}.

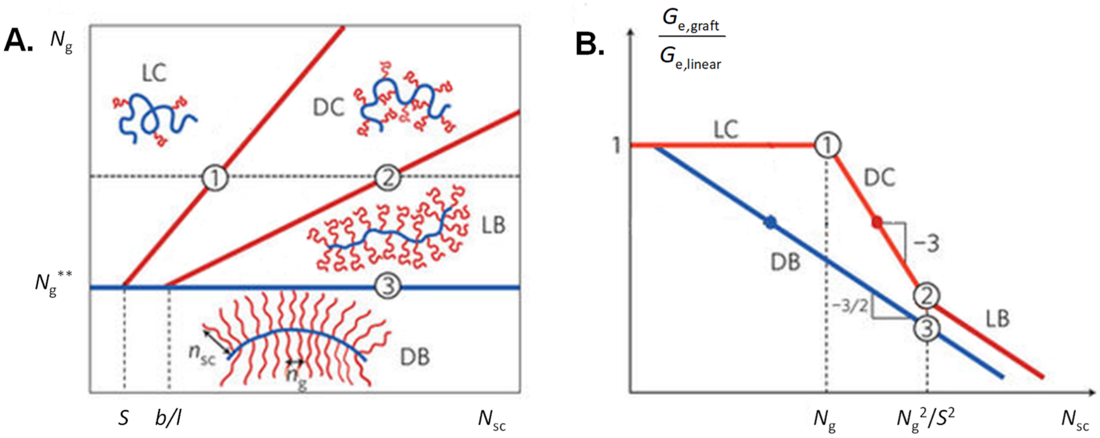

Figure 1.2: (*A*) Diagram of states for graft polymers based on the side chain degree of polymerization (N_{sc}) and inverse grafting density ($N_{\mathrm{g}} = 1 / z$). Loose comb (LC), dense comb (DC), loose brush (LB), and dense brush (DB) regimes are anticipated by theory. The conformations of the side chains and backbone vary in each regime. (*B*) Predicted entanglement plateau modulus of graft polymer melts ($G_{\mathrm{e,graft}}$) relative to linear polymer melts ($G_{\mathrm{e,linear}}$) as a function of N_{sc}. The normalized modulus decreases with increasing N_{sc}, and the scaling exponent changes in each regime. Adapted with permission from Ref. 9.

The predictions in Figure 1.2 reinforce the intimate connections between polymer conformation and physical properties. The predictions also highlight the need for additional studies. Recent computer simulations support the mapping of four distinct conformational regimes onto the molecular parameter space,[29-30] but the locations of the boundaries between regimes and the expected physical behavior in each regime remain topics of ongoing debate. In other words: for any backbone and side chain chemistries and any chain dimensions, what distinguishes bottlebrush polymers from other graft polymers? How do the physical properties vary in the bottlebrush regime?

Furthermore, any universal model for graft polymer conformation must be consistent with experimental measurements. However, experimental studies remain limited due to long-standing synthetic challenges associated with preparing well-defined model systems. Achieving precise control over key structural parameters — N_{bb}, N_{sc}, z, and the graft distribution — while maintaining narrow dispersity and enabling systematic variations presents significant challenges. This thesis will first describe our work to improve control over the graft polymer architecture (Chapter 2), then explore the physical consequences of polymer architecture in various contexts (Chapters 3–6). In order to motivate the challenges and opportunities for molecular design, the next section of this introduction will review existing synthetic routes to bottlebrush polymers.

1-2 Bottlebrush Polymer Synthesis

Bottlebrush polymers present unique synthetic challenges due to the steric demands imposed by the densely grafted architecture. Despite these challenges, advances in controlled polymerization[31-34] have enabled several routes to well-defined bottlebrush polymers. Several excellent reviews have catalogued these synthetic strategies.[35-38] This section will provide a brief overview, then introduce our approach.

Bottlebrush polymers can be synthesized according to one of three strategies: grafting-to, grafting-from, and grafting-through (Figure 1.3). Each strategy offers distinct advantages and disadvantages toward molecular design.

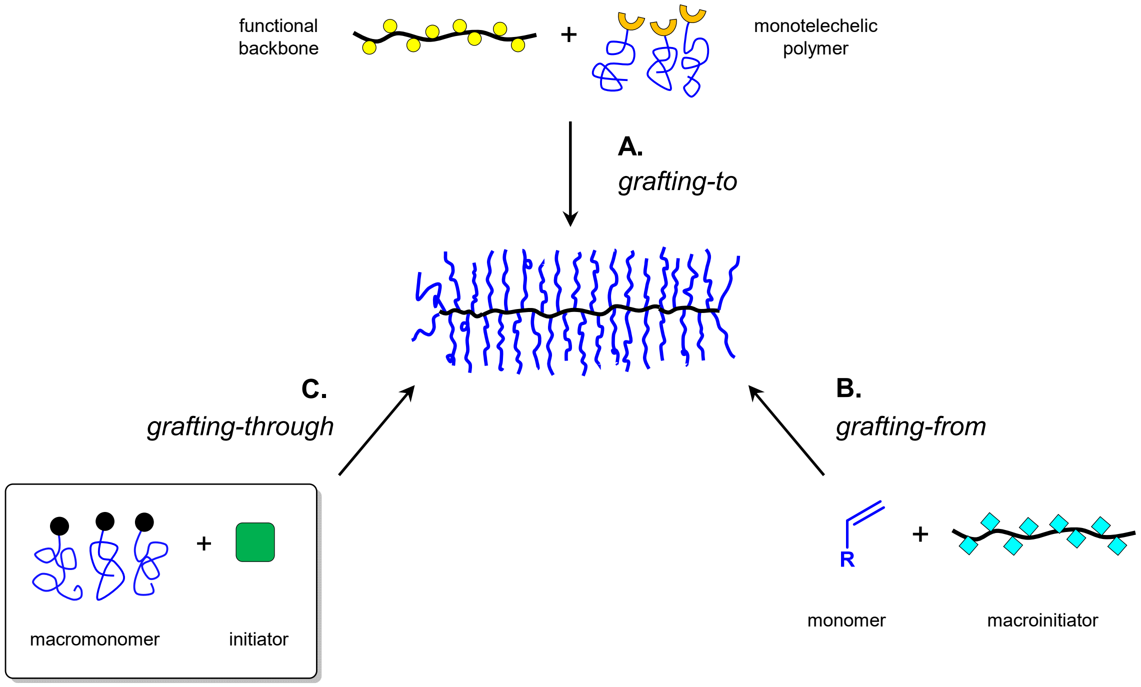

Figure 1.3: Three routes to synthesize bottlebrush polymers. (*A*) Grafting-to strategies attach monotelechelic chains to a pre-formed polymer backbone. (*B*) Grafting-from strategies grow side chains from a pre-formed macroinitiator. (*C*) Grafting-through strategies polymerize macromonomers in order to grow the brush through the backbone.

- The **grafting-to** approach attaches pre-formed monotelechelic chains to a pre-formed polymer backbone (Figure 1.3A). Grafting-to permits detailed characterization and modular variation of the side chains and backbone; however, steric demands typically limit the grafting density, result in non-uniform graft distributions, and require additional purification steps to remove unreacted chains.[39-42] Highly efficient coupling reactions (such as copper-catalyzed azide-alkyne click chemistry) can mitigate some of these limitations,[43-44] but in general high grafting densities ($z > 0.9$) can only be achieved with short side chains.
- The **grafting-from** approach grows side chains from a pre-formed macroinitiator (Figure 1.3B). Controlled radical polymerization enables the grafting-from synthesis of bottlebrushes with long backbones and narrow molecular weight distributions.[45-46] However, steric crowding typically limits the initiation efficiency along the backbone, leading to low grafting densities and non-uniform side chain

lengths.[47] In addition, determining z and N_{sc} is challenging, complicating the interpretation of molecular structure/property relationships.

- Lastly, the **grafting-through** approach grows the bottlebrush architecture through the backbone by polymerizing macromonomers (Figure 1.3C). Each macromonomer consists of a polymer chain with a polymerizable end group. In this way, grafting-through *guarantees* 100% grafting density and uniform side chain lengths. However, the inherently low concentration of polymerizable end groups typically limits the backbone degrees of polymerization that can be achieved.

In general, grafting-to and grafting-from strategies offer limited control over the side chain length, grafting density, and graft distribution due to steric crowding along the pre-formed backbone. In contrast, the grafting-through synthesis of bottlebrushes *guarantees* quantitative grafting density and uniform side chain lengths. Robust and efficient reactions are required in order to realize the full potential of the grafting-through approach. A wide variety of polymerization methods have been exploited, including atom-transfer radical polymerization (ATRP),[48-53] nitroxide-mediated polymerization (NMP),[54] anionic polymerization,[55-57] Suzuki polycondensation,[58-59] and cyclopolymerization of terminal diynes.[60] However, in many examples, the macromonomer synthesis is challenging, the functional group tolerance is limited, or only short backbone degrees of polymerization can be obtained.

Grafting-through ring-opening metathesis polymerization (ROMP) overcomes these limitations, providing a powerful route to well-defined graft polymers.[61-65] ROMP is a chain-growth polymerization in which cyclic monomers are opened and connected via the rearrangement of carbon-carbon double bonds (Scheme 1.1). Initiation occurs when a cyclic olefin monomer coordinates to the metal alkylidene catalyst. Subsequent [2+2] cycloaddition generates a metallacyclobutane intermediate, which then undergoes cycloreversion to produce a new olefin and a new metal alkylidene species. The high ring strain of the cyclic monomer disfavors unproductive cycloreversion and drives the reaction forward. Propagation occurs as these events are repeated until the monomer is completely consumed, equilibrium is reached, or termination occurs.

Scheme 1.1: Mechanism of ring-opening metathesis polymerization (ROMP). In well-defined catalysts, the metal center (M) is tungsten, molybdenum, or ruthenium.

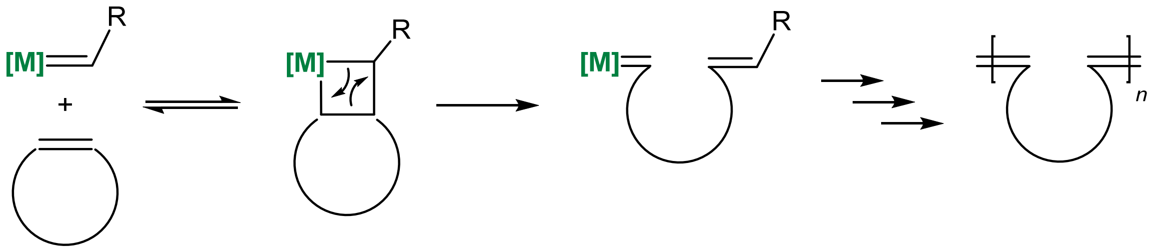

Judicious choice of the cyclic monomer and metathesis catalyst can achieve *living* ROMP. In a living polymerization, chain termination and chain transfer reactions are eliminated. As a result, living polymerizations generally exhibit a linear increase in molecular weight with conversion and a narrow molecular weight distribution ($Đ$ < 1.1).[61,66] This precision and control are highly desirable for materials design. In addition, the synthesis of well-defined model systems is crucial to enable the study of key structure-property relationships.

Norbornenes have emerged as the monomers of choice for living ROMP due to their high ring strain,[67] widespread commercial availability, and ease of functionalization. Early reports of grafting-through ROMP employed ω-norbornenyl macromonomers and a well-defined ruthenium or molybdenum metathesis catalyst;[68-72] however, these examples were not living due to the slow rate of initiation relative to propagation. Recent work has overcome this limitation by using the fast-initiating, highly active third-generation Grubbs catalyst, $(H_2IMes)(pyr)_2(Cl)_2Ru{=}CHPh$ (**G3**).[73-75] The living grafting-through ROMP of ω-norbornenyl macromonomers catalyzed by **G3** provides access to well-defined bottlebrush polymers (Figure 1.4). The macromonomers are connected one by one, stitching the bottlebrush architecture together through the backbone, until they are all consumed. Due to the high ring of norbornene and the high activity of **G3**, ultrahigh molecular weights (M_w > 4 MDa, N_{bb} > 1000) and excellent control over the molecular weight distribution ($Đ$ < 1.1) can be achieved.[76]

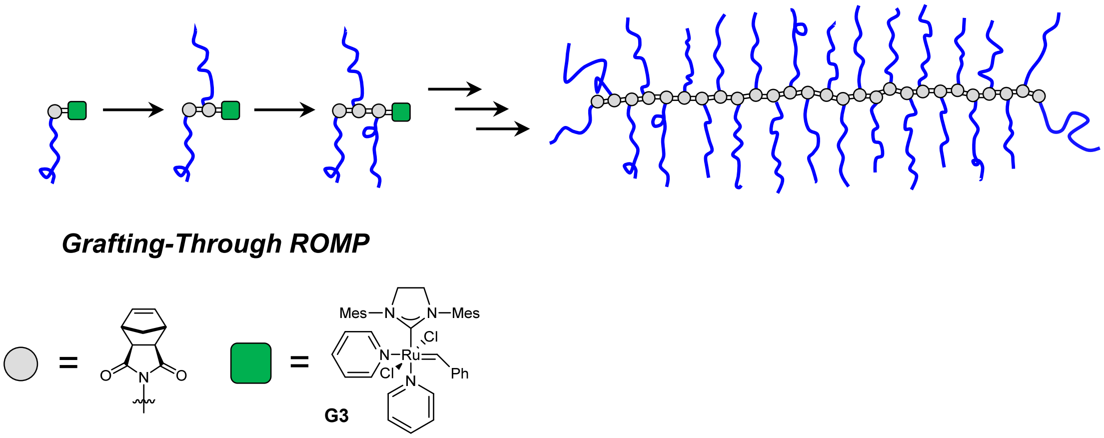

Figure 1.4: Living grafting-through ROMP of ω-norbornenyl macromonomers mediated by the fast-initiating **G3** catalyst. Macromonomers are stitched together through the backbone, providing access to well-defined bottlebrush polymers.

Living grafting-through ROMP enables precise, modular control over the graft polymer architecture. In the absence of termination events, ROMP proceeds until all of the macromonomer is consumed. At this point, even though propagation ceases, the catalyst is still active. The polymerization can be quenched to yield a bottlebrush *homopolymer* (Figure 1.5A); alternatively, a macromonomer with different side chain can be introduced, leading to AB bottlebrush *block polymers* (Figure 1.5B). The backbone degrees of polymerization for each block are directly determined by the macromonomer and catalyst stoichiometry: for example, given x equivalents of Macromonomer A and x equivalents of Macromonomer B relative to 1 equivalent of **G3**, $N_{\mathrm{bb,A}} = N_{\mathrm{bb,B}} = x$.

The relative block lengths can be changed simply by changing the macromonomer stoichiometry. Comparing Figure 1.5B–C, the *total* backbone degree of polymerization is fixed ($N_{\mathrm{bb}} = N_{\mathrm{bb,A}} + N_{\mathrm{bb,B}} = 2x$), but the relative block lengths in Figure 1.5C differ by an increment of $2y$. The grafting-through strategy also permits varying the side chain length (N_{sc}) while fixing all other aspects of the molecular architecture, simply by changing the macromonomer molecular weight (Figure 1.5D).

Chapter 2 will describe an approach we developed to tune the grafting density and graft distribution. Compared to fully grafted bottlebrushes (Figure 1.5A–D), the grafting density can be lowered by copolymerizing macromonomers with small-molecule co-monomers (Figure 1.5E). These co-monomers “dilute” the grafting density by increasing the number of backbone repeat units between grafts. In each block, if the macromonomer and diluent are similarly reactive, the graft distribution is uniform along the backbone (Figure 1.5E); if the relative reactivities differ, gradient or blocky distributions result (Figure 1.5F).

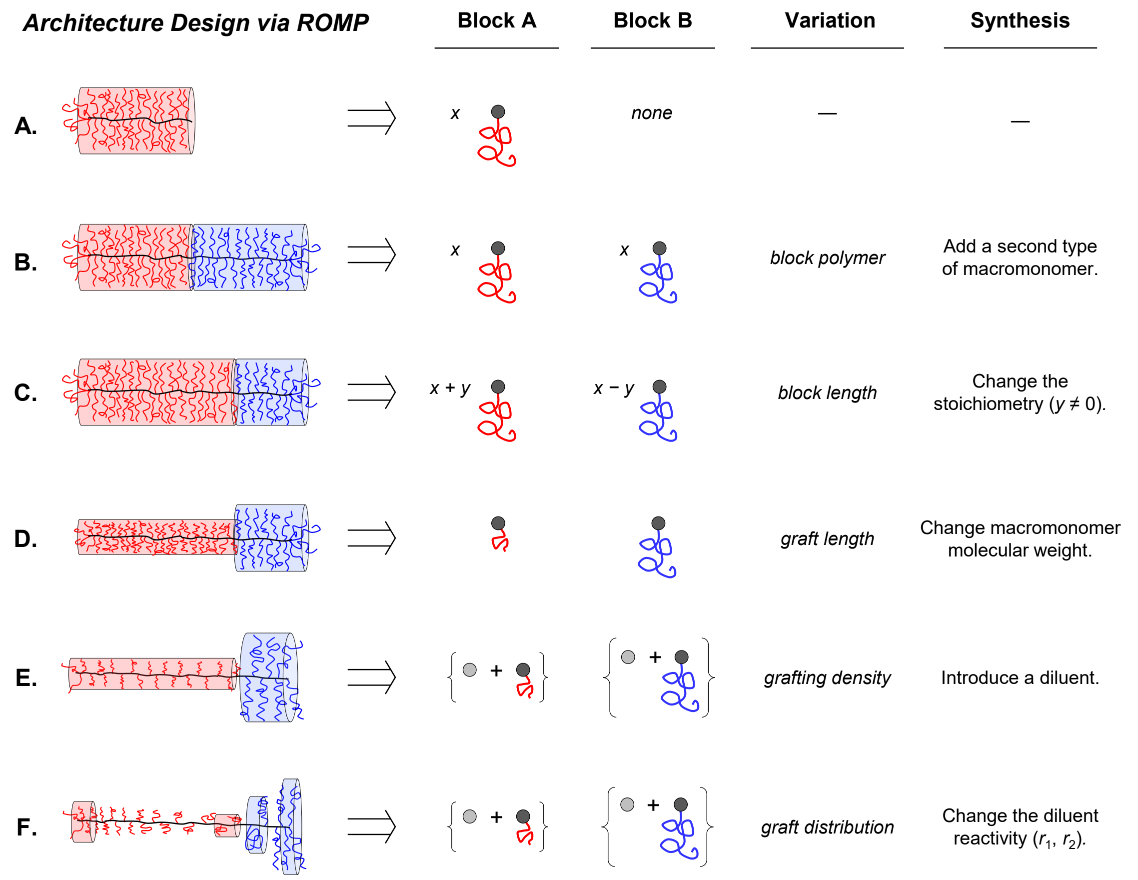

Figure 1.5: Opportunities for architectural design via living grafting-through ROMP. Schematic illustrations of polymer architectures are provided on the left. For ease of visualization, the polymers are illustrated in the limit of fully extended backbones, and cylinders indicate the anticipated local cross-sectional radii of gyration. Red and blue side chains indicate different chemical compositions (*i.e.*, Block A and Block B, respectively). For each row (B–F), the architectural variation compared to the previous row (*second to last column*) and required synthetic change (*last column*) are provided.

Living grafting-through ROMP emerges as a powerful route to well-defined bottlebrush polymers. The livingness of ROMP ensures low dispersity and enables tuning the backbone degrees of polymerization, while the grafting-through strategy guarantees fixed side chain degrees of polymerization and controlled grafting density. This exquisite control over the molecular architecture enables the study of fundamental structure-property relationships as well as the design of functional materials.

Block polymers, such as those illustrated in Figure 1.5B–F, represent an attractive platform for materials design. Chapters 3–6 of this thesis will discuss our work to study the impact of molecular architecture on the properties and phase behavior of block polymers. Section 1-3 will provide an overview of key concepts in block polymer self-assembly.

1-3 Block Polymer Self-Assembly

Block polymers are advanced materials synthesized by joining two or more polymer chains of different chemical compositions. The chemical incompatibility between components favors minimizing the number of contacts and therefore the interfacial area. In simple mixtures of oil and water, this thermodynamic penalty to mixing drives *macrophase* separation. In contrast, in block polymers, the single covalent linkage between blocks constrains separation to the *nanoscale*. A rich variety of periodic nanostructures can result.[34,77-80]

For the simplest possible block architecture (a linear AB diblock polymer), three synthetic parameters influence self-assembly: (1) the total degree of polymerization, N; (2) the block volume fractions ($f_A = 1-f_B$); and (3) the free-energy penalty mixing blocks, χ_{AB}. Figure 1.6 illustrates the equilibrium morphologies commonly observed for linear AB diblock polymers: body-centered cubic spheres, hexagonally packed cylinders, gyroids, and lamellae.[81-83] Recent reports have also identified complex low-symmetry structures in linear AB diblock polymers, such as Frank-Kasper phases and quasicrystal approximants.[84-88] This diverse phase space highlights the potential of block polymer self-assembly to tune the composition, geometry, and length scales of materials.

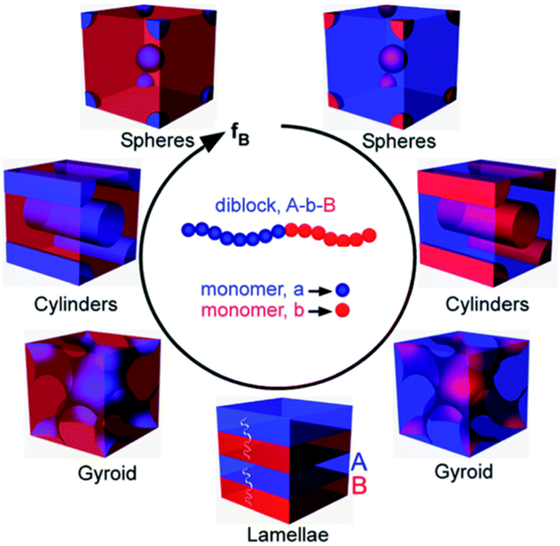

Figure 1.6: Equilibrium morphologies observed linear AB diblock polymers, the simplest polymer architecture. Reproduced with permission from Ref. 89.

The introduction of polymers with complex architectures creates additional opportunities for controlling self-assembly and properties. Graft polymers, due to their remarkable spatial dimensions and modular structures, offer several advantages for materials design. For example, due to steric-induced stiffening (Section 1-1), bottlebrush polymers display higher entanglement molecular weights,[4,9,90-91] lower melt viscosities,[3,92-93] and faster ordering kinetics[17,94] than their linear analogues. Recent reports have demonstrated that these unique dynamic properties enable bottlebrush block polymers to rapidly self-assemble to ultralarge domain sizes, on the order of the wavelength of visible light (d^* >100 nm) or even infrared radiation ($d^* > 400$ nm).[16-18,95] As a result, the bottlebrush architecture can enable the fabrication of materials that are generally inaccessible using linear polymers and other low-z analogues.

Figure 1.7 compiles examples of the relationship between d^* and the total backbone degree of polymerization (N_{bb}) for fully grafted bottlebrush diblock polymers. All brush diblock polymers feature poly(D,L-lactide) (PLA) and polystyrene (PS) side chains of similar molecular weights. In addition, all polymers were processed in the same way (*i.e.*, by thermal annealing) and assemble to long-range-ordered lamellar structures. Living grafting-through ROMP allows N_{bb} to be tuned over a wide range ($10 < N_{\mathrm{bb}} < 1000$), which in turn enables control over d^* ($10 < d^* < 1000$).

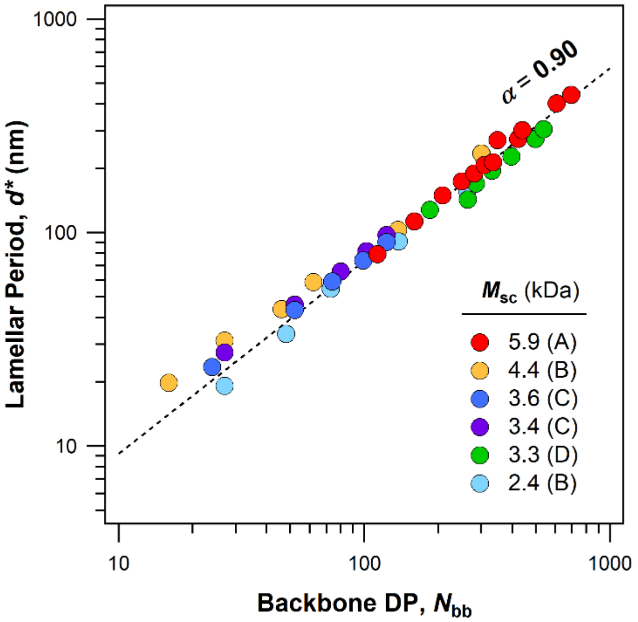

Figure 1.7: Compiled reported examples of the scaling of the lamellar period (d^*) with the backbone length (N_{bb}) for six series of bottlebrush diblock polymers. All polymers are fully grafted and feature symmetric PLA and PS side chains. The average side chain molecular weights (M_{sc}, in kDa) are provided in the legend. The letters in parentheses indicate the corresponding reference: (*A*) = Ref. 17, (*B*) = Ref. 94, (*C*) = Ref. 96, and (*D*) = Ref. 97. A dotted line corresponding to $\alpha = 0.90$ is included for comparison.

Figure 1.8 compares the self-assembly of linear ($z = 0$) and fully grafted bottlebrush ($z = 1$) block polymers to lamellar morphologies. For symmetric linear diblock polymers, arguments based on free energy demands accurately predict the scaling behavior ($d^* \sim N_{bb}^{\alpha}$). The scaling exponent α is 1/2 in the weak segregation limit ($\chi N_{bb} \approx 10.5$) and plateaus at 2/3 in the strong segregation limit ($\chi N_{bb} >> 10.5$).[83,98] The small scaling exponent is inherently related to the coil-like chain conformations. In contrast, bottlebrush block polymers display much larger scaling exponents ($\alpha = 0.8$–0.9),[16-17,94,99] consistent with their extended, wormlike backbone conformations. Understanding the connections between the molecular architecture, physical properties, and self-assembled structure will create further opportunities for materials design.

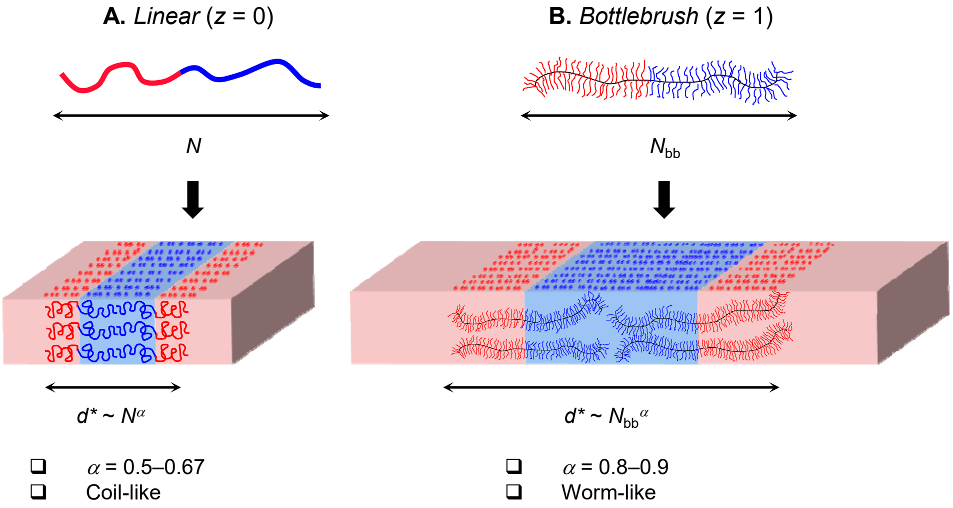

Figure 1.8: Self-assembly of (*A*) linear and (*B*) bottlebrush diblock polymers to lamellar morphologies. The scaling of the lamellar period with backbone degree of polymerization ($d^* \sim N_{\mathrm{bb}}^{\alpha}$) differs as a consequence of the molecular architecture.

1-4 Thesis Outline

This thesis presents our work studying the impact of the graft polymer architecture on block polymer self-assembly. Our work connects (1) the synthesis of polymers with precisely tailored molecular architectures, (2) the study of fundamental structure-property relationships, and (3) the design of functional materials.

All of the work described in this thesis has been crucially enabled by robust chemistry — that is, by our ability to synthesize well-defined polymers by ring-opening metathesis polymerization (ROMP). In order to highlight the central role of chemistry, this thesis is not structured in chronological order. Instead, we will first discuss our recent contributions to expanding the ROMP synthetic method (Chapter 2). Copolymerizing a macromonomer and a small-molecule co-monomer provides access to well-defined polymers spanning the linear, comb, and bottlebrush regimes.

The synthetic advances introduced in Chapter 2 enable systematic variations of the grafting density, graft distribution, and backbone degrees of polymerization. In Chapter 3, we will explore the physical consequences of these architectural variations in two contexts: block polymer self-assembly and linear rheological properties. Chapters 4 and 5 discuss the phase behavior of fully grafted ABC bottlebrush triblock terpolymers featuring low-χ

interactions between the end blocks. The interplay of low-χ design and the molecular architecture reveals competing influences, which emerge in our discovery of a unique partially mixed lamellar morphology (LAM$_{\mathrm{P}}$) and other physical consequences. Lastly, Chapter 6 describes applications of bottlebrush polymers as functional materials. Self-assembly enables mesoscale structural control over many materials properties, such as reflectivity, conductivity, and modulus. Collectively, our work creates new opportunities for molecular and materials design.

1-5 References

(1) Fredrickson, G. H. *Macromolecules* **1993**, *26*, 2825–2831.
(2) Mikhaylov, I. V.; Darinskii, A. A. *Polym. Sci. Ser. A* **2015**, *57*, 239–250.
(3) Dalsin, S. J.; Hillmyer, M. A.; Bates, F. S. *ACS Macro Lett.* **2014**, *3*, 423–427.
(4) Dalsin, S. J.; Hillmyer, M. A.; Bates, F. S. *Macromolecules* **2015**, *48*, 4680–4691.
(5) López-Barrón, C. R.; Brant, P.; Eberle, A. P. R.; Crowther, D. J. *J. Rheol.* **2015**, *59*, 865–883.
(6) Pakula, T.; Zhang, Y.; Matyjaszewski, K.; Lee, H.-i.; Boerner, H.; Qin, S.; Berry, G. C. *Polymer* **2006**, *47*, 7198–7206.
(7) Cai, L.-H.; Kodger, T. E.; Guerra, R. E.; Pegoraro, A. F.; Rubinstein, M.; Weitz, D. A. *Adv. Mater.* **2015**, *27*, 5132–5140.
(8) Vatankhah-Varnoosfaderani, M.; Daniel, W. F. M.; Zhushma, A. P.; Li, Q.; Morgan, B. J.; Matyjaszewski, K.; Armstrong, D. P.; Spontak, R. J.; Dobrynin, A. V.; Sheiko, S. S. *Adv. Mater.* **2017**, *29*, 1604209.
(9) Daniel, W. F. M.; Burdynska, J.; Vatankhah-Varnoosfaderani, M.; Matyjaszewski, K.; Paturej, J.; Rubinstein, M.; Dobrynin, A. V.; Sheiko, S. S. *Nat. Mater.* **2016**, *15*, 183–189.
(10) Lee, S.; Spencer, N. D. *Science* **2008**, *319*, 575–576.
(11) Bolton, J.; Bailey, T. S.; Rzayev, J. *Nano Lett.* **2011**, *11*, 998–1001.
(12) Ahn, S.-k.; Carrillo, J.-M. Y.; Keum, J. K.; Chen, J.; Uhrig, D.; Lokitz, B. S.; Sumpter, B. G.; Michael Kilbey, S. *Nanoscale* **2017**, *9*, 7071–7080.
(13) Bates, C. M.; Chang, A. B.; Momčilović, N.; Jones, S. C.; Grubbs, R. H. *Macromolecules* **2015**, *48*, 4967–4973.
(14) Bates, C. M.; Chang, A. B.; Schulze, M. W.; Momčilović, N.; Jones, S. C.; Grubbs, R. H. *J. Polym. Sci., Part B: Polym. Phys.* **2016**, *54*, 292–300.
(15) McNicholas, B. J.; Blakemore, J. D.; Chang, A. B.; Bates, C. M.; Kramer, W. W.; Grubbs, R. H.; Gray, H. B. *J. Am. Chem. Soc.* **2016**, *138*, 11160–11163.
(16) Rzayev, J. *Macromolecules* **2009**, *42*, 2135–2141.
(17) Sveinbjörnsson, B. R.; Weitekamp, R. A.; Miyake, G. M.; Xia, Y.; Atwater, H. A.; Grubbs, R. H. *Proc. Natl. Acad. Sci. U.S.A.* **2012**, *109*, 14332–14336.

(18) Miyake, G. M.; Weitekamp, R. A.; Piunova, V. A.; Grubbs, R. H. *J. Am. Chem. Soc.* **2012**, *134*, 14249–14254.
(19) Birshtein, T. M.; Borisov, O. V.; Zhulina, Y. B.; Khokhlov, A. R.; Yurasova, T. A. *Polym. Sci. U.S.S.R.* **1987**, *29*, 1293–1300.
(20) Saariaho, M.; Ikkala, O.; Szleifer, I.; Erukhimovich, I.; ten Brinke, G. *J. Chem. Phys.* **1997**, *107*, 3267–3276.
(21) Saariaho, M.; Szleifer, I.; Ikkala, O.; Brinke, G. t. *Macromol. Theory Simul.* **1998**, *7*, 211–216.
(22) Kikuchi, M.; Lien, L. T. N.; Narumi, A.; Jinbo, Y.; Izumi, Y.; Nagai, K.; Kawaguchi, S. *Macromolecules* **2008**, *41*, 6564–6572.
(23) Kikuchi, M.; Nakano, R.; Jinbo, Y.; Saito, Y.; Ohno, S.; Togashi, D.; Enomoto, K.; Narumi, A.; Haba, O.; Kawaguchi, S. *Macromolecules* **2015**, *48*, 5878–5886.
(24) Subbotin, A.; Saariaho, M.; Stepanyan, R.; Ikkala, O.; ten Brinke, G. *Macromolecules* **2000**, *33*, 6168–6173.
(25) Saariaho, M.; Subbotin, A.; Szleifer, I.; Ikkala, O.; ten Brinke, G. *Macromolecules* **1999**, *32*, 4439–4443.
(26) Subbotin, A.; Saariaho, M.; Ikkala, O.; ten Brinke, G. *Macromolecules* **2000**, *33*, 3447–3452.
(27) Nakamura, Y.; Norisuye, T. *Polym J* **2001**, *33*, 874–878.
(28) Hatanaka, Y.; Nakamura, Y. *Polymer* **2013**, *54*, 1538–1542.
(29) Paturej, J.; Sheiko, S. S.; Panyukov, S.; Rubinstein, M. *Sci. Adv.* **2016**, *2*, e1601478.
(30) Liang, H.; Cao, Z.; Wang, Z.; Sheiko, S. S.; Dobrynin, A. V. *Macromolecules* **2017**, *50*, 3430–3437.
(31) Hadjichristidis, N.; Pitsikalis, M.; Pispas, S.; Iatrou, H. *Chem. Rev.* **2001**, *101*, 3747–3792.
(32) Polymeropoulos, G.; Zapsas, G.; Ntetsikas, K.; Bilalis, P.; Gnanou, Y.; Hadjichristidis, N. *Macromolecules* **2017**, *50*, 1253–1290.
(33) Matyjaszewski, K.; Tsarevsky, N. V. *Nature Chem.* **2009**, *1*, 276–288.
(34) Bates, C. M.; Bates, F. S. *Macromolecules* **2017**, *50*, 3–22.
(35) Zhang, M.; Müller, A. H. E. *J. Polym. Sci., Part A: Polym. Chem.* **2005**, *43*, 3461–3481.
(36) Sheiko, S. S.; Sumerlin, B. S.; Matyjaszewski, K. *Prog. Polym. Sci.* **2008**, *33*, 759–785.
(37) Verduzco, R.; Li, X.; Pesek, S. L.; Stein, G. E. *Chem. Soc. Rev.* **2015**, *44*, 2405–2420.
(38) Müllner, M.; Müller, A. H. E. *Polymer* **2016**, *98*, 389–401.
(39) Schappacher, M.; Deffieux, A. *Macromolecules* **2005**, *38*, 7209–7213.
(40) Gao, H.; Matyjaszewski, K. *J. Am. Chem. Soc.* **2007**, *129*, 6633–6639.
(41) Lanson, D.; Ariura, F.; Schappacher, M.; Borsali, R.; Deffieux, A. *Macromolecules* **2009**, *42*, 3942–3950.
(42) Chen, P.; Li, C.; Liu, D.; Li, Z. *Macromolecules* **2012**, *45*, 9579–9584.
(43) Engler, A. C.; Lee, H. i.; Hammond, P. T. *Angew. Chem., Int. Ed.* **2009**, *48*, 9334–9338.
(44) De, S.; Khan, A. *Chem. Commun.* **2012**, *48*, 3130–3132.
(45) Beers, K. L.; Gaynor, S. G.; Matyjaszewski, K.; Sheiko, S. S.; Möller, M. *Macromolecules* **1998**, *31*, 9413–9415.

(46) Börner, H. G.; Duran, D.; Matyjaszewski, K.; da Silva, M.; Sheiko, S. S. *Macromolecules* **2002**, *35*, 3387–3394.

(47) Sumerlin, B. S.; Neugebauer, D.; Matyjaszewski, K. *Macromolecules* **2005**, *38*, 702–708.

(48) Shinoda, H.; Matyjaszewski, K. *Macromolecules* **2001**, *34*, 6243–6248.

(49) Börner, H. G.; Matyjaszewski, K. *Macromol. Symp.* **2002**, *177*, 1–16.

(50) Chul, H. S.; Shijun, J.; Mircea, T.; Tomasz, K.; Krzysztof, M.; C., G. A.; Maurice, B. *J. Polym. Sci., Part A: Polym. Chem.* **2002**, *40*, 2736–2749.

(51) Neugebauer, D.; Zhang, Y.; Pakula, T.; Sheiko, S. S.; Matyjaszewski, K. *Macromolecules* **2003**, *36*, 6746–6755.

(52) Shinoda, H.; Matyjaszewski, K.; Okrasa, L.; Mierzwa, M.; Pakula, T. *Macromolecules* **2003**, *36*, 4772–4778.

(53) Neugebauer, D.; Zhang, Y.; Pakula, T. *J. Polym. Sci., Part A: Polym. Chem.* **2006**, *44*, 1347–1356.

(54) Hawker, C. J.; Mecerreyes, D.; Elce, E.; Dao, J.; Hedrick, J. L.; Barakat, I.; Dubois, P.; Jérôme, R.; Volksen, W. *Macromol. Chem. Phys.* **1997**, *198*, 155–166.

(55) Ederle, Y.; Isel, F.; Grutke, S.; Lutz, P. J. *Macromol. Symp.* **1998**, *132*, 197–206.

(56) Pantazis, D.; Chalari, I.; Hadjichristidis, N. *Macromolecules* **2003**, *36*, 3783–3785.

(57) Koji, I.; Junichiro, S. *J. Appl. Polym. Sci.* **2003**, *87*, 1790–1793.

(58) Sheng, Z.; Yu, Z.; Haijian, T.; Yufeng, Z.; Yu, P.; Feng, Z.; Qikai, Z.; Zhihao, S.; Xinghe, F. *J. Polym. Sci., Part A: Polym. Chem.* **2014**, *52*, 1519–1524.

(59) Zeigler, D. F.; Mazzio, K. A.; Luscombe, C. K. *Macromolecules* **2014**, *47*, 5019–5028.

(60) Kang, E.-H.; Lee, I.-H.; Choi, T.-L. *ACS Macro Lett.* **2012**, *1*, 1098–1102.

(61) Bielawski, C. W.; Grubbs, R. H. *Prog. Polym. Sci.* **2007**, *32*, 1–29.

(62) Leitgeb, A.; Wappel, J.; Slugovc, C. *Polymer* **2010**, *51*, 2927–2946.

(63) Sutthasupa, S.; Shiotsuki, M.; Sanda, F. *Polym. J.* **2010**, *42*, 905–915.

(64) Martinez, H.; Ren, N.; Matta, M. E.; Hillmyer, M. A. *Polym. Chem.* **2014**, *5*, 3507–3532.

(65) Grubbs, R. H.; Khosravi, E. *Handbook of Metathesis: Polymer Synthesis*; Wiley, 2015.

(66) Matyjaszewski, K. *Macromolecules* **1993**, *26*, 1787–1788.

(67) Schleyer, P. v. R.; Williams, J. E.; Blanchard, K. R. *J. Am. Chem. Soc.* **1970**, *92*, 2377–2386.

(68) Breunig, S.; Héroguez, V.; Gnanou, Y.; Fontanille, M. *Macromol. Symp.* **1995**, *95*, 151–166.

(69) Heroguez, V.; Breunig, S.; Gnanou, Y.; Fontanille, M. *Macromolecules* **1996**, *29*, 4459–4464.

(70) Mecerreyes, D.; Dahan, D.; Lecomte, P.; Dubois, P.; Demonceau, A.; Noels, A. F.; Jérôme, R. *J. Polym. Sci., Part A: Polym. Chem.* **1999**, *37*, 2447–2455.

(71) Allcock, H. R.; de Denus, C. R.; Prange, R.; Laredo, W. R. *Macromolecules* **2001**, *34*, 2757–2765.

(72) Jha, S.; Dutta, S.; Bowden, N. B. *Macromolecules* **2004**, *37*, 4365–4374.

(73) Bielawski, C. W.; Grubbs, R. H. *Angew. Chem., Int. Ed.* **2000**, *39*, 2903–2906.

(74) Choi, T.-L.; Grubbs, R. H. *Angew. Chem. Int. Ed.* **2003**, *42*, 1743–1746.

(75) Xia, Y.; Kornfield, J. A.; Grubbs, R. H. *Macromolecules* **2009**, *42*, 3761–3766.

(76) Haugan, I. N.; Maher, M. J.; Chang, A. B.; Lin, T.-P.; Grubbs, R. H.; Hillmyer, M. A.; Bates, F. S. *ACS Macro Lett.* **2018**, *7*, 525–530.
(77) Bates, F. S.; Fredrickson, G. H. *Phys. Today* **1999**, *52*, 32–38.
(78) Bates, F. S.; Fredrickson, G. H. *Annu. Rev. Phys. Chem.* **1990**, *41*, 525–557.
(79) Park, C.; Yoon, J.; Thomas, E. L. *Polymer* **2003**, *44*, 6725–6760.
(80) Bates, F. S.; Hillmyer, M. A.; Lodge, T. P.; Bates, C. M.; Delaney, K. T.; Fredrickson, G. H. *Science* **2012**, *336*, 434–440.
(81) Leibler, L. *Macromolecules* **1980**, *13*, 1602–1617.
(82) Khandpur, A. K.; Foerster, S.; Bates, F. S.; Hamley, I. W.; Ryan, A. J.; Bras, W.; Almdal, K.; Mortensen, K. *Macromolecules* **1995**, *28*, 8796–8806.
(83) Matsen, M. W.; Bates, F. S. *Macromolecules* **1996**, *29*, 1091–1098.
(84) Lee, S.; Bluemle, M. J.; Bates, F. S. *Science* **2010**, *330*, 349–353.
(85) Gillard, T. M.; Lee, S.; Bates, F. S. *Proc. Natl. Acad. Sci. U.S.A.* **2016**, *113*, 5167–5172.
(86) Kim, K.; Schulze, M. W.; Arora, A.; Lewis, R. M.; Hillmyer, M. A.; Dorfman, K. D.; Bates, F. S. *Science* **2017**, *356*, 520–523.
(87) Lee, S.; Leighton, C.; Bates, F. S. *Proc. Natl. Acad. Sci. U.S.A.* **2014**, *111*, 17723–17731.
(88) Schulze, M. W.; Lewis, R. M.; Lettow, J. H.; Hickey, R. J.; Gillard, T. M.; Hillmyer, M. A.; Bates, F. S. *Phys. Rev. Lett.* **2017**, *118*, 207801.
(89) Hu, H.; Gopinadhan, M.; Osuji, C. O. *Soft Matter* **2014**, *10*, 3867–3889.
(90) Abbasi, M.; Faust, L.; Riazi, K.; Wilhelm, M. *Macromolecules* **2017**, *50*, 5964–5977.
(91) Hu, M.; Xia, Y.; McKenna, G. B.; Kornfield, J. A.; Grubbs, R. H. *Macromolecules* **2011**, *44*, 6935–6943.
(92) Jeong, S. H.; Kim, J. M.; Baig, C. *Macromolecules* **2017**, *50*, 4491–4500.
(93) Lohse, D. J.; Milner, S. T.; Fetters, L. J.; Xenidou, M.; Hadjichristidis, N.; Mendelson, R. A.; García-Franco, C. A.; Lyon, M. K. *Macromolecules* **2002**, *35*, 3066–3075.
(94) Gu, W.; Huh, J.; Hong, S. W.; Sveinbjornsson, B. R.; Park, C.; Grubbs, R. H.; Russell, T. P. *ACS Nano* **2013**, *7*, 2551–2558.
(95) Runge, M. B.; Bowden, N. B. *J. Am. Chem. Soc.* **2007**, *129*, 10551–10560.
(96) Lin, T.-P.; Chang, A. B.; Luo, S.-X.; Chen, H.-Y.; Lee, B.; Grubbs, R. H. *ACS Nano* **2017**, *11*, 11632–11641.
(97) Macfarlane, R. J.; Kim, B.; Lee, B.; Weitekamp, R. A.; Bates, C. M.; Lee, S. F.; Chang, A. B.; Delaney, K. T.; Fredrickson, G. H.; Atwater, H. A.; Grubbs, R. H. *J. Am. Chem. Soc.* **2014**, 17374–17377.
(98) Semenov, A. V. *Sov. Phys.-JETP (Engl. Transl.)* **1985**, *61*, 733–742.
(99) Xia, Y.; Olsen, B. D.; Kornfield, J. A.; Grubbs, R. H. *J. Am. Chem. Soc.* **2009**, *131*, 18525–18532.

Chapter 2

Control over the Graft Polymer Architecture via Ring-Opening Metathesis Polymerization

1. Lin, T.-P.; Chang, A. B.; Chen, H.-Y.; Liberman-Martin, A. L.; Bates, C. M.; Voegtle, M. J.; Bauer, C. A.; Grubbs, R. H. Control of Grafting Density and Distribution in Graft Polymers by Living Ring-Opening Metathesis Copolymerization. *J. Am. Chem. Soc.* **2017**, *139*, 3896–3903.

2. Chang, A. B.;+ Lin, T.-P.;+ Thompson, N. B.; Luo, S.-X.; Liberman-Martin, A. L.; Chen, H.-Y.; Grubbs, R. H. Design, Synthesis, and Self-Assembly of Polymers with Tailored Graft Distributions. *J. Am. Chem. Soc.* **2017**, *139*, 17683–17693. (+*Equal contributions.*)

ABSTRACT

Grafting density and graft distribution impact the chain dimensions and physical properties of polymers. However, achieving precise control over these structural parameters presents long-standing synthetic challenges. In this chapter, we introduce a versatile strategy to synthesize polymers with tailored architectures via grafting-through ring-opening metathesis polymerization (ROMP). One-pot copolymerization of an *ω*-norbornenyl macromonomer and a discrete norbornenyl co-monomer (diluent) provides opportunities to control the backbone sequence and therefore the side chain distribution. Toward sequence control, the homopolymerization kinetics of 23 diluents were studied, representing diverse variations in the stereochemistry, anchor groups, and substituents. These modifications tuned the homopolymerization rate constants over two orders of magnitude ($0.36\ \mathrm{M}^{-1}\ \mathrm{s}^{-1} < k_{\mathrm{homo}} < 82\ \mathrm{M}^{-1}\ \mathrm{s}^{-1}$). Rate trends were identified and elucidated by complementary mechanistic and density functional theory (DFT) studies. Building on this foundation, complex architectures were achieved through copolymerizations of selected diluents with a poly(D,L-lactide) (**PLA**), polydimethylsiloxane (**PDMS**), or polystyrene (**PS**) macromonomer. The cross-propagation rate constants were obtained by non-linear least squares fitting of the instantaneous co-monomer concentrations according to the Mayo-Lewis terminal model. In-depth kinetic analyses indicate a wide range of

accessible macromonomer/diluent reactivity ratios ($0.08 < r_1/r_2 < 20$), corresponding to blocky, gradient, or random backbone sequences. Collectively, the insights provided herein into the ROMP mechanism, monomer design, and homo- and copolymerization rate trends offer a general strategy for the design and synthesis of graft polymers with arbitrary architectures. Controlled copolymerization therefore expands the parameter space for molecular and materials design.

Table of Contents

2-1 Introduction

Molecular architecture impacts the chemical and physical properties of all polymers. Achieving precise control over the chain connectivity, sequence, and symmetry presents synthetic challenges as well as rich opportunities for materials design. Over the past several decades, advances in controlled polymerization have enabled the synthesis of polymers with complex architectures.[1-4] Graft polymers are a class of such nonlinear architectures featuring polymeric side chains attached to a polymeric backbone. The grafting density and distribution of grafts along the backbone determine the steric interactions between side chains and in turn influence the physical properties. Graft polymers display many unique properties compared to their linear analogues, such as extended chain conformations,[5-8] increased entanglement molecular weights,[9-12] and architecture-dependent rheological behavior.[13-16] Recent studies have harnessed these properties in a wide variety of applications in photonics,[17-19] drug delivery,[20-22] transport,[23-

[24] and thermoplastics.[25-26] Continued progress in synthetic command over polymer architecture enables further studies of structure-property relationships and inspires new potential applications.

Graft polymers represent ideal platforms to study how chain connectivity defines nanostructures and thereby physical properties. Despite the importance of grafting density and graft distribution, synthetic strategies that permit precise control of these parameters are currently limited. Grafting-to[27-30] and grafting-from[31-34] approaches require multiple steps in which side chains are either attached to or grown from a pre-formed backbone. Steric congestion along the backbone typically prevents precise control over the molecular weight, grafting density, and side chain distribution. As a result, the synthesis of well-defined *architectural* variants – let alone materials with variable *chemical* compositions – is challenging. Grafting-through ring-opening metathesis polymerization (ROMP) closes this gap by affording wide functional group tolerance and enabling simultaneous control over side chain and backbone lengths.[35-37] In this chapter, we will first introduce a ROMP strategy that provides access to polymers with uniform grafting densities spanning the linear to bottlebrush regimes (Sections 2-2 to 2-7). We will then expand the scope of architectural design to graft polymers with tapered and blocky graft distributions (Sections 2-8 to 2-11).

Our approach employs controlled copolymerization of a macromonomer and a small-molecule diluent. The relative reactivity of the two co-monomers directly dictates the spatial arrangement of the side chains. For example, if the macromonomer and diluent copolymerize at approximately the same rate, the side chains are therefore uniformly distributed along the polymer backbone (Figure 2.1A). Such polymers are widely termed "cylindrical molecular brushes" due to their steric-induced stiffness and axes of symmetry.[38-42] These cylindrical brushes can be modeled as wormlike chains with the same average cross-sectional radius (R_c) along the entire backbone.[5,43-45] On the other hand, if the macromonomer and diluent copolymerize at different rates, the resulting gradient sequences are anticipated to template different side chain conformations. Depending on the extent of side chain stretching, R_c varies and tapered, non-cylindrical molecular shapes result (Figure 2.1B). Control over the co-monomer distribution therefore opens opportunities to manipulate the chain dimensions and physical properties.

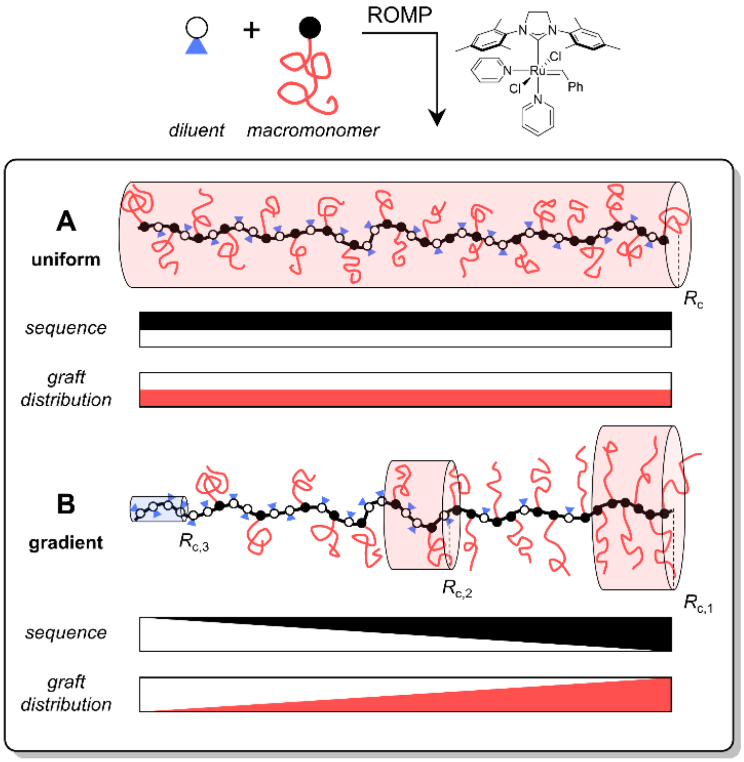

Figure 2.1: Grafting-through ROMP of a small-molecule diluent (*white*) and a macromonomer (*black*). Since the side chains (*red*) are connected to certain backbone units, control over the backbone sequence directly determines the side chain distribution: (*A*) uniform, (*B*) gradient, etc. The anticipated average cross-sectional radius of gyration (R_c) is indicated. For ease of visualization, chains are illustrated in the limit of fully extended backbones.

In this work, we provide the first demonstration that varying the stereochemistry and steric profiles of discrete co-monomers enables the synthesis of well-defined polymers with tunable grafting density and graft distribution. We will first discuss the homopolymerization kinetics of three ω-norbornenyl macromonomers and three discrete norbornenyl diluents, then build complexity through controlled copolymerizations. Trends in the homo- and cross-propagation rates will be outlined to provide guidance for the future rational design of polymer architectures with arbitrary graft chemistry and distribution. In Chapter 3 of this thesis, we will discuss the physical consequences of varying the grafting density and graft distribution in the contexts of block polymer self-assembly and rheology. Living ROMP enables these diverse studies, providing new opportunities for molecular and materials design.

2-2 Monomer Design

In pursuit of control over the graft polymer architecture, the homopolymerization kinetics of macromonomers and diluents were first investigated. Cyclic olefinic monomers that inherently favor alternating sequences were avoided,[46-47] since strict alternation would only afford 50% grafting density and preclude control over the graft distribution. Norbornene-functionalized derivatives, which rarely result in alternating polynorbornenes,[48-50] were selected for the present study. Relief of the high ring strain in norbornene, mediated by highly active ruthenium metathesis catalysts, enables grafting-through ROMP to produce well-defined bottlebrush polymers.[51-53] We note that random copolymerizations of norbornenes have been previously inferred,[52,54-55] suggesting potential opportunities for advanced sequence control; however, quantitative sequence determinations are lacking. For the present studies, ω-norbornenyl polystyrene (**PS**, M_n = 3990 g/mol), polylactide (**PLA**, M_n = 3230 g/mol), and polydimethylsiloxane (**PDMS**, M_n = 1280 g/mol) macromonomers featuring an *exo*-imide anchor group were prepared (Figure 2.2). (Synthetic details are provided in Appendix A, Section A-2.) **PS** and **PLA** macromonomers of similar molecular weights have been previously employed in the synthesis of well-defined bottlebrush polymers,[19,23] making them attractive candidates for our studies. For the small-molecule diluents, we explored a family of *endo*,*exo*-norbornenyl diesters (dimethyl **DME**, diethyl **DEE**, di-*n*-butyl **DBE**, each with molecular weight <300 g/mol) that could be easily assembled by Diels-Alder reactions of cyclopentadiene and the appropriate fumarate (Appendix A, Section A-3). We anticipated different propagation rates for these norbornenyl diesters,[56] amenable to tuning the relative reactivity of diverse diluent/macromonomer pairs. Section 2.8 of this chapter expands the scope of monomer design to other types of diluents.

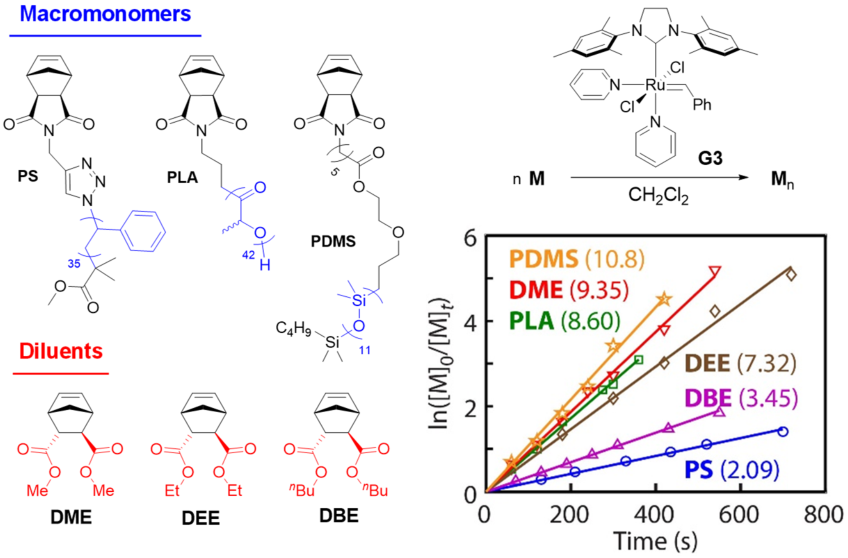

Figure 2.2: (*left*) Structures of macromonomers (**PS**, **PLA**, **PDMS**) and diluents (**DME**, **DEE**, **DBE**). (*right*) Plots of $\ln([M]_0/[M]_t)$ versus time, showing first-order kinetics for the homopolymerization of norbornene monomers (0.05 M) catalyzed by **G3** (0.5 mM) in CH_2Cl_2 at 298 K (orange stars: **PDMS**, inverted red triangles: **DME**, green squares: **PLA**, brown diamonds: **DEE**, purple triangles: **DBE**, blue circles = **PS**). The numbers in parentheses indicate k_{obs} (10^{-3} s^{-1}) under the reaction conditions.

2-3 Homopolymerization Kinetics

ROMP of each monomer in CH_2Cl_2 (0.05 M) was mediated by the highly active third-generation olefin metathesis catalyst,[57] $(H_2IMes)(pyr)_2(Cl)_2Ru{=}CHPh$ (**G3**, 0.5 mM). At different time points, aliquots were extracted from the reaction mixture and immediately quenched in a separate vial containing a large excess of ethyl vinyl ether. Subsequently, the quenched reactions were analyzed by size-exclusion chromatography (SEC) and ^1H NMR spectroscopy, allowing evaluation of the conversion, molecular weight, and molecular weight dispersity. (See Appendix A, Section A-4 for standard procedures.) As shown in Figure 2.2, the depletion of monomers is first-order. Since the rate of initiation for **G3** is much faster than that of propagation under these conditions,[57-58] the observed first-order rate constant (k_{obs}) can be used to calculate the second-order self-propagation rate constant (k_{homo}) according to Eq. 2-1 (M = monomer):

$$-\frac{d[M]_t}{dt} = k_{obs}[M]_t = k_{homo}[G3]_0[M]_t \qquad \text{Eq. 2-1}$$

For many monomers, the rate constants were determined at least in triplicate. The calculated values typically varied by no more than five percent (Figure 2.3).

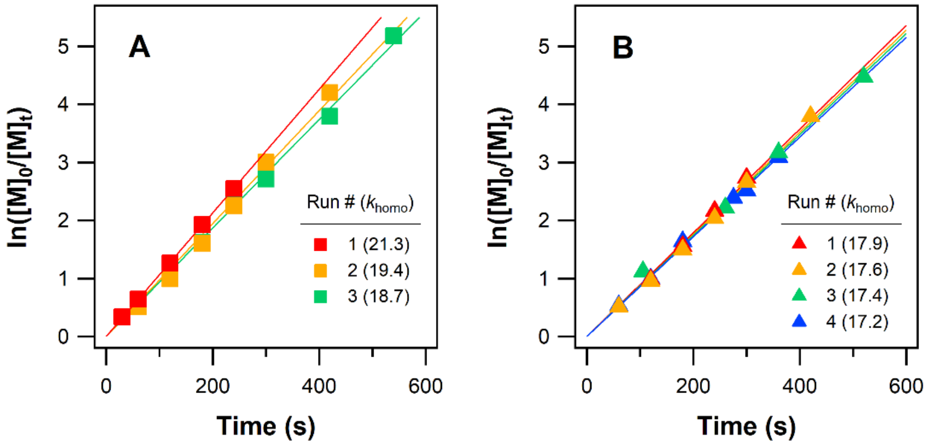

Figure 2.3: Representative repeated runs to determine k_{homo} (M^{-1} s^{-1}) for (*A*) **DME** and (*B*) and **PLA**. For all diluents and macromonomers studied herein, the measured rate constants are consistent across multiple runs.

The rate constant k_{homo}, which is independent of the catalyst concentration, is directly relevant to our copolymerization kinetic analyses. The homopolymerization kinetic results are summarized in Table 2.1.

Table 2.1: Homopolymerizations of macromonomers and diluents in CH_2Cl_2 at 298 K.

Monomer	k_{homo} (M^{-1} s^{-1})	**Expected M_n[a] (kg/mol)**	**Measured M_n[b] (kg/mol)**	**Đ[b]**	**Conv. (%)**
PS	4.18	399	375	1.06	94[c]
PLA	17.2	323	319	1.01	99[c]
PDMS	21.6	128	131	1.02	99[c]
DME	18.7	21.0	21.7	1.02	100[d]
DEE	14.6	23.8	24.2	1.02	100[d]
DBE	6.90	29.4	29.6	1.02	100[d]

[a] Based on [M]:[**G3**] = 100:1.
[b] Determined by SEC light scattering detector.
[c] Determined by SEC differential refractive index detector.
[d] Determined by ^{1}H NMR.

Comparing the three macromonomers, **PDMS** possesses the largest k_{homo} (21.6 M^{-1} s^{-1}). The k_{homo} of **PLA** (17.2 M^{-1} s^{-1}) is around four times as large as that measured for **PS** (4.18 M^{-1} s^{-1}), consistent with previous observations.[52] The k_{homo} values of the norbornenyl diesters trend inversely with the bulkiness of the ester substituents as anticipated. Indeed, the k_{homo} measured for **DME** (18.7 M^{-1} s^{-1}) is larger than that of **DEE** (14.6 M^{-1} s^{-1}) or **DBE** (6.90 M^{-1} s^{-1}). Collectively, these results reinforce the important role that the norbornene monomer sterics play in the rate of ROMP. Sections 2-8 and 2-9 will expand the scope of monomer design and further explore the role of steric effects.

2-4 Developing an Analytical Method for Copolymerization Kinetics

Homopolymerization kinetic analyses indicate that ROMP of each individual macromonomer or diluent is well-behaved. However, controlling side chain density and distribution also requires studying the *copolymerization* kinetics. The copolymerization kinetics were analyzed based on the Mayo-Lewis terminal model.[59-60] The terminal model assumes that, for a mixture of two monomers M_1 and M_2, there are two propagating species (M_1* and M_2*) whose reactivities solely depend on the last-incorporated monomer.[59] The copolymerization kinetics can be captured by four propagation reactions involving M_1* and M_2*, each described by a unique rate constant k. Scheme 2.1 shows the relevant reactions for a mixture of a discrete diluent (M_2) and a macromonomer (M_1): (A) diluent self-propagation ($M_2^* \rightarrow M_2^*$, k_{22}), (B) cross-propagation via addition of M_1 to M_2* ($M_2^* \rightarrow M_1^*$, k_{21}), (C) macromonomer self-propagation ($M_1^* \rightarrow M_1^*$, k_{11}), and (D) cross-propagation via addition of M_2 to M_1* ($M_1^* \rightarrow M_2^*$, k_{12}).

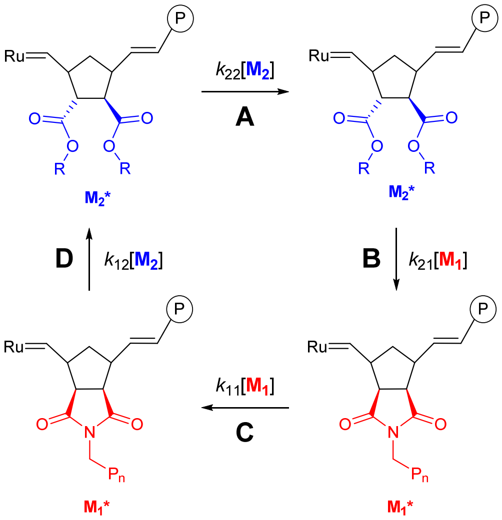

Scheme 2.1: Propagation reactions for the copolymerization of a discrete diluent (M_2, *dx*-DE shown for example) and a macromonomer (M_1) according to a terminal model. M_2* and M_1* are the corresponding propagating alkylidene species. (*A*) Diluent self-propagation (k_{22}), (*B*) cross-propagation (k_{21}), (*C*) macromonomer self-propagation (k_{11}), (*D*) cross-propagation (k_{12}).

The reactivity ratios ($r_1 = k_{11}/k_{12}$, $r_2 = k_{22}/k_{21}$) are defined by the tendency for the propagating species to react with the same monomer over the other. As depicted in Scheme 2.2, the copolymerization is inherently directed by the reactivity ratios, leading to sequences such as alternating, blocky, random, or gradient.

Over the past several decades, a number of methods have been established to determine the reactivity ratios for copolymerizations. Popular techniques include the Mayo-Lewis,[59-60] Fineman-Ross,[61] and Kelen-Tüdös[62] methods, among others.[63] The validity of these linear regression methods has been established in many contexts; however, we note that they are derived from equations based on the steady-state approximation, with the assumption that the rates of crossover are identical: that is, $k_{12}[M_1^*]_t[M_2]_t = k_{21}[M_2^*]_t[M_1]_t$. As such, these methods are only strictly valid under steady-state conditions in which the change in monomer feed is insignificant.[64] Obtaining kinetic data in the required low-conversion regime is prohibitively challenging for fast polymerization reactions such as **G3**-mediated ROMP. Due to this constraint, a new analytical approach that bypasses the steady-state approximation is needed.

Scheme 2.2: Mayo-Lewis terminal model describing the copolymerization of M_1 and M_2.

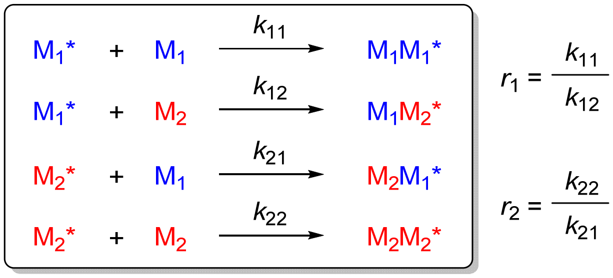

Case I: r_1, r_2 << 1 (alternating)

$M_1M_2M_1M_2M_1M_2M_1M_2M_1M_2M_1M_2M_1M_2M_1M_2M_1M_2M_1M_2$

Case II: r_1, r_2 >> 1 (blocky)

$M_1M_1M_1M_1M_1M_1M_1M_1M_1M_1M_2M_2M_2M_2M_2M_2M_2M_2M_2M_2$

Case III: $r_1 = r_2 = 1$ (random)

$M_2M_2M_1M_2M_1M_1M_1M_2M_1M_2M_1M_2M_2M_1M_1M_2M_1M_2M_2M_1$

Case IV: $r_1 < 1 < r_2$ (gradient)

$M_2M_2M_2M_2M_1M_2M_2M_2M_1M_1M_2M_2M_1M_1M_1M_2M_1M_1M_1M_1$

According to the terminal model, the time-dependent concentrations of M_1, M_2, M_1*, and M_2* can be described by the following differential equations:

$$-\frac{\mathrm{d}[\mathrm{M}_1]_t}{\mathrm{d}t} = k_{11}[\mathrm{M}_1{}^*]_t[\mathrm{M}_1]_t + k_{21}[\mathrm{M}_2{}^*]_t[\mathrm{M}_1]_t \qquad \text{Eq. 2-2}$$

$$-\frac{\mathrm{d}[\mathrm{M}_2]_t}{\mathrm{d}t} = k_{12}[\mathrm{M}_1{}^*]_t[\mathrm{M}_2]_t + k_{22}[\mathrm{M}_2{}^*]_t[\mathrm{M}_2]_t \qquad \text{Eq. 2-3}$$

$$-\frac{\mathrm{d}[\mathrm{M}_1{}^*]_t}{\mathrm{d}t} = k_{12}[\mathrm{M}_1{}^*]_t[\mathrm{M}_2]_t - k_{21}[\mathrm{M}_2{}^*]_t[\mathrm{M}_1]_t \qquad \text{Eq. 2-4}$$

$$-\frac{\mathrm{d}[\mathrm{M}_2{}^*]_t}{\mathrm{d}t} = k_{21}[\mathrm{M}_2{}^*]_t[\mathrm{M}_1]_t - k_{12}[\mathrm{M}_1{}^*]_t[\mathrm{M}_2]_t \qquad \text{Eq. 2-5}$$

While exact analytical solutions for Eqs. 2-2 to 2-5 cannot be obtained, numerical solutions for $[M_1]_t$, $[M_2]_t$, $[M_1*]_t$, and $[M_2*]_t$ can be found if the propagation rate constants are known. In our study, the homopolymerization rate constants k_{11} and k_{22} can be independently measured (Table 2.1). Furthermore, the instantaneous monomer concentrations $[M_1]_t$ and $[M_2]_t$ during the copolymerization can be determined by quenching aliquots at known times t, and in living ROMP, the sum of $[M_1*]_t$ and $[M_2*]_t$ should be [**G3**]$_0$. As a result, the best numerical solutions for k_{12} and k_{21} can be determined using a non-linear least-square curve fitting method.

2-5 Copolymerization Kinetics

We first investigated the copolymerization of **PS** (0.05 M) and **DME** (0.05 M) mediated by **G3** (0.5 mM) in CH_2Cl_2 (Figure 2.4A). The conditions, including the monomer and catalyst concentrations, were identical to those employed in homopolymerization reactions. Aliquots were extracted at different time points, quenched, and subjected to SEC and NMR analyses. The SEC traces indicated the continuing depletion of **PS** as well as the concomitant growth of the copolymer (Figure 2.4B). In addition, the instantaneous concentrations of both monomers could be determined by ^1H NMR integration of their distinct norbornenyl olefinic resonances. Plotting $\ln([M]_0/[M]_t)$ as a function of time (Figure 2.4C) suggested that the decay of **PS** and **DME** approached *pseudo* first order. However, we note that first-order kinetics are only strictly applicable in the event that both $[M_1*]_t$ and $[M_2*]_t$ are constant (see Eqs. 2-2 and 2-3). With the same

G3 concentration of 0.5 mM, the propagation rates for **PS** and **DME** in the copolymerization reaction were, respectively, faster and slower than those measured independently in the homopolymerization reactions (Figure 2.4C). The increase in the rates of **PS** consumption in the copolymerization reaction could be attributed to cross-propagation being faster than self-propagation. Interestingly, the opposite trend was observed for **DME**.

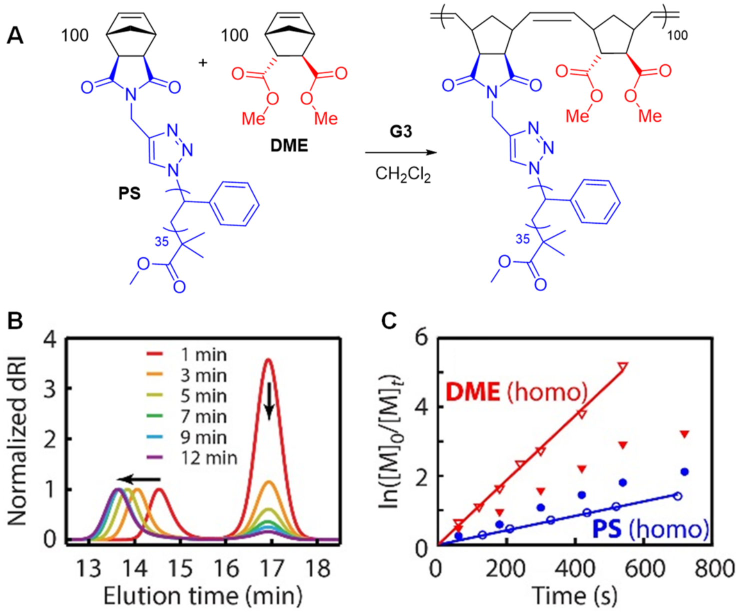

Figure 2.4: (*A*) Copolymerization of **PS** (0.05 M) and **DME** (0.05 M) catalyzed by **G3** (0.5 mM) in CH_2Cl_2 at 298 K. (*B*) Normalized differential refractive index (dRI) trace from size-exclusion chromatography. (*C*) Plots of $\ln([M]_0/[M]_t)$ versus time as monitored by ^1H NMR spectroscopy (filled blue circles = **PS**, filled red triangles = **DME**). Unfilled blue circles (**PS**), unfilled red triangles (**DME**), and the solid lines, plotted for comparison, were obtained from homopolymerization reactions under the same conditions.

To gain further insight, the kinetic profile of the copolymerization of **PS** and **DME** (1:1) was fitted to the terminal model using our analytical methods with known values of $k_{\text{PS-PS}}$, $k_{\text{DME-DME}}$, [**PS**]$_0$, [**DME**]$_0$, and [**G3**]$_0$ (Figure 2.5A). The calculated curves of monomer conversion versus total conversion agreed satisfactorily with the experimental data (Figure 2.5B). The calculated rate constants and reactivity ratios for various macromonomer/diluent copolymerization pairs are provided in Table 2.1.

Table 2.1: Copolymerization rate constants and reactivity ratios in CH_2Cl_2 at 298 K.

Entry	$\mathbf{M_1}$	$\mathbf{M_2}$	$\mathbf{[M_1]_0}$ **(M)**	$\mathbf{[M_2]_0}$ **(M)**	k_{11} **(M^{-1} s^{-1})**	$k_{12}{}^{a}$ **(M^{-1} s^{-1})**	k_{22} **(M^{-1} s^{-1})**	$k_{21}{}^{a}$ **(M^{-1} s^{-1})**	r_1	r_2	r_1r_2
1	PS	DME	0.050	0.050	4.18	7.74	18.7	13.2	0.54	1.41	0.76
2	PS	DME	0.050	0.100	4.18	7.58	18.7	14.6	0.55	1.28	0.71
3	PS	DEE	0.050	0.050	4.18	7.73	14.6	8.75	0.54	1.67	0.90
4	PS	DBE	0.050	0.050	4.18	5.23	6.90	5.66	0.80	1.22	0.97
5	PS	DBE	0.075	0.025	4.18	5.24	6.90	5.93	0.80	1.16	0.93
6	PLA	DME	0.050	0.050	17.2	18.8	18.7	16.9	0.92	1.11	1.02
7	PLA	DBE	0.050	0.050	17.2	16.7	6.90	7.95	1.03	0.87	0.90
8	PDMS	DME	0.050	0.050	21.6	19.9	18.7	19.9	1.09	0.94	1.02
9	PDMS	DBE	0.050	0.055	21.6	19.5	6.90	15.9	1.11	0.43	0.48

[a] Obtained from least-square curve fitting.

Least-squares fitting of the copolymerization data for **PS** and **DME** (1:1) generates $k_{\text{PS-DME}}$ and $k_{\text{DME-PS}}$ values of 7.74 and 13.2 $M^{-1}\ s^{-1}$, respectively (Table 2.2, Entry 1). The reactivity ratios ($r_{\text{PS}} = 0.54$, $r_{\text{DME}} = 1.41$) indicate gradient copolymerization and can be used to simulate the instantaneous copolymer composition (Section 2-6). Copolymerizing **PS** and **DME** in a 1:1 feed ratio could therefore be expected to yield a polymer bearing 50% grafting density and a gradient distribution of **PS** side chains. In order to further examine the validity of our methods, the copolymerization of **PS** and **DME** in a 1:2 feed ratio was carried out and subjected to the same analyses (Figure 2.5C–D), yielding comparable $k_{\text{PS-DME}}$ and $k_{\text{DME-PS}}$ values (Table 2.2, Entry 2). As such, these experiments support the ability of the terminal model to capture the copolymerization kinetics of **G3**-catalyzed ROMP.

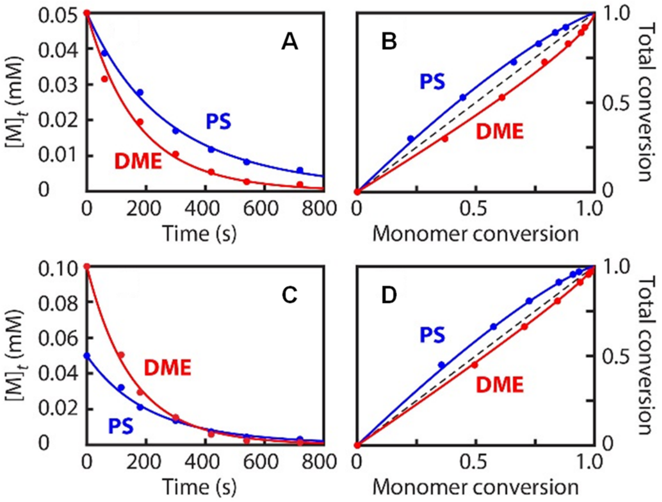

Figure 2.5: Non-linear least-square curve fitting for the copolymerization of (*A*, *B*) **PS** (0.05 M) and **DME** (0.05 M) and (*C*, *D*) **PS** (0.05 M) and **DME** (0.10 M) in CH_2Cl_2 at 298 K. $[\textbf{G3}]_0 = 0.5$ mM. Calculated fits (solid lines) show close agreement with the measured values (points). In (*B*, *D*), the dashed lines, included for comparison, indicate ideal random copolymerization ($r_1 = r_2 = 1$).

We next examined the 1:1 copolymerization of **PS** and **DEE** (Figure 2.6A–B). The measured $k_{\text{PS-DEE}}$ (7.73 $M^{-1}\ s^{-1}$, Table 2.2, Entry 3) is very close to $k_{\text{PS-DME}}$ (7.58–7.74 $M^{-1}\ s^{-1}$), indicating similar chemical reactivity of the propagating species **PS*** toward **DME** and **DEE**. In sharp contrast, $k_{\text{DEE-PS}}$ (8.75 $M^{-1}\ s^{-1}$) is notably smaller than $k_{\text{DME-PS}}$ (13.2–14.6 $M^{-1}\ s^{-1}$). This observation suggests that the **PS*** alkylidene steric/electronic effects are important in governing the rate of ROMP (perhaps more so than that of the approaching norbornenyl diester). The calculated reactivity ratios r_{PS} (0.54) and r_{DEE} (1.67) indicate gradient copolymerization. In addition, the $r_{\mathrm{PS}} \times r_{\mathrm{DEE}}$ product of 0.90 suggests an almost ideal copolymerization process in which each propagating species, **PS*** and **DEE***, has the same preference for **PS** over **DEE**; that is, $k_{\mathrm{PS\text{-}PS}}/k_{\mathrm{PS\text{-}DME}} \approx k_{\mathrm{DME\text{-}PS}}/k_{\mathrm{DME\text{-}DME}}$. The copolymerizations of **PS** and **DBE** in 1:1 (Figure 2.6C–D) and 3:1 (Figure 2.6E–F) feed ratios have also been examined. The propagation rate constants obtained from these experiments are approximately equal (Table 2.2, Entries 4–5), as expected, again reflecting the competence of our analytical methods. The **PS**/**DBE** copolymerization is best described as near-ideal, approaching random, as evidenced by the reactivity ratios ($r_{\mathrm{PS}} = 0.8$, $r_{\mathrm{DBE}} = 1.16$–1.22) as well as their product ($r_{\mathrm{PS}} \times r_{\mathrm{DBE}} = 0.93$–$0.97$).

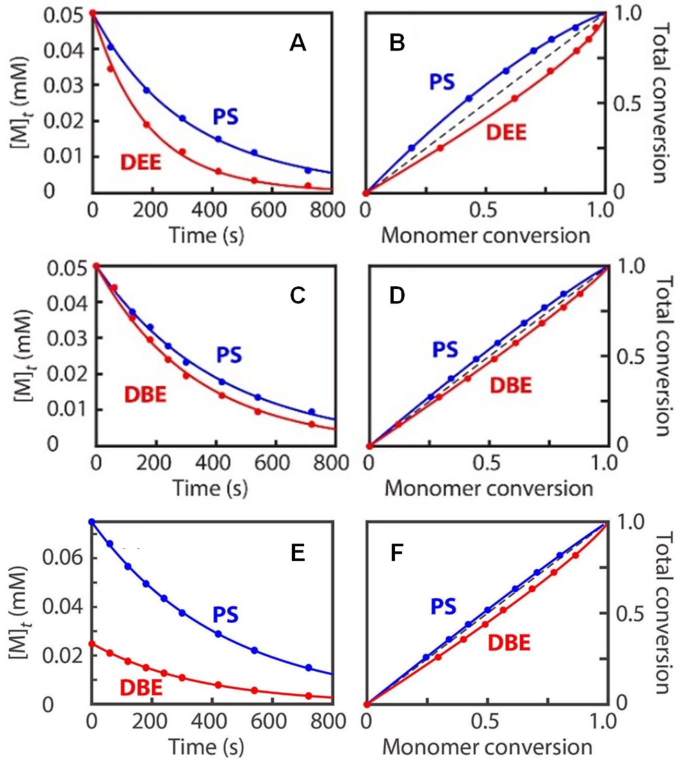

Figure 2.6: Non-linear least-square curve fitting for the copolymerization of various macromonomer/diluent pairs: (*A*, *B*) **PS** (0.05 M) and **DEE** (0.05 M); (*C*, *D*) **PS** (0.05 M) and **DBE** (0.05 M); (*E*, *F*) **PS** (0.075 M) and **DBE** (0.025 M). [**G3**]$_0$ = 0.5 mM, solvent = CH_2Cl_2, temperature = 298 K.

For studies and applications in which uniform grafting density is desired, the ability to access random copolymers is crucial. The copolymerization reactions of **PS** with diluents imply that random copolymerization ($r_1 \approx r_2 \approx 1$) might be achieved when both self-propagation rate constants are similar ($k_{11} \approx k_{22}$). To examine this hypothesis, we turned our attention to the copolymerization of **PLA** (k_{homo} = 17.2 M^{-1} s^{-1}) and **DME** (k_{homo} = 18.7 M^{-1} s^{-1}). These experiments indicate that the rate of consumption of **PLA** is only marginally slower than that of **DME**, consistent with an approximately random copolymerization (Figure 2.7A–B; Table 2.2, Entry 6). Similarly, random copolymerization was observed for **PLA/DBE** (Figure 2.7C–D; Table 2.2, Entry 7) as well as **PDMS/DME** (Figure 2.7E–F; Table 2.2, Entry 8). Lastly, gradient copolymers (Table 2.2, Entry 9; $r_{\mathrm{PDMS}} = 1.11$, $r_{\mathrm{DBE}} = 0.43$) were obtained by copolymerizing **PDMS** with **DBE** (Figure 2.7G–H). The reactivity ratio product ($r_{\mathrm{PDMS}} \times r_{\mathrm{DBE}} = 0.48$) indicates a departure from ideal copolymerization. This observation is seemingly correlated with the large differences in the self-propagation rate constants. Taken collectively, the copolymerization of a norbornene-functionalized macromonomer (**PS**, **PLA**, or **PDMS**) with a diluent (**DME**, **DEE**, or **DBE**) could generate either gradient or random copolymers. Kinetic analyses reveal similar k_{12} values (**PS** = 5.23 - 7.74 M^{-1} s^{-1}, **PLA** = 16.7–18.8 M^{-1} s^{-1}, **PDMS** = 19.5–19.9 M^{-1} s^{-1}) and disparate k_{21} values (**PS** = 5.66–14.6 M^{-1} s^{-1}, **PLA** = 7.95–16.9 M^{-1} s^{-1}, **PDMS** = 15.9–19.9 M^{-1} s^{-1}), reflecting the significance of the alkylidene ligands in directing the metathesis rates. This observation could potentially be attributed to the different steric, electronic, and ligating environments exerted by the anchor group (*exo*-imide for macromonomer versus *endo*,*exo*-diester for diluent). The importance of the anchor group has been recently discussed by Matson and coworkers in the context of self-propagation rates.[65] Sections 2-8 and 2-9 in this thesis will further expand the understanding of anchor group effects on ROMP kinetics.

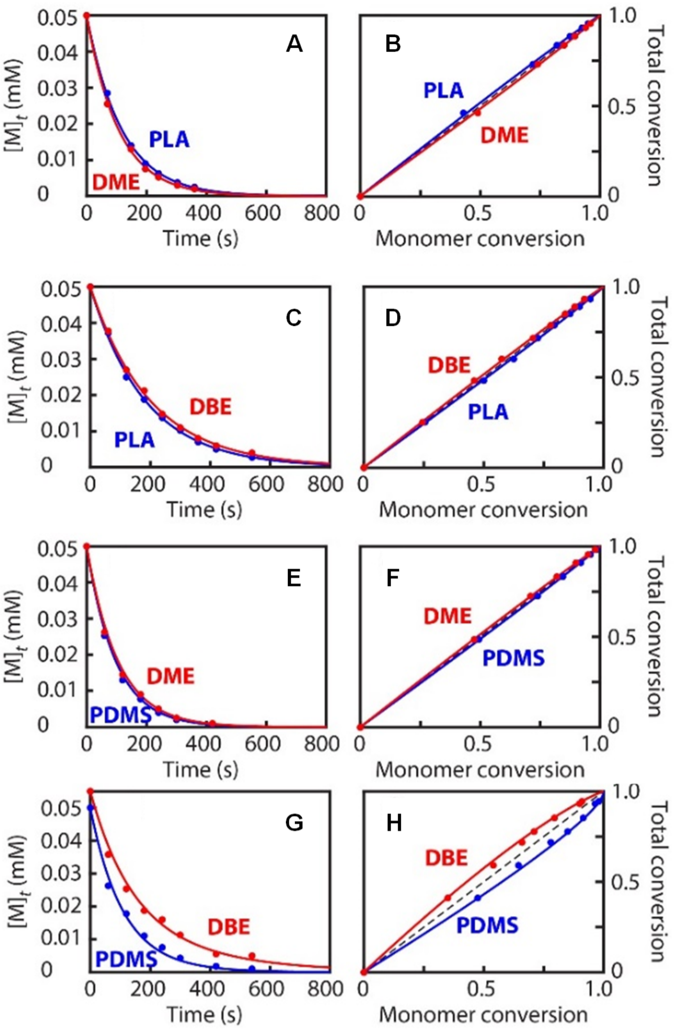

Figure 2.7: Non-linear least-square curve fitting for the copolymerization of various macromonomer/diluent pairs: (*A*, *B*) **PLA**/**DME**; (*C*, *D*) **PLA**/**DBE**; (*E*, *F*) **PDMS**/**DME**; (*G*, *H*) **PDMS**/**DBE** (0.055 M). Reaction conditions: $[M]_0 = 0.05$ M unless otherwise indicated, $[\mathbf{G3}]_0 = 0.5$ mM, solvent = CH_2Cl_2, temperature = 298 K.

2-6 Instantaneous Copolymer Composition

From the copolymerization kinetics, the rate of monomer incorporation at any given time could be calculated according to Eqs. 2-2 and 2-3, allowing the prediction of instantaneous copolymer composition as a function of total conversion. For example, copolymerizing **PS** and **DME** in a 1:1 feed ratio results in (**PS**-*grad*-**DME**)$_n$ best described as a gradient graft polymer (Figure 2.8A). Such a copolymer at 100% conversion possesses, on average, 50% grafting density (*i.e.*, one polystyrene brush per two norbornene backbone repeat units). The difference in reactivity ratios leads to richer **DME** composition at early conversion and higher **PS** incorporation toward the end. Similar gradient graft polymers have been previously accessed by grafting-from ATRP methods.[33-34] The brush distribution gradient is much less pronounced in copolymers (**PLA**-*ran*-**DME**)n (Figure 2.8B) and (**PDMS**-*ran*-**DME**)n (Figure 2.8C), in which the side chains are uniformly grafted across the entire polynorbornene backbone. Lastly, copolymerizing **PDMS**/**DBE** in a 1:1 ratio generates the gradient copolymer (**PDMS**-*grad*-**DBE**)n (Figure 2.8D). Unlike (**PS**-*grad*-**DME**)n, our simulations indicate that (**PDMS**-*grad*-**DBE**)n is more densely grafted at early conversion. Coupled with sequential polymerization, copolymerizing **PS**/**DME** and **PDMS**/**DBE** could be exploited in the synthesis of normal tapered or inverse tapered block copolymers.[66] The synthesis of such block copolymers and the impact of molecular architecture on the phase behavior are discussed in Chapter 3.

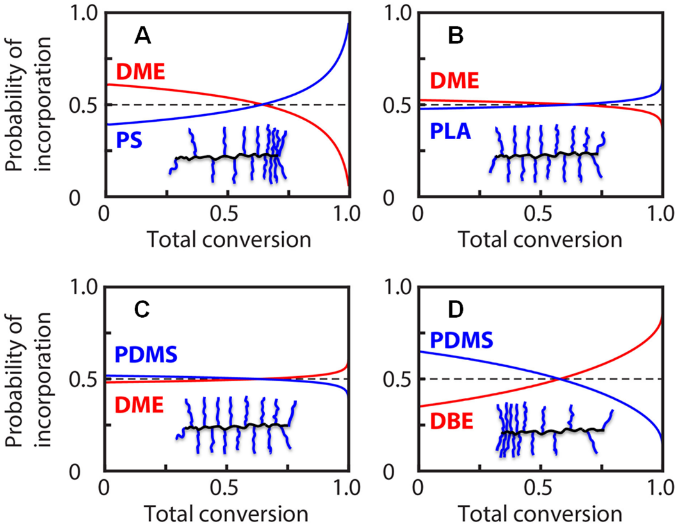

Figure 2.8: Simulated copolymer compositions for (*A*) **PS**:**DME** = 1:1, (*B*) **PLA**:**DME** = 1:1, (*C*) **PDMS**:**DME** = 1:1, and (*D*) **PDMS**:**DBE** = 1:1. Insets show schematic illustrations of the corresponding graft polymers; for ease of visualization, the side chains and backbones are shown in the fully extended limit.

2-7 Synthesis of Architectures with Variable Grafting Density

To showcase the synthetic versatility of our approach, we targeted an array of polymers ($(\mathbf{PLA}^{z}\text{-}ran\text{-}\mathbf{DME}^{1-z})_n$) with variable grafting densities (z = 1.00, 0.75, 0.50, 0.25) and backbone lengths (n = 167, 133, 100, 67, 33). These polymers could be easily prepared by mixing **PLA**, **DME**, and **G3** in different ratios according to Eqs. 2-6 and 2-7 (M_1 = macromonomer, M_2 = diluent):

$$z = [M_1]_0 / ([M_1]_0 + [M_2]_0) \qquad \text{Eq. 2-6}$$

$$n = ([M_1]_0 + [M_2]_0) / [\mathbf{G3}]_0 \qquad \text{Eq. 2-7}$$

These copolymerization reactions were carried out under very mild conditions in CH_2Cl_2 (298 K, $[\mathbf{G3}]_0$ = 0.5 mM, 15 min), and complete monomer consumption was verified by ^1H NMR spectroscopy. As shown in Figure 2.9, the SEC analyses of the resulting polymers indicated low dispersities ($Đ$ = 1.01–1.03) as well as excellent agreement between the measured and targeted molecular weights throughout the series (Appendix A, Table A.1).

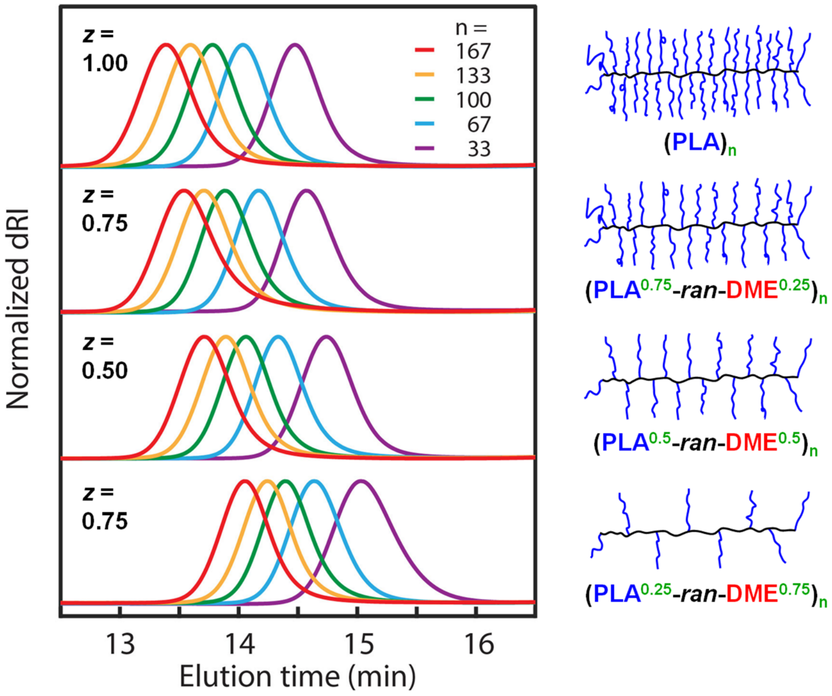

Figure 2.9: SEC traces of $(\mathbf{PLA}^{z}\text{-}ran\text{-}\mathbf{DME}^{1-z})_n$ where z = grafting density (1.0, 0.75, 0.50, or 0.25) and n = total backbone degree of polymerization (red: 167, orange: 133, green: 100, blue: 67, purple: 33).

Reinforcing the NMR and SEC data, differential scanning calorimetry (DSC) provided further evidence supporting the incorporation of both macromonomer and diluent (Appendix A, Figure A.5). For example, DSC data collected on $(\mathbf{PS}^{0.5}\text{-}ran\text{-}\mathbf{DBE}^{0.5})_{200}$ shows glass transition temperature (T_g) at 95 °C, which lies between the T_g values of $\mathbf{PS}_{100}$ (102 °C) and $\mathbf{DBE}_{100}$ (71 °C).

2-8 Expanding Monomer Design

Section 2-2 introduced *endo,exo*-norbornenyl dialkylesters as appropriate discrete monomers (diluents) to control the grafting density of polymers with poly(D,L-lactide) (**PLA**, M_n = 3230 g/mol), polydimethylsiloxane (**PDMS**, M_n = 1280 g/mol), or polystyrene (**PS**, M_n = 3990 g/mol) side chains.[67] Across all macromonomer/diluent combinations and feed ratios, kinetic analyses indicated approximately equal rates of co-monomer consumption and therefore approximately uniform side chain distributions. (See for example (**PLA**^{z}-*ran*-**DME**$^{1-z}$)$_n$ in Section 2-7.) Obtaining *non-uniform* side chain distributions requires changing the relative reactivity of the macromonomer and diluent (Figure 2.1B). We propose that designing new small-molecule co-monomers is the most convenient route. This strategy avoids potentially tedious end-group modifications to the macromonomers and retains the synthetic utility of one-pot batch copolymerization. While semi-batch methods (involving continuous addition of one monomer to another) can afford wide control over polymer sequences,[68-69] they require additional instrumentation and optimization of factors such as feed ratio and feed rate.[70-71] Similarly, while sequential addition of macromonomers with different molecular weights can also provide access to tapered architectures,[72] this approach requires the preparation of multiple well-defined macromonomers and fixes the grafting density at 100%.

Scheme 2.3: Expanding monomer design for ring-opening metathesis copolymerization.

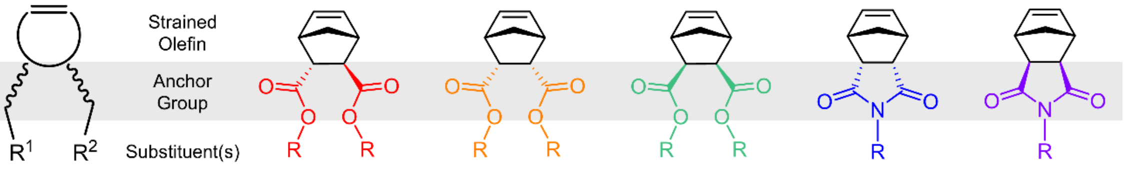

***dx*-DE** ***dd*-DE** ***xx*-DE** ***d*-I** ***x*-I**

dx-DE	*dx*-DE	*dd*-DE	*xx*-DE	*d*-I	*x*-I
1a Me	**1f** ^{t}Bu	**2a** Me	**3a** Me	**4a** Me	**5a** Me
1b Et	**1g** CH$_2$CF$_3$	**2b** Et	**3b** Et	**4b** ^{n}Bu	**5b** ^{n}Bu
1c ^{n}Pr	**1h** Ph	**2c** ^{n}Pr	**3c** ^{n}Pr	**4c** ^{t}Bu	**5c** Ph
1d ^{n}Bu	**1i** *p*-CF$_3$Ph	**2d** ^{n}Bu	**3d** ^{n}Bu		
1e ^{i}Pr	**1j** *p*-MeOPh				

Scheme 2.3 highlights opportunities for monomer design. The polymerizable strained olefin, anchor group, and substituents can all be readily modified. Substituted norbornenes were selected for our study due to (1) the ease of modifying the

stereochemistry and functional groups and (2) the high ring strain, which disfavors unproductive [2+2] cycloreversion.[73] The importance of the anchor group in homopolymerization kinetics has been demonstrated for both discrete norbornenes[56,74] and more recently, ω-norbornenyl macromonomers.[65] In contrast, anchor group effects on the copolymerization of discrete monomers and macromonomers have not been studied. In order to investigate these effects, discrete substituted norbornenes with five different types of anchor groups were synthesized: *endo,exo*-diester (*dx*-DE, **1**), *endo,endo*-diester (*dd*-DE, **2**), *exo,exo*-diester (*xx*-DE, **3**), *endo*-imide (*d*-I, **4**), and *exo*-imide (*x*-I, **5**). For each anchor group, monomers with different substituents (R) were prepared, including for example homologous alkyl groups or *para*-substituted phenyl rings. All monomers can be prepared in high yields in one or two steps from commercially available starting materials. (Further synthetic details can be found in Appendix A-3.) These steric and electronic variations provide a diverse library of co-monomers for ROMP.

The homopolymerization kinetics of all monomers were studied under the same conditions (Section 2-3). Studying trends in k_{homo} with variations in steric and electronic structure guides monomer design. The first class of monomers studied herein features *endo,exo*-diester anchor groups (*dx*-DE). The homopolymerization kinetics of ten *dx*-DE monomers with different substituents were analyzed (**1a**–**1j**, Figure 2.10). The monomers were readily synthesized by esterification of commercially available norbornene *endo,exo*-dicarboxylic acid with the appropriate alcohol (**1a**–**d**, Scheme A.11). (For the synthesis of the bulkier monomers **1e**–**1j**, the acyl chloride derivatives were required; Scheme A.12.) In a series of monomers with homologous alkyl substituents (R = methyl, ethyl, *n*-propyl, *n*-butyl; **1a**–**d**), k_{homo} decreases with increasing substituent size. Increasing the steric bulk with isopropyl- and *tert*-butyl-substituted monomers (**1e**–**f**) further decreases k_{homo}. These results indicate that sterics clearly impact the homopolymerization kinetics: for example, the methyl-substituted monomer polymerizes over three times faster than the *tert*-butyl-substituted analogue ($k_{\mathrm{homo}} = 18.7$ versus $5.36\ \mathrm{M^{-1}\ s^{-1}}$). The effects of electronic variations were also studied. Monomers with ethyl (**1b**, $14.6\ \mathrm{M^{-1}\ s^{-1}}$) and trifluoroethyl (**1g**, $10.5\ \mathrm{M^{-1}\ s^{-1}}$) substituents polymerize at approximately the same rate. Comparison of *dx*-DE monomers with different *para*-substituted phenyl rings further reveals that the electronic effects are minor. *dx*-norbornenyl diphenylester (**1h**) has a larger k_{homo} ($8.36\ \mathrm{M^{-1}\ s^{-1}}$) than monomers with either an electron-withdrawing *para*-trifluoromethyl group (**1i**, 5.14 M^{-1} s^{-1}) or an electron-donating *para*-methoxy group (**1j**, 7.76 M^{-1} s^{-1}). These electronic variations may exist too far away from the polymerizable olefin to affect k_{homo}. Modifying norbornene itself rather than the distal substituents (for example, by substituting oxanorbornene or otherwise changing the bridge position) may result in more apparent electronic effects.

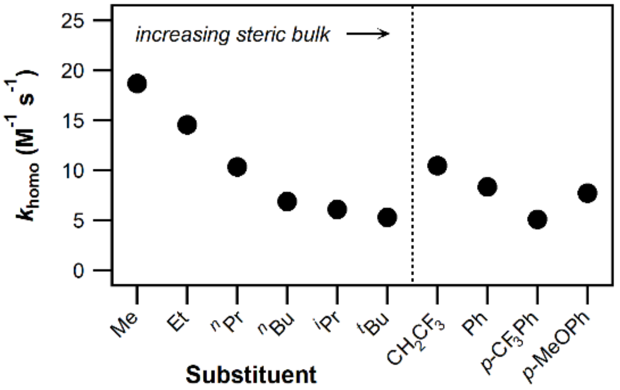

Figure 2.10: Homopolymerization rate constants (k_{homo}) for substituted *endo,exo*-norbornenyl diester monomers (left to right: **1a**–**j**). k_{homo} decreases with increasing steric bulk (R = Me to ᵗBu, **1a**–**f**). k_{homo} does not change significantly with electronic changes via fluorination (**1g**) or *para*-substitution of a phenyl ring (**1h**–**j**).

Changing the stereochemistry of the diester anchor groups further demonstrates the effects of steric variations on polymerization rates. (Synthetic details: Schemes A.13–A.14.) Comparing series with the same substituents (Figure 2.11A) indicates that *dx*-DE monomers (**1a**–**d**) all polymerize significantly faster than the corresponding *endo,endo* isomers (*dd*-DE, **2a**–**d**) and slightly slower than the corresponding *exo,exo* isomers (*xx*-DE, **3a**–**d**). For example, the measured k_{homo} for *dx*-norbornenyl dimethylester is 18.7 M^{-1} s^{-1}, while k_{homo} values for the *dd*-DE and *xx*-DE analogues are 2.24 M^{-1} s^{-1} and 30.8 M^{-1} s^{-1}, respectively. The same anchor group trend occurs for ethyl-, *n*-propyl-, and *n*-butyl-substituted norbornenyl diesters and is anticipated to be independent of the substituent.

In order to further examine the relationship between anchor groups and homopolymerization kinetics, norbornenyl monomers with *endo*-imide (*d*-I) and *exo*-imide (*x*-I) linkages were also synthesized (Schemes A.15–A.16). The *x*-I anchor group has been widely incorporated in macromonomers toward the synthesis of bottlebrush polymers by grafting-through ROMP,[21,65,75-77] motivating our interest in imide-based diluents. Compared to diester anchor groups, imides are more rigid due to their fused rings and thereby change the monomer steric profile. The electronic character differs as well, since the electron density of an imide oxygen is typically greater than the electron density of an ester oxygen. The interplay of steric and electronic influences will be discussed further in Section 2-9.

Figure 2.11B compares k_{homo} for monomers with each of the five anchor groups. The *endo*/*exo* rate difference between *d*-I and *x*-I is magnified compared to the *endo*/*exo* rate differences observed among the diester-substituted monomers. The k_{homo} values for methyl-substituted *dd*-DE and *xx*-DE are 2.24 and 30.8 M^{-1} s^{-1} respectively, representing a tenfold rate difference; in comparison, the k_{homo} values for methyl-substituted *d*-I and *x*-I are 0.814 and 82.4 M^{-1} s^{-1} respectively, representing a *hundredfold* rate difference. Figure 2.11B also shows that the steric effects of the R group are smaller for *x*-I and *d*-I compared to the diester series. For monomers containing the same substituents, the following trend in k_{homo} is observed: *d*-I < *dd*-DE < *dx*-DE < *xx*-DE < *x*-I.

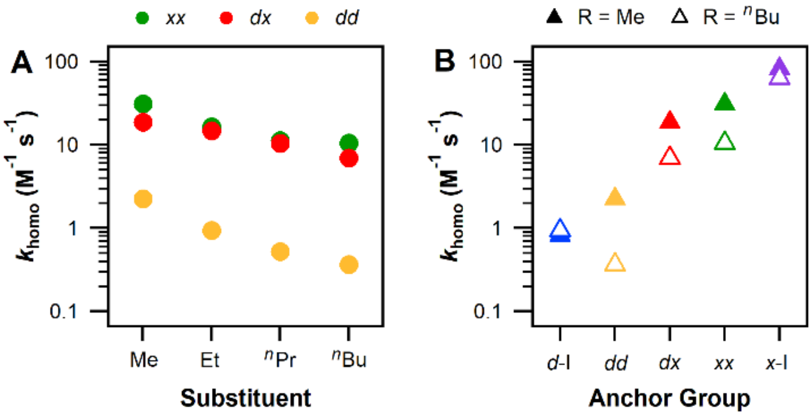

Figure 2.11: (*A*) Homopolymerization rate constants (k_{homo}) for monomers with *exo,exo*-diester (*xx*, green), *endo,exo*-diester (*dx*, red), and *endo,endo*-diester (*dd*, yellow) anchor groups. Comparison of k_{homo} for monomers with R = Me, Et, ⁿPr, and ⁿBu supports the steric influences of stereochemistry and substituent size. (*B*) k_{homo} for Me- and ⁿBu-substituted monomers with each of the five anchor groups; *endo*-imide (*d*-I, blue) and *exo*-imide (*x*-I, purple).

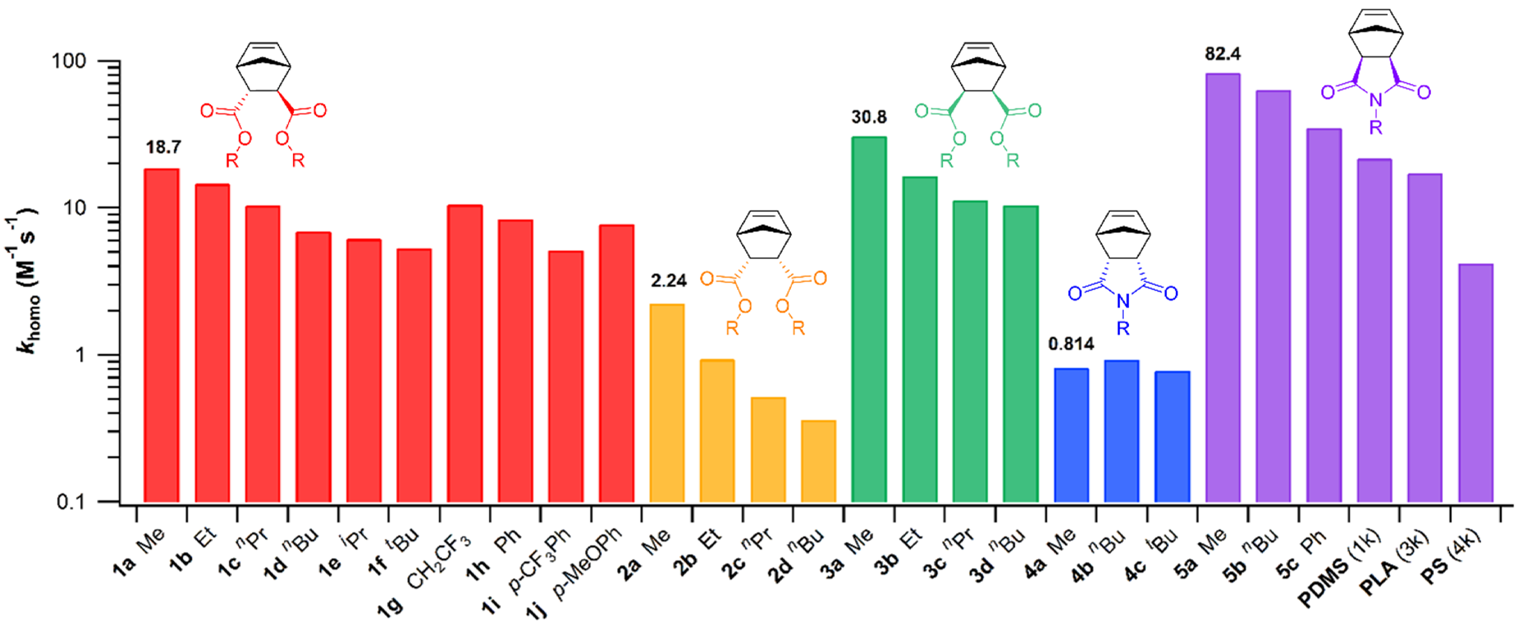

Figure 2.1: Plot of k_{homo} values for all monomers studied herein. The monomers are sorted according to their anchor groups: *left to right*: *endo,exo*-diester (red, **1a**–**j**), *endo,endo*-diester (yellow, **2a**–**d**), *exo,exo*-diester (green, **3a**–**d**), *endo*-imide (blue, **4a**–**c**), and *exo*-imide (purple, **5a**–**c** and macromonomers). k_{homo} values for methyl-substituted monomers are provided for comparison.

Figure 2.12 and Table A.2 summarize the homopolymerization kinetics for all monomers studied herein. Variations in the anchor groups and substituents afford a wide range of k_{homo} over two orders of magnitude, spanning 0.362 M^{-1} s^{-1} (**2d**) to 82.4 M^{-1} s^{-1} (**5a**). This library of monomers can be readily diversified by simple esterification reactions, providing a versatile platform for tuning the polymerization rates. Understanding the origin of trends in k_{homo} provides insight into the ROMP mechanism. While developing a complete mechanistic understanding is outside the scope of this study, we aim to identify key components of k_{homo} in order to facilitate applications of this method as well as future monomer design.

2-9 Origin of Rate Trends

Polymerization rates are determined by a combination of steric and electronic factors. Our results suggest that steric effects dominate: (1) In a series of monomers with homologous alkyl R groups, the electronic character is similar but k_{homo} decreases as the steric bulk increases (Figure 2.10). (2) k_{homo} is relatively insensitive to distal electronic variations (for example, via *para*-substitution of phenyl R groups, Figure 2.10). (3) k_{homo} decreases for *endo*-substituted monomers compared to the corresponding *exo* isomers (Figure 2.11). In agreement with this work, previous studies of the ROMP of norbornene derivatives have also observed that *endo* isomers polymerize more slowly than their *exo* counterparts.[74,78-81]

The observed rate trends could be motivated by a combination of factors, including but not limited to pyridine coordination, olefin coordination, cycloaddition, and formation of a six-membered chelate involving the ruthenium center and the ester- or imide-functionalized chain end.[82] In order to deconvolute these potential contributions to k_{homo}, we examined the mechanism of ROMP. Based on previously reported results for related phosphine-based catalysts,[83-85] we propose a dissociative pathway (Figure 2.13) in which pyridine dissociation ($K_{\mathrm{eq},1} = k_1/k_{-1}$, $K_{\mathrm{eq},2} = k_2/k_{-2}$) generates a 14-electron intermediate (b) that can coordinate with a free olefin (c, $K_{\mathrm{eq},3} = k_3/k_{-3}$). The olefin adduct then undergoes cycloaddition (k_4) to form a metallacyclobutane intermediate. Subsequent cycloreversion yields a P_{n+1} alkylidene and regenerates the 14-electron species. From a Van't Hoff analysis, Guironnet and coworkers recently reported an equilibrium constant $K_{\mathrm{eq},1} = k_1/k_{-1}$

= 0.5 M in CD_2Cl_2 at 298 K.[86] In agreement with this work, we observed a similar $K_{eq,1}$ value from ^{1}H NMR pyridine titration experiments (0.25 M, Figure A.6. The large $K_{eq,1}$ value indicates that >99.8% of the precatalyst **G3** exists as the monopyridine adduct in solution under the conditions employed in our homo- and copolymerization studies ([**G3**]$_0$ = 0.5 mM). As a result, the concentration of free pyridine is approximately equal to the initial concentration of **G3** (*i.e.,* [pyr] ≈ [**G3**]$_0$). We derived a simplified rate expression corresponding to a proposed dissociative ROMP pathway in which olefin coordination is the rate-limiting step (Appendix A-7.2):[87]

$$-\frac{d[M]_t}{dt} = k_{homo}[\mathbf{G3}]_0[M]_t \approx \frac{K_{eq,2}k_3}{K_{eq,2}+[pyr]}[\mathbf{G3}]_0[M]_t \qquad \text{Eq. 2-8}$$

In this rate expression, $K_{eq,2}$ corresponds to dissociation of the second pyridine and is affected by the identity of the alkylidene ligand. At high catalyst concentrations ([pyr] >> $K_{eq,2}$), a pseudo-zeroth-order dependence on [**G3**]$_0$ is observed.[86] At low catalyst concentrations however, we observed a rate dependence on [**G3**]$_0$ for monomers **5a** and **5b** (Figure A.7). Collectively, these kinetic analyses are consistent with a dissociative pathway.[88]

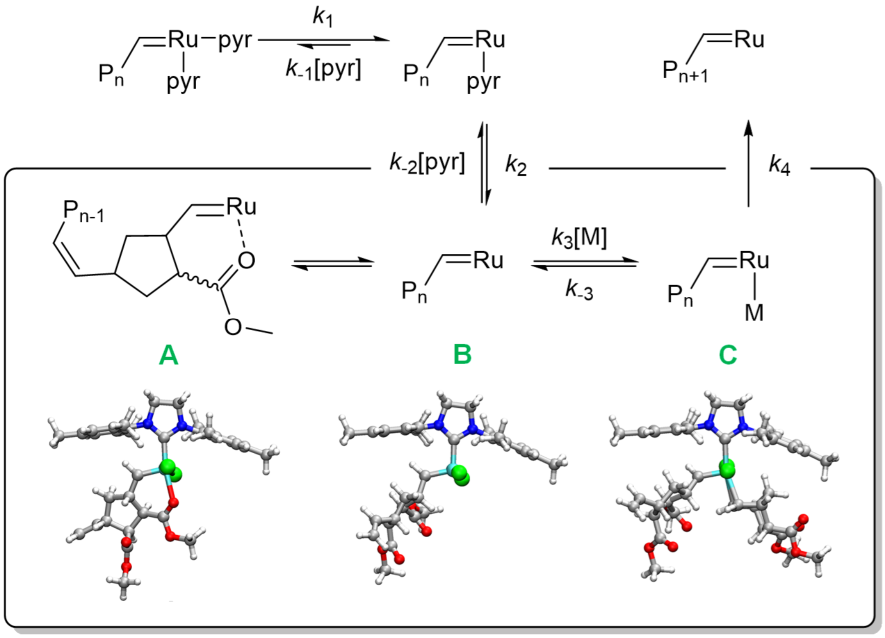

Figure 2.13: Proposed dissociative ROMP pathway for **G3**. The DFT-optimized structures of three catalytically relevant ruthenium catalyst species are shown: (*A*) six-membered Ru–O chelate, (*B*) 14-electron vacant species, and (*C*) olefin adduct.

Density functional theory (DFT) methods were employed to address potential chelation effects. Chelation sequesters the catalyst in an unproductive form (Figure 2.13A) and therefore slows the polymerization rate.[89] For methyl-substituted *endo,endo*- and *exo,exo*-norbornenyl diesters (**2a** and **3a**, respectively), the ground-state potential energy surfaces corresponding to one productive ROMP cycle were computed (Figure 2.14). The relative free energies at 298 K (ΔG) indicate that formation of the six-membered chelate is more favorable for the *endo* isomer ($\Delta\Delta G_{\text{chelate}}$ = 9.64 kcal mol^{-1}) than for the *exo* isomer ($\Delta\Delta G_{\text{chelate}}$ = 5.87 kcal mol^{-1}). The calculated free energies corresponding to olefin coordination to the vacant species, $\Delta\Delta G_{\text{binding}}$, are similar for the *endo* and *exo* isomers (8.86 and 8.91 kcal mol^{-1}, respectively). These results indicate that disruption of chelation by olefin binding should be more favorable for *exo* isomers than *endo* isomers (by 3.72 kcal mol^{-1}). This disparity provides a plausible motive for the observed *endo*/*exo* rate differences (k_{homo} = 30.8 M^{-1} s^{-1} for **3a**, 2.24 M^{-1} s^{-1} for **2a**). These results are consistent with previous reports on the ROMP of discrete norbornenyl monomers with similar ruthenium catalysts[82,84,90] and are anticipated to be valid whether olefin coordination ($k_3 << k_4$) or cycloaddition ($k_3 >> k_4$) is the rate-limiting step.[91] Insights into the rate trends from mechanistic studies help identify important elements of monomer design and, therefore, opportunities for controlled copolymerization.

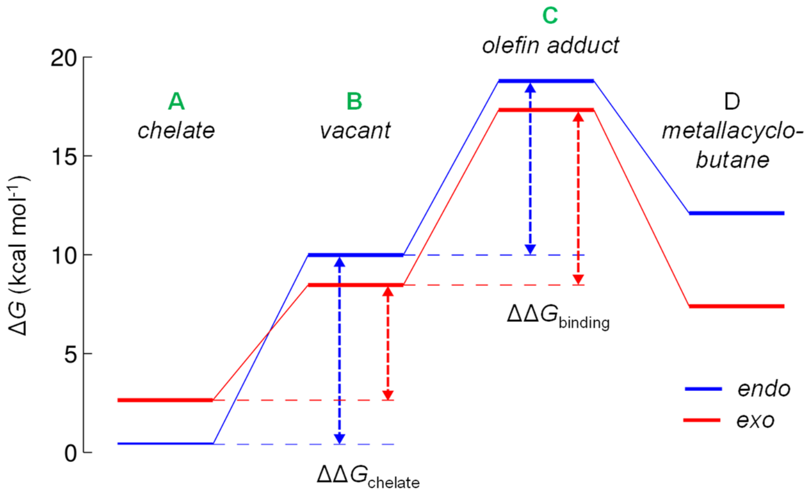

Figure 2.14: DFT-calculated free energy diagram corresponding to one ROMP cycle for *endo*- (**2a**, blue) and *exo*-substiuted (**3a**, red) norbornenyl monomers. The following intermediates were calculated: (*A*) six-membered Ru–O chelate, (*B*) 14-electron vacant species, (*C*) olefin adduct, and (*D*) metallacyclobutane. See also Figure 2.13.

2-10 Copolymerization Kinetics

In order to analyze the copolymerization kinetics of a macromonomer and a discrete co-monomer, we adapted the Mayo-Lewis terminal model was adapted for **G3**-catalyzed ROMP (Section 2-4).[67] The conversion over time of all species (*i.e.*, monomers M_1 and M_2 and propagating alkylidenes M_1* and M_2*) can be described by a system of four ordinary differential equations (Eqs. 2-2 to 2-5). Non-linear least squares regression (Section 2-4) was used to fit the instantaneous monomer concentrations over the entire course of the copolymerization. Finding the best numerical solutions for the cross-propagation rates k_{12} and k_{21} enables determination of the reactivity ratios, $r_1 = k_{11}/k_{12}$ and $r_2 = k_{22}/k_{21}$.

The relative reactivity, captured by r_1 and r_2, determines the polymer sequence. r_1 and r_2 can be tuned by building on insights into homopolymerization rate trends. Monomer design ultimately enables architecture design: for a polymerizable macromonomer with any side chain chemistry, a discrete co-monomer can be selected among those in Scheme 2.3 or otherwise designed to target desired backbone sequences. In turn, control over the backbone sequence directly controls side chain distribution. We will first discuss general trends and opportunities for copolymerization, then outline potential implications for polymer architectures by design.

In order to study the impact of monomer structure on the copolymerization kinetics, we selected 13 diluents and copolymerized each with the same ω-norbornenyl macromonomer (**PLA**, M_n = 3230 g/mol) (Figure 2.15A). Figure 2.15B arranges these discrete co-monomers in order of increasing k_{22}. For all copolymerization experiments, the total backbone degree of polymerization (N_{bb}) and monomer feed ratio (f) were fixed: given x equivalents of the diluent and y equivalents of **PLA** relative to 1 equivalent of **G3**, $N_{bb} = x + y \approx 200$ and $f = x/y \approx 1$. The copolymerization conditions, including monomer and catalyst concentrations, were identical to those for the homopolymerization experiments described in Section 2-3: $[M_1]_0 = [M_2]_0 = 50$ mM, [**G3**]$_0$ = 0.5 mM.[92] The kinetics were monitored in the same way as the homopolymerization kinetics, *i.e.*, by quenching aliquots of the polymerization mixture. The instantaneous concentrations of the macromonomer and diluent were determined by integrating the olefin resonances in ^{1}H NMR spectra, and k_{12} and k_{21} were obtained by non-linear least squares regression. SEC data for all copolymers indicate low dispersities (*Đ* < 1.1) and similar molecular weights (Figure 2.16, Table A.3).

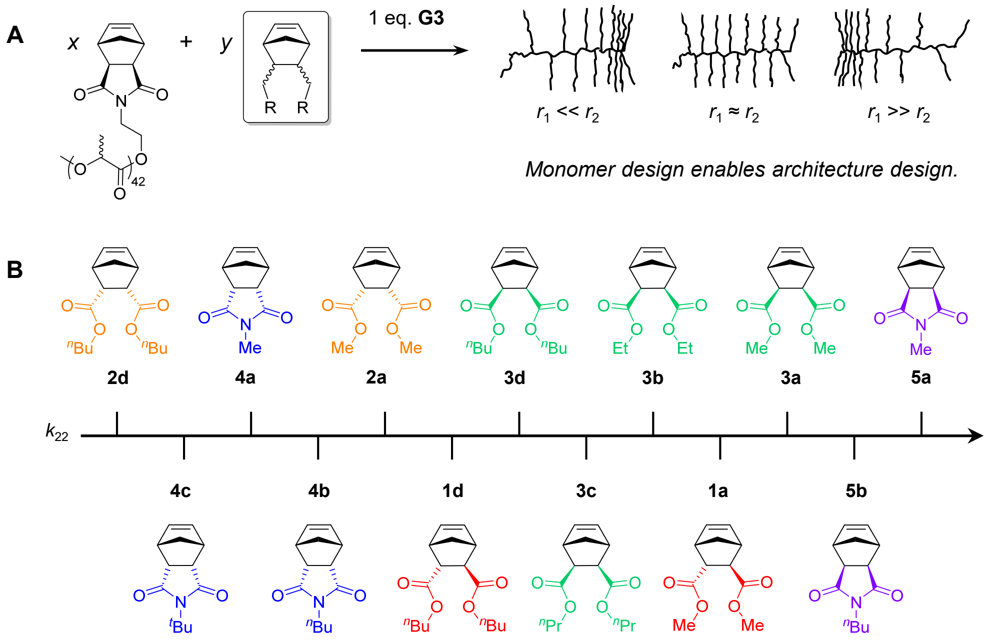

Figure 2.15: (*A*) Copolymerization scheme: the same macromonomer (**PLA**, M_1) was copolymerized with 13 different diluents (M_2). The feed ratio ($x/y = 1$) and total backbone length ($x + y = 200$) were fixed. (*B*) M_2 arranged in order of increasing k_{22}.

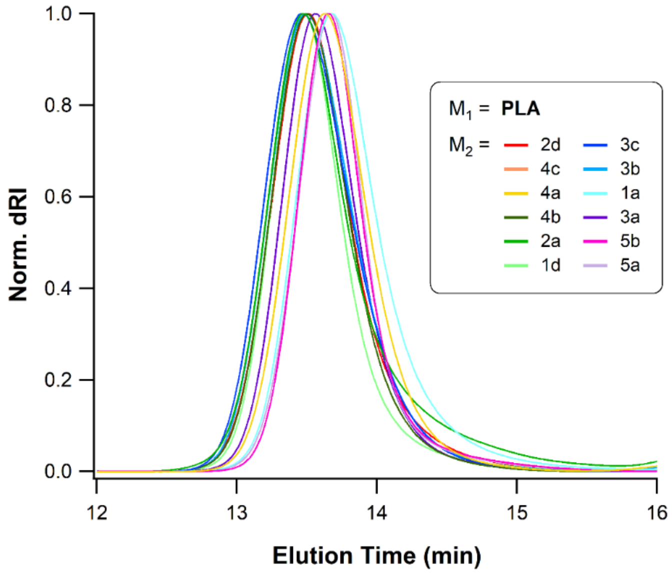

Figure 2.16: SEC traces for **PLA** + diluent copolymerizations at full conversion.

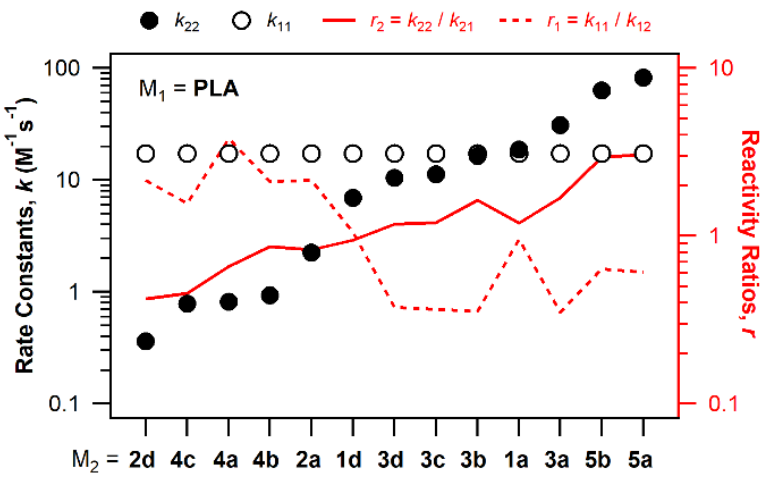

Figure 2.17: **PLA**/diluent copolymerization data. Left axis, black: self-propagation rate constants (k_{22}: filled circles, k_{11}: open circles). Right axis, red: reactivity ratios (r_2: solid line, r_1: dotted line)

Figure 2.17 shows the self-propagation rate constants (k_{11}, k_{22}) and reactivity ratios (r_1, r_2) for the copolymerization of **PLA** (M_1) with different diluents (M_2). (All data, including the cross-propagation rate constants k_{12} and k_{21}, are compiled in Table A.4.) k_{11} is constant throughout the series (= 17.2 M^{-1} s^{-1}) since M_1 is the same in each co-monomer pair, while k_{22} varies over a wide range due to anchor group and substituent effects (**2d**: 0.362 M^{-1} s^{-1} to **5a**: 82.4 M^{-1} s^{-1}). As k_{22} increases, r_2 also increases. The magnitude of r_2 reflects the reactivity of the propagating alkylidene M_2* toward free M_1 and M_2.[93] In the case that $r_2 < 1$, for example when **PLA** is copolymerized with *dd*-DE or *d*-I diluents (**2d** to **2a**, $0.4 < r_2 < 0.9$), M_2* preferentially adds M_1. In the opposite case $r_2 > 1$, for example when **PLA** is copolymerized with *dx*-DE, *xx*-DE, or *x*-I diluents (**3d** to **5a**, $1.2 < r_2 < 3.1$), M_2* preferentially adds M_2 instead. In other words, if a diluent is the terminal unit of the propagating species, the probability of incorporating either a macromonomer or another diluent reflects the difference between the homopolymerization rate constants: when $k_{22} < k_{11}$, $r_2 < 1$ and M_2* favors *macromonomer* addition; on the other hand, when $k_{22} > k_{11}$, $r_2 > 1$ and M_2* favors *diluent* addition.[94] Translating these trends to the copolymer sequence also requires examination of r_1, which reflects consumption of the other propagating species M_1*. Figure 2.17 shows that, as k_{22} increases, r_1 generally decreases, opposite the trend observed for r_2. These observations suggest that both M_1* and M_2* (1) favor incorporating M_2 when $k_{22} \gtrsim k_{11}$ and (2) favor incorporating M_1 when $k_{22} < k_{11}$. In other words, both cross-propagation terms (k_{12} and k_{21}) are functions of the incoming olefin (to first order) and appear relatively insensitive to the nature of the pendant chain.

We note that, while r_1 generally decreases with increasing k_{22}, the trend is not monotonic. These results highlight the additional complexity that copolymerization introduces. While informative, the difference between the homopolymerization rate constants (k_{11}−k_{22}) is not a universal predictor for the values of r_1 and r_2 (nor therefore the copolymer sequence). For example, when **PLA** is copolymerized with a *xx*-DE diluent, r_2 varies but r_1 remains the same ($= 0.36 \pm 0.02$), regardless of whether $k_{22} < k_{11}$ (**3d**, **3c**, and **3b**) or $k_{22} > k_{11}$ (**3a**). Meanwhile, when **PLA** is copolymerized with the *dx*-DE analogue of **3a** (*i.e.*, **1a**), the self-propagation rates are equal ($k_{22} = k_{11}$) and both r_1 and r_2 are approximately equal to 1. These observations suggest that the key interactions identified in our study of diluent homopolymerization rate trends do not fully capture the relative reactivity upon copolymerization. The individual second-order rate constants (k_{11}, k_{12}, k_{21}, k_{22}) are affected by both (1) pyridine binding ($K_{\mathrm{eq},2}$) and (2) chelation and olefin binding (k_3). Both those terms are inherently dictated by the identities of the approaching olefin monomer and the propagating alkylidene. While elucidating the origin of copolymerization rate trends is outside the scope of this report, we note that the large disparity between the molecular weights of the PLA macromonomer and diluents (10- to 20-fold) likely plays a significant role in the departure from simple chain-end control. Under the copolymerization conditions (rapid stirring in dilute solution), simple diffusion of free monomers to the catalyst active site is not expected to limit propagation. However, beyond the anchor group and substituent effects outlined for discrete diluents, the presence of polymeric side chains in proximity to the metal center should amplify steric congestion. Excluded volume interactions and solvent quality may further affect the steric and electronic environment around the propagating metal center.

2-11 Tuning Graft Polymer Architecture

Monitoring the copolymerization kinetics enables determination of the instantaneous composition and therefore the graft polymer architecture. Using the experimentally determined rate constants, the probability of incorporating either a diluent or a macromonomer at any point in the growing chain can be simulated (Section 2-6).[67]

Figure 2.18 plots these probabilities as a function of the total conversion for several **PLA**/diluent pairs. If $r_1 > r_2$, gradient sequences are obtained. The copolymers are rich in M_1 at early conversions and rich in M_2 at later conversions, producing tapered side chain distributions (*e.g.*, **PLA** + **4a**, Figure 2.18A). If $r_1 \approx r_2 \approx 1$, the copolymer backbone sequence is approximately random and therefore the side chains are uniformly distributed (*e.g.* **PLA** + **1a**, Figure 2.18B). Lastly, if $r_1 < r_2$, the inverse-tapered graft polymers are obtained, which are rich in M_2 at early conversions and rich in M_1 at later conversions (*e.g.*, **PLA** + **5a**, Figure 2.18C).

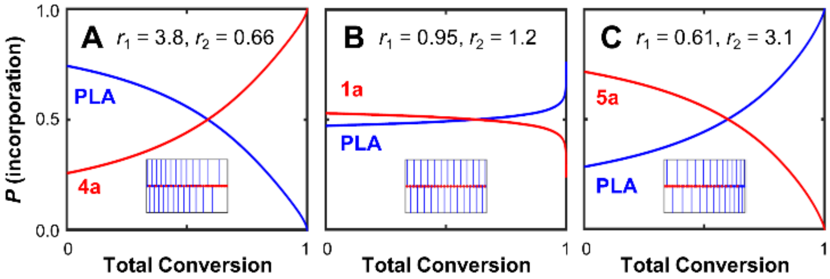

Figure 2.18: Simulated sequences and (inset) graft polymer architectures for the copolymerization of **PLA** with different diluents: (*A*) **4a**, (*B*) **1a**, or (*C*) **5a**. For ease of visualization, the simulated structures show fully extended side chains and backbones.

The ROMP copolymerization strategy outlined herein provides a general approach to architecture design for any side chain chemistry. In principle, given any polymerizable macromonomer, a diluent can be designed to access any desired sequence. Although the magnitudes of r_1 and r_2 cannot presently be predicted *de novo*, insights into the relationships among r_1, r_2, and diluent structure should guide the selection of appropriate macromonomer/diluent pairs. In order to further illustrate these design principles, the copolymerization kinetics of various diluents with either a **PDMS** (M_n = 1280 g/mol) or **PS** (M_n = 3990 g/mol) macromonomer were also studied. **PDMS** and **PS** polymerize faster (k_{11} = 21.6 M^{-1} s^{-1}) and slower (k_{11} = 4.18 M^{-1} s^{-1}) than **PLA**, respectively. The selected diluents all homopolymerize slower than **PDMS** ($k_{22} < k_{11}$, with the exception of **3a**) and faster than **PS** ($k_{22} > k_{11}$). The self-propagation rate constants and reactivity ratios are provided in Figure 2.19 and compiled in Tables A.5–A.6. SEC data are provided in Tables A.7–A.8 and Figures A.8–A.9.

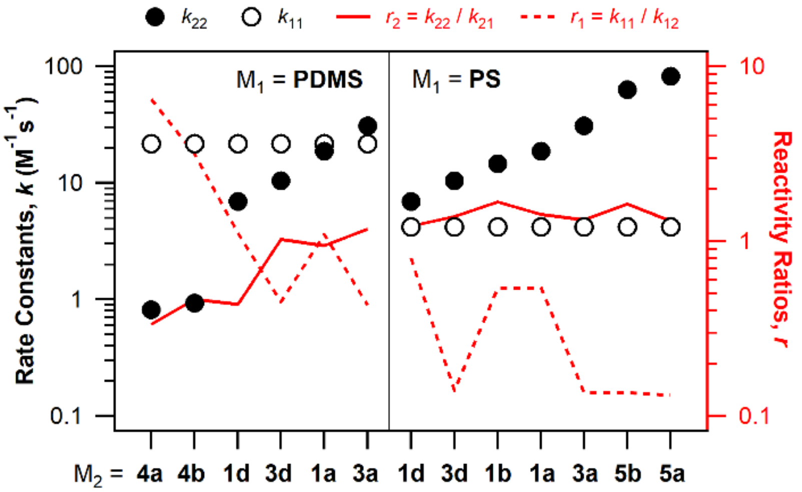

Figure 2.19: Data for the copolymerization of M_1 = **PDMS** (left) or **PS** (right) with different diluents. Left axis, black: self-propagation rate constants (k_{22}: filled circles, k_{11}: open circles). Right axis, red: reactivity ratios (r_2: solid line, r_1: dotted line).

Copolymerizations of **PDMS** with each of the selected diluents generally follow the same trends outlined for **PLA**/diluent copolymerizations. As k_{22} increases while k_{11} remains constant, r_2 increases and r_1 decreases. In other words, as k_{22} increases, both M_1* and M_2* increasingly favor incorporating M_2 instead of M_1. The *xx*-DE diluents (**3a**, **3d**) are again outliers, leading to smaller values of r_1 than diluents with any other anchor group. As a result, at least for copolymerizations with **PDMS** or **PLA** macromonomers, the *xx*-DE anchor group inherently favors gradient sequences that are M_2-rich at early conversions and M_1-rich at later conversions. Copolymerizations of **PS** with any of the selected diluents reveal a similar kinetic preference for gradient sequences. Unlike copolymerizations with either **PLA** or **PDMS**, regardless of the relative magnitude of k_{22} ($2.7 < k_{22}-k_{11} < 78$ M^{-1} s^{-1}), r_2 remains constant (≈ 1). The constant magnitude of r_2 suggests that M_2* displays similar reactivity toward **PS** and any diluent. Meanwhile, since M_1* favors incorporating M_2 ($r_1 < 1$), gradient sequences result.

The copolymerization kinetics for **PLA**, **PDMS**, and **PS** collectively illustrate how different diluents can be used to control the graft polymer architecture. The magnitudes of r_1 and r_2 determine the backbone sequence, which can be alternating ($r_1 \approx r_2 \approx 0$), blocky ($r_1, r_2 >> 1$), gradient ($r_1 >> r_2$ or $r_1 << r_2$), or random ($r_1 \approx r_2 \approx 1$).[93] The backbone sequence in turn directly determines the side chain distribution. Figure 2.20 illustrates the wide range of distributions obtained by copolymerizing **PLA**, **PDMS**, or **PS** with selected diluents. The relative reactivities of the macromonomers and diluents are interpreted in terms of the quotient r_1/r_2, which reflects the kinetic preference for the chain end (either M_1^* or M_2^*) to incorporate M_1 over M_2.

PLA/diluent copolymerizations obtain r_1/r_2 ranging from 0.20 (**PLA** + **5a**) to 5.8 (**PLA** + **4a**). Copolymerizing **PDMS** with **4a**, one of the slowest-polymerizing diluents studied herein, produces a remarkably large difference between r_1 and r_2: r_1/r_2 = 19. This large disparity in reactivity results in a highly gradient – potentially even blocky – distribution of side chains. Since $r_1 >> r_2$, the graft polymers are densely grafted (*i.e.*, rich in M_1) at early conversions and loosely grafted (*i.e.*, rich in M_2) at later conversions. Copolymerizing **PS** with **5b**, one of the fastest-polymerizing diluents introduced in this report, also affords a wide gap in reactivity: r_1/r_2 = 0.084. Compared to **PDMS** + **4a**, the inverse-tapered sequence is obtained. The ability to invert the gradient direction may not affect the properties of homopolymers, but it is valuable in the design of block polymers and other multicomponent materials. In Chapter 3, we will demonstrate the physical consequences of varying the sequence distribution in the context of block polymer self-assembly.

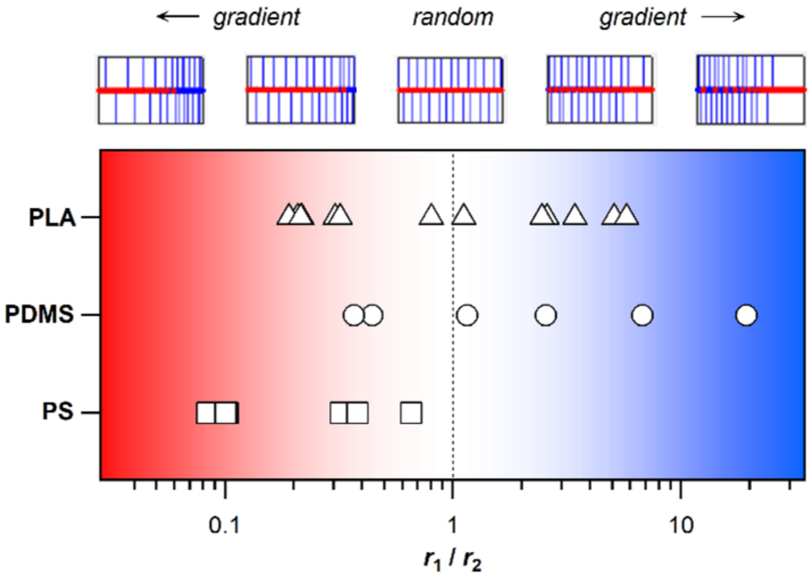

Figure 2.20: Reactivity ratio map. The copolymerization kinetics studied for **PLA**, **PDMS**, and **PS** are interpreted in terms of the quotient r_1/r_2, plotted on the x-axis. For ease of visualization, the simulated structures show fully extended side chains and backbones.

2-12 Conclusion

Grafting-through ring-opening metathesis polymerization (ROMP) provides a versatile strategy for the design and synthesis of polymers with tailored side chain distributions. Controlled copolymerization of an ω-norbornenyl macromonomer and a discrete norbornenyl diluent constructs graft architectures through the backbone; as a result, the backbone sequence directly dictates the side chain distribution. Since tuning the backbone sequence requires changing the relative reactivity of the co-monomers, we first investigated steric and electronic effects on the homopolymerization kinetics of 23 diluents. Varying the stereochemistry, anchor groups, and substituents varies the homopolymerization rate constants over two orders of magnitude ($0.36\ \mathrm{M}^{-1}\ \mathrm{s}^{-1} \leq k_{\mathrm{homo}} \leq 82\ \mathrm{M}^{-1}\ \mathrm{s}^{-1}$), reflecting a wide scope of monomer reactivity. These small-molecule monomers can be readily prepared and diversified, providing a convenient library for future development. In order to provide further guidance, we identified rate trends and studied their origins through complementary mechanistic studies. Density functional theory (DFT) calculations suggest that formation of a Ru–O six-membered chelate (which sequesters the catalyst in an unproductive form) is significantly different for *endo* and *exo* isomers. Future studies will expand our understanding of the ROMP mechanism for both diluents and macromonomers. Other factors that could affect the ROMP kinetics, including for example solvent quality and additives, will also be explored.

Building on these results, we studied the copolymerization kinetics of selected diluents and a poly(D,L-lactide) (**PLA**), polydimethylsiloxane (**PDMS**), or polystyrene (**PS**) macromonomer. The co-monomer concentrations were monitored by ^{1}H NMR, and the cross-propagation rate constants were calculated by non-linear least squares regression based on the Mayo-Lewis terminal model. Trends involving the measured self-propagation rate constants and the calculated reactivity ratios (r_1 and r_2) were identified. In general, for the 26 co-monomer pairs studied, the greater the difference between homopolymerization rates, the greater the gradient tendency ($r_1/r_2 >> 1$ or $r_1/r_2 << 1$). The backbone sequence – and therefore the polymer architecture – can be tailored simply by choosing the appropriate diluent among the library introduced herein or by designing an appropriate monomer. We note that, at present, *de novo* prediction of the reactivity ratios from the macromonomer and diluent chemical structures is not possible. However, we anticipate that the versatility of this design strategy, coupled with the broad functional group tolerance of ROMP and its living character, should enable the design and synthesis of graft polymers with almost any desired graft chemistry and graft distribution. The design strategy outlined herein provides extensive customizability in terms of polymer structure and functionality, illuminating new opportunities for molecular and materials design.

2-13 References

(1) Hadjichristidis, N.; Pitsikalis, M.; Pispas, S.; Iatrou, H. *Chem. Rev.* **2001**, *101*, 3747–3792.

(2) Polymeropoulos, G.; Zapsas, G.; Ntetsikas, K.; Bilalis, P.; Gnanou, Y.; Hadjichristidis, N. *Macromolecules* **2017**, *50*, 1253–1290.

(3) Matyjaszewski, K.; Tsarevsky, N. V. *Nature Chem.* **2009**, *1*, 276–288.

(4) Bates, C. M.; Bates, F. S. *Macromolecules* **2017**, *50*, 3–22.

(5) Kikuchi, M.; Nakano, R.; Jinbo, Y.; Saito, Y.; Ohno, S.; Togashi, D.; Enomoto, K.; Narumi, A.; Haba, O.; Kawaguchi, S. *Macromolecules* **2015**, *48*, 5878–5886.

(6) Liang, H.; Cao, Z.; Wang, Z.; Sheiko, S. S.; Dobrynin, A. V. *Macromolecules* **2017**, *50*, 3430–3437.

(7) Paturej, J.; Sheiko, S. S.; Panyukov, S.; Rubinstein, M. *Sci. Adv.* **2016**, *2*, e1601478.

(8) Rathgeber, S.; Pakula, T.; Wilk, A.; Matyjaszewski, K.; Beers, K. L. *J. Chem. Phys.* **2005**, *122*, 124904.

(9) Abbasi, M.; Faust, L.; Riazi, K.; Wilhelm, M. *Macromolecules* **2017**, *50*, 5964–5977.

(10) Dalsin, S. J.; Hillmyer, M. A.; Bates, F. S. *Macromolecules* **2015**, *48*, 4680–4691.

(11) Hu, M.; Xia, Y.; McKenna, G. B.; Kornfield, J. A.; Grubbs, R. H. *Macromolecules* **2011**, *44*, 6935–6943.

(12) Daniel, W. F. M.; Burdynska, J.; Vatankhah-Varnoosfaderani, M.; Matyjaszewski, K.; Paturej, J.; Rubinstein, M.; Dobrynin, A. V.; Sheiko, S. S. *Nat. Mater.* **2016**, *15*, 183–189.

(13) Mai, D. J.; Marciel, A. B.; Sing, C. E.; Schroeder, C. M. *ACS Macro Lett.* **2015**, *4*, 446–452.

(14) Kapnistos, M.; Kirkwood, K. M.; Ramirez, J.; Vlassopoulos, D.; Leal, L. G. *J. Rheol.* **2009**, *53*, 1133–1153.

(15) Read, D. J.; Auhl, D.; Das, C.; den Doelder, J.; Kapnistos, M.; Vittorias, I.; McLeish, T. C. B. *Science* **2011**, *333*, 1871–1874.

(16) Jeong, S. H.; Kim, J. M.; Baig, C. *Macromolecules* **2017**, *50*, 4491–4500.

(17) Liberman-Martin, A. L.; Chu, C. K.; Grubbs, R. H. *Macromol. Rapid Commun.* **2017**, *38*, 1700058.

(18) Runge, M. B.; Bowden, N. B. *J. Am. Chem. Soc.* **2007**, *129*, 10551–10560.

(19) Sveinbjörnsson, B. R.; Weitekamp, R. A.; Miyake, G. M.; Xia, Y.; Atwater, H. A.; Grubbs, R. H. *Proc. Natl. Acad. Sci. U.S.A.* **2012**, *109*, 14332–14336.

(20) Qiu, L. Y.; Bae, Y. H. *Biomaterials* **2007**, *28*, 4132–4142.

(21) Johnson, J. A.; Lu, Y. Y.; Burts, A. O.; Lim, Y.-H.; Finn, M. G.; Koberstein, J. T.; Turro, N. J.; Tirrell, D. A.; Grubbs, R. H. *J. Am. Chem. Soc.* **2011**, *133*, 559–566.

(22) Bhattarai, N.; Ramay, H. R.; Gunn, J.; Matsen, F. A.; Zhang, M. *J. Control. Release* **2005**, *103*, 609–624.

(23) Bates, C. M.; Chang, A. B.; Momčilović, N.; Jones, S. C.; Grubbs, R. H. *Macromolecules* **2015**, *48*, 4967–4973.

(24) Bates, C. M.; Chang, A. B.; Schulze, M. W.; Momčilović, N.; Jones, S. C.; Grubbs, R. H. *J. Polym. Sci., Part B: Polym. Phys.* **2016**, *54*, 292–300.

(25) Jiang, F.; Wang, Z.; Qiao, Y.; Wang, Z.; Tang, C. *Macromolecules* **2013**, *46*, 4772–4780.

(26) Zhang, J.; Schneiderman, D. K.; Li, T.; Hillmyer, M. A.; Bates, F. S. *Macromolecules* **2016**, *49*, 9108–9118.

(27) Ma, H.; Wang, Q.; Sang, W.; Han, L.; Liu, P.; Chen, J.; Li, Y.; Wang, Y. *Macromol. Rapid Commun.* **2015**, *36*, 726–732.

(28) Prudnikova, K.; Yucha, R. W.; Patel, P.; Kriete, A. S.; Han, L.; Penn, L. S.; Marcolongo, M. S. *Biomacromolecules* **2017**, *18*, 1713–1723.

(29) Noel, A.; Borguet, Y. P.; Wooley, K. L. *ACS Macro Lett.* **2015**, *4*, 645–650.

(30) Wang, Q.; Ma, H.; Sang, W.; Han, L.; Liu, P.; Shen, H.; Huang, W.; Gong, X.; Yang, L.; Wang, Y.; Li, Y. *Polym. Chem.* **2016**, *7*, 3090–3099.

(31) Grubbs, R. B.; Hawker, C. J.; Dao, J.; Fréchet, J. M. J. *Angew. Chem., Int. Ed.* **1997**, *36*, 270–272.

(32) Shinoda, H.; Matyjaszewski, K. *Macromolecules* **2001**, *34*, 6243–6248.

(33) Börner, H. G.; Duran, D.; Matyjaszewski, K.; da Silva, M.; Sheiko, S. S. *Macromolecules* **2002**, *35*, 3387–3394.

(34) Lee, H.-i.; Matyjaszewski, K.; Yu, S.; Sheiko, S. S. *Macromolecules* **2005**, *38*, 8264–8271.

(35) Sutthasupa, S.; Shiotsuki, M.; Sanda, F. *Polym. J.* **2010**, *42*, 905–915.

(36) Bielawski, C. W.; Grubbs, R. H. *Prog. Polym. Sci.* **2007**, *32*, 1–29.

(37) Leitgeb, A.; Wappel, J.; Slugovc, C. *Polymer* **2010**, *51*, 2927–2946.

(38) Zhang, B.; Gröhn, F.; Pedersen, J. S.; Fischer, K.; Schmidt, M. *Macromolecules* **2006**, *39*, 8440–8450.

(39) Sheiko, S. S.; Sumerlin, B. S.; Matyjaszewski, K. *Prog. Polym. Sci.* **2008**, *33*, 759–785.

(40) Zhang, M.; Müller, A. H. E. *J. Polym. Sci., Part A: Polym. Chem.* **2005**, *43*, 3461–3481.

(41) Lee, H.-i.; Pietrasik, J.; Sheiko, S. S.; Matyjaszewski, K. *Prog. Polym. Sci.* **2010**, *35*, 24–44.

(42) Peng, S.; Bhushan, B. *RSC Adv.* **2012**, *2*, 8557–8578.

(43) Pesek, S. L.; Li, X.; Hammouda, B.; Hong, K.; Verduzco, R. *Macromolecules* **2013**, *46*, 6998–7005.

(44) Pesek, S. L.; Xiang, Q.; Hammouda, B.; Verduzco, R. *J. Polym. Sci., Part B: Polym. Phys.* **2017**, *55*, 104–111.

(45) Gerle, M.; Fischer, K.; Roos, S.; Müller, A. H. E.; Schmidt, M.; Sheiko, S. S.; Prokhorova, S.; Möller, M. *Macromolecules* **1999**, *32*, 2629–2637.

(46) Al Samak, B.; G. Carvill, A.; J. Rooney, J.; M. Thompson, J. *Chem. Commun.* **1997**, 2057–2058.

(47) Elling, B. R.; Xia, Y. *J. Am. Chem. Soc.* **2015**, *137*, 9922–9926.

(48) Sutthasupa, S.; Shiotsuki, M.; Masuda, T.; Sanda, F. *J. Am. Chem. Soc.* **2009**, *131*, 10546–10551.
(49) Jeong, H.; John, J. M.; Schrock, R. R. *Organometallics* **2015**, *34*, 5136–5145.
(50) Jang, E. S.; John, J. M.; Schrock, R. R. *ACS Cent. Sci.* **2016**, *2*, 631–636.
(51) Jha, S.; Dutta, S.; Bowden, N. B. *Macromolecules* **2004**, *37*, 4365–4374.
(52) Xia, Y.; Olsen, B. D.; Kornfield, J. A.; Grubbs, R. H. *J. Am. Chem. Soc.* **2009**, *131*, 18525–18532.
(53) Li, Z.; Zhang, K.; Ma, J.; Cheng, C.; Wooley, K. L. *J. Polym. Sci., Part A: Polym. Chem.* **2009**, *47*, 5557–5563.
(54) Lu, H.; Wang, J.; Lin, Y.; Cheng, J. *J. Am. Chem. Soc.* **2009**, *131*, 13582–13583.
(55) Zhang, H.; Zhang, Z.; Gnanou, Y.; Hadjichristidis, N. *Macromolecules* **2015**, *48*, 3556–3562.
(56) Moatsou, D.; Hansell, C. F.; O'Reilly, R. K. *Chem. Sci.* **2014**, *5*, 2246–2250.
(57) Love, J. A.; Morgan, J. P.; Trnka, T. M.; Grubbs, R. H. *Angew. Chem. Int. Ed.* **2002**, *41*, 4035–4037.
(58) Trzaskowski, B.; Grela, K. *Organometallics* **2013**, *32*, 3625–3630.
(59) Mayo, F. R.; Lewis, F. M. *J. Am. Chem. Soc.* **1944**, *66*, 1594–1601.
(60) Mayo, F. R.; Walling, C. *Chem. Rev.* **1950**, *46*, 191–287.
(61) Fineman, M.; Ross, S. D. *J. Polym. Sci.* **1950**, *5*, 259–262.
(62) Kelen, T.; Tüdös, F. *Journal of Macromolecular Science, Chemistry* **1975**, *A9*, 1–27.
(63) Jaacks, V. *Die Makromolekulare Chemie* **1972**, *161*, 161–172.
(64) Sevink, G.; Zvelindovsky, A.; Fraaije, J.; Huinink, H. *J. Chem. Phys.* **2001**, *115*, 8226–8230.
(65) Radzinski, S. C.; Foster, J. C.; Chapleski, R. C.; Troya, D.; Matson, J. B. *J. Am. Chem. Soc.* **2016**, *138*, 6998–7004.
(66) Singh, N.; Tureau, M. S.; Epps, T. H. *Soft Matter* **2009**, *5*, 4757–4762.
(67) Lin, T.-P.; Chang, A. B.; Chen, H.-Y.; Liberman-Martin, A. L.; Bates, C. M.; Voegtle, M. J.; Bauer, C. A.; Grubbs, R. H. *J. Am. Chem. Soc.* **2017**, *139*, 3896–3903.
(68) Dettmer, C. M.; Gray, M. K.; Torkelson, J. M.; Nguyen, S. T. *Macromolecules* **2004**, *37*, 5504–5512.
(69) Matyjaszewski, K.; Ziegler, M. J.; Arehart, S. V.; Greszta, D.; Pakula, T. *J. Phys. Org. Chem.* **2000**, *13*, 775–786.
(70) Sun, X.; Luo, Y.; Wang, R.; Li, B. G.; Zhu, S. *AIChE J.* **2008**, *54*, 1073–1087.
(71) Wang, R.; Luo, Y.; Li, B.-G.; Zhu, S. *AIChE J.* **2007**, *53*, 174–186.
(72) Radzinski, S. C.; Foster, J. C.; Scannelli, S. J.; Weaver, J. R.; Arrington, K. J.; Matson, J. B. *ACS Macro Lett.* **2017**, *6*, 1175–1179.
(73) Grubbs, R. H.; Khosravi, E. *Handbook of Metathesis: Polymer Synthesis*; Wiley, 2015.
(74) Slugovc, C.; Demel, S.; Riegler, S.; Hobisch, J.; Stelzer, F. *Macromol. Rapid Commun.* **2004**, *25*, 475–480.
(75) Xia, Y.; Kornfield, J. A.; Grubbs, R. H. *Macromolecules* **2009**, *42*, 3761–3766.
(76) Miyake, G. M.; Weitekamp, R. A.; Piunova, V. A.; Grubbs, R. H. *J. Am. Chem. Soc.* **2012**, *134*, 14249–14254.
(77) Radzinski, S. C.; Foster, J. C.; Matson, J. B. *Polym. Chem.* **2015**, *6*, 5643–5652.
(78) Wolfe, P. S.; Wagener, K. B. *Macromolecules* **1999**, *32*, 7961–7967.

(79) Rule, J. D.; Moore, J. S. *Macromolecules* **2002**, *35*, 7878–7882.

(80) Pollino, J. M.; Stubbs, L. P.; Weck, M. *Macromolecules* **2003**, *36*, 2230–2234.

(81) Seehof, N.; Grutke, S.; Risse, W. *Macromolecules* **1993**, *26*, 695–700.

(82) Liu, P.; Taylor, B. L. H.; Garcia-Lopez, J.; Houk, K. N.: Computational Studies of Ruthenium-Catalyzed Olefin Metathesis. In *Handbook of Metathesis*; Wiley-VCH Verlag GmbH & Co. KGaA, 2015; pp 199–252.

(83) Sanford, M. S.; Love, J. A.; Grubbs, R. H. *J. Am. Chem. Soc.* **2001**, *123*, 6543–6554.

(84) Adlhart, C.; Chen, P. *J. Am. Chem. Soc.* **2004**, *126*, 3496–3510.

(85) Vyboishchikov, S. F.; Bühl, M.; Thiel, W. *Chem. Eur. J.* **2002**, *8*, 3962–3975.

(86) Walsh, D. J.; Lau, S. H.; Hyatt, M. G.; Guironnet, D. *J. Am. Chem. Soc.* **2017**, *139*, 13644–13647.

(87) See Appendix A for the full derivation. We could not exclude the possibility that cycloaddition is the rate-limiting step, which would result in a more complicated rate expression.

(88) Further discussion of the ROMP mechanism can be found in Appendix A. We note that, at present, we cannot conclusively rule out an dissociate/associative pathway.

(89) Fürstner, A.; Thiel, O. R.; Lehmann, C. W. *Organometallics* **2002**, *21*, 331–335.

(90) Benitez, D.; Tkatchouk, E.; Goddard, W. A. *Organometallics* **2009**, *28*, 2643–2645.

(91) In-depth DFT investigation of the ROMP mechanism, including calculation of transition-state structures and identification of the rate-limiting step, will be the subject of future work.

(92) In order to account for pyridine binding, it is critical to use the same $[\mathbf{G3}]_0$ concentration in both homo- and copolymerization reactions. .

(93) Odian, G. *Principles of Polymerization*; 4th ed.; Wiley-Interscience: Hoboken, New Jersey, 2004.

(94) Meijs, G. F.; Rizzardo, E. *J. Macromol. Sci., Polym. Rev.* **1990**, *30*, 305–377.

Chapter 3

Impacts of the Graft Polymer Architecture on Physical Properties

1. Chang, A. B.;$^+$ Lin, T.-P.;$^+$ Thompson, N. B.; Luo, S.-X.; Liberman-Martin, A. L.; Chen, H.-Y.; Grubbs, R. H. Design, Synthesis, and Self-Assembly of Polymers with Tailored Graft Distributions. *J. Am. Chem. Soc.* **2017**, *139*, 17683–17693. ($^+$*Equal contributions.*)

2. Lin, T.-P.;$^+$ Chang, A. B.;$^+$ Luo, S.-X.; Chen, H.-Y.; Lee, B.; Grubbs, R. H. Effects of Grafting Density on Block Polymer Self-Assembly: From Linear to Bottlebrush. *ACS Nano* **2017**, *11*, 11632–11641. ($^+$*Equal contributions.*)

3. Haugan, I. N.; Maher, M. J.; Chang, A. B.; Lin, T.-P.; Grubbs, R. H.; Hillmyer, M. A.; Bates, F. S. Consequences of Grafting Density on the Linear Viscoelastic Behavior of Graft Polymers. *ACS Macro Lett.* **2018**, *7*, 525–530.

ABSTRACT

Living ring-opening metathesis polymerization (ROMP) enables precise control over the graft polymer architecture. In this chapter, we will discuss the physical consequences of varying the molecular architecture in two contexts: block polymer self-assembly and linear rheology. The impacts of grafting density and graft distribution on block polymer self-assembly will be first described. AB graft diblock polymers with tapered, uniform, and inverse-tapered molecular "shapes" were synthesized by ROMP. Small-angle X-ray scattering (SAXS) analysis of the self-assembled structures indicates that the graft distribution influences shape-filling demands and therefore the backbone conformation. Across seventeen series of uniformly grafted block polymers spanning the linear, comb, and bottlebrush regimes ($0 \leq z \leq 1$), the scaling of the lamellar period with the total backbone degree of polymerization ($d^* \sim N_{\mathrm{bb}}^{\alpha}$) was studied. The scaling exponent α monotonically decreases with decreasing grafting density (z) and exhibits an apparent transition at a critical $z \approx 0.2$, suggesting significant changes in the chain conformations. In complementary studies, the linear viscoelastic behavior of eight series of graft homopolymers was investigated as a function of grafting density ($0 \leq z \leq 1$) and backbone length ($10 < N_{\mathrm{bb}} < 3000$). Dynamic master curves reveal that these polymers display Rouse-

like and reptation dynamics with a sharp transition in the zero-shear viscosity data, demonstrating that grafting density strongly impacts the onset of entanglements. The scaling of the entanglement plateau modulus with *z* was found to conflict with existing theoretical models for graft polymers, but a molecular interpretation based on thin flexible chains at low *z* and thick semiflexible chains at high *z* anticipates the sharp transition between the limiting dynamic regimes. Collectively, the behavior disclosed herein provides valuable insights into the static and dynamic impacts of the graft polymer architecture, enabling comparisons with existing theory and introducing new opportunities for materials design.

Table of Contents

3-1 Impact of Graft Distribution on Block Polymer Self-Assembly

Grafting density and graft distribution are important parameters that govern polymer architectures and physical properties. We recently developed a grafting-through ring-opening metathesis copolymerization approach to tune the grafting density and graft distribution (Chapter 2). In this section, we will further demonstrate the utility of the ROMP method by describing the synthesis of AB diblock polymers with variable side chain distributions, then examine how differences in chain connectivity affect self-assembly.

Three different AB graft diblock polymers were synthesized by controlled ROMP. Simple substitutions of the discrete co-monomers ensure that the block polymers differ *only* in the distribution of the grafts. All other aspects of the structure and chemistry are identical:

- All block polymers feature PDMS and PS side chains. The grafting-through approach guarantees that the side chain molecular weights are the same within each block (**PDMS**: 1280 g mol^{-1}, **PS**: 3990 g mol^{-1}).
- The grafting density in each block is 50%.
- The backbone degree of polymerization in each block is the same. For the A block (**PDMS** + diluent), $N_{\text{bb,A}} = 150$; for the B block (**PS** + diluent), $N_{\text{bb,B}} = 50$.
- The above constraints enforce equal block volume fractions for all three block polymers: $f = 0.50$.

The side chain distributions can be varied while fixing all of the preceding parameters by switching the identity of the diluents in each block. Scheme 3.1 illustrates the resulting block polymer structures with uniform (**BP-1**) or gradient (**BP-2**, **BP-3**) graft distributions. The backbones are drawn in the fully extended limit for ease of visualization, and the side chain conformations and cross-sectional radii are depicted as anticipated by existing theory.[1-4]

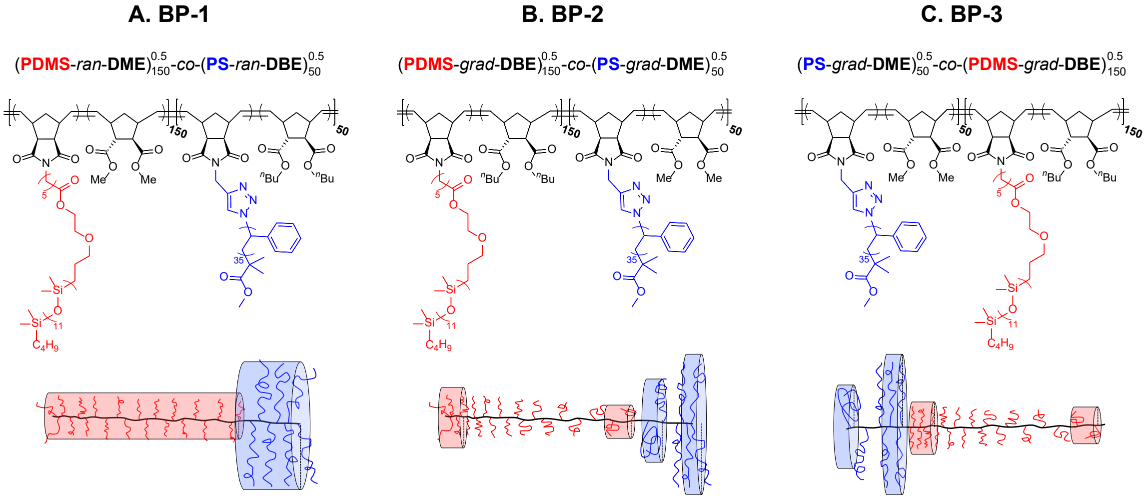

Scheme 3.1: Illustrations of three AB graft diblock polymers differing only in the side chain distribution: (*A*) uniform (**BP-1**), (*B*) gradient (**BP-2**), and (*C*) inverse-gradient (**BP-3**). (*top*) Chemical structures. (*bottom*) Schematic illustrations of the anticipated molecular "shapes," shown in the limit of fully extended backbones for ease of visualization.

BP-1 was synthesized by first copolymerizing **PDMS** and *endo,exo*-norbornenyl dimethylester (*dx*-DMeE, **1a**) in a 1:1 feed ratio. Since $r_1 = 1.1$ and $r_2 = 0.94$, the first block has an ideal random backbone sequence and therefore uniform side chain distribution.

After complete consumption of **PDMS** and *dx*-DMeE, the chain ends were still living, and the second block (B) was added via a 1:1 mixture of **PS** and *endo,exo*-norbornenyl di-*n*-butylester (*dx*-D^{n}BuE, **1d**). Since r_1 = 0.80 and r_2 = 1.2, the side chain distribution in the second block is also effectively uniform. A graft polymer with a gradient side chain distribution (**BP-2**) was synthesized by keeping all conditions exactly the same but simply switching the diluents. The first block (A) was synthesized by copolymerizing **PDMS** with *dx*-D^{n}BuE instead of *dx*-DMeE; since r_1 = 1.1 and r_2 = 0.43, the block is rich in the macromonomer at early conversions and rich in the diluent at late conversions. Addition of **PS** + *dx*-DMeE as the second block (B; r_1 = 0.54, r_2 = 1.4) therefore produces a block polymer with low grafting density at the block-block junction and increasing grafting density moving toward the free chain ends. A third distinct graft block polymer (**BP-3**) was synthesized by keeping all conditions exactly the same as those for **BP-2** but simply switching the order in which the blocks were added. By polymerizing block B (**PS** + *dx*-DMeE) first and block A (**PDMS** + *dx*-D^{n}BuE) second, the product features the inverse-tapered architecture compared to **BP-2**. Scheme 3.1 provides the chemical structures of **BP-1**, **-2**, and **-3**. Analysis by SEC (Appendix B, Figure B.2) and ^{1}H NMR (Figure B.3) confirms that their overall molecular weights and chemical compositions are identical.

The three graft block polymers were annealed for 24 hours at 140 °C under vacuum and modest applied pressure. The resulting microphase-separated structures were characterized by synchrotron-source small-angle X-ray scattering (SAXS). Comparison of the SAXS patterns (Figure 3.1) indicates that all three samples form long-range-ordered lamellar morphologies but also reveals two crucial differences. First, the lamellar periods ($d^* = 2\pi/q^*$) differ. Equal values of d^* are perhaps expected since the chemical compositions and backbone and side chain lengths are all identical; on the contrary, **BP-1** exhibits d^* = 51.0 nm (Figure 3.1A), while **BP-2** (3.1B) and **BP-3** (3.1C) exhibit d^* = 49.5 and 46.5 nm, respectively. Second, the relative thicknesses of the A and B domains (d_A and d_B) also differ. Compared to **BP-1**, **BP-2** forms more symmetric lamellae, as evidenced by the weak intensities of the even-order diffraction peaks (q_2, q_4, …). The inverse-gradient **BP-3** forms lamellae that are the most symmetric of all; in fact, the complete extinction of even-order peaks suggests that d_A and d_B are equal.

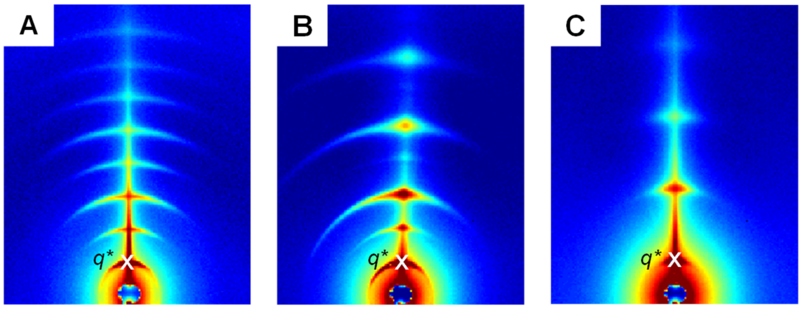

Figure 3.1: SAXS patterns corresponding to the annealed graft block polymers: (*A*) **BP-1**, (*B*) **BP-2**, (*C*) **BP-3**. The white "x"' indicates the first-order diffraction peak, q^*.

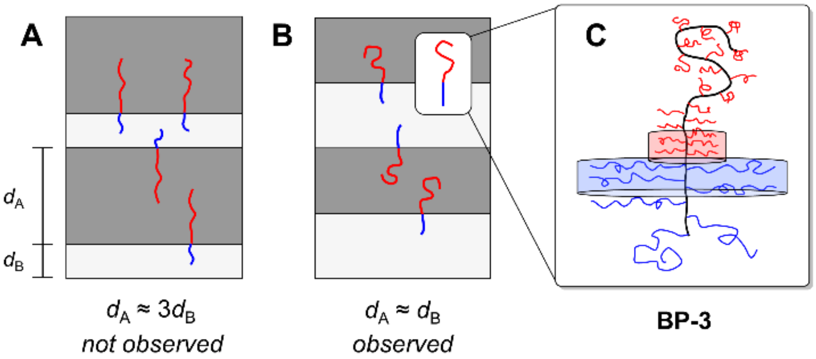

Figure 3.2: Schematic illustration of the relationships between chain dimensions and the lamellar period. (*A*) $d_A \approx 3d_B$ is expected if the backbones are fully stretched (since $N_{bb,A} = 3N_{bb,B}$), but it is consistent with SAXS data. (*B*) Instead, $d_A \approx d_B$ is observed. This requires bending of the A block backbone. (*C*) Illustration of **BP-3** and revised chain conformations.

This symmetry is perhaps surprising: although the block volume fractions are equal ($f = 0.50$), the backbone lengths are highly asymmetric: $N_{bb,A} = 3N_{bb,B}$. The graft polymer backbones are clearly not fully extended as illustrated in Scheme 3.1. If the backbone were fully extended, $d_A = 3d_B$ is expected for all samples (Figure 3.2A). Every fourth diffraction peak (q_4, q_8, …) would be weak, which is *inconsistent* with the SAXS data. Figure 3.3 compares simulated and measured 1D-averaged SAXS data for **BP-3**, supporting the assignment of symmetric layer structures instead ($d_A = d_B$, Figure 3.2B). The SAXS data indicates that the backbones are flexible and that changing the side chain distribution affects the backbone conformation. Gradient distributions in which the grafting density is *either* lowest (**BP-2**) or highest (**BP-3**) at the block-block junction enable more efficient packing than uniform distributions (**BP-1**). Closer packing balances the backbone asymmetry with the demands of equal block volumes, most likely via bending of the A (PDMS) block backbone (Figure 3.2C).

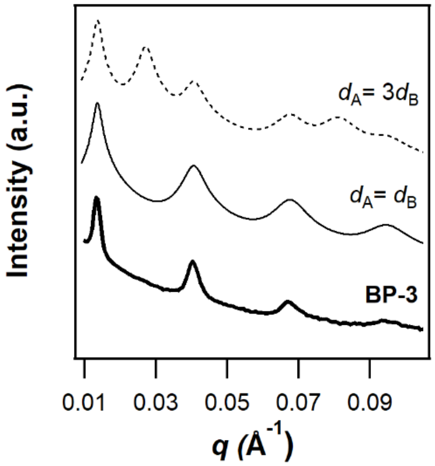

Figure 3.3: Comparison of simulated (*top, middle)* and measured (*bottom*) 1D-averaged SAXS data. The experimental data closely matches the expected SAXS pattern corresponding to lamellae with symmetric ($d_A = d_B$) domains.

For all samples, the backbones should be strongly stretched at the domain interface as a consequence of segregation. In the case of **BP-2**, the chains should have the highest local backbone stiffness but also the greatest free volume at the free chain ends. Compared to the uniformly grafted **BP-1**, this may better accommodate high grafting density in the center of the domains. In the case of **BP-3**, since the backbones are already strongly stretched at the domain interfaces, the high grafting density may not significantly stretch the backbones further, resulting in the smallest *d** among all three graft polymers. Low grafting density at the free chain ends should result in comparatively low backbone stiffness and therefore better accommodate bending in the A block (Figure 3.2C). Collectively, these results indicate that the side chain distribution affects chain stretching and packing. This result indicates that molecular “shape” is indeed an important design parameter, allowing materials to possess non-equilibrium density distributions.

3-2 Impact of Grafting Density on Block Polymer Self-Assembly

3-2.1 Introduction

We recently reported the efficient synthesis of graft polymers with controlled grafting density (z), defined as the average number of polymer side chains per backbone repeat unit (Chapter 2). In this section, we will discuss the effects of grafting density on the scaling of the lamellar period (d^*) with the total backbone degree of polymerization (N_{bb}). The scaling of d^* reflects steric demands and penalties to chain stretching, thus providing valuable insight into the physical consequences of varying polymer architectures. d^* is an attractive parameter to study because it has an unambiguous physical definition (unlike potentially model-dependent parameters such as χ) and can be directly measured by scattering and electron microscopy.[5]

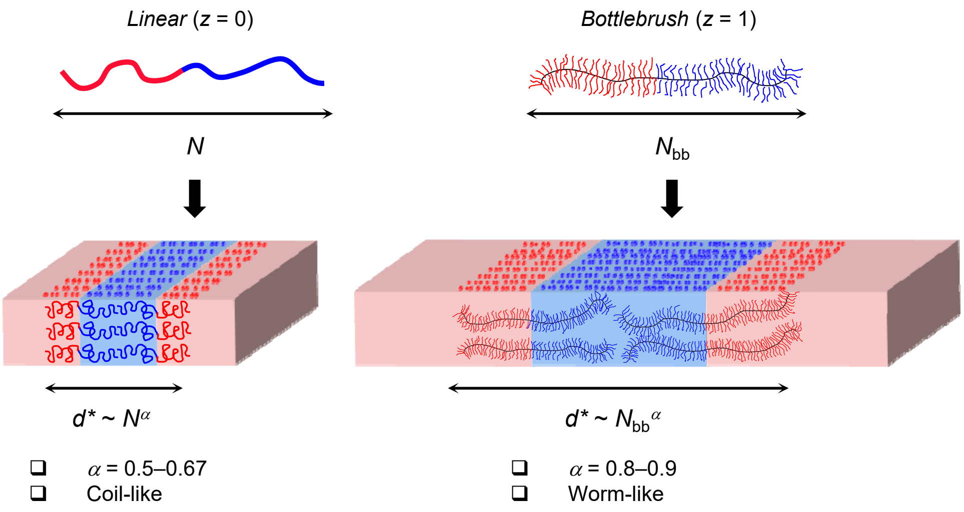

Figure 3.4: Self-assembly of linear and bottlebrush diblock polymers into lamellae.

Figure 3.4 illustrates the self-assembly of linear (z = 0) diblock polymers into lamellar morphologies. For symmetric linear diblock polymers, arguments based on free energy demands accurately predict the scaling behavior ($d^* \sim N_{bb}^{\alpha}$). The scaling exponent α is 1/2 in the weak segregation limit ($\chi N_{bb} \approx 10.5$) and plateaus at 2/3 in the strong segregation limit ($\chi N_{bb} >> 10.5$).[6-7] The small scaling exponent is inherently related to the coil-like chain conformations. In contrast, reports of scaling behavior for block polymers with bottlebrush (z = 1) and other complex, non-linear architectures are limited due to the synthetic challenges associated with (1) precisely controlling the architecture, molecular weight, and composition and (2) efficiently preparing multiple samples to study trends.

Bottlebrush polymers have recently emerged as an advanced class of non-linear architectures that manifest unique physical, mechanical, and dynamic properties.[8-15] Like their linear analogues, bottlebrush diblock polymers can access lamellar morphologies (Figure 3.4). However, bottlebrush block polymers display much larger scaling exponents (α = 0.8–0.9),[16-19] consistent with extended backbone conformations. Steric repulsion between the densely grafted side chains imparts a certain bending rigidity to the backbone, which can be modeled as a wormlike chain.[20-23] The unique properties of bottlebrush polymers have been previously exploited for applications in photonics,[24-27] lithography,[28-29] and surface coatings.[30] For example, the bottlebrush architecture minimizes chain entanglement and promotes rapid self-assembly to structures with ultra-large d^*, enabling the fabrication of photonic materials that reflect visible and even infrared radiation. In contrast, such materials are generally inaccessible using linear and low-z analogues due to the ultra-high molecular weights required as well as their low entanglement molecular weights.

The effects of grafting density on the rheological properties of homopolymers have received tremendous interest.[31-39] However, the impacts of grafting density on block polymer self-assembly have not been explored.[40-43] Elucidating these physical principles is not only of fundamental importance but should also guide material design. With this mindset, we launched the study on block polymers with systematically modified grafting densities ($0 \leq z \leq 1$) spanning the linear, comb, and bottlebrush regimes. The self-assembly of these block polymers was examined by small-angle X-ray scattering (SAXS), allowing determination of the scaling behavior. These studies reveal vital information on the backbone conformations, and the determined scaling laws allow the prediction of lamellar periods toward improved materials design.

3-2.2 *Synthesis of Block Polymers with Variable Grafting Density (**System I**)*

Ring-opening metathesis polymerization (ROMP) is a powerful strategy to synthesize well-defined bottlebrush polymers.[44-47] We targeted poly(D,L-lactide)-*b*-polystyrene (**PLA**-*b*-**PS**) graft diblock polymers to permit comparisons with brush PLA-*b*-

PS systems previously investigated in the context of self-assembly.[17-19,27,48] All polymerizations were performed in CH_2Cl_2 at room temperature under inert atmosphere. To vary the grafting density (Scheme 3.2), the first block was synthesized by copolymerizing a **PLA** macromonomer (M_n = 3230 g/mol) with a discrete co-monomer (*i.e.*, diluent), **DME** (*endo*,*exo*-norbornenyl dimethyl ester, M_n = 210 g/mol). As discussed in Chapter 2-7, the grafting density (z) is precisely determined by the feed ratio according to Eq. 3-1:

$$z = \frac{[\mathbf{PLA}]_0}{[\mathbf{PLA}]_0 + [\mathbf{DME}]_0} \qquad \text{Eq. 3-1}$$

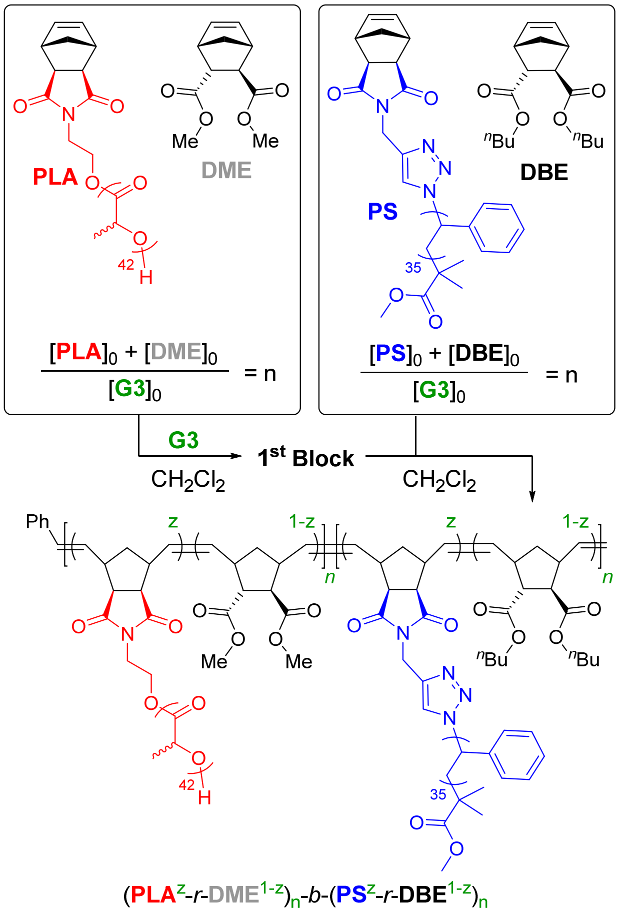

Scheme 3.2: Synthesis of (**PLA**^{z}-*r*-**DME**$^{1-z}$)$_n$-*b*-(**PS**^{z}-*r*-**DBE**$^{1-z}$)$_n$ block polymers (**System I**) featuring variable backbone degrees of polymerization ($N_{bb} = 2n$ = 44–363) and grafting densities (z = 1.00, 0.75, 0.50, 0.35, 0.25, 0.20, 0.15, 0.05, 0).

After both co-monomers were fully consumed (verified by ^{1}H NMR), a mixture of a **PS** macromonomer (M_n = 3990 g/mol) and another discrete diluent, **DBE** (*endo*,*exo*-norbornenyl di-*n*-butyl ester, M_n = 294 g/mol), was introduced as the second block. The **PS**/**DBE** feed ratio was the same as the **PLA**/**DME** feed ratio in the first block. The determined reactivity ratios (block A: $r_{\mathrm{PLA}} = 0.92$, $r_{\mathrm{DME}} = 1.11$; block B: $r_{\mathrm{PS}} = 0.80$, $r_{\mathrm{DBE}} = 1.16$) suggest that the copolymerization is statistically random with minimal compositional drift. (See Chapter 2-5.) Monitoring the instantaneous monomer concentrations over time indicates that the macromonomer and diluent are incorporated at approximately equal rates in each block, consistent with uniform *z* throughout the entire block polymer. The backbone degrees of polymerization (*n*) for the first and second blocks were equal and determined by the ratio of the total monomer concentration to catalyst (**G3**) concentration (Eqs. 3-2–3-3:

$$n = \frac{[\mathbf{PLA}]_0 + [\mathbf{DME}]_0}{[\mathbf{G3}]_0} = \frac{N_{\mathrm{bb}}}{2} \quad \text{Eq. 3-2}$$

$$n = \frac{[\mathbf{PS}]_0 + [\mathbf{DBE}]_0}{[\mathbf{G3}]_0} = \frac{N_{\mathrm{bb}}}{2} \quad \text{Eq. 3-3}$$

For **System I**, nine different series with variable grafting densities (z = 1.00, 0.75, 0.50, 0.35, 0.25, 0.20, 0.15, 0.05, and 0) were prepared. Each series includes five to seven block polymers with fixed composition and varying backbone lengths (N_{bb} = 44–363). To achieve consistent control over *z*, the targeted macromonomer/diluent feed ratios were verified by ^{1}H NMR prior to initiating the first block with **G3**. After reaching >99% conversion, the reaction mixtures were quenched by addition of excess ethyl vinyl ether. The block polymers were precipitated into methanol at −78 ℃, isolated by filtration, and dried under vacuum for >24 h. The first blocks and precipitated products were analyzed by NMR and size-exclusion chromatography (SEC), allowing determination of the molecular weights and therefore N_{bb}. These analyses indicated that our methodology produced well-defined, monodisperse ($Đ$ = 1.01–1.18) graft block polymers. The compositions of all samples in **System I** are presented in Table 3.1.

Table 3.1: Total number-average molecular weights (M_n) and total backbone degrees of polymerization (N_{bb}) (**PLA**^{z}-*r*-**DME**$^{1-z}$)$_n$-*b*-(**PS**^{z}-*r*-**DBE**$^{1-z}$)$_n$ graft block polymers (**System I**).

z	ID	M_n (kDa)	N_{bb}
1.00	A1	158	44
	A2	304	84
	A3	465	129
	A4	596	165
	A5	718	199
0.75	B1	234	84
	B2	361	130
	B3	467	168
	B4	606	219
0.50	C1	166	86
	C2	243	126
	C3	315	163
	C4	400	207
0.35	D1	124	87
	D2	181	127
	D3	238	167
	D4	301	211
	D5	369	258
	D6	430	301
0.25	E1	98.8	90
	E2	146	134
	E3	167	153
	E4	200	183
	E5	216	197
	E6	244	223
	E7	286	262
0.20	F1	119	128
	F2	153	166
	F3	195	211
	F4	216	234
	F5	230	249
	F6	248	268
	F7	294	318
0.15	G1	163	216
	G2	178	235
	G3	189	250
	G4	216	286
	G5	232	307
	G6	246	325
0.05	H1	91.7	218
	H2	103	246
	H3	111	264
	H4	124	294
	H5	129	308
	H6	142	339
0.00	I1	46.5	184
	I2	55.4	219
	I3	62.7	249
	I4	72.4	287
	I5	82.3	326
	I6	91.5	363

3-2.3 Self-Assembly and Scaling of the Lamellar Period

The isolated polymers were thermally annealed at 140℃ for 24 hours under modest pressure. Scanning electron microscope (SEM) images obtained for select block polymers with $N_{bb} \approx 200$ indicate long-range-ordered lamellar morphologies (Figure 3.5). Samples were also characterized by synchrotron-source small-angle X-ray scattering (SAXS). Raw 2D SAXS data are provided in Appendix B (Figure B.4). Representative azimuthally averaged SAXS profiles, corresponding to five samples with $z = 1$, are shown in Figure 3.6A. For all series, the scattering patterns are consistent with well-ordered lamellae.

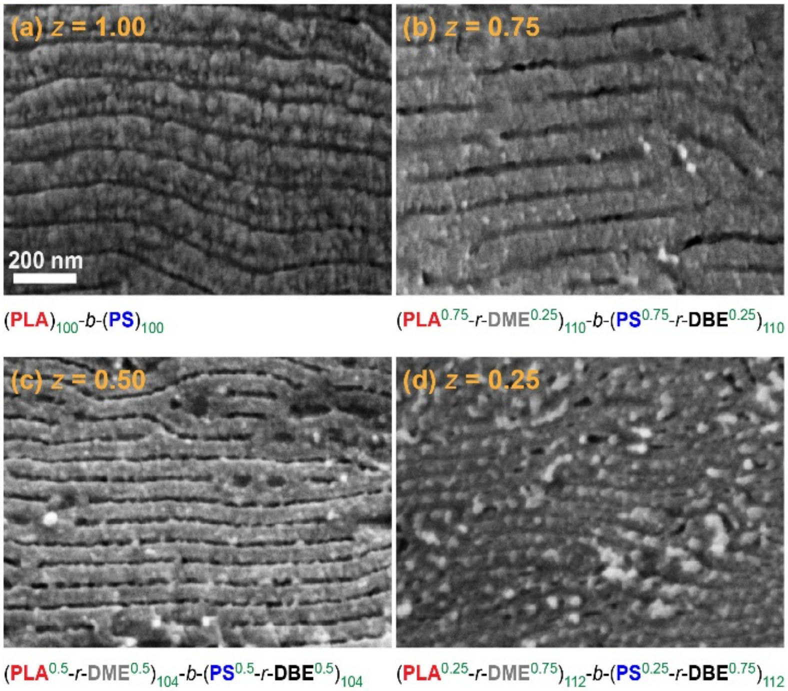

(PLA)$_{100}$-*b*-(PS)$_{100}$ (PLA$^{0.75}$-*r*-DME$^{0.25}$)$_{110}$-*b*-(PS$^{0.75}$-*r*-DBE$^{0.25}$)$_{110}$

(PLA$^{0.5}$-*r*-DME$^{0.5}$)$_{104}$-*b*-(PS$^{0.5}$-*r*-DBE$^{0.5}$)$_{104}$ (PLA$^{0.25}$-*r*-DME$^{0.75}$)$_{112}$-*b*-(PS$^{0.25}$-*r*-DBE$^{0.75}$)$_{112}$

Figure 3.5: Scanning electron micrographs of graft block polymers with (*A*) z = 1.00, **(PLA)**$_{100}$-*b*-**(PS)**$_{100}$; (*B*) z = 0.75, **(PLA**$^{0.75}$-*r*-**DME**$^{0.25}$)$_{110}$-*b*-**(PS**$^{0.75}$-*r*-**DBE**$^{0.25}$)$_{110}$; (*C*) z = 0.50, **(PLA**$^{0.5}$-*r*-**DME**$^{0.5}$)$_{104}$-*b*-**(PS**$^{0.5}$-*r*-**DBE**$^{0.5}$)$_{104}$; and (*D*) z = 0.25, **(PLA**$^{0.25}$-*r*-**DME**$^{0.75}$)$_{112}$-*b*-**(PS**$^{0.25}$-*r*-**DBE**$^{0.75}$)$_{112}$.

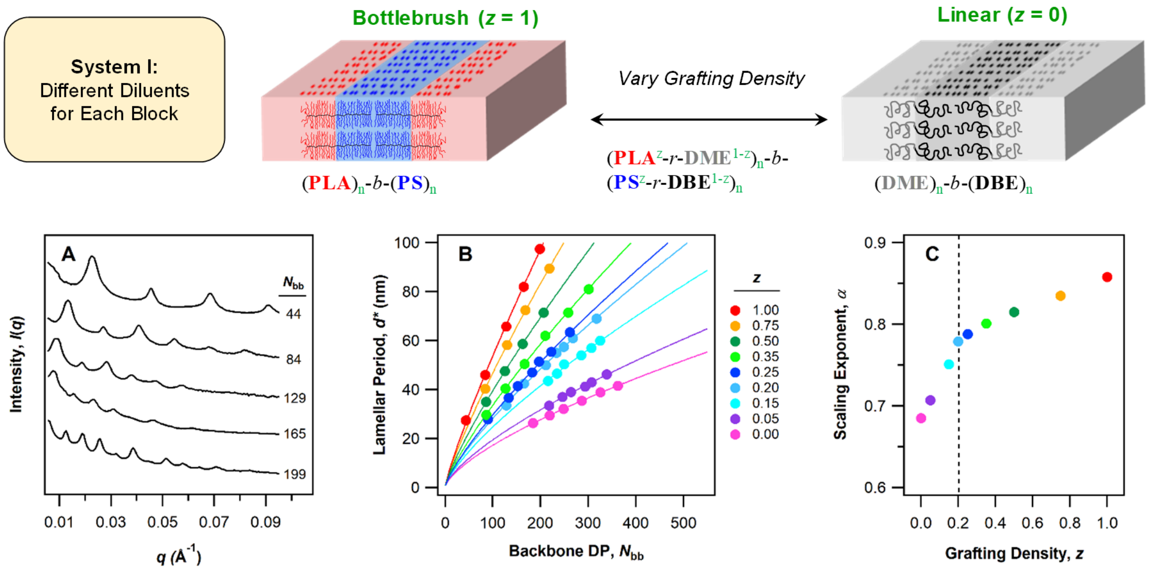

Figure 3.6: (*top*) Scheme of **System I**, comprising graft block polymers **(PLA**^{z}-*r*-**DME**$^{1-z}$)$_{n}$-*b*-(**PS**^{z}-*r*-**DBE**$^{1-z}$)$_{n}$ with variable total backbone degrees of polymerization (N_{bb} = 2n) and grafting densities (z). (*A*) Stacked 1D azimuthally averaged SAXS profiles for z = 1, indicating well-ordered lamellar morphologies. (*B*) Experimental data for the lamellar period (d*) and N_{bb} (circles), as well as calculated power-law fits ($d^* \sim N_{bb}^{\alpha}$, lines). (*C*) Plot of the scaling exponents (α) as a function of z. A transition occurs around z = 0.2 (dotted line).

For all graft block polymers, the lamellar periods (d^*) were determined by indexing the raw SAXS data. Figure 3.6B shows plots of d^* *versus* N_{bb}. The scaling relationships for each series were calculated using a least-square power-law fitting function in *Igor*. To gain additional insight into the scaling behavior, the calculated scaling exponents α were plotted as a function of z (Figure 3.6C). For the $z = 1$ series, the large magnitude of α (0.86) is consistent with previously reported values for symmetric PLA-*b*-PS bottlebrush block polymers ($\alpha = 0.8–0.9$).[16-20,49] At the other extreme, the $z = 0$ series exhibits $\alpha = 0.69$, very close to the theoretical value ($\alpha = 2/3$) for strongly segregated symmetric linear diblock polymers.[7] The variable-z series ($z = 0.75, 0.50, 0.35, 0.25, 0.20, 0.15, 0.05$) constitute intermediate regimes bridging the two extremes. Comparing all series, the scaling exponents decrease monotonically with decreasing z. However, while α modestly decreases from 0.86 ($z = 1.00$) to 0.78 ($z = 0.20$), it then sharply decreases with decreasing z to 0.69 ($z = 0$). Collectively, these trends suggest changes in the backbone conformation with decreasing grafting density. Consistent with recent experimental and theoretical reports, at a certain critical z the conformational regime may transition from densely grafted brushes to loosely grafted brushes or combs.[50-51] These changes significantly impact the physical properties of graft homopolymers, such as the plateau modulus and extensibility. However, the effects of grafting density on block polymer phase behavior are unexplored to date. In Section 3-2.5, we will propose a model for the observed scaling behavior.

3-2.4 Synthesis and Self-Assembly: ***System II***

In this work, individual blocks can be treated as effectively homogeneous. No evidence of microphase separation is observed, even at low grafting densities and high total backbone degrees of polymerization [*e.g.*, each block $(\mathbf{PLA}^{0.05}\text{-}r\text{-}\mathbf{DME}^{0.95})_{200}$ and $(\mathbf{PS}^{0.05}\text{-}r\text{-}\mathbf{DBE}^{0.95})_{200}$, Figure B.5]. To a first approximation, variations in χ between the backbone and side chains do not appear significant. However, varying the grafting density in **System I** may also affect the effective χ *between* blocks. Changing χ would influence d^* and potentially complicate the interpretations of the observed scaling trends. For symmetric linear diblock polymers, d^* exhibits a weak dependence on χ in the strongly segregated regime ($d^* \sim \chi^{1/6}$) and is independent of χ in the weakly segregated regime. In the mean-field Flory-Huggins lattice model, χ is determined by the number of nearest neighbor contacts per monomer. In our materials, since the number ratio of diluents to side chain monomers (*i.e.*, either lactide or styrene repeats) is very small, the diluents are not expected to significantly affect χ. We anticipate that the large size disparity between macromonomers and diluents should make polymer architecture the primary factor responsible for the observed trends.

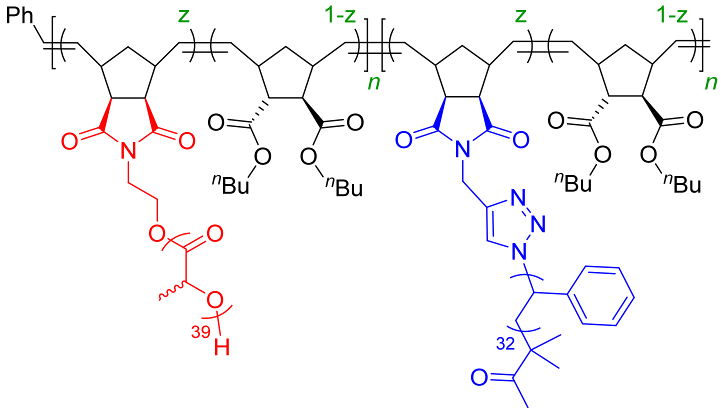

Scheme 3.3: $(\mathbf{PLA}^{z}\text{-}r\text{-}\mathbf{DBE}^{1-z})_{\mathrm{n}}\text{-}b\text{-}(\mathbf{PS}^{z}\text{-}r\text{-}\mathbf{DBE}^{1-z})_{n}$ of variable backbone degrees of polymerization ($N_{\mathrm{bb}} = 2n = 82$–$533$) and grafting densities (z = 0.75, 0.50, 0.35, 0.25, 0.15, 0.12, 0.06, and 0.05).

To test this hypothesis, we synthesized **System II**, using the same diluent (**DBE**) to vary z in both blocks (Scheme 3.3). The lowest-z extreme ($z = 0$) in **System II** is the homopolymer $(\mathbf{DBE})_{\mathrm{n}}$, which does not microphase separate. Macromonomers **PLA** (M_{n} = 3030 g/mol) and **PS** (M_{n} = 3800 g/mol) of similar molecular weights as those in **System I** were used. The determined reactivity ratios ($r_{\mathrm{PLA}} = 1.04$, $r_{\mathrm{DBE}} = 0.89$; $r_{\mathrm{PS}} = 0.83$, $r_{\mathrm{DBE}} = 1.16$) indicate random copolymerization within each block and therefore uniform grafting density. As for **System I**, polymers of general formula $(\mathbf{PLA}^{z}\text{-}r\text{-}\mathbf{DBE}^{1-z})_{\mathrm{n}}\text{-}b\text{-}(\mathbf{PS}^{z}\text{-}r\text{-}\mathbf{DBE}^{1-z})_{\mathrm{n}}$ were prepared ($N_{\mathrm{bb}} = 2n = 82$–$533$; z = 0.75, 0.50, 0.35, 0.25, 0.15, 0.12, 0.06, 0.05). The isolated monodisperse ($Đ$ = 1.02–1.19) copolymers were characterized by NMR and SEC. The compositions of all samples in **System II** are presented in Table 3.2.

Table 3.2: Total number-average molecular weights (M_n) and total backbone degrees of polymerization (N_{bb}) (**PLA**^{z}-*r*-**DBE**$^{1-z}$)$_n$-*b*-(**PS**^{z}-*r*-**DBE**$^{1-z}$)$_n$ graft block polymers (**System II**).

z	**ID**	M_n **(kDa)**	N_{bb}	z	**ID**	M_n **(kDa)**	N_{bb}
0.75	J1	116	44	0.15	N1	98.5	129
	J2	215	82		N2	161	212
	J3	330	125		N3	193	253
	J4	402	152		N4	213	279
	J5	521	198		N5	251	329
	J6	649	246		N6	299	392
0.50	K1	249	135	0.12	O1	150	224
	K2	322	174		O2	183	274
	K3	396	213		O3	221	330
	K4	472	254		O4	248	370
	K5	529	285		O5	274	409
	K6	603	325		O6	302	451
0.35	L1	241	174	0.06	P1	156	324
	L2	307	221		P2	177	367
	L3	364	263		P3	199	413
	L4	436	314		P4	226	469
	L5	472	341		P5	257	533
	L6	538	388	0.05	Q1	152	337
0.25	M1	232	216		Q2	169	376
	M2	277	258		Q3	184	408
	M3	335	312		Q4	203	451
	M4	384	358				
	M5	406	378				
	M6	472	439				

The samples were thermally annealed under the same conditions as **System I.** All of the polymers in **System II** self-assembled into well-ordered lamellae as evidenced by SAXS (Appendix B, Figure B.6). Azimuthally averaged 1D SAXS plots obtained for the z = 0.75 series are shown in Figure 3.7A as representative examples. Figure 3.7B shows the power-law fits (d^* vs. N_{bb}) for each series. The α values in **System II** are uniformly smaller compared to their counterparts of the same grafting density in **System I**. This observation could be attributed to the larger changes in χ between blocks upon decreasing z. The z = 0.05 series displays an α value of 0.52, approaching the theoretical value in the weak segregation limit ($\alpha = 1/2$).[6-7] Comparing Figures 3.6C and 3.7C suggests that the different d^* and α values likely reflect changes in χ. The linear diblock polymer (**DME**)$_n$-*b*-(**DBE**)$_n$, which is exactly the $z = 0$ series in **System I**, is itself strongly segregated, whereas the $z = 0$ series in **System II** is the homopolymer (**DBE**)$_n$. However, we note that the transition between regions of shallow and steep decreases in α with decreasing z occurs at nearly the same z in both systems ($z \approx 0.2$), suggesting that such transition is intrinsically related to polymer architecture rather than segregation strengths.

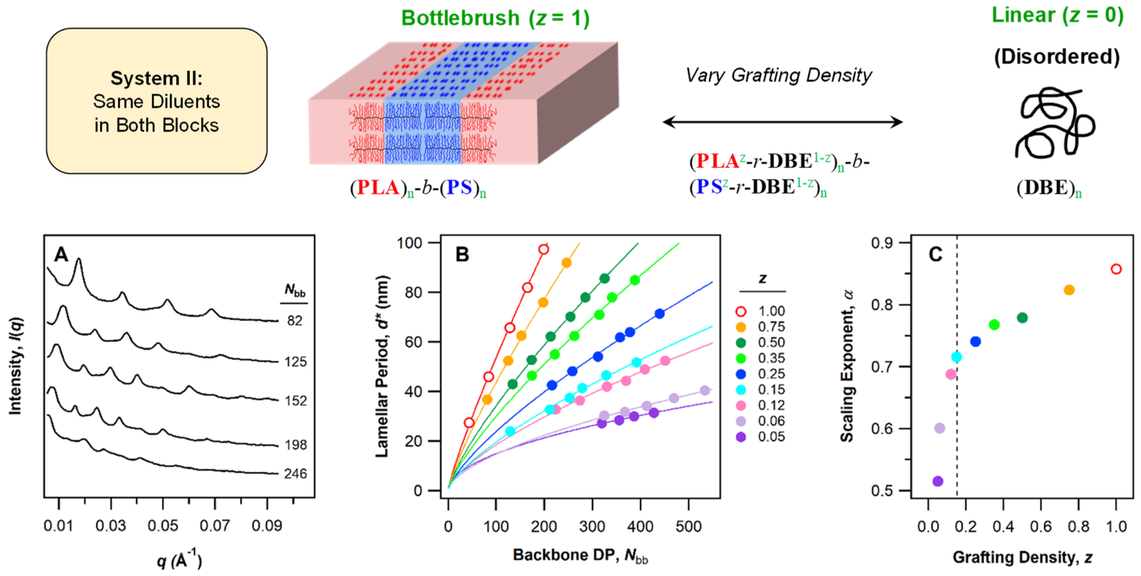

Figure 3.7: (*top*) Scheme of **System II**, comprising graft block polymers (**PLA**^{z}-*r*-**DME**$^{1-z}$)$_n$-*b*-(**PS**^{z}-*r*-**DBE**$^{1-z}$)$_n$ with variable total backbone degrees of polymerization ($N_{bb} = 2n$) and grafting densities (z). (*A*) Stacked 1D azimuthally averaged SAXS profiles for $z = 0.75$, indicating well-ordered lamellar morphologies. (*B*) Experimental data for the lamellar period (d^*) and N_{bb} (circles), as well as calculated power-law fits ($d^* \sim N_{bb}{}^{\alpha}$, lines). (*C*) Plot of the scaling exponents (α) as a function of z. A transition occurs around $z = 0.2$ (dotted line). Note that in (*B*) and (*C*), unfilled circles correspond to data for **System I** ($z = 1.00$), in which the side chain molecular weights are slightly higher.

We further highlight the significance of grafting density effects on the scaling of the lamellar period by predicting the required N_{bb} to reach an arbitrary value of $d^* = 200$ nm (Figure 3.8). Such a large d^* is desired for photonic applications. At the same z, N_{bb} required to reach $d^* = 200$ is larger for block polymers in **System II** than in **System I** as a result of differences in segregation strengths. In both systems, the predicted N_{bb} values exponentially increase with decreasing z below the observed transition ($z < 0.20$). In the linear block polymer limit ($z = 0$, **System I**), the required N to reach $d^* = 200$ nm is close to 4000. Such high-molecular-weight linear polymers are extremely challenging to synthesize, and as a result there are very few examples of linear block polymers that can self-assemble to visible-light-reflecting photonic crystals.[52] Existing examples are typically limited by low conversion and inability to process the materials from the melt. In contrast, a 50% grafted block polymer should only require $N_{\mathrm{bb}} \approx 730$. Manipulating the grafting density through copolymerization therefore constitutes a promising strategy to overcome limitations associated with both synthesis and processing. Further discussion of grafting density as a design parameter for polymer photonic crystals can be found in Chapter 6-2.2.

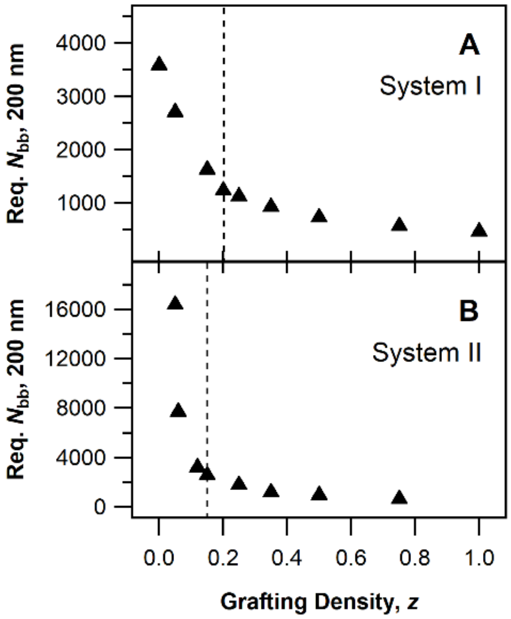

Figure 3.8: Plots of predicted N_{bb} required to access $d^* = 200$ nm as a function of grafting density (z) for (A) **System I** and (B) **System II**.

3-2.5 Interpretation of the Scaling Trends

We derive a potential model in order to relate the observed changes in α with grafting density (z) to the conformations of the graft polymer backbone and side chains. Key experimental results to capture include (1) the monotonic decrease in α with z (Figures 3.6C and 3.7C), (2) the apparent transition between shallow and steep decreases in α at a critical $z_c = 0.2$, and (3) potential segregation effects that emerge at low z. Comparison of two systems – one in which all series ($z \geq 0$) are in the strongly segregated limit (SSL)

(**System I**) and one that bridges the strongly and weakly segregated limits (WSL) (**System II**) – suggests that architecture effects, not segregation effects, are primarily responsible for the observed trends. We will begin by framing our results in the context of existing theory for the self-assembly of diblock polymers, then propose a functional form for the observed relationship between z and d^*, *i.e.*, $d^* \sim N_{\mathrm{bb}}^{f(z)}$. We note that, in part due to the long-standing challenges associated with synthesizing well-defined graft polymers, there is not currently a theoretical or experimental consensus detailing the effects of grafting density on block polymer self-assembly.

The scaling of the lamellar period (d^*) is well-understood in the case of symmetric linear diblock polymers.[6-7,53] The magnitude of d^* is determined by the balance between the elastic energy (F_{stretch}), which resists chain stretching, and the interfacial energy (F_{int}), which resists expansion of block junctions along the domain interfaces. The stretching free energy per polymer chain is inversely proportional to the mean-square end-to-end distance, $\langle R^2 \rangle$:

$$\frac{F_{\mathrm{stretch}}}{kT} \sim \frac{d^{*2}}{\langle R^2 \rangle} \qquad \text{Eq. 3-4}$$

When the chain is flexible, the mean-square end-to-end distance is given by $\langle R^2 \rangle = a_0^2 N_{\mathrm{bb}}$, where a_0 is the statistical segment length and N_{bb} is the backbone degree of polymerization. (Note that in the case of linear polymers, N_{bb} is identical to the *total* degree of polymerization.) The interfacial energy per polymer chain is

$$\frac{F_{\mathrm{int}}}{kT} \sim \gamma A \qquad \text{Eq. 3-5}$$

where γ is the surface tension and A is the area per chain. These parameters can be approximated by $\gamma = \chi^{\frac{1}{2}} a_0^{-2}$ and $A \sim N_{\mathrm{bb}} a_0{}^3 / d^*$, leading to the following expression:

$$\frac{F_{\mathrm{int}}}{kT} \sim \frac{N_{\mathrm{bb}} a_0 \chi^{\frac{1}{2}}}{d^*} \qquad \text{Eq. 3-6}$$

In the SSL, the elastic energy and interfacial energy are balanced ($F_{\mathrm{stretch}} = F_{\mathrm{int}}$), and thus we obtain

$$d^{*} \sim \chi^{\frac{1}{6}} N^{\frac{1}{3}} [\langle R^2 \rangle]^{\frac{1}{3}} \sim a_0 \chi^{\frac{1}{6}} N_{\mathrm{bb}}{}^{\frac{2}{3}} \qquad \text{Eq. 3-7}$$

In the WSL, the chains do not significantly stretch at the interface because χ is small, and thus F_{int} is effectively negligible. Therefore,

$$d^{*} \sim [\langle R^2 \rangle]^{\frac{1}{2}} \sim a_0 N_{\mathrm{bb}}{}^{\frac{1}{2}} \qquad \text{Eq. 3-8}$$

Collectively, following Eqs. 3-7 and 3-8, the scaling relationship for diblock polymers has the general form

$$d^{*} \sim a_0 N_{\mathrm{bb}}{}^{\alpha} \qquad \text{Eq. 3-9}$$

For flexible linear diblock polymers, typically $1/2 \leq \alpha \leq 2/3$. In contrast, when the polymer is semi-flexible, the same general form applies but the scaling exponent α is larger.[54-55] Bottlebrush diblock polymers typically exhibit α close to 0.9, reflecting the extended backbone conformations due to the sterically demanding architecture.[18-19,27] We note that, in the limit of extremely long backbones, when the persistence length and cross-sectional diameter are much shorter than the contour length of the brush, the chain should become flexible and α should approach 2/3.[20,56] In the current study however, the graft polymers exclusively reside in the regime in which the backbone persistence length (l_{p}) is not negligible compared to N_{bb}.

For non-flexible polymers, the mean-square end-to-end distance can be written as

$$\langle R^2 \rangle = a_0^2 C_{\infty} N_{\mathrm{bb}} \qquad \text{Eq. 3-10}$$

by adopting Flory's characteristic ratio, $C_{\infty} = 2l_{\mathrm{p}}/a_0$. Therefore,

$$\langle R^2 \rangle = 2a_0 l_{\mathrm{p}} N_{\mathrm{bb}} \qquad \text{Eq. 3-11}$$

For bottlebrush polymers, l_{p} is a function of the side chain degree of polymerization (N_{sc}) and z.[51,57] l_{p} is also anticipated to be a function of N_{bb} by theory and simulations,[50,58] but the functional form of this relationship is currently a matter of some debate. We will assume that C_{∞} is a function of N_{bb} and z in order to study how the backbone stiffness affects d^{*}.

Two boundary conditions of this function are known. First, when $z = 0$, $C_{\infty} = 1$ by definition since the backbone is identical to a flexible linear polymer. Second, in the opposite limit, when $z = 1$, C_∞ should approach N_{bb}. To satisfy these conditions, we write the following power function describing the relationship between C_∞ and N_{bb}:

$$C_\infty = N_{\mathrm{bb}}{}^{mz+b} \qquad \text{Eq. 3-12}$$

We now insert Eq. 3-12 into Eq. 3-10, then rewrite the expressions for d^* in the SSL (Eq. 3-7) and WSL (Eq. 3-8) in terms of C_∞:

$$d^* \sim \begin{cases} a_0 \chi^{\frac{1}{6}} C_\infty{}^{\frac{1}{3}} N_{\mathrm{bb}}{}^{\frac{2}{3}} & \text{SSL} \\ a_0 C_\infty{}^{\frac{1}{2}} N_{\mathrm{bb}}{}^{\frac{1}{2}} & \text{WSL} \end{cases} \qquad \text{Eq. 3-13}$$

Therefore, the experimentally observed scaling exponents α can be written as follows:

$$\alpha = \begin{cases} \dfrac{mz + b + 2}{3} & \text{SSL} \\ \dfrac{mz + b + 1}{2} & \text{WSL} \end{cases} \qquad \text{Eq. 3-14}$$

We now apply Eq. 14 to **Systems I** and **II** in order to evaluate how C_∞, as a proxy for the backbone stiffness, changes with z. In **System I**, different diluents (**DME** and **DBE**) are used to vary z in each block. The linear diblock polymer **DME**-*b*-**DBE** exhibits $\alpha = 0.69 \approx 2/3$. This result suggests that, even in the $z = 0$ limit, the block polymers in **System I** are strongly segregated. Since α should only increase with z, all series in **System I** are expected to be in the SSL. Figure 3.9A shows the lines of best fit for experimentally determined values of α and z. Two regions were identified, diverging at a critical grafting density $z_{\mathrm{c,I}}$: (1) when $z < 0.2$, α steeply decreases with decreasing z; (2) when $z > 0.2$, α slightly decreases with decreasing z. In the first region, $\alpha = 0.46z + 0.68$; in the second region, $\alpha = 0.091z + 0.77$. The lines of best fit intersect at $z_{\mathrm{c,I}} = 0.23$. We obtain the following expressions for C_∞:

$$C_\infty = \begin{cases} N_{\mathrm{bb}}{}^{1.39z} & z < 0.23 \\ N_{\mathrm{bb}}{}^{0.27z+0.30} & z > 0.23 \end{cases} \qquad \text{Eq. 3-15}$$

Introducing Eq. 3-15 into Eq. 3-10 enables calculations of the normalized root-mean-square end-to-end distances ($\sqrt{\langle R^2 \rangle}/a_0$) as a function of z (Figure 3.9A). The transition in $\sqrt{\langle R^2 \rangle}/a_0$ occurs near $z_{\mathrm{c,I}}$: $z = 0.27$.

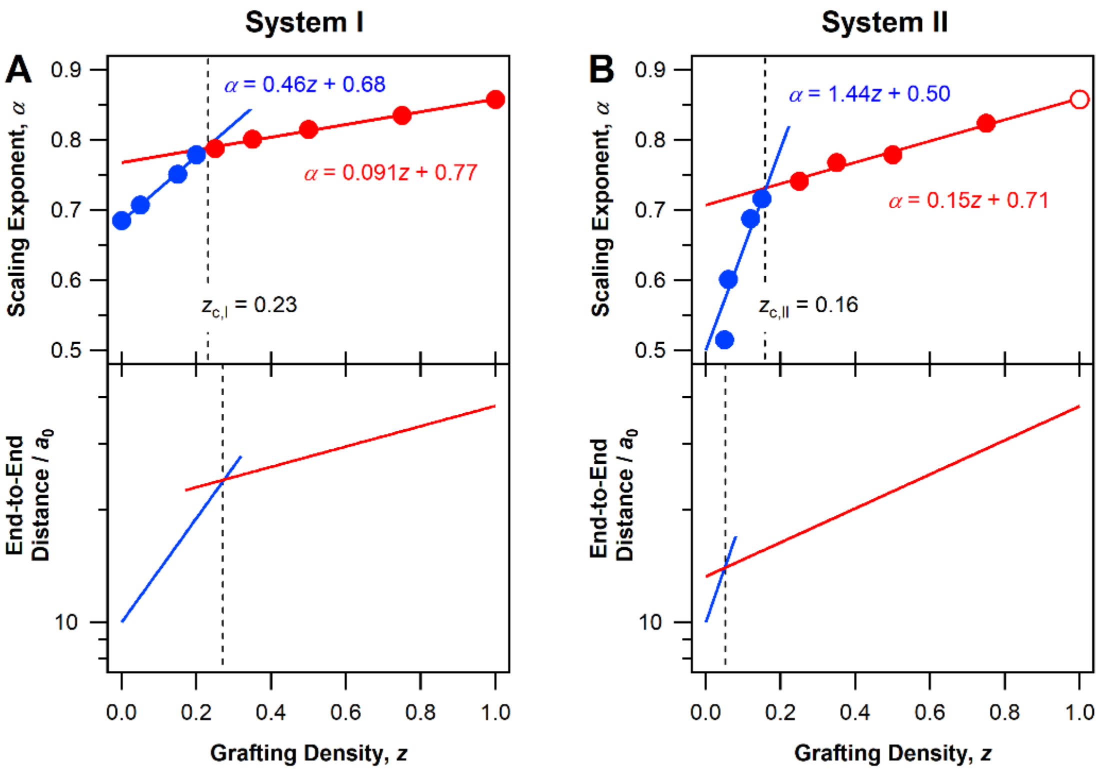

Figure 3.9: Analysis of scaling trends with grafting density (z) for (*A*) **System I** and (*B*) **System II**. (*top*) Experimentally determined values and lines of best fit for the scaling exponent (α) *versus* z. The lines intersect at a critical z_c, associated with a transition in the backbone stiffness. In (b), the unfilled circle (z = 1.00) indicates data for **System I**. (*bottom*) Calculated root-mean-square end-to-end distances, normalized by the backbone statistical segment length ($\sqrt{\langle R^2 \rangle}/a_0$), fixing N_{bb} = 100.

Unlike **System I**, **System II** uses the same diluent (**DBE**) for both blocks. The z = 0 limit constitutes a linear homopolymer rather than a diblock polymer, and therefore the segregation behavior and chain stretching at the domain interface differ between **Systems I** and **II**. Applying the same analysis for **System II**, when the grafting density is low ($z <$ 0.2) we obtain $\alpha = 1.44z + 0.50$ (Figure 3.9B). In this region, the block polymers experience intermediate to weak segregation ($\alpha < 2/3$). Reflecting the boundary condition C_∞ = 1 at z = 0, the y-intercept was fixed at 1/2. Therefore, applying Eq. 3-14 in the WSL, m = 2.87 and b = 0. By comparison to **System I** and literature results, we expect the series to experience strong segregation at a certain z. We will assume that, at least when $z >$ 0.2, the block polymers are in the SSL. Therefore, $\alpha = 0.15z + 0.71$ suggests m = 0.46, b = 0.12.

The lines of best fit intersect at $z_{c,\mathrm{II}} = 0.16$. From these results, for **System II** we obtain the following expression for C_∞:

$$C_\infty = \begin{cases} {N_{\mathrm{bb}}}^{2.87z} & z < 0.16 \\ {N_{\mathrm{bb}}}^{0.46z+0.12} & z > 0.16 \end{cases} \qquad \text{Eq. 3-16}$$

Figure 3.9B (*bottom*) shows the values of $\sqrt{\langle R^2 \rangle}/a_0$ calculated for **System II** per Eq. 3-16. Surprisingly, $\sqrt{\langle R^2 \rangle}/a_0$ exhibits an apparent transition at $z = 0.05$, much lower than the value $z_{c,\mathrm{II}} = 0.16$ identified by fitting the experimental data (Figure 3.9B, *top*). In contrast, for **System I** the transitions in α and $\sqrt{\langle R^2 \rangle}/a_0$ occur at approximately the same z (Figure 3.9A). Since $\sqrt{\langle R^2 \rangle}/a_0$ is obtained from fitting α in two regions (diverging at a critical z_c and assuming either weak or strong segregation), the transitions should occur at the same z if the proposed model accurately describes the entire z range. The observed mismatch suggests that our model does not reflect all factors affecting d^* in the transition region. The preceding discussions have focused on the backbone stiffness. However, the potential contributions of χ and side chain conformations should also be considered.

Figure 3.9 indicates that changes in C_∞ alone do not fully capture the scaling of the lamellar period. Changes in the segregation strength that emerge with decreasing z are likely also significant. In **System I**, the diluents are different and the polymers are already stretched at $z = 0$ (inferred based on $\alpha > 2/3$). Since the backbones are already stretched, increasing z may not significantly affect χ between the two grafted blocks or backbone stretching. A high grafting density (large z_c) may be required to further stretch the chains. In **System II** however, the $z = 0$ limit describes linear homopolymers, which are expected to adopt unperturbed conformations. Therefore, the onset of backbone and side chain stretching should occur at a lower z_c. The effects of segregation, as well as the precise location of the transition between SSL and WSL with z, are important factors to consider.

To conclude our interpretation of the scaling relationships, we address the potential role of the side chains in the experimentally observed transition at $z_c \approx 0.20$. Our analysis is consistent with C_∞ changing abruptly at z_c. We note that, for **System I**, all series ($0 \leq z \leq 1$) are in the SSL. Steric repulsion between the side chains is expected to be the primary factor responsible for increasing C_∞. The location of the transition z_c is therefore expected to be related to the onset of side chain overlap. The radius of gyration of a side chain is

$$R_{\mathrm{g,sc}} = a_{\mathrm{sc}}\,(N_{\mathrm{sc}}/6)^{\frac{1}{2}} \qquad \text{Eq. 3-17}$$

where a_{sc} is the statistical segment length of the side chain. In order for the side chains to retain their unperturbed conformations, the contour length of a section of backbone separating adjacent side chains (L_g) should be larger than the side chain diameter, $d_{\mathrm{sc}} = 2R_{\mathrm{g,sc}}$. As z increases, the side chains are expected to stretch to accommodate tethering at shorter L_g.[57] Consistent with a convention employed by previous theories and experiments for bottlebrush polymers,[20] we assume that the contour length per polynorbornene backbone segment is constant (L_s = 0.62 nm). The number of backbone segments between adjacent grafting points (inclusive) is provided by $1/z$, and L_g follows:

$$L_\mathrm{g} = \frac{L_\mathrm{s}}{z} \qquad \text{Eq. 3-18}$$

When $L_\mathrm{g} > d_{\mathrm{sc}}$, the backbone is expected to behave as a flexible Gaussian chain. When $L_\mathrm{g} < d_{\mathrm{g,sc}}$, the backbone is expected to stretch, ultimately leading to wormlike chain conformations at sufficiently high z. The stiffness of the brush is expected to increase when two neighboring grafts contact each other in the limiting range of the torsional angle. We define z_s as the grafting density at the onset of backbone stretching due to torsional limitations ($L_\mathrm{g} = d_{\mathrm{sc}}$):

$$z_\mathrm{s} \equiv \frac{L_\mathrm{s}}{2a_{\mathrm{sc}}\,(N_{\mathrm{sc}}/6)^{\frac{1}{2}}} \qquad \text{Eq. 3-19}$$

As an approximation, we estimate that the transition in the brush conformation responsible for the transition in α occurs when $z = z_\mathrm{s}$. We note that stretching of the side chains at $z > z_\mathrm{s}$ may not permit this simple approximation, since stretching of the graft polymer backbone and side chains should compete to balance conformational entropy. We further assume $N_{\mathrm{sc}} = 36$ and $L_\mathrm{s} \approx a_{\mathrm{sc}}$, producing $z_\mathrm{s} = 0.20$. For both **Systems I** and **II**, the experimentally observed transition in α occurs at $z_\mathrm{c} \approx z_\mathrm{s}$ ($z_{\mathrm{c,I}} = 0.23$, $z_{\mathrm{c,II}} = 0.16$). This observation suggests that the steep increase in α at small z is mainly due to the stretching of the backbone, whereas the modest increase in α at high z is mainly due to the increasing torsional angle demanded by decreasing L_g.

These results collectively suggest that changes in the end-to-end distance $\langle R^2 \rangle$ are primarily responsible for the increase in α with increasing z. $\langle R^2 \rangle$ may increase due to a combination of backbone stretching, torsional limitations, and χ effects. $\langle R^2 \rangle$ exhibits two regimes in terms of z dependence, potentially corresponding to a transition between loose and densely grafted brushes.[50-51] In our model, we propose functional forms for (1) the relationship between backbone stiffness and backbone length ($C_\infty \sim N_{bb}^{f(z)}$) and (2) the relationship between the lamellar period scaling exponent and grafting density ($\alpha \sim mz + b$). We anticipate that the materials and framework outlined herein should stimulate additional theories and experiments.

The self-assembly of block polymers enables diverse practical applications. We herein provide experimental evidence that quantitatively correlates grafting density with scaling of the lamellar period. Through the analyses of well-defined graft block polymer assemblies, we show that the scaling exponent undergoes a sharp transition at $z \approx 0.20$. The observed transition is attributed to different conformational regimes dictated by backbone chain conformations. We expect that the determined scaling relationships for various grafting density series could be exploited to guide material design.

3-3 Impact of Grafting Density on Linear Rheology

The preceding sections have demonstrated the impact of varying the molecular architecture on *static* properties, such as the scaling of the block polymer lamellar period. This section will provide insight into the *dynamic* consequences.

Graft polymers bearing poly(D,L-lactide) side chains were synthesized by living ring-opening metathesis copolymerization (Chapter 2). The grafting density (z) was varied across the linear, comb, and bottlebrush regimes ($0 \leq z \leq 1$), and for each z, the side chain molecular weight (N_{sc}) was fixed while the total backbone degree of polymerization (N_{bb}) was varied. The linear rheology of these $(\mathbf{PLA}^{z}\text{-}r\text{-}\mathbf{DME}^{1-z})_n$ graft polymers was studied as a function of z and N_{bb} by our collaborators at the University of Minnesota (Ingrid Haugan Smidt, Dr.

Michael Maher, Prof. Marc Hillmyer, and Prof. Frank Bates). This section will present our contributions to the synthesis and molecular characterization, then summarize key insights into the chain conformation. We will discuss the impact of grafting density in the context of linear rheology, but since the measurements and analysis were performed by our collaborators, we defer further discussion to the published reference.[59]

Graft polymers have inspired significant interest due to their unique properties (*e.g.*, high entanglement molecular weight[50,60-62] and low viscosity[39,63-64]) and diverse applications. Recent theoretical and experimental efforts have focused on translating the dynamics of *linear* polymers into models to predict the physical properties of *graft* polymers. However, the underlying dynamics of graft architectures remain relatively unexplored. Due to long-standing synthetic challenges, theoretical efforts to develop a universal model of graft polymer dynamics[22,50-51,65-67] have outpaced experimental studies.

We recently developed a ring-opening metathesis copolymerization strategy that enables precise control over z, N_{sc}, and N_{bb} (Chapter 2). Eight series of $(\mathbf{PLA}^{z}\text{-}r\text{-}\mathbf{DME}^{1-z})_n$ graft polymers (z = 1.00, 0.50, 0.40, 0.25, 0.20, 0.15, 0.05, 0) were synthesized by copolymerizing an ω-norbornenyl **PLA** macromonomer ($M_{n,PLA}$ = 3450 g/mol) with a discrete norbornenyl dimethyl ester diluent, **DME**. We note that the side chains do not entangle since $M_{n,PLA} < M_{e,PLA}$, the entanglement molecular weight of poly(D,L-lactide). Grafting-through ROMP guarantees fixed N_{sc} and permits varying N_{bb} while maintaining low dispersity ($Đ < 1.2$). **Table 3.3** summarizes the molecular characterization data. SEC traces are provided in Appendix B (Figure B.7).

The impact of grafting density on the viscoelastic behavior was systematically studied by dynamic mechanical analysis. Dynamic master curves were created by time–temperature superposition (TTS) of the data relative to the reference temperature $T_{ref} = T_g +$ 34 °C. The thermorheological simplicity of all samples was validated in four ways: (1) the appearance of only one glass transition temperature (T_g) as determined by differential scanning calorimetry; (2) no microphase separation between the grafts and backbone based on SAXS; (3) ability to fit all data to the Williams–Landel–Ferry (WLF) model with a single set;[68] and (4) continuity in van Gurp-Palmen plots.[69]

Table 3.3: Molecular and thermal characterization data for (**PLA**^{z}-*r*-**DME**$^{1-z}$)$_{n}$ graft polymers.

Sample ID	z	M_w (kg/mol)	N_{bb}[a]	$Đ$	T_g (°C)	η_0 (10^3 Pa·s)
(PLA)$_{12}$	1.00	40.3	12	1.04	54	6.1
(PLA)$_{24}$	1.00	81.6	24	1.01	53	12
(PLA)$_{55}$	1.00	189	55	1.01	52	18
(PLA)$_{97}$	1.00	335	97	1.03	52	39
(PLA)$_{200}$	1.00	676	200	1.03	52	94
(PLA)$_{510}$	1.00	1770	510	1.05	53	270
(PLA)$_{1100}$	1.00	3960	1100	1.10	54	540
(PLA)$_{2900}$	1.00	10000	2900	1.37	51	30000
(PLA$^{0.5}$-*r*-DME$^{0.5}$)$_{22}$	0.50	40.7	22	1.04	53	9.0
(PLA$^{0.5}$-*r*-DME$^{0.5}$)$_{85}$	0.50	156	85	1.02	52	22
(PLA$^{0.5}$-*r*-DME$^{0.5}$)$_{460}$	0.50	840	460	1.04	53	170
(PLA$^{0.5}$-*r*-DME$^{0.5}$)$_{960}$	0.50	1760	960	1.06	54	620
(PLA$^{0.5}$-*r*-DME$^{0.5}$)$_{2600}$	0.50	4840	2600	1.13	53	4600
(PLA$^{0.4}$-*r*-DME$^{0.6}$)$_{440}$	0.40	658	440	1.04	52	–
(PLA$^{0.4}$-*r*-DME$^{0.6}$)$_{1600}$	0.40	2440	1600	1.11	51	–
(PLA$^{0.25}$-*r*-DME$^{0.75}$)$_{40}$	0.25	41.2	40	1.04	53	7.3
(PLA$^{0.25}$-*r*-DME$^{0.75}$)$_{62}$	0.25	63.2	62	1.02	52	17
(PLA$^{0.25}$-*r*-DME$^{0.75}$)$_{88}$	0.25	90.0	88	1.01	54	16
(PLA$^{0.25}$-*r*-DME$^{0.75}$)$_{130}$	0.25	133	130	1.02	53	33
(PLA$^{0.25}$-*r*-DME$^{0.75}$)$_{210}$	0.25	217	210	1.01	53	55
(PLA$^{0.25}$-*r*-DME$^{0.75}$)$_{270}$	0.25	276	270	1.02	53	100
(PLA$^{0.25}$-*r*-DME$^{0.75}$)$_{330}$	0.25	341	330	1.02	53	120
(PLA$^{0.25}$-*r*-DME$^{0.75}$)$_{410}$	0.25	417	410	1.02	53	190
(PLA$^{0.25}$-*r*-DME$^{0.75}$)$_{640}$	0.25	650	640	1.03	54	450
(PLA$^{0.25}$-*r*-DME$^{0.75}$)$_{840}$	0.25	855	840	1.03	53	880
(PLA$^{0.25}$-*r*-DME$^{0.75}$)$_{1500}$	0.25	1480	1500	1.07	54	5100
(PLA$^{0.25}$-*r*-DME$^{0.75}$)$_{1800}$	0.25	1850	1800	1.11	53	12000
(PLA$^{0.2}$-*r*-DME$^{0.8}$)$_{120}$	0.20	103	120	1.02	52	–
(PLA$^{0.2}$-*r*-DME$^{0.8}$)$_{1100}$	0.20	905	1100	1.04	53	–
(PLA$^{0.15}$-*r*-DME$^{0.85}$)$_{88}$	0.15	60.9	88	1.02	55	25
(PLA$^{0.15}$-*r*-DME$^{0.85}$)$_{170}$	0.15	116	170	1.01	56	100
(PLA$^{0.15}$-*r*-DME$^{0.85}$)$_{420}$	0.15	292	420	1.02	55	1600
(PLA$^{0.15}$-*r*-DME$^{0.85}$)$_{720}$	0.15	501	720	1.03	56	12000
(PLA$^{0.15}$-*r*-DME$^{0.85}$)$_{1500}$	0.15	1010	1500	1.04	53	200000
(PLA$^{0.05}$-*r*-DME$^{0.95}$)$_{200}$	0.05	76.1	200	1.01	59	130
(PLA$^{0.05}$-*r*-DME$^{0.95}$)$_{410}$	0.05	154	410	1.01	59	1200
(PLA$^{0.05}$-*r*-DME$^{0.95}$)$_{950}$	0.05	352	950	1.02	59	14000
(DME)$_{100}$	0	20.1	100	1.01	83	8.1
(DME)$_{200}$	0	41.2	200	1.01	89	55
(DME)$_{510}$	0	107	510	1.01	88	200
(DME)$_{900}$	0	188	900	1.01	89	11000

[a] Weight-average total backbone degree of polymerization.

The zero-shear viscosities were obtained from the terminal regimes of the dynamic master curves ($\eta_0 = G''/\omega$) and plotted as a function of the weight-average total molecular weight, M_w (Figure 3.10). The data in Figure 3.10 can be fit using $\eta_0 \sim M_w^{\beta}$ with β = either 1 or 3, consistent with Rouse or reptation scaling, respectively. For the $z = 0.25$ series, an abrupt transition in β is observed ($M_w \approx 600$ kg/mol), suggesting that these graft polymers follow the same fundamental relaxation processes as linear polymers. The increased viscosities of the highest-molecular-weight samples in the $z = 0.50$ and $z = 1.0$ series are also consistent with a transition from Rouse to reptation scaling. These results demonstrate that at a fixed total M_w, η_0 can be tuned over several orders of magnitude by adjusting the grafting density.

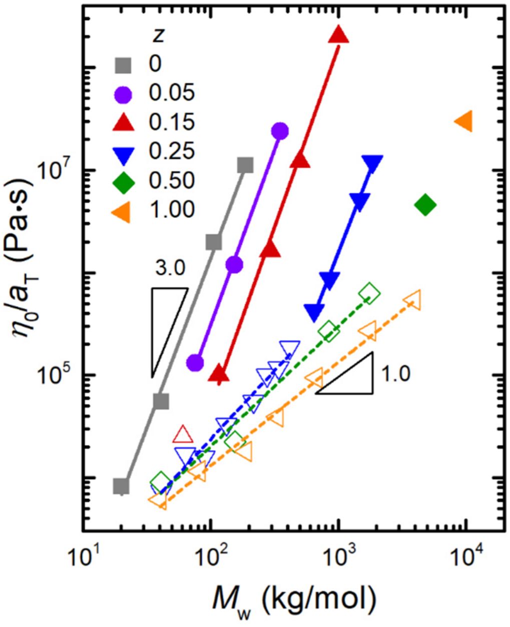

Figure 3.10: Reduced zero-shear viscosity (η_0 / a_T) versus M_w for six series with varying grafting density, z. Unentangled and entangled polymers are shown with open and filled symbols, respectively. Power-law fits are shown corresponding to Rouse (*dotted line*) or reptation (*solid line*) scaling.

For the series of graft polymers discussed in this chapter, the plateau modulus (G_e) was estimated from van Gurp-Palmen plots of the highest-M_w sample for each z (Appendix B, Figure B.8):

$$M_e = \frac{\rho RT}{G_e} \qquad \text{Eq. 3-20}$$

where the melt density ρ = 1.25 g/cm^3 and $T = T_{\mathrm{ref}}$. Daniel and coworkers have recently developed scaling laws based on theory to predict how G_e varies as a function of N_{sc} and the volume-normalized inverse grafting density ($n_g = z^{-1}$). (See also the discussion in Chapter 1.) As the scaling of G_e normalized by the plateau modulus of the analogous linear melt (= $G_e / G_{e,\mathrm{lin}}$) varies, four distinct conformational regimes are predicted to emerge: (1) loose combs (LC), dense combs (DC), loose brushes (LB) and dense brushes (DB) (Figure 3.11A).[50] In comparison, our experimental data features a sharp transition from the DB regime ($G_e / G_{e,\mathrm{lin}} \sim n_g^{1.2}$) at high z to the LC regime at low z (Figure 3.11B). Contrary to predictions from theory, the DC and LB regimes are not observed.

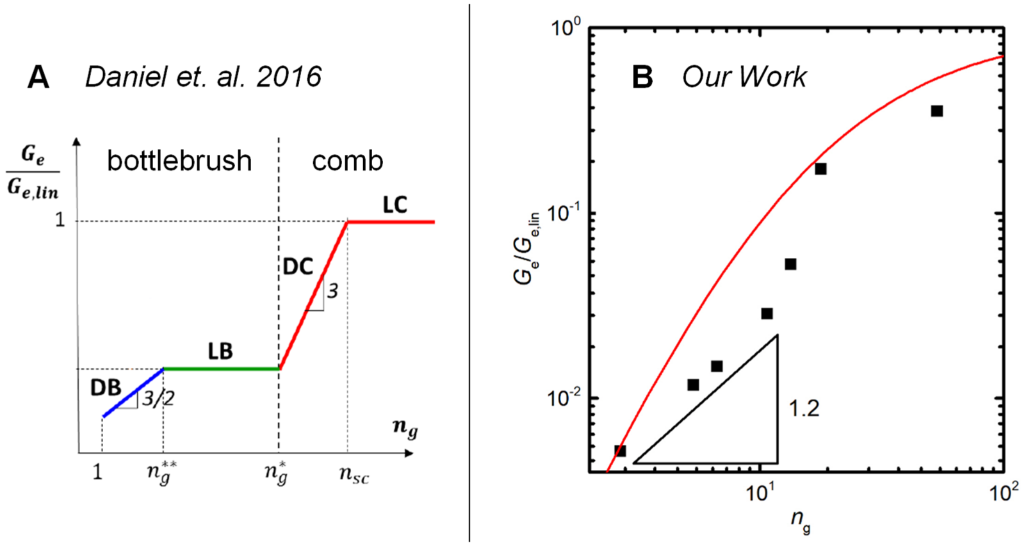

Figure 3.11. Dependence of the plateau modulus of graft polymer melts normalized by the plateau modulus of the analogous linear melt ($G_e / G_{e,\mathrm{lin}}$) on the average backbone length between grafts (n_g). Different conformational regimes are identified as a function of n_g at constant N_{sc}. (*A*) Regimes predicted by Daniel et al. based on theory.[50] Adapted with permission from Nature Publishing Group. (*B*) Experimental data for (**PLA**^{z}-*r*-**DME**$^{1-z}$)$_n$ graft polymers.

Comparison of our experimental data and the existing theory exposes differences between real polymers and idealized model systems. For example, the theory assumes that $l_K >> n_g$ in all four scaling regimes, where l_K is the Kuhn length of the backbone. In practice however, n_g approaches l_K prior to reaching the dense brush limit. In addition, the side chains are assumed to pervade a configurational volume significantly larger than the actual space occupied by the side chain. However, the real side chains in our case are relatively short (N_{sc} = 45). As a consequence, the transition from barely overlapping to overly crowded side chains occurs across a rather narrow range of n_g, effectively bypassing the LB regime.

Increasing the length of the side chains would help reconcile this disparity between experiment and theory, but such changes may lead to side chain entanglement, complicating backbone relaxation.[33,70-75] Side chain entanglement would also negate the advantages of reduced modulus associated with the dense brush limit, forfeiting any supersoft quality imparted on the material by the architecture. The practical reality of these physical phenomena obscures the predictions of the theory in the ideal limit.

We propose an alternative model to predict the onset of entanglements in graft polymers. The model will be outlined herein to invite comparisons to the static consequences of graft polymer architecture discussed in Sections 3-1 and 3-2; additional discussion can be found in the published reference.[59] Relevant parameters include the side chain diameter ($d_{\mathrm{sc}} = 2R_{\mathrm{g,sc}}$) and the average backbone length between grafts (L_{g}), defined according to Eqs. 3-17 and 3-19, respectively (Section 3-3). Figure 3.12A shows the expected scaling of d_{sc} and $L_{\mathrm{g,sc}}$ in the LC regime.

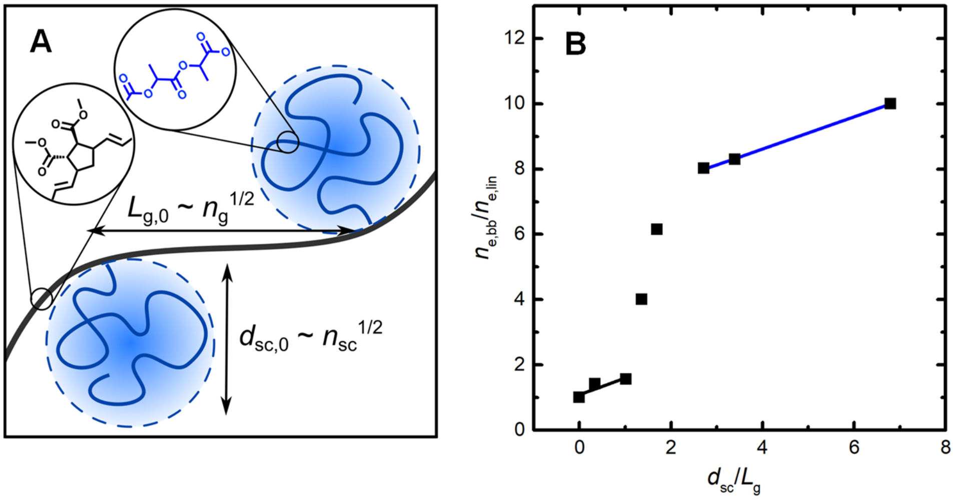

Figure 3.12: (*A*) Illustration of a comb polymer at low grafting density, in which the backbone and side chain are both unperturbed Gaussian coils. The unperturbed backbone length between grafts, $L_{\mathrm{g,0}}$, and side chain diameter, d_{sc}, are indicated. (*B*) Entanglement data plotted as $N_{\mathrm{e,bb}} / N_{\mathrm{e,lin}}$ versus $d_{\mathrm{sc}} / L_{\mathrm{g}}$. The black and blue lines correspond to the low- and high-*z* limits, respectively. When $d_{\mathrm{sc}} / L_{\mathrm{g}} > 1$, steric repulsion between the side chains reduces the density of entanglements.

Figure 3.12B expresses the linear rheology data in terms of the backbone degree of polymerization between entanglements ($N_{\mathrm{e,bb}}$) normalized by the degree of polymerization between entanglements of the corresponding linear melt ($N_{\mathrm{e,lin}}$). Plotting $N_{\mathrm{e,bb}} / N_{\mathrm{e,lin}}$ versus

d_{sc} / L_g emphasizes the limiting behavior in the brush (d_{sc} / L_g > 1) and comb (d_{sc} / L_g < 1) limits. A sharp transition occurs when the side chains begin to overlap (d_{sc} / $L_g \approx 1$), corresponding to $z \approx 0.20$ in the studied system.

We note that a sharp transition near $z = 0.20$ is also observed in the scaling of the block polymer lamellar period, Section 3-3. The block polymers have effectively the same d_{sc} values as the PLA graft homopolymers studied by rheology, enabling direct comparison. Figure 3.13 plots the scaling exponents (α) for **System I** (Figure 3.9A) and the $N_{e,bb}$ / $N_{e,lin}$ values for PLA graft homopolymers (Figure 3.12B) versus z. Remarkably, although the relevant physical phenomena are very different, both sets of data feature a sharp transition near $z = 0.20$. This result suggests potential deep connections between conformational changes with grafting density and physical properties. Future work will further explore these connections through complementary simulation and scattering studies. Improving understanding will enable progress toward a universal model for graft polymer conformation and properties.

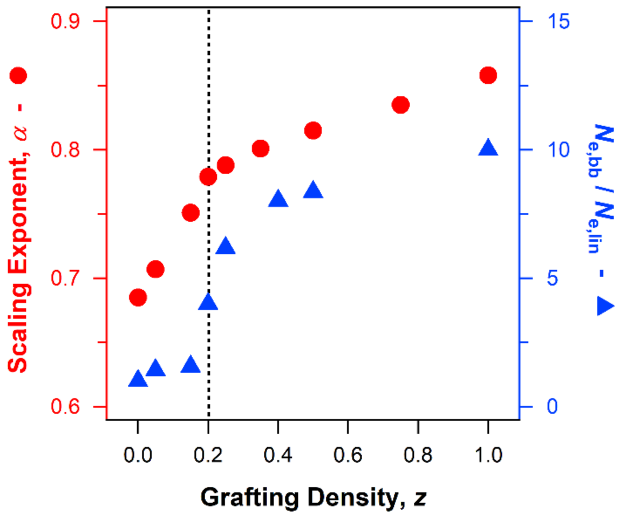

Figure 3.13: Direct comparison of the static and dynamic consequences of grafting density, z. (*left axis, red*) Scaling exponent α describing the change in the block polymer lamellar period with total backbone degree of polymerization ($d^* \sim N_{bb}^{\alpha}$). (*right axis, blue*) Normalized backbone degree of polymerization between entanglements ($N_{e,bb}$ / $N_{e,lin}$).

In conclusion, the linear viscoelastic responses of eight sets of polymers with variable grafting densities were studied. At high grafting density, the polymers behave as dense brushes (DB), where $G_e \sim n_g^{1.2}$ in good agreement with existing theory. Reducing the grafting density results in a sharp transition to the loose comb (LC) regime. We propose a simple criterion for anticipating the onset of entanglement dynamics in graft polymers based on d_{sc} / L_g, the ratio of the diameter of gyration of the side chains to the average backbone contour length between grafts. When $d_{sc}/L_g < 1$ the polymers behave as thin flexible chains with conformations dictated by the backbone chemistry, while $d_{sc}/L_g > 1$ leads to thick semiflexible cylinders and a chain configuration governed by the molecular architecture.

3-4 References

(1) Pesek, S. L.; Li, X.; Hammouda, B.; Hong, K.; Verduzco, R. *Macromolecules* **2013**, *46*, 6998–7005.

(2) Pesek, S. L.; Xiang, Q.; Hammouda, B.; Verduzco, R. *J. Polym. Sci., Part B: Polym. Phys.* **2017**, *55*, 104–111.

(3) Kikuchi, M.; Nakano, R.; Jinbo, Y.; Saito, Y.; Ohno, S.; Togashi, D.; Enomoto, K.; Narumi, A.; Haba, O.; Kawaguchi, S. *Macromolecules* **2015**, *48*, 5878–5886.

(4) Gerle, M.; Fischer, K.; Roos, S.; Müller, A. H. E.; Schmidt, M.; Sheiko, S. S.; Prokhorova, S.; Möller, M. *Macromolecules* **1999**, *32*, 2629–2637.

(5) Sing, C. E.; Zwanikken, J. W.; Cruz, M. O. d. l. *J. Chem. Phys.* **2015**, *142*, 034902.

(6) Matsen, M. W.; Bates, F. S. *Macromolecules* **1996**, *29*, 1091–1098.

(7) Semenov, A. V. *Sov. Phys.-JETP (Engl. Transl.)* **1985**, *61*, 733–742.

(8) Hadjichristidis, N.; Pitsikalis, M.; Iatrou, H.; Pispas, S. *Macromol. Rapid Commun.* **2003**, *24*, 979–1013.

(9) Sheiko, S. S.; Sumerlin, B. S.; Matyjaszewski, K. *Prog. Polym. Sci.* **2008**, *33*, 759–785.

(10) Peng, S.; Bhushan, B. *RSC Adv.* **2012**, *2*, 8557–8578.

(11) Rzayev, J. *ACS Macro Lett.* **2012**, *1*, 1146–1149.

(12) Müllner, M.; Müller, A. H. E. *Polymer* **2016**, *98*, 389–401.

(13) Yavitt, B. M.; Gai, Y.; Song, D.-P.; Winter, H. H.; Watkins, J. J. *Macromolecules* **2017**, *50*, 396–405.

(14) Verduzco, R.; Li, X.; Pesek, S. L.; Stein, G. E. *Chem. Soc. Rev.* **2015**, *44*, 2405–2420.

(15) Vatankhah-Varnosfaderani, M.; Daniel, W. F. M.; Everhart, M. H.; Pandya, A. A.; Liang, H.; Matyjaszewski, K.; Dobrynin, A. V.; Sheiko, S. S. *Nature* **2017**, *549*, 497–501.

(16) Xia, Y.; Olsen, B. D.; Kornfield, J. A.; Grubbs, R. H. *J. Am. Chem. Soc.* **2009**, *131*, 18525–18532.

(17) Rzayev, J. *Macromolecules* **2009**, *42*, 2135–2141.

(18) Gu, W.; Huh, J.; Hong, S. W.; Sveinbjornsson, B. R.; Park, C.; Grubbs, R. H.; Russell, T. P. *ACS Nano* **2013**, *7*, 2551–2558.

(19) Sveinbjörnsson, B. R.; Weitekamp, R. A.; Miyake, G. M.; Xia, Y.; Atwater, H. A.; Grubbs, R. H. *Proc. Natl. Acad. Sci. U.S.A.* **2012**, *109*, 14332–14336.

(20) Dalsin, S. J.; Rions-Maehren, T. G.; Beam, M. D.; Bates, F. S.; Hillmyer, M. A.; Matsen, M. W. *ACS Nano* **2015**, *9*, 12233–12245.

(21) Lecommandoux, S.; Chécot, F.; Borsali, R.; Schappacher, M.; Deffieux, A.; Brûlet, A.; Cotton, J. P. *Macromolecules* **2002**, *35*, 8878–8881.

(22) Cao, Z.; Carrillo, J.-M. Y.; Sheiko, S. S.; Dobrynin, A. V. *Macromolecules* **2015**, *48*, 5006–5015.

(23) Zhang, B.; Gröhn, F.; Pedersen, J. S.; Fischer, K.; Schmidt, M. *Macromolecules* **2006**, *39*, 8440–8450.

(24) Miyake, G. M.; Piunova, V. A.; Weitekamp, R. A.; Grubbs, R. H. *Angew. Chem., Int. Ed.* **2012**, *51*, 11246–11248.

(25) Miyake, G. M.; Weitekamp, R. A.; Piunova, V. A.; Grubbs, R. H. *J. Am. Chem. Soc.* **2012**, *134*, 14249–14254.

(26) Piunova, V. A.; Miyake, G. M.; Daeffler, C. S.; Weitekamp, R. A.; Grubbs, R. H. *J. Am. Chem. Soc.* **2013**, *135*, 15609–15616.

(27) Macfarlane, R. J.; Kim, B.; Lee, B.; Weitekamp, R. A.; Bates, C. M.; Lee, S. F.; Chang, A. B.; Delaney, K. T.; Fredrickson, G. H.; Atwater, H. A.; Grubbs, R. H. *J. Am. Chem. Soc.* **2014**, 17374–17377.

(28) Sun, G.; Cho, S.; Clark, C.; Verkhoturov, S. V.; Eller, M. J.; Li, A.; Pavía-Jiménez, A.; Schweikert, E. A.; Thackeray, J. W.; Trefonas, P.; Wooley, K. L. *J. Am. Chem. Soc.* **2013**, *135*, 4203–4206.

(29) Kawamoto, K.; Zhong, M.; Gadelrab, K. R.; Cheng, L.-C.; Ross, C. A.; Alexander-Katz, A.; Johnson, J. A. *J. Am. Chem. Soc.* **2016**, *138*, 11501–11504.

(30) Liu, M.; Li, W.; Qiu, F.; Shi, A.-C. *Macromolecules* **2012**, *45*, 9522–9530.

(31) Daniels, D. R.; McLeish, T. C. B.; Crosby, B. J.; Young, R. N.; Fernyhough, C. M. *Macromolecules* **2001**, *34*, 7025–7033.

(32) McLeish, T. C. B. *Advances in Physics* **2002**, *51*, 1379–1527.

(33) Kapnistos, M.; Vlassopoulos, D.; Roovers, J.; Leal, L. G. *Macromolecules* **2005**, *38*, 7852–7862.

(34) Chambon, P.; Fernyhough, C. M.; Im, K.; Chang, T.; Das, C.; Embery, J.; McLeish, T. C. B.; Read, D. J. *Macromolecules* **2008**, *41*, 5869–5875.

(35) Kapnistos, M.; Kirkwood, K. M.; Ramirez, J.; Vlassopoulos, D.; Leal, L. G. *J. Rheol.* **2009**, *53*, 1133–1153.

(36) Larson, R. G. *Science* **2011**, *333*, 1834–1835.

(37) van Ruymbeke, E.; Lee, H.; Chang, T.; Nikopoulou, A.; Hadjichristidis, N.; Snijkers, F.; Vlassopoulos, D. *Soft Matter* **2014**, *10*, 4762–4777.

(38) Mai, D. J.; Marciel, A. B.; Sing, C. E.; Schroeder, C. M. *ACS Macro Lett.* **2015**, *4*, 446–452.

(39) Jeong, S. H.; Kim, J. M.; Baig, C. *Macromolecules* **2017**, *50*, 4491–4500.

(40) Olvera de la Cruz, M.; Sanchez, I. C. *Macromolecules* **1986**, *19*, 2501–2508.

(41) Grayer, V.; Dormidontova, E. E.; Hadziioannou, G.; Tsitsilianis, C. *Macromolecules* **2000**, *33*, 6330–6339.

(42) Zhang, J.; Schneiderman, D. K.; Li, T.; Hillmyer, M. A.; Bates, F. S. *Macromolecules* **2016**, *49*, 9108–9118.

(43) Gai, Y.; Song, D.-P.; Yavitt, B. M.; Watkins, J. J. *Macromolecules* **2017**, *50*, 1503–1511.

(44) Martinez, H.; Ren, N.; Matta, M. E.; Hillmyer, M. A. *Polym. Chem.* **2014**, *5*, 3507–3532.

(45) Bielawski, C. W.; Grubbs, R. H. *Prog. Polym. Sci.* **2007**, *32*, 1–29.

(46) Leitgeb, A.; Wappel, J.; Slugovc, C. *Polymer* **2010**, *51*, 2927–2946.

(47) Sutthasupa, S.; Shiotsuki, M.; Sanda, F. *Polym. J.* **2010**, *42*, 905–915.

(48) Hong, S. W.; Gu, W.; Huh, J.; Sveinbjornsson, B. R.; Jeong, G.; Grubbs, R. H.; Russell, T. P. *ACS Nano* **2013**, *7*, 9684–9692.

(49) Chang, A. B.; Bates, C. M.; Lee, B.; Garland, C. M.; Jones, S. C.; Spencer, R. K. W.; Matsen, M. W.; Grubbs, R. H. *Proc. Natl. Acad. Sci. U.S.A.* **2017**, *114*, 6462–6467.

(50) Daniel, W. F. M.; Burdynska, J.; Vatankhah-Varnoosfaderani, M.; Matyjaszewski, K.; Paturej, J.; Rubinstein, M.; Dobrynin, A. V.; Sheiko, S. S. *Nat. Mater.* **2016**, *15*, 183–189.

(51) Paturej, J.; Sheiko, S. S.; Panyukov, S.; Rubinstein, M. *Sci. Adv.* **2016**, *2*, e1601478.

(52) Mapas, J. K. D.; Thomay, T.; Cartwright, A. N.; Ilavsky, J.; Rzayev, J. *Macromolecules* **2016**, *49*, 3733–3738.

(53) Bates, F. S.; Fredrickson, G. H. *Annu. Rev. Phys. Chem.* **1990**, *41*, 525–557.

(54) Matsen, M. W. *J. Chem. Phys.* **1996**, *104*, 7758–7764.

(55) Jiang, Y.; Zhang, X.; Miao, B.; Yan, D.; Chen, J. Z. Y. *Soft Matter* **2016**, *12*, 2481–2490.

(56) Elli, S.; Ganazzoli, F.; Timoshenko, E. G.; Kuznetsov, Y. A.; Connolly, R. *J. Chem. Phys.* **2004**, *120*, 6257–6267.

(57) Fredrickson, G. H. *Macromolecules* **1993**, *26*, 2825–2831.

(58) Hsu, H.-P.; Paul, W.; Rathgeber, S.; Binder, K. *Macromolecules* **2010**, *43*, 1592–1601.

(59) Haugan, I. N.; Maher, M. J.; Chang, A. B.; Lin, T.-P.; Grubbs, R. H.; Hillmyer, M. A.; Bates, F. S. *ACS Macro Lett.* **2018**, *7*, 525–530.

(60) Pakula, T.; Zhang, Y.; Matyjaszewski, K.; Lee, H.-i.; Boerner, H.; Qin, S.; Berry, G. C. *Polymer* **2006**, *47*, 7198–7206.

(61) Mpoukouvalas, A.; Li, W.; Graf, R.; Koynov, K.; Matyjaszewski, K. *ACS Macro Lett.* **2013**, *2*, 23–26.

(62) Cai, L.-H.; Kodger, T. E.; Guerra, R. E.; Pegoraro, A. F.; Rubinstein, M.; Weitz, D. A. *Adv. Mater.* **2015**, *27*, 5132–5140.

(63) Dalsin, S. J.; Hillmyer, M. A.; Bates, F. S. *ACS Macro Lett.* **2014**, *3*, 423–427.

(64) Lohse, D. J.; Milner, S. T.; Fetters, L. J.; Xenidou, M.; Hadjichristidis, N.; Mendelson, R. A.; García-Franco, C. A.; Lyon, M. K. *Macromolecules* **2002**, *35*, 3066–3075.

(65) Liang, H.; Cao, Z.; Wang, Z.; Sheiko, S. S.; Dobrynin, A. V. *Macromolecules* **2017**, *50*, 3430–3437.

(66) Cao, Z.; Daniel, W. F. M.; Vatankhah-Varnosfaderani, M.; Sheiko, S. S.; Dobrynin, A. V. *Macromolecules* **2016**, *49*, 8009–8017.

(67) Saariaho, M.; Szleifer, I.; Ikkala, O.; Brinke, G. t. *Macromol. Theory Simul.* **1998**, *7*, 211–216.

(68) Williams, M. L.; Landel, R. F.; Ferry, J. D. *J. Am. Chem. Soc.* **1955**, *77*, 3701–3707.

(69) van Gurp, M.; Palmen, J. *Rheology Bulletin* **1998**, *67*, 5.

(70) Hu, M.; Xia, Y.; McKenna, G. B.; Kornfield, J. A.; Grubbs, R. H. *Macromolecules* **2011**, *44*, 6935–6943.

(71) Dalsin, S. J.; Hillmyer, M. A.; Bates, F. S. *Macromolecules* **2015**, *48*, 4680–4691.

(72) Tsukahara, Y.; Namba, S.-i.; Iwasa, J.; Nakano, Y.; Kaeriyama, K.; Takahashi, M. *Macromolecules* **2001**, *34*, 2624–2629.

(73) Graessley, W. W. *Macromolecules* **1982**, *15*, 1164–1167.

(74) Kempf, M.; Ahirwal, D.; Cziep, M.; Wilhelm, M. *Macromolecules* **2013**, *46*, 4978–4994.

(75) Lin, Y.; Zheng, J.; Yao, K.; Tan, H.; Zhang, G.; Gong, J.; Tang, T.; Xu, D. *Polymer* **2015**, *59*, 252–259.

Chapter 4

Manipulating the ABCs of Self-Assembly via Low-χ Block Polymer Design

1. Chang, A. B.; Bates, C. M.; Lee, B.; Garland, C. M.; Jones, S. C.; Spencer, R. K.; Matsen, M. W.; Grubbs, R. H. Manipulating the ABCs of Self-Assembly via Low-χ Block Polymer Design. *Proc. Natl. Acad. Sci.* **2017**, *114*, 6462–6467.

2. Sunday, D. F.;* Chang, A. B.;* Liman, C. D.; Gann, E.; DeLongchamp, D. M.; Matsen, M. W.; Grubbs, R. H.; Soles, C. L. Evidence for Backbone Flexibility of Bottlebrush Block Copolymers Driven by Low-χ Assembly. **2018**. *submitted.* (**Corresponding authors.*)

ABSTRACT

Molecular sequence and interactions dictate the mesoscale structure of all self-assembling soft materials. Block polymers harness this relationship to access a rich variety of nanostructured materials but typically require energetically unfavorable (high-χ) interactions between blocks. In this chapter, we demonstrate that the converse approach, encoding low-χ interactions in ABC bottlebrush triblock terpolymers ($\chi_{AC} \lesssim 0$), promotes organization into a unique mixed-domain lamellar morphology which we designate $\mathrm{LAM_P}$. Transmission electron microscopy indicates that $\mathrm{LAM_P}$ exhibits ACBC domain connectivity, in contrast to conventional three-domain lamellae ($\mathrm{LAM_3}$) with ABCB periods. Complementary small angle X-ray scattering experiments reveal an unusual trend: as the total polymer molecular weight increases, the domain spacing *decreases.* Self-consistent field theory reinforces these observations and predicts that $\mathrm{LAM_P}$ is thermodynamically stable below a critical χ_{AC}, above which $\mathrm{LAM_3}$ emerges. Both experiments and theory expose close analogies to ABA' triblock copolymer phase behavior, collectively suggesting that low-χ interactions between chemically similar or distinct blocks intimately influence self-assembly. These conclusions provide new opportunities in block polymer design with potential consequences spanning all self-assembling soft materials.

Table of Contents

4-1 Introduction

Block polymers are a diverse class of soft materials capable of self-assembling into complex periodic nanostructures. Synthetic command over composition, dispersity, sequence, and molecular architecture enables control over the mesoscopic order and macroscopic thermal, mechanical, rheological, and transport properties.[1-4] The phase behavior of "simple" linear AB diblock copolymers is universally parameterized by the segregation strength $\chi_{AB}N$ and relative volume fraction f, where χ_{AB} represents the effective Flory-Huggins binary interaction parameter and N is the total volume-averaged degree of polymerization. Mixing behavior, captured through the mean-field concept of χ_{AB}, is central to block polymer self-assembly: the competing demands of minimizing interfacial energy and maximizing configurational entropy only favor microphase separation when A-B interactions are repulsive ($\chi_{AB} > 0$).[5-6] Extension to higher-order multiblock polymers introduces additional interaction parameters (χ_{ij}) that impact self-assembly and properties.[7] For example, introducing a mutually incompatible C block ($\chi_{AC} > 0$, $\chi_{BC} > 0$) generates a host of new morphologies dictated by the chain connectivity (ABC, ACB, or BAC) and intrinsic χ_{ij} values.[8-9] In this rich phase space, designing multiblock polymers with a combination of miscible and immiscible blocks can also access new structures and impart useful functions.[10-11] Perhaps the best known examples of such systems are linear ABA' triblock copolymers ($\chi_{AB} > 0$, $\chi_{AA'} \approx 0$): their high-value industrial applications as thermoplastic elastomers are entirely enabled by A/A' mixing and chain connectivity, which together create physically crosslinked materials with excellent processability and mechanical properties.[12] The self-assembly of yet more complex systems, including ABA'C tetrablock polymers[13-14] and $A_n(BA')_m$ heteroarm star polymers,[15] is also crucially determined by A/A' miscibility. These examples illuminate interesting parallels and contrasts between block polymer phase behavior and protein self-assembly. Nature delivers exquisite control over protein folding by precisely tailoring amino acid sequences and intramolecular interactions that are often attractive (*e.g.*, hydrogen bonding), while block polymer design to date exploits simple molecular connectivity and primarily repulsive interactions ($\chi > 0$) to induce microphase separation.

Previous reports have investigated the role of negligible ($\chi \approx 0$) or attractive ($\chi < 0$) intermolecular interactions on the phase behavior of various homopolymer (AB/A')[16-17] and block polymer (AB/A'C)[18-19] blends. In contrast, studies in which the macromolecules themselves are intramolecularly encoded with miscible blocks are to the best of our knowledge limited to the aforementioned A/A' self-similar interactions. In this report, we study ABC bottlebrush triblock terpolymers with grafted poly(D,L-lactide), poly(styrene), and poly(ethylene oxide) side chains (LSO), featuring low-χ interactions ($\chi_{AC} \lesssim 0$) between distinct A and C end blocks. These materials generate a unique mixed morphology with atypical mesoscopic domain connectivity, which we denote LAM_P. Additionally, under certain conditions of molecular asymmetry, another consequence of low-χ design manifests in decreasing domain spacing with increasing total molecular weight. Valuable insight into the molecular origins of this unusual behavior is achieved by comparison with analogous ABA' brush triblock copolymers – grafted poly(D,L-lactide)-*block*-poly(styrene)-*block*-poly(D,L-lactide) (LSL') – and self-consistent field theory (SCFT). The experimental and theoretical conclusions described herein regarding low-χ block polymers reveal unexpected breadth in self-assembly and should create new opportunities for molecular and materials design.

4-2 Synthesis and Structure of Low-χ Block Polymers

ABC and ABA' brush triblock polymers containing grafted poly(D,L-lactide) (PLA, A block), polystyrene (PS, B block), and poly(ethylene oxide) (PEO, C block) side chains were synthesized by ring-opening metathesis polymerization (ROMP).[20-22] The living nature and synthetic utility of ROMP enable the formation of well-defined block polymers with precisely controlled molecular weight, narrow molecular weight dispersity, and diverse pendant functionalities. Figure 4.1 illustrates the molecular structure of the LSO and LSL' brush triblock polymers studied herein and highlights the relative interaction parameters dictated by block chemistry and sequence. Both LSO and LSL' feature low-χ interactions between the end blocks (χ_{AC}, $\chi_{\mathrm{AA'}} \lesssim 0$), which in particular distinguish LSO from typical frustrated ABC triblock polymers that include similar relative χ values but highly unfavorable A/C interactions ($\chi_{\mathrm{AC}} >> 0$).[9,23] N_{A}, N_{B}, and (N_{C} or $N_{\mathrm{A'}}$) indicate the number-average degrees of polymerization through the polynorbornene backbone for blocks containing PLA, PS, and (PEO or PLA) grafts, respectively. Characterization data for all LSO and LSL' samples are provided in Tables 4.1 and 4.2, respectively. Synthetic details (Schemes C.1–C.2) and size-exclusion chromatograms (Figures C.1–C.3) for all samples are provided in Appendix C.

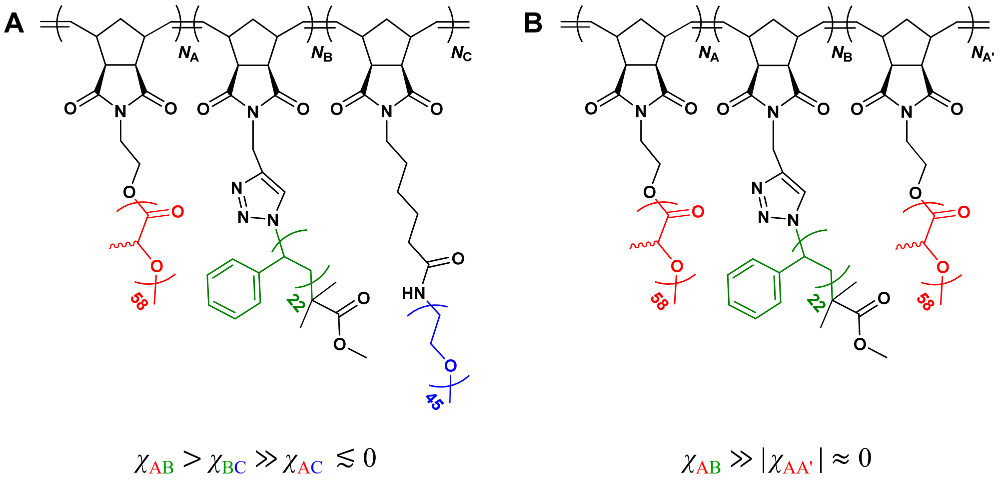

Figure 4.1: Molecular structures and relative interaction parameters for (*A*) LSO and (*B*) LSL' brush triblock polymers.

Table 4.1: Molecular composition and characterization data for all LSO samples. Samples are identified as LSO* or LSO-N_C (fixed N_A and N_B and variable N_C). For each block i, N_i indicates the number-average degrees of polymerization through the backbone and f_i indicates the volume fraction (estimated using values in Table C.1).

Sample[a]	N_A[b]	N_B[b]	N_C[b]	f_A[c]	f_B[d]	f_C[e]	M_n **(kDa)**	**Đ** ($M_\mathrm{w}/M_\mathrm{n}$)
LSO*	28	27	5	0.57	0.37	0.06	203.2	1.02
LSO-0	26	24	0	0.61	0.39	0.00	178.4	1.00
LSO-2	26	24	2	0.60	0.38	0.02	182.9	1.01
LSO-4	26	24	4	0.58	0.37	0.05	187.5	1.01
LSO-6	26	24	6	0.57	0.36	0.07	192.0	1.00
LSO-8	26	24	8	0.56	0.35	0.09	196.6	1.00
LSO-10	26	24	10	0.54	0.35	0.11	201.1	1.00
LSO-12	26	24	12	0.53	0.34	0.13	205.7	1.01
LSO-14	26	24	14	0.52	0.33	0.15	210.2	1.01
LSO-16	26	24	16	0.51	0.32	0.17	214.8	1.07
LSO-20	26	24	20	0.49	0.31	0.20	223.9	1.00

Table 4.2: Molecular composition and characterization data for LSL'-$N_\mathrm{A'}$ series (fixed N_A and N_B and variable $N_\mathrm{A'}$). For each block i, N_i indicates the number-average degrees of polymerization through the backbone and f_i indicates the volume fraction (estimated using values in Table C.1).

Sample[a]	N_A[b]	N_B[b]	$N_\mathrm{A'}$[b]	f_A[c]	f_B[d]	$f_\mathrm{A'}$[e]	M_n **(kDa)**	**Đ** ($M_\mathrm{w}/M_\mathrm{n}$)
LSL'-0	30	28	0	0.61	0.39	0.00	206.6	1.01
LSL'-2	30	28	2	0.58	0.37	0.05	217.2	1.01
LSL'-5	30	28	5	0.56	0.35	0.09	227.8	1.05
LSL'-7	30	28	7	0.53	0.34	0.13	238.4	1.03
LSL'-10	30	28	10	0.51	0.33	0.16	248.9	1.02
LSL'-12	30	28	12	0.49	0.31	0.20	259.5	1.03
LSL'-14	30	28	14	0.47	0.30	0.23	270.1	1.02
LSL'-17	30	28	17	0.45	0.29	0.26	280.7	1.02
LSL'-19	30	28	19	0.44	0.28	0.28	291.3	1.03
LSL'-24	30	28	24	0.41	0.26	0.33	312.5	1.03

4-3 Self-Consistent Field Theory

Self-consistent field theory (SCFT), generally regarded as the state of the art for block polymer melts,[24] was used to model our polymers and provide insight into their self-assembly. The standard model for branched polymers was modified to account for the strong steric interactions that occur in bottlebrushes due to the high grafting density of the side chains, as was done previously for similar bottlebrush diblock copolymers.[25] Gaussian chains were used to represent the $N_\mathrm{b} = N_\mathrm{A} + N_\mathrm{B} + N_\mathrm{C}$ (LSO) or $N_\mathrm{b} = N_\mathrm{A} + N_\mathrm{B} + N_\mathrm{A'}$ (LSL') side chains, and the volumes and unperturbed end-to-end lengths of the side chains were set to known literature values.[26-27] For the backbone, a worm-like chain of fixed persistence length was employed to handle the strong lateral tension that occurs due to side chain crowding. The interactions between the three side chain species (PLA, PS, and PEO) were represented in the Hamiltonian by standard Flory-Huggins terms controlled by χ_LS, χ_SO, and χ_LO. The equilibrium lamellar period (d^*) was obtained by minimizing the free energy (F). Figure 4.2 provides a schematic of chain dimensions. Additional SCFT details, including values for input parameters (Table C.1), are provided in Appendix C-3.

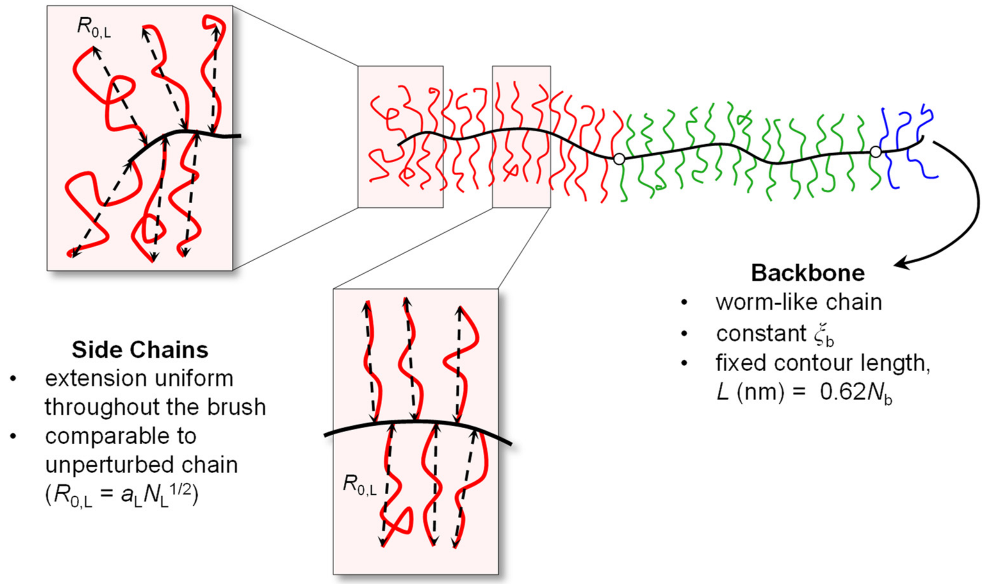

Figure 4.2: Schematic of realistic LSO* chain dimensions used in SCFT calculations. The side chains are not expected to extend significantly more than their unperturbed end-to-end distance $R_{0,\gamma} = a_\gamma N_\gamma^{1/2}$ (where a_γ is the statistical segment length and N_γ is the degree of polymerization of γ = L, S, or O). The backbone is treated as a worm-like chain of constant persistence length ξ_b and fixed contour length L.

4-4 Unique Domain Connectivity: LAM_P

We begin by presenting data and calculations corresponding to LSO brush triblock terpolymers (Figure 4.1A), then draw close analogies to LSL' (Figure 4.1B) phase behavior. All materials self-assemble into well-ordered lamellar morphologies. Transmission electron micrographs of thin sections of LSO* (N_A = 28, N_B = 27, N_C = 5) stained over ruthenium tetroxide (RuO_4) vapor reveal a three-color, four-layer lamellar morphology (Figure 4.3A). (Additional images are provided in Appendix C, Figure C.4)

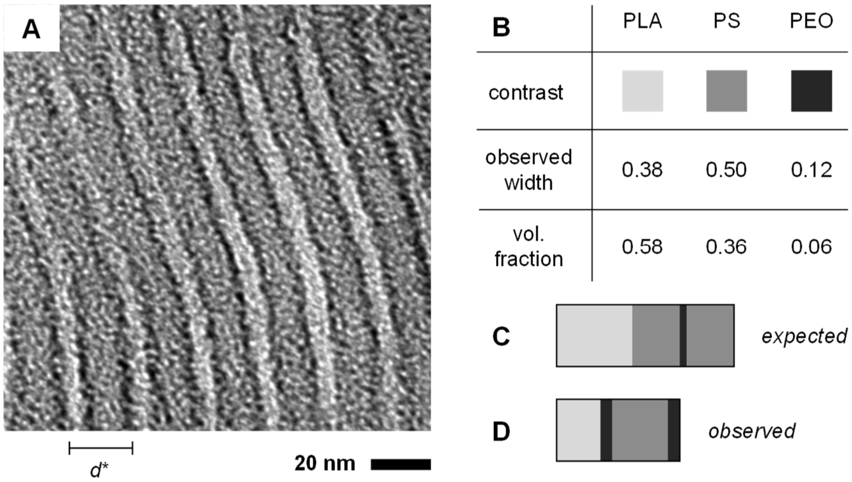

Figure 4.3: (*A*) TEM of LSO* stained with RuO_4. (*B*) Relative contrast from the stain, relative widths of corresponding layers observed by TEM, and side chain volume fractions measured by ^1H NMR. (*C*) One LAM_3 period with the expected ABCB domain connectivity and layer widths based on data in (*B*). (*D*) One LAM_P period observed in (*A*), exhibiting mesoscopic ACBC domain connectivity.

Exposing L, S, and O to RuO_4 vapor results in unstained, slightly stained, and strongly stained domains respectively, as deduced from literature results: PS is selectively stained in PLA/PS mixtures,[28-29] and PEO is stained to a greater extent than PS.[30-31] Surprisingly, the extent of staining and layer widths observed by TEM are completely inconsistent with both the side chain volume fractions measured by ^1H NMR ($f_L = 0.57, f_S = 0.37, f_O = 0.06$) (Figure 4.3B) and the ABCB connectivity required by the expected three-domain microstructure, LAM_3 (Figure 4.3C).[8-9] The conflict between LAM_3 and the pattern observed by TEM can only be resolved by invoking partial mixing between the A and C end blocks, apparently driven by low-χ interactions ($\chi_{AC} \lesssim 0$). The resulting morphology exhibits mesoscopic ACBC connectivity (Figure 4.3D), consistent with the observed staining pattern. Since the three blocks are not well-segregated, the side chain volume fractions are not required to equal the relative domain widths. Reflecting the crucial role of partial mixing, this new morphology is herein designated LAM_P.

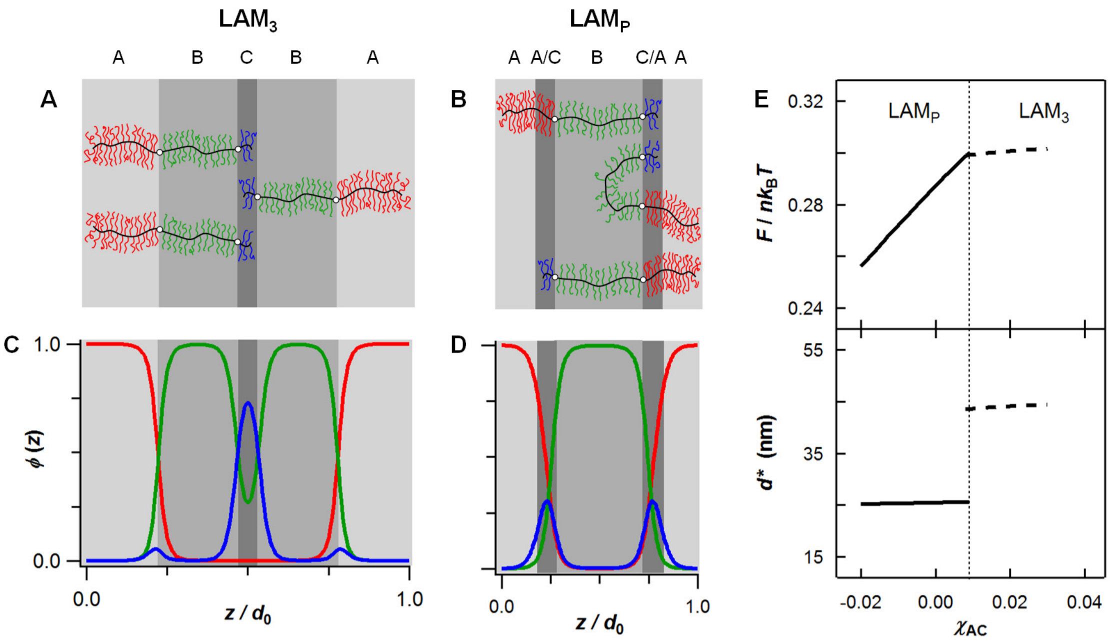

Figure 4.4: Illustrations and SCFT data distinguishing LAM_3 and LAM_P morphologies. In *A–D*, the light, medium, and dark gray layers represent PLA, PS, and PEO (or mixed PLA/PEO) domains, respectively. (*A*, *B*) LSO chain packing in (*A*) LAM_3 and (*B*) LAM_P. (*C*, *D*) SCFT composition profiles for LSO* within one normalized lamellar period (z/d_0), where $\phi(z)$ is the relative segment concentration of each component. (*C*) $\chi_{AC} > \chi^C$: LAM_3 with $d^* = 43.5$ nm. (*D*) $\chi_{AC} < \chi^C$: LAM_P with $d^* = 25.6$ nm. (E) SCFT calculations of the normalized free energy (*top*) and domain spacing (*bottom*) versus $\chi_{AC} \equiv \chi_{LO}$ for LSO*. The transition from mixed (LAM_P) to unmixed (LAM_3) morphologies is first-order, occurring at a critical value χ^C (dotted line); for $\chi_{AB} = 0.080$ and $\chi_{BC} = 0.049$, $\chi^C = 0.009$.

SCFT fully supports the distinction between LAM_3 (Figure 4.4A) and LAM_P (Figure 4.4B), controlled primarily by the relative and absolute interaction parameters. Composition profiles for LSO* were calculated over one lamellar period using realistic PLA-PS ($\chi_{AB} \equiv \chi_{LS}$) and PS-PEO ($\chi_{BC} \equiv \chi_{SO}$) values estimated in the literature: $\chi_{LS} = 0.080$ [32] and $\chi_{SO} = 0.049$ [33] at 140 °C, renormalized to a common monomer reference volume (118 Å^3). (We note that literature χ values obtained by fitting experimental data to mean-field approximations are often inaccurate, potentially affecting the agreement between experiment and theory.[34]) PLA-PEO interactions ($\chi_{AC} \equiv \chi_{LO}$) were arbitrarily varied in the simulations, and LAM_3 is correctly predicted to occur at moderate to large χ_{AC} (Figure 4.4C), in broad agreement with previous experimental and theoretical studies of frustrated ABC triblock terpolymers.[35-37] In contrast, LAM_P exclusively emerges when χ_{AC} is sufficiently small to favor partial A/C block-block mixing (Figure 4.4D). Using this collection of physical parameters, a first-order phase transition between LAM_3 and LAM_P was predicted to occur at a critical value $\chi^C = 0.009$ (Figure 4.4E). The mesoscopic ACBC domain connectivity and relative domain widths predicted for LAM_P perfectly match the pattern observed in Figure 4.3A and reinforce the microscopic origins of mixing deduced from TEM.

4-5 Decreasing Domain Spacing with Increasing Total Molecular Weight

A series of LSO brush triblock terpolymers with fixed $N_A = 26$ and $N_B = 24$ (guaranteed by a common parent diblock) and variable N_C (Scheme C.2) highlights additional consequences of block-block mixing. N_C was varied in increments of two or four backbone repeat units, from $N_C = 0$ (LSO-0) to $N_C = 20$ (LSO-20) (Table 4.1). (Note that, due to the high molecular weight of each PEO macromonomer, the total molecular weight varies by >45,000 g/mol across this series.)

All samples were annealed at 140 °C under modest applied pressure, and the ordered structures that developed were identified by synchrotron small-angle X-ray scattering (SAXS). (See Appendix C-5 for further information.) SAXS measurements reveal an unusual trend: as the total molecular weight (M) increases over the range of compositions where LAM_P forms ($0 < f_O \leq 0.20$), the lamellar period (d^*) strongly *decreases*: $d^* \sim M^{-0.87}$ (Figure 4.5). For comparison, Figure 4.5 also includes literature data for linear poly(isoprene-*b*-styrene-*b*-ethylene oxide) (ISO) and poly(styrene-*b*-isoprene-*b*-ethylene oxide) (SIO) triblock terpolymers similarly synthesized by varying the O block length from a common parent diblock. The domain spacing trends observed for both ISO and SIO series typify the expected increase in lamellar period with increasing M: $\alpha_{ISO} \approx 0.90$ [38-39] and $\alpha_{SIO} \approx 0.56$.[40] Clearly, α_{LSO} is strikingly different. Additional data illustrating the unusual negative trend for LSO are summarized in Appendix C-6, Table C.2. Schematic illustrations of assigned structures (Figure C.5), indexed 2D SAXS data

(Figure C.6), 1D azimuthally averaged intensity reductions (Figure C.7), and TEM images (Figure C.8) are also provided.

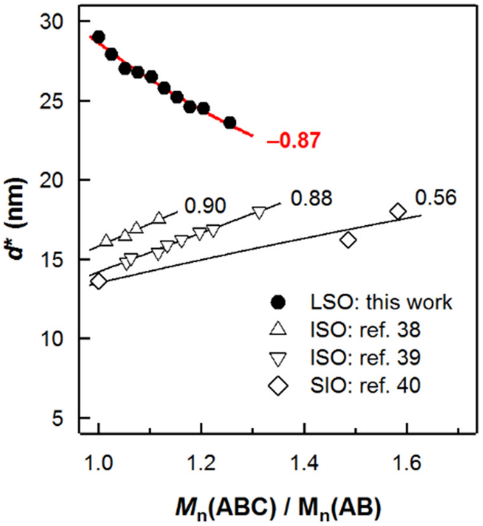

Figure 4.5: Lamellar periods (d^*) versus normalized molecular weight for brush LSO (this work) and linear ISO and SIO triblock terpolymers (literature data). Calculated exponents (best fit) to the power law $d^* \sim M^\alpha$ are included for comparison.

A series of LSL' brush triblock copolymers was similarly synthesized from identical macromonomers, generating an analogous series with variable end block length from a parent LS diblock ($N_A = 30$, $N_B = 28$). Like LSO, this LSL' series exhibits decreasing lamellar periods with increasing end block length (*i.e.*, increasing total molecular weight) (Figure 4.6A). Additional morphological data for LSL' are provided in Appendix C-7 (Table C.3 and Figures C.9–C.10). Differential scanning calorimetry (DSC) data for LSL' and LSO are compared in Figure 4.6B and provide quantitative evidence of block-block mixing in LSO. For all LSO samples, a single glass transition temperature (T_g) was observed between $T_{g,PLA}$ (55 °C) and $T_{g,PEO}$ (−70 °C) (Appendix C-8, Figure C.11). As N_C (and therefore the weight fraction of PEO) increases, T_g decreases, consistent with continued dilution of mixed A/C domains by the low-T_g component. The presence of only one T_g in polymer blends is generally regarded as evidence for miscibility[41-42] and is consistent with the behavior of PLA and PEO homopolymers, which mix over wide ranges of molecular weights and blend compositions.[43-44] In the analogous LSL' series, a single T_g

corresponding to the PLA block is observed that does not change as $N_{A'}$ increases, since mixed domains inherently remain pure PLA (Figure C.12).

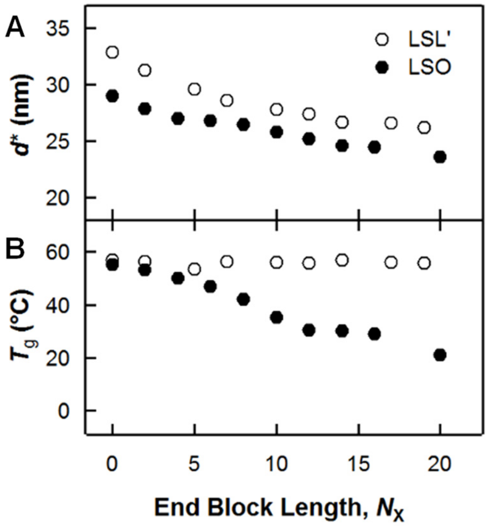

Figure 4.6: Consequences of varying end block length N_X in LSL' and LSO. (*A*) Domain spacing d^*. (*B*) Apparent PLA glass transition temperatures (T_g); for all samples, a single T_g ($T_{g,PEO} < T_g \leq T_{g,PLA}$) was observed.

4-6 Role of Low-χ Interactions

We have investigated herein the impact of low-χ block-block interactions on structure and physical properties by studying densely grafted ABC and ABA' brush triblock polymers. The LSO polymers described above self-assemble into lamellae with unique domain connectivity (ACBC), which we denote LAM_P. In contrast, linear ABC triblock terpolymers (*e.g.*, ISO and SIO) have been extensively studied and typically form two- or three-domain lamellar morphologies (LAM_2 or LAM_3) depending on block lengths and relative interaction parameters. In the conventional LAM_3 morphology generated by both ISO and SIO, the mesoscopic domain connectivity (ABCB) necessarily reflects the underlying molecular sequence. In other words, the self-assembly of ABC… multiblock polymers into lamellae (*i.e.*, structures periodic in one dimension) typically requires A, B, C, … domains to be connected in that order due to the covalent linkages between blocks. The crucial differences distinguishing LSO and ostensibly similar ISO/SIO triblocks could potentially be attributed to either the polymer architecture (brush vs. linear) or block-block interactions. We note that architecture-induced segmental mixing has been demonstrated in ABC heteroarm star terpolymers, wherein forming low-energy morphologies may force one arm to transit across an incompatible domain ($\chi > 0$).[45-46] However, these architecture effects do not pertain to brush LSO since the blocks are connected end-to-end in the same way as linear ABC triblock terpolymers. The data presented in Figures 4.3–4.6 instead indicate that block-block interactions, captured through the mean-field concept of Flory-Huggins binary interaction parameters (χ_{ij}), are the dominant factors governing the unique behavior of LSO.

Both the relative *and* absolute magnitudes of each χ_{ij}, convolved with the molecular sequence, underpin the self-assembly of multiblock polymers. For example, given I, S, and O blocks with $\chi_{IO} > \chi_{IS} \approx \chi_{SO}$,[47-48] SIO connectivity imposes costly high-χ interactions between adjacent blocks ($\chi_{BC} > \chi_{AB} \approx \chi_{AC}$), while ISO connectivity alleviates this penalty by not inherently requiring I/O (A/C) interfaces. ISO and SIO phase diagrams are consequently distinct due to so-called frustration. The influence of each χ_{ij} is less understood. In contrast to (SI/IS)O materials where every $\chi_{ij} >> 0$, the LSO polymers studied herein feature low χ_{AC} between the end blocks ($\chi_{LO} \lesssim 0$). Actual literature estimates for χ_{LO} range from 0.0038 to −0.161 depending on end groups and measurement techniques.[49-50] Combining any $-0.161 < \chi_{LO} < 0.0038$ with the aforementioned literature values $\chi_{LS} = 0.080$ and $\chi_{SO} = 0.049$ yields a frustrated system. SCFT simulations (Figure 4.4) suggest that the magnitude of χ_{LO}, beyond simple frustration effects, dictates the unique LAM$_P$ self-assembly observed in Figure 4.3. Calculations for LSO indicate that LAM$_P$ is stable when $\chi_{LO} < \chi^C$, which marks a first-order phase transition between LAM$_P$ and LAM$_3$ (Figure 4.4E). The predicted value of χ^C is sensitive to physical parameters including the statistical segment lengths and χ_{ij} and is consequently difficult to quantitatively associate with experiments. Using the aforementioned literature values corresponding to L, S, and O pairwise interactions, we estimate $\chi^C \approx 0.009$, which sets an approximate upper bound on the value of χ_{LO} since no evidence of LAM$_3$ is experimentally observed. Experiment and theory collectively suggest that low-χ interactions ($\chi_{AC} \lesssim 0$) underpin the self-assembly of LSO to LAM$_P$.

4-7 Molecular Asymmetry Effects

The pronounced decrease in domain spacing observed for LSO and LSL' upon increasing N_C or $N_{A'}$ (at constant N_A, N_B) also emerge as consequences of the low-χ design, involving molecular asymmetry, block-block mixing, and screening effects. SCFT simulations of linear ABA' triblock copolymers have previously revealed that asymmetry in A/A' block lengths can induce a decrease in domain spacing.[51] The explanation is twofold. First, A/A' asymmetry lowers the stretching energy in A domains,[52] which can be understood by imagining equivalent A block lengths and then transferring material from one end to the other; as asymmetry increases, the overall A segment distribution shifts away from the interface, increasing d^*. Second, when the end blocks are sufficiently asymmetric, a significant proportion of the shorter A blocks can pull out into B domains (Figure 4.7A). Although chain pullout incurs an enthalpic penalty ($\chi_{AB} > 0$), this effect is more than compensated by relaxation of the B block, which is entropically favored and further increases d^*. The synthesis of ABA' triblocks from a common diblock precursor exhibits the same trend: growing longer A' blocks decreases molecular asymmetry and correspondingly lowers d^*. Experimental studies of linear ABA' triblock copolymers have corroborated this theory of end block asymmetry,[53-54] and the LSL' and LSO brush triblock polymers studied herein exhibit strikingly similar behavior. We conclude that architecture is not a critical molecular design parameter dictating the trends in d^* (Figures 4.5–4.6); instead, the close parallels between the self-assembly of ABA' triblock copolymers and appropriately designed ABC triblock terpolymers implicate block-block mixing. ABA' samples (linear or brush) clearly have mixed A/A' domains before chain pullout, and a negligible χ_{LO} in LSO should also promote end block mixing. Application of the stretching energy and chain pullout concepts developed to rationalize ABA' self-assembly therefore also captures the essence of ABC systems (Figure 4.7B). Molecular weight dispersity additionally favors pullout of shorter end blocks (A' or C), while longer ones remain anchored in mixed domains.

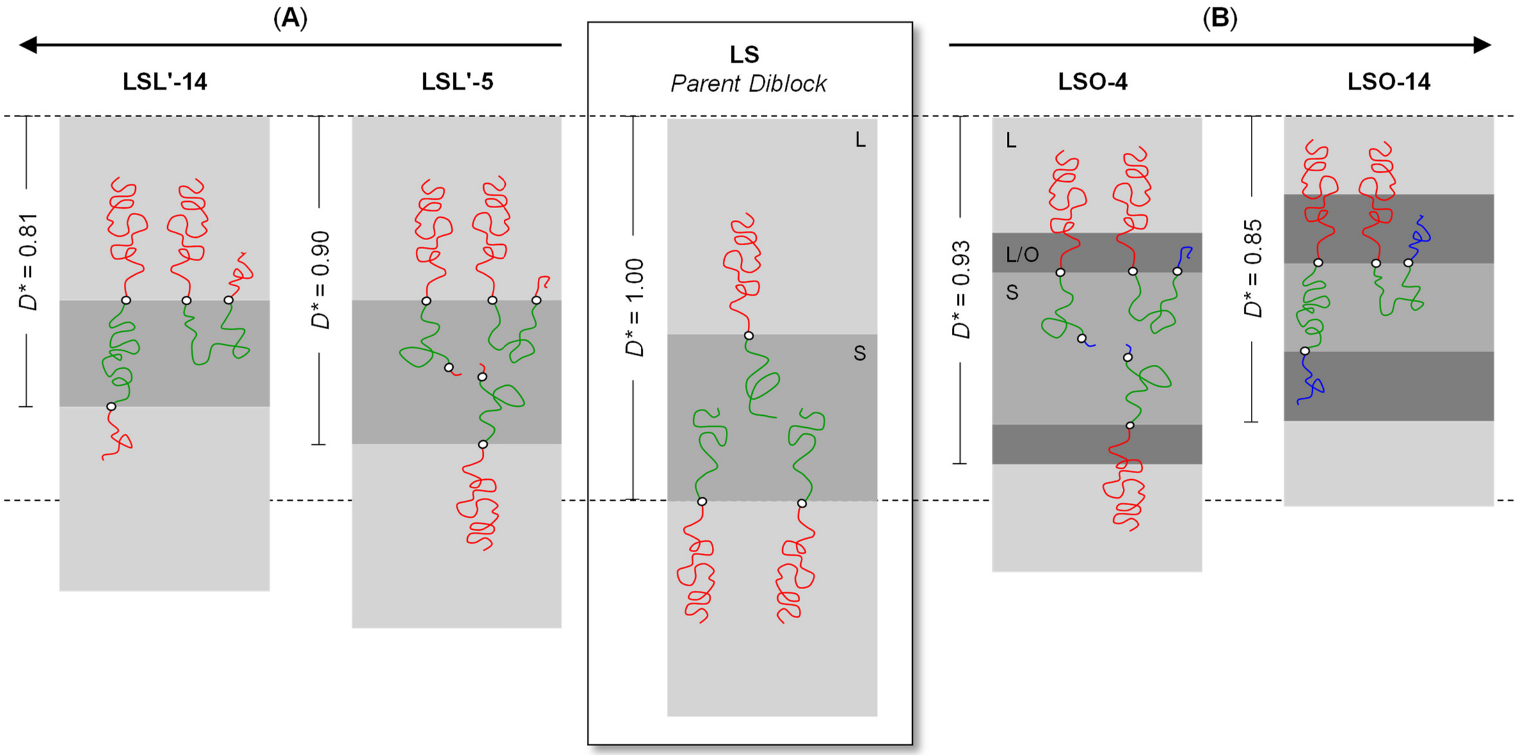

Figure 4.7: Illustration of chain pullout to explain the trends in d^* for LSL' and LSO brush triblock polymers with varying end block length (equivalently, varying molecular asymmetry). Linear chains are depicted to aid visualization. As the end block length N_X increases from a fixed parent LS diblock, d^* decreases (here, $D^* \equiv d^*/d^*_{LS}$, where d^*_{LS} is the period of the parent LS diblock). (*A*) X = A' (LSL'): short PLA end blocks pull out of PLA domains into PS domains. (*B*) X = C (LSO): short PEO end blocks pull out of mixed PLA/PEO domains into PS domains.

Informed SCFT simulations of LSO indicate the stability of LAM_P over a wide range of N_C (Appendix C-9, Figure C.13). In addition, simulations incorporating an exponential distribution of end block dispersity for both LSO and LSL' (Tables C.4–C.5) show good agreement between the predicted and measured magnitudes of d^*. The simulations capture a sharp initial decrease in d^* when the backbone lengths of the third block are short (N_C, $N_{\text{A}'} \leq 7$), reinforcing the significance of molecular asymmetry and chain pullout. As the end block lengths continue to increase however, the predicted values of d^* monotonically increase, in contrast to the experimental trends. These disparities may reflect (1) inaccuracies in the χ_ij values employed,[34] (2) larger dispersities in N_C and $N_{\text{A}'}$ than anticipated by theory, or (3) potential non-equilibrium effects (Chapter 5-2).

4-8 Screening Unfavorable Block-Block Interactions

In LSO, the effects of molecular asymmetry and chain pullout are amplified by the screening of high-χ block-block interactions. The most unfavorable contacts in LSO (L/S) can be partially mitigated by inserting PEO between PLA and PS domains near the interface, since $\chi_\text{LS} > \chi_\text{SO}$ and $\chi_\text{LO} \lesssim 0$. This possibility is naturally permitted in the disordered state, but upon self-assembly to the conventional LAM_3 morphology, chain connectivity necessarily creates energetically costly PLA/PS interfaces. Screening L/S contacts in LAM_3 would typically require altering the block sequence to LOS, an impossible task post-synthesis, but LAM_P restores this opportunity by incorporating partial mixing between the end blocks. This phenomenon decouples the molecular block sequence from the self-assembled domain pattern. Screening unfavorable block-block interactions in LSO likely also contributes to the molecular origins of the domain spacing trend. As PEO inserts between PLA and PS blocks at the interface, it should expand the intermolecular distance in the plane of the lamellae and therefore contract the lamellar period (i.e., d^*). Similar mixing consequences have been observed in block polymer/homopolymer blends in which the homopolymer localizes at the block-block interfaces.[55-57] Chapter 5 will discuss the phase behavior of blends of LS brush diblock copolymers with linear O homopolymers. Consequences of low-χ interactions manifest in blends as well as in LSO brush triblock terpolymers.

4-9 Dispersity and Architecture

Comparing LSO, LSL', and linear (IS/SI)O reinforces the importance of low-χ interactions and rejects other potential explanations for the unique mesoscopic ACBC domain connectivity and domain spacing trend. Dispersity differences among the blocks can be discounted since all samples across the LSO, LSL', ISO, and SIO series depicted in Figures 4.5–4.6 were synthesized by living polymerizations (either ROMP or anionic polymerization) from parent diblock precursors. Since O comprises the C block in each ABC series, PEO clearly does not inherently cause domain contraction with increasing O block lengths or weight fractions. Chapter 5 of this thesis will discuss crystallization and other potential effects associated with increasing PEO content

We expect that the phenomena described above, illustrating the physical consequences of designing polymers with certain miscible blocks, are general to the class of soft materials with χ_{AB}, $\chi_{BC} >> |\chi_{AC}| \approx 0$. Although bottlebrush polymers were employed in the present study, SCFT calculations predict identical behavior for analogous linear triblock terpolymers with the same absolute and relative χ parameters (Appendix C, Figure C.14). While bottlebrush polymers experience some steric-induced stiffening compared to linear polymers,[58-59] our results suggest that brush LSO and LSL' are actually relatively flexible. The backbone flexibility should enable brush LS(O/L') to adopt looping midblock configurations (Figures 4.4 and 4.7), just like linear AB(C/A') triblocks with compatible end blocks.[60-61] Informed SCFT calculations indicate that the effective backbone persistence length of brush LSO and LSL' corresponds to approximately 5 norbornene repeat units.[25] Since the B midblocks of LSO and LSL' are much longer than 5 units ($N_B \geq 24$), they should readily form loops, although undoubtedly less than the 60% predicted for flexible (linear) triblocks.[62] Our results, placed in the context of recent work on bottlebrush block polymer self-assembly, suggest that polymer architecture is not a major factor controlling the formation of partially mixed morphologies. Instead, the primary driving force appears to be the magnitude of χ_{AC}. Designed low-χ interactions emerge as tools to manipulate block polymer self-assembly.

4-10 Evidence for Backbone Flexibility

In the preceding sections, we proposed that the bottlebrush architecture should readily permit the formation of looping midblocks in brush LSO triblock terpolymers. However, loops demand significant curvature of the backbones, opposing the highly extended nature of bottlebrush polymers. Certain physical consequences of the relative stiffness of bottlebrush block polymers compared to linear analogues have been discussed in Chapter 3 of this thesis. For example, the scaling of the lamellar period with the total backbone degree of polymerization depends on the grafting density z, such that $d^* \sim N_{\mathrm{bb}}^{\alpha(z)}$ and $\alpha \sim z$ (Chapter 3-3).[63] The apparent stiffness of bottlebrush polymers in these contexts raises interesting questions about the limits of backbone flexibility and the corresponding implications for physical properties. In order to address these questions, we further studied the unusual phase behavior of LSO brush triblock terpolymers using resonant soft X-ray reflectivity (RSoXR) and near edge X-ray fine structure absorption spectroscopy (NEXAFS). Insight from these measurements supports the assignment of a new partially mixed morphology (LAM$_{\mathrm{P}}$) and provides unambiguous evidence for the backbone flexibility of bottlebrush polymers in both thin films and the melt.

Both RSoXR[64-65] and NEXAFS[66-67] take advantage of the sensitivity of soft X-rays to variations in chemical composition in order to evaluate the concentration — and in some cases, the orientation — of molecular bonds in a material. Near an atomic absorption edge, the complex index of refraction, $n(\mathrm{E}) = 1 - \delta(\mathrm{E}) + i\beta(\mathrm{E})$, varies significantly as a function of energy and molecular composition due to electronic transitions between occupied and unoccupied orbitals. This sensitivity to chemical structure can be used to tune the contrast between different components in soft materials, enabling the direct study of composition distributions in all-organic thin films.[68-70] Whereas NEXAFS is primarily surface-sensitive, RSoXR can depth-profile the molecular composition of films up to several hundred nanometers thick depending on the X-ray energy. This exquisite chemical sensitivity over multiple length scales enable NEXAFS and RSoXR measurements of brush LSO thin films to probe the composition profile and brush backbone conformations.

Brush LSO samples were prepared by spin-coating thin films from propylene glycol methyl ether acetate (PGMEA) onto silicon wafers. Among the selected brush LSO triblock terpolymers, the backbone degrees of polymerization for the PLA and PS blocks were fixed

(N_A = 26, N_B = 24) while the backbone degree of polymerization for the PEO block was varied (N_C = 8, 12, 16, 20) (Figure 4.8A). These samples correspond to LSO-8, LSO-12, LSO-16, and LSO-20 in Table 4.1. Reference samples corresponding to the constituent brush diblock polymers (SO and LS, Figure 4.8B) and homopolymers (L, S, O, and polynorbornene, Figure 4.8C) were also prepared. Transmission absorption measurements of these reference samples were used to evaluate the optical constants of each component toward correlating the measured scattering length density (SLD) with the chemical composition.

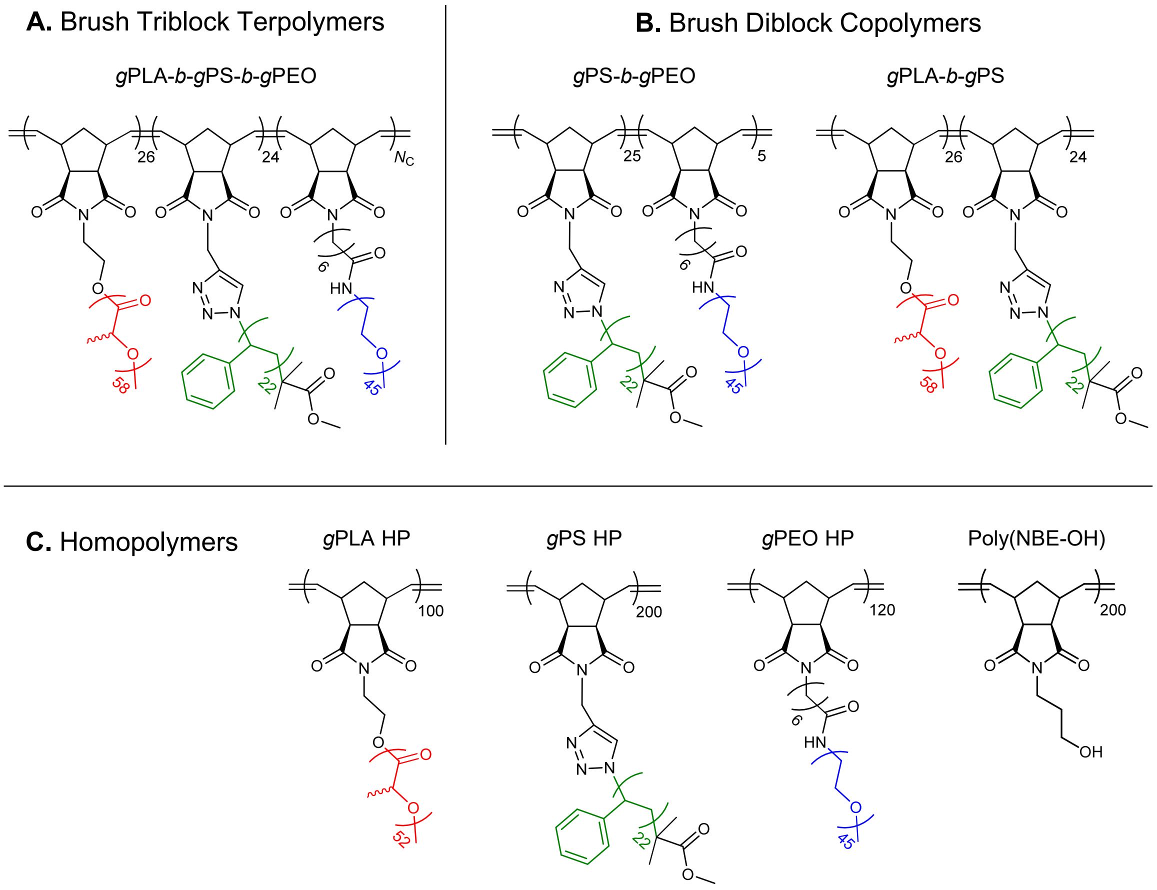

Figure 4.8: (*A*) Brush LSO triblock terpolymers samples prepared for reflectivity measurements: N_C = 8, 12, 16, 20 (Table 4.1). (*B, C*) Reference samples, including (*B*) brush diblock copolymers (SO and LS) and (*C*) homopolymers of each component (*i.e.*, brush PLA, brush PS, brush PEO, and the polynorbornene backbone).

Atomic force microscopy (AFM) confirms that all films are uniform and under 100 nanometers thick. Representative micrographs are shown in Figure 4.9. Under most conditions, the films dewetted, forming islands and holes that rendered the samples ill-suited for reflectivity measurements. Optimization of the annealing process achieved uniform thin films. Surprising, the commensurability conditions for the brush block polymers differed from the well-established conditions for linear analogues. For typical *linear* block polymers, lamellae form parallel to the substrate when the total film thickness is either a half-integer multiple of d^* (asymmetric wetting) or a full-integer multiple of d^* (symmetric wetting). In contrast, the LS and LSO block polymers assembled at $3.25d^*$. Further studies are underway in order to explore the impact of molecular architecture on the commensurability conditions.

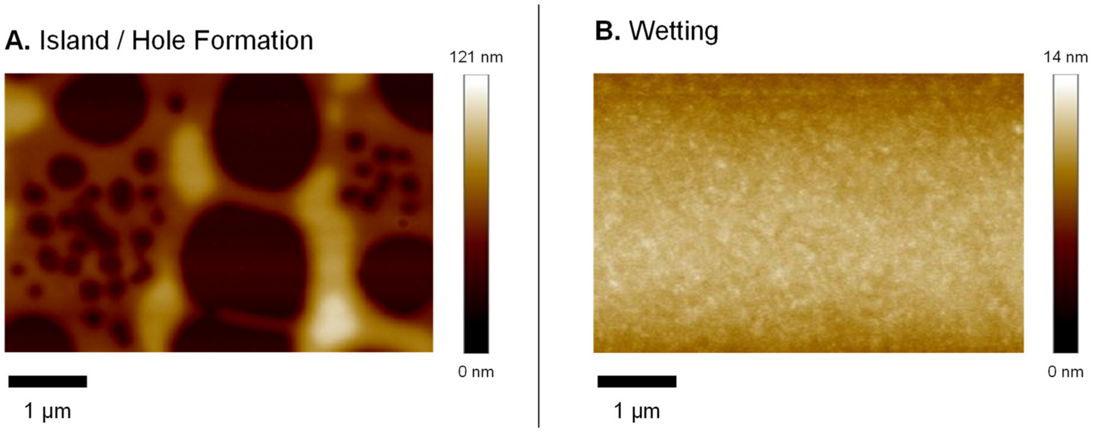

Figure 4.9: Representative atomic force micrographs (AFM) corresponding to spin-coated films of LSO-0 on silicon. (*A*) Under many conditions, the films dewetted, forming islands and holes. The commensurability conditions differ for brush and linear block polymers. (*B*) Under optimized conditions, the films wet the substrate.

Reflectivity measurements of the brush LSO films were conducted near the carbon edge in order to tune the contrast among the three components (L, S, and O). The experimental and simulated reflectivity data for LSO-12 ($N_C = 12$) are shown in Figure 4.10A. Measurements were performed at (1) 270 eV, which is effectively non-resonant and primarily sensitive to the electron density; (2) 284 eV, near the characteristic absorption peak for aromatic carbon-carbon bonds (≈ 285 eV) and therefore highly sensitive to PS blocks; and (3) 286 eV, near the characteristic absorption peak for carbonyl bonds (≈ 288 eV) and therefore highly sensitive to PLA blocks. Measurements at these three energies enable determination of the component distributions throughout the film.

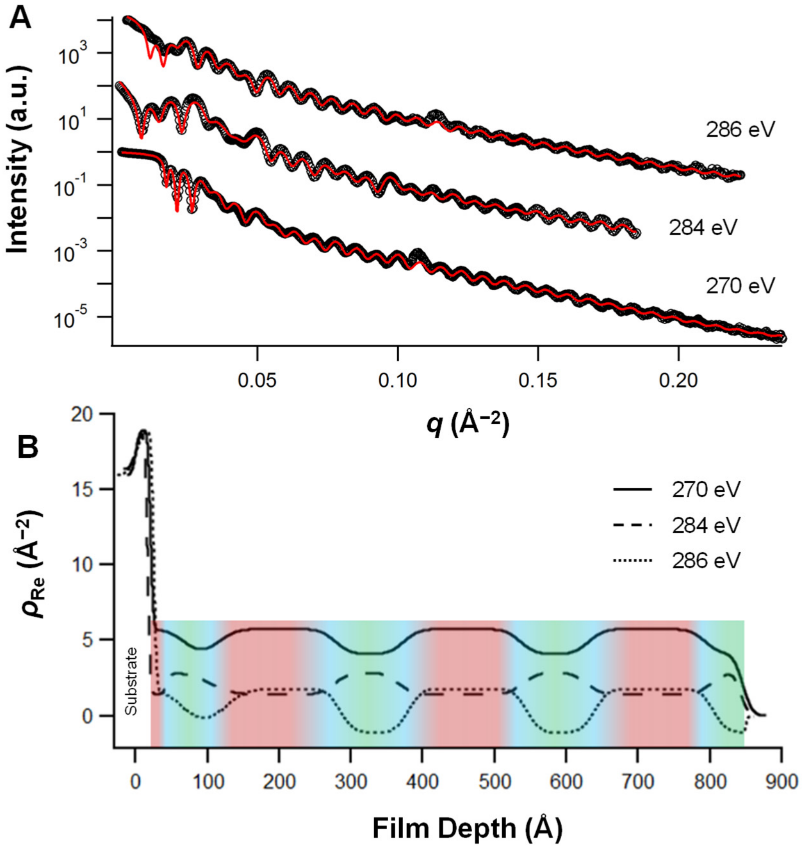

Figure 4.10: (*A*) Experimental (*black circles*) and simulated (*red lines*) reflectivity profiles determined for LSO-12 at three different energies: 286, 284, and 270 eV. (*B*) Composition profile for LSO-12 determined from reflectivity measurements. The red, green, and blue colors highlight the correspondence between each block and its SLD.

The real component of the SLD profile (ρ_R), determined from fits to the experimental data, is shown in Figure 4.10B for all three energies. Several models were tested while fitting the RSoXR data. First, an ABCBA-type model with a PEO layer isolated between PS layers was tested, representing the conventional LAM$_3$ morphology expected for triblock terpolymers. The LAM$_3$ model failed to fit the experimental data, eliminating the possibility that the material may organize differently in thin films compared to the bulk. Two other models, consistent with the LAM$_P$ morphology proposed in our previous work, were explored. The first model assumed an *explicit* PEO layer residing at the interface between the PS and PLA domains, while the second model incorporated an *implicit* PEO layer between the PS and PLA domains. The best fits for both models reduce to identical SLD profiles where the PEO layer cannot be explicitly observed, indicating that a bilayer model accurately captures the measured SLD profile. The calculated profiles suggest that LSO-12 forms a lamellar morphology with a PS layer at the top surface followed by alternating domains of PS and PLA with PEO at the interfaces. Near the silicon substrate, the layers become less distinct and the interfaces become broader, potentially due to restricted motion at the surface.

In order to obtain greater insight into the results, SCFT calculations were employed to simulate $\rho_R(z)$. SCFT has been previously used to capture bottlebrush behavior by modifying the standard worm-like chain model to account for the strong steric interactions resulting from the highly grafted side chains.[25,71-72] The composition profiles predicted by SCFT show excellent agreement with the experimental results (Figure 4.11).

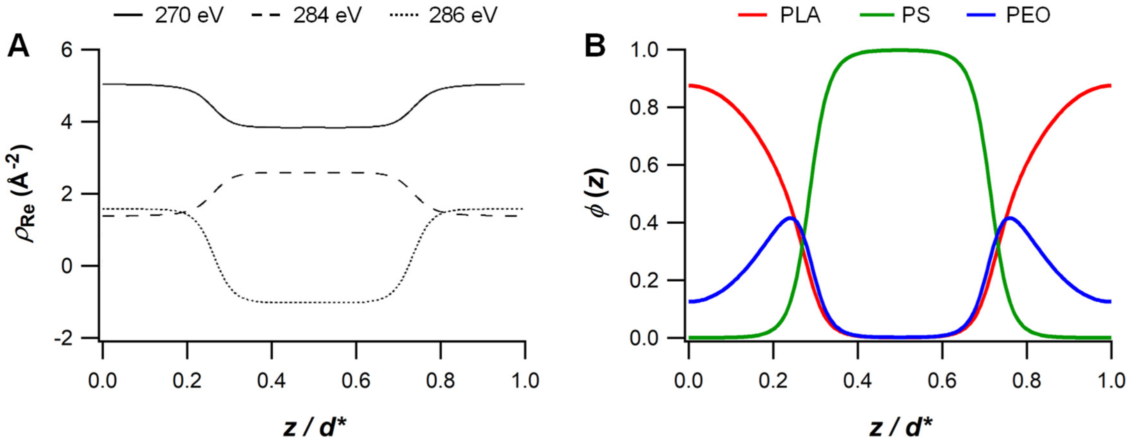

Figure 4.11: Composition profiles for LSO-12 determined by (*A*) fitting experimental reflectivity data or (*B*) SCFT. The relative segment concentrations of each component are provided over one normalized lamellar period (*z* / *d**). (*A*) Profiles were determined from RSoXR measurements at 270 eV (—), 284 eV (- - -), and 286 eV (.......); see Figure 4.10. (*B*) Profiles were calculated for PLA (*red*), PS (*green*), and PEO (*blue*). Comparison of reflectivity and SCFT profiles indicate close agreement between the measured and predicted results.

One surprising result that emerges from the reflectivity profiles is the presence of the PS block at the air interface. In order to evaluate the surface composition, NEXAFS measurements around the carbon edge were performed for LSO-12 and reference bottlebrush homopolymers (Figure 4.12). NEXAFS measurements were collected at the SXR beamline[73] of the Australian Synchrotron and corrected and normalized with QANT.[74] NEXAFS is an analogous resonant soft X-ray spectroscopy that is highly sensitive to the chemical composition within the first 5 nanometers of a free surface. The LSO-12 NEXAFS spectra show a strong absorption peak at ≈285 eV, corresponding to the 1s→π* transition for the aromatic rings in polystyrene. A second distinct peak is observed at ≈288 eV, corresponding to the 1s→π* transition for the carbonyl bond in PLA. (A small peak is also present at 288 eV in the brush PS homopolymer reference sample, due to the bisimide linkages in the backbone of the brush and the methyl ester end group on the PS side chain.) Quantitative fitting of the LSO-12 spectrum suggests that there is ~80 % by volume of PS at the air interface, consistent with RSoXR analysis. Since NEXAFS is sensitive to several nanometers beneath the surface, some or all of the PLA and PEO in the signal likely originates beneath the PS layer. Because PS comprises the midblock of the brush LSO triblock, the backbones must be curved to allow PS to segregate to the surface. In other words, the ABC bottlebrush *must* form loops — analogous to flexible linear ABA' triblocks — despite the significant conformational and packing challenges looping imposes for the backbone and side chains. In fact, the composition of the surface layer and narrow thickness relative to a fully extended chain suggest that the surface layer is composed almost entirely of looped chains. The free energy penalty from these conformational effects is clearly outweighed by the enthalpic preference for mixing PLA and PEO chains ($\chi_{\mathrm{LO}} \lesssim 0$).

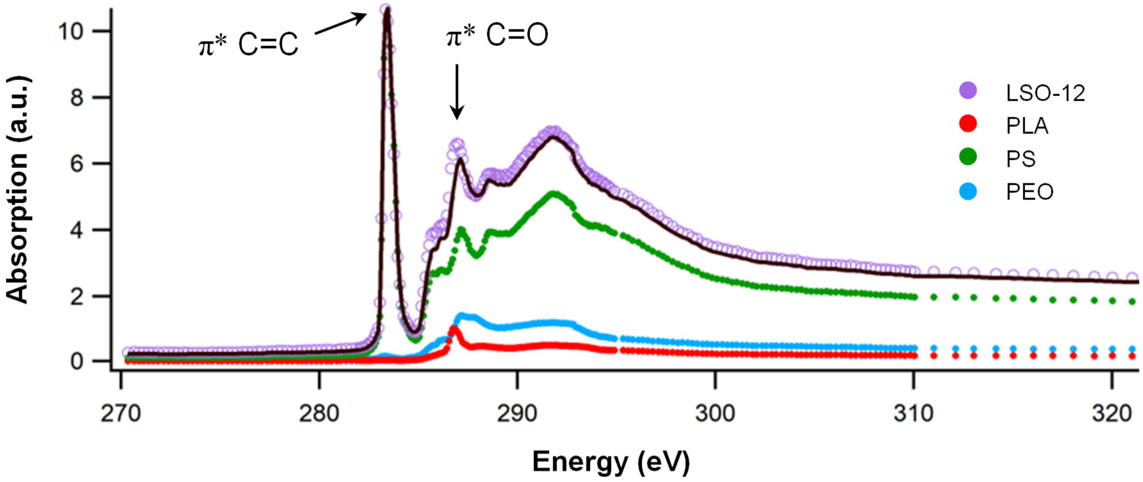

Figure 4.12: NEXAFS analysis of LSO-12 at the carbon edge. Arrows indicate transitions for PS (C=C 1s→π* for the aromatic rings, E = 284.5 eV) and PLA (C=O 1s→π* for the carbonyl, E = 288 eV).

Informed SCFT calculations provide further support for backbone curvature. Figure 4.13 shows the predicted distributions of PS and the polynorbornene backbone within one normalized period. The profiles indicate that the backbone concentration drops significantly in the center of the PS domain, then increases near the PS/PLA interface. This dip in the backbone concentration is consistent with a large fraction of the blocks forming loops. Reflectivity measurements at the nitrogen edge (407, 402, and 390 eV) were performed in attempts to experimentally determine the backbone distribution (that is, by tracking the bisimide functionality). However, the low nitrogen content (<1 wt%) and high absorptions coefficients did not allow resolution of the backbone concentration profile. Ongoing work aims to optimize the systems to enable determination of the backbone distribution, with the goal of additionally measuring the backbone *orientation*.

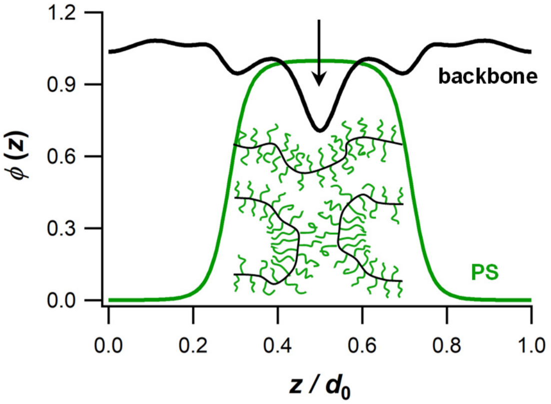

Figure 4.13: SCFT composition profile for LSO-12 within one normalized lamellar period (z / d^*), where $\phi(z)$ is the relative segment concentration. Calculated profiles for PS (*green*) and the backbone (*black*) are shown; PLA and PEO are not included. (See Figure 4.11B.) A schematic illustration of midblock configurations is provided. The arrow indicates a decrease in the backbone concentration at the center of the PS domain, suggesting a large fraction of looping midblocks.

Additional insight can be attained by examining trends in the lamellar periods and absolute domain thicknesses extracted from RSoXR measurements (Table 4.3). The overall changes in d^* with the backbone degree of polymerization of the PEO block closely agree with the d^* values determined from SAXS measurements of these materials in the bulk.[71] The advantage of reflectivity is that the composition and thicknesses of individual layers can be directly interrogated. As N_C increases, the mixed PLA/PEO domain maintains a constant thickness $d_{L+O} \approx 16.8$ nm, while the thickness of the PS domain decreases from 9.4 nm for LSO-8 to 6.5 nm for LSO-20. At the same time, the interfacial width increases from 3.8 nm to 7.5 nm. The data are compiled in Table 4.3, and a schematic illustration of chain configurations and relevant parameters is provided in Figure 4.14.

Table 4.3: Parameters resulting from the fits to the LSO reflectivity profiles. Uncertainties represent 95% confidence intervals determined by the directed evolution Monte Carlo Markov chain algorithm.[75]

Sample	*d** (SAXS) (nm)	*d** (RSoXR) (nm)	d_S (nm)	d_{L+O} (nm)	Interfacial Width (nm)	PS Surface Thickness (nm)
LSO-8	26.8	26.1 ± 0.5	9.4 ± 0.3	16.7 ± 0.3	3.8 ± 0.5	4.6 ± 0.2
LSO-12	25.2	25.7 ± 0.6	8.8 ± 0.3	16.9 ± 0.3	4.5 ± 0.6	4.2 ± 0.3
LSO-16	24.6	25.2 ± 0.5	8.4 ± 0.3	16.8 ± 0.2	4.8 ± 0.8	3.8 ± 0.2
LSO-20	23.6	23.1 ± 0.5	6.5 ± 0.2	16.6 ± 0.3	7.5 ± 0.8	3.3 ± 0.2

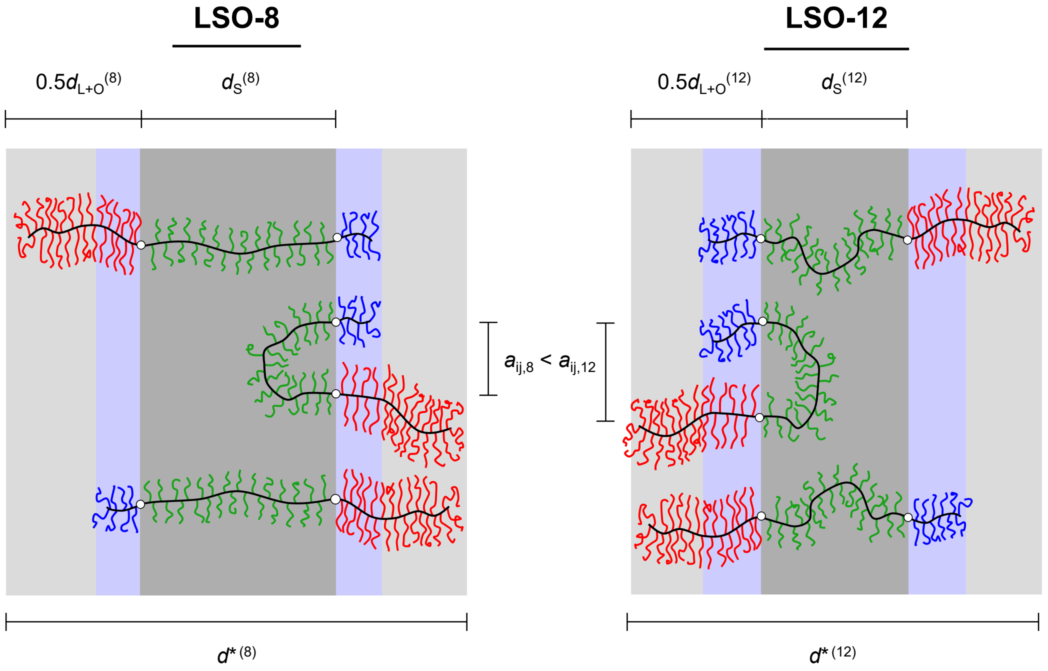

Figure 4.14: Schematic illustration of chain configurations over one lamellar period (*d**) for LSO-8 (*left*) and LSO-12 (*right*). Relevant length scales are indicated, including *d**, the thickness of the mixed PLA/PEO layers (d_{L+O}), the thickness of the PS layers (d_S), and the average distance between block junctions at the interface (a_{ij}).

The combination of these trends suggests that compatibilization at the interface is the primary factor motivating the unusual decrease in *d** with increasing total molecular weight. Blending PLA and PEO at the interface screens the unfavorable, high-χ interactions between PS and PLA. As increasingly longer PEO blocks are localized at the interface between domains, the average distance between block-block junctions (a_{ij}) increases. In order to maintain uniform melt density, *d** (the orthogonal length scale) must decrease.[55] This change in the cross-sectional area at the interface would typically reduce the thicknesses of both L/O and S domains, but it is offset here by the increasingly long PEO blocks anchored in the PLA-rich phases. Figure 4.15 highlights the relationship between *d** and a_{ij}.

Chain pullout has also been suggested as a reason for the period reduction in this system (Section 4-7): by analogy to linear ABA' triblock copolymers, when the end block lengths are sufficiently asymmetric, the shorter end blocks are expected to partially "pull out" into the B domains (Figure 4.7).[51,53] While this mechanism may contribute in part to the *d** trend, it is inconsistent with the relative and absolute PLA and PS layer thicknesses determined by RSoXR. Furthermore, the SCFT calculations predict that the volume fraction of PEO at the center of the PS lamellae is only ~1% for LSO-8, reducing to nearly 0% in LSO-20. The small change in volume fraction is insufficient to effect the >10% change in *d** between LSO-8 and LSO-20. Finally, the relationship between the thickness of the PS surface layer and the interior PS layers suggest that there is a similarly large fraction of loops for those layers beneath the surface. For all samples, the thickness of the PS interior layers is slightly larger than twice the thickness of the surface layer. As the surface layer must be composed primarily of loops, this suggests a high fraction present in the interior layers as well. The correspondence between the thin film period determined by RSoXR and the bulk period from SAXS measurements indicate that this behavior is likely consistent across both thin films and bulk samples.

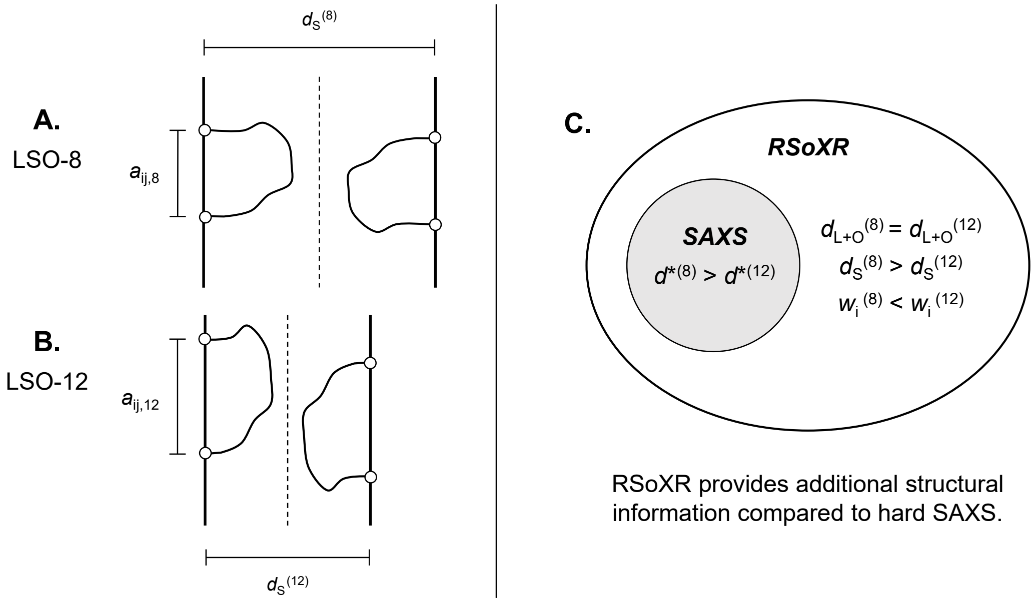

Figure 4.15: (*A, B*) Configurations of looping midblocks inferred from reflectivity measurements for (*A*) LSO-8 and (*B*) LSO-12; see also Figure 4.14. As N_C increases from 8 to 12, the thickness of the PS domain (d_S) decreases. A concomitant increase in the average distance between block junctions at the interface (a_{ij}) is expected. (*C*) Like SAXS, RSoXR enables determination of d^*. However, RSoXR provides additional information due to its sensitivity to chemical composition.

RSoXR and NEXAFS measurements demonstrate that bottlebrush block polymers can adopt a surprising degree of flexibility. The measurements demonstrate that, under certain conditions, the midblock in a bottlebrush triblock terpolymer is largely present at the air interface, providing evidence that the brush polymer forms loops despite the steric-induced stiffening of the backbone. The relationships between the thicknesses of this surface layer and the interior PS layers suggests that interior domains may also consist largely of looped configurations. This result raises interesting questions about *how* the side chains pack in looping midblocks and under what conditions curvature is allowed by the densely grafted polymer architecture. In linear block polymers, the ratio of looping and bridging blocks significantly impacts the mechanical performance and other physical properties. Further studies will explore how the midblock configuration influences the properties of bottlebrush block polymers. The unusual commensurability conditions (assembly at 3.25d^*) will also be studied. Improving understanding of these phenomena will enable bottlebrush polymers to be better tailored for their many diverse potential applications.

4-11 Conclusions

The insights gained herein from both experiment and theory illustrate the profound influence low-χ interactions exert on self-assembly. Proper selection of χ_{ij} and f can generate unusual morphologies characterized by partial block mixing (LAMP), decouple molecular sequence from mesoscopic connectivity, and provide counterintuitive control over domain spacing. While high-χ block polymers have been the subject of widespread interest, low-χ systems remain relatively unexplored, yet the latter generate fascinating physics that are anticipated to gain importance as sequence complexity further evolves. Expanding the block polymer design toolkit to include low-χ interactions creates new opportunities to tailor mesoscale structure and should find utility in the future design of functional materials.

4-12 References

(1) Thomas, E. L. *Science* **1999**, *286*, 1307.
(2) Park, C.; Yoon, J.; Thomas, E. L. *Polymer* **2003**, *44*, 6725–6760.
(3) Lutz, J.-F.; Ouchi, M.; Liu, D. R.; Sawamoto, M. *Science* **2013**, *341*, 628–637.
(4) Bates, C. M.; Bates, F. S. *Macromolecules* **2016**, *50*, 3–22.
(5) Leibler, L. *Macromolecules* **1980**, *13*, 1602–1617.
(6) Bates, F. S.; Fredrickson, G. H. *Phys. Today* **1999**, *52*, 32–38.
(7) Bates, F. S.; Hillmyer, M. A.; Lodge, T. P.; Bates, C. M.; Delaney, K. T.; Fredrickson, G. H. *Science* **2012**, *336*, 434–440.
(8) Zheng, W.; Wang, Z.-G. *Macromolecules* **1995**, *28*, 7215–7223.
(9) Bailey, T. S. Morphological behavior spanning the symmetric AB and ABC block copolymer states. University of Minnesota, 2001.
(10) Xie, N.; Liu, M.; Deng, H.; Li, W.; Qiu, F.; Shi, A.-C. *J. Am. Chem. Soc.* **2014**, *136*, 2974–2977.
(11) Gao, Y.; Deng, H.; Li, W.; Qiu, F.; Shi, A.-C. *Phys. Rev. Lett.* **2016**, *116*, 068304.
(12) Legge, N. R. *Rubber Chem. Technol.* **1987**, *60*, 83–117.
(13) Bluemle, M. J.; Zhang, J.; Lodge, T. P.; Bates, F. S. *Macromolecules* **2010**, *43*, 4449–4452.
(14) Lee, S.; Bluemle, M. J.; Bates, F. S. *Science* **2010**, *330*, 349–353.
(15) Lynd, N. A.; Oyerokun, F. T.; O'Donoghue, D. L.; Handlin, D. L.; Fredrickson, G. H. *Macromolecules* **2010**, *43*, 3479–3486.
(16) Hashimoto, T.; Tanaka, H.; Hasegawa, H. *Macromolecules* **1990**, *23*, 4378–4386.
(17) Matsen, M. W. *Macromolecules* **1995**, *28*, 5765–5773.
(18) Kimishima, K.; Jinnai, H.; Hashimoto, T. *Macromolecules* **1999**, *32*, 2585–2596.
(19) Tang, C.; Sivanandan, K.; Stahl, B. C.; Fredrickson, G. H.; Kramer, E. J.; Hawker, C. J. *ACS Nano* **2010**, *4*, 285–291.

(20) Sveinbjörnsson, B. R.; Weitekamp, R. A.; Miyake, G. M.; Xia, Y.; Atwater, H. A.; Grubbs, R. H. *Proc. Natl. Acad. Sci. U.S.A.* **2012**, *109*, 14332–14336.

(21) Bates, C. M.; Chang, A. B.; Momčilović, N.; Jones, S. C.; Grubbs, R. H. *Macromolecules* **2015**, *48*, 4967–4973.

(22) Bates, C. M.; Chang, A. B.; Schulze, M. W.; Momčilović, N.; Jones, S. C.; Grubbs, R. H. *J. Polym. Sci., Part B: Polym. Phys.* **2016**, *54*, 292–300.

(23) Radlauer, M. R.; Sinturel, C.; Asai, Y.; Arora, A.; Bates, F. S.; Dorfman, K. D.; Hillmyer, M. A. *Macromolecules* **2016**, *50*, 446–458.

(24) Fredrickson, G. H. *The Equilibrium Theory of Inhomogeneous Polymers*; Oxford University Press: New York, 2006.

(25) Dalsin, S. J.; Rions-Maehren, T. G.; Beam, M. D.; Bates, F. S.; Hillmyer, M. A.; Matsen, M. W. *ACS Nano* **2015**, *9*, 12233–12245.

(26) Fetters, L. J.; Lohse, D. J.; Richter, D.; Witten, T. A.; Zirkel, A. *Macromolecules* **1994**, *27*, 4639–4647.

(27) Dorgan, J. R.; Janzen, J.; Knauss, D. M.; Hait, S. B.; Limoges, B. R.; Hutchinson, M. H. *J. Polym. Sci., Part B: Polym. Phys.* **2005**, *43*, 3100–3111.

(28) Olayo-Valles, R.; Lund, M. S.; Leighton, C.; Hillmyer, M. A. *J. Mater. Chem.* **2004**, *14*, 2729–2731.

(29) Vayer, M.; Nguyen, T. H.; Sinturel, C. *Polymer* **2014**, *55*, 1048–1054.

(30) Trent, J. S.; Scheinbeim, J. I.; Couchman, P. R. *Macromolecules* **1983**, *16*, 589–598.

(31) Gai, Y.; Song, D.-P.; Yavitt, B. M.; Watkins, J. J. *Macromolecules* **2017**, *50*, 1503–1511.

(32) Zalusky, A. S.; Olayo-Valles, R.; Wolf, J. H.; Hillmyer, M. A. *J. Am. Chem. Soc.* **2002**, *124*, 12761–12773.

(33) Cochran, E. W.; Morse, D. C.; Bates, F. S. *Macromolecules* **2003**, *36*, 782–792.

(34) Beardsley, T. M.; Matsen, M. W. *Phys. Rev. Lett.* **2016**, *117*, 217801.

(35) Stadler, R.; Auschra, C.; Beckmann, J.; Krappe, U.; Voight-Martin, I.; Leibler, L. *Macromolecules* **1995**, *28*, 3080–3097.

(36) Balsamo, V.; Gil, G.; Urbina de Navarro, C.; Hamley, I. W.; von Gyldenfeldt, F.; Abetz, V.; Cañizales, E. *Macromolecules* **2003**, *36*, 4515–4525.

(37) Liu, M.; Li, W.; Qiu, F.; Shi, A.-C. *Macromolecules* **2012**, *45*, 9522–9530.

(38) Bailey, T. S.; Hardy, C. M.; Epps, T. H.; Bates, F. S. *Macromolecules* **2002**, *35*, 7007–7017.

(39) Meuler, A. J.; Ellison, C. J.; Qin, J.; Evans, C. M.; Hillmyer, M. A.; Bates, F. S. *J. Chem. Phys.* **2009**, *130*, 234903.

(40) Bailey, T. S.; Pham, H. D.; Bates, F. S. *Macromolecules* **2001**, *34*, 6994–7008.

(41) Couchman, P. R. *Macromolecules* **1978**, *11*, 1156–1161.

(42) Gaikwad, A. N.; Wood, E. R.; Ngai, T.; Lodge, T. P. *Macromolecules* **2008**, *41*, 2502–2508.

(43) Younes, H.; Cohn, D. *Eur. Polym. J.* **1988**, *24*, 765–773.

(44) Sheth, M.; Kumar, R. A.; Davé, V.; Gross, R. A.; McCarthy, S. P. *J. Appl. Polym. Sci.* **1997**, *66*, 1495–1505.

(45) Sioula, S.; Hadjichristidis, N.; Thomas, E. L. *Macromolecules* **1998**, *31*, 5272–5277.

(46) Tang, P.; Qiu, F.; Zhang, H.; Yang, Y. *J. Phys. Chem. B* **2004**, *108*, 8434–8438.

(47) Frielinghaus, H.; Hermsdorf, N.; Almdal, K.; Mortensen, K.; Messé, L.; Corvazier, L.; Fairclough, J. P. A.; Ryan, A. J.; Olmsted, P. D.; Hamley, I. W. *Europhys. Lett.* **2001**, *53*, 680–686.
(48) Chatterjee, J.; Jain, S.; Bates, F. S. *Macromolecules* **2007**, *40*, 2882–2896.
(49) Mao, H.; Hillmyer, M. A. *Macromol. Chem. Phys.* **2008**, *209*, 1647–1656.
(50) Lai, W.-C.; Liau, W.-B.; Lin, T.-T. *Polymer* **2004**, *45*, 3073–3080.
(51) Matsen, M. W. *J. Chem. Phys.* **2000**, *113*, 5539–5544.
(52) Milner, S. T.; Witten, T. A. *J. Phys. France* **1988**, *49*, 1951–1962.
(53) Hamersky, M. W.; Smith, S. D.; Gozen, A. O.; Spontak, R. J. *Phys. Rev. Lett.* **2005**, *95*, 168306.
(54) Smith, S. D.; Hamersky, M. W.; Bowman, M. K.; Rasmussen, K. Ø.; Spontak, R. J. *Langmuir* **2006**, *22*, 6465–6468.
(55) Winey, K. I.; Thomas, E. L.; Fetters, L. J. *Macromolecules* **1991**, *24*, 6182–6188.
(56) Koizumi, S.; Hasegawa, H.; Hashimoto, T. *Macromolecules* **1994**, *27*, 7893–7906.
(57) Chen, S.-C.; Kuo, S.-W.; Jeng, U. S.; Su, C.-J.; Chang, F.-C. *Macromolecules* **2010**, *43*, 1083–1092.
(58) Fredrickson, G. H. *Macromolecules* **1993**, *26*, 2825–2831.
(59) Mikhaylov, I. V.; Darinskii, A. A. *Polym. Sci. Ser. A* **2015**, *57*, 239–250.
(60) Zhulina, E. B.; Halperin, A. *Macromolecules* **1992**, *25*, 5730–5741.
(61) Kane, L.; Spontak, R. J. *Macromolecules* **1994**, *27*, 1267–1273.
(62) Matsen, M. W.; Thompson, R. B. *J. Chem. Phys.* **1999**, *111*, 7139–7146.
(63) Lin, T.-P.; Chang, A. B.; Luo, S.-X.; Chen, H.-Y.; Lee, B.; Grubbs, R. H. *ACS Nano* **2017**, *11*, 11632–11641.
(64) Wang, C.; Araki, T.; Ade, H. *Appl. Phys. Lett.* **2005**, *87*, 214109.
(65) Sunday, D. F.; Kline, R. J. *Macromolecules* **2015**, *48*, 679–686.
(66) Rosenberg, R. A.; Love, P. J.; Rehn, V. *Phys. Rev. B* **1986**, *33*, 4034–4037.
(67) Patel, S. N.; Su, G. M.; Luo, C.; Wang, M.; Perez, L. A.; Fischer, D. A.; Prendergast, D.; Bazan, G. C.; Heeger, A. J.; Chabinyc, M. L.; Kramer, E. J. *Macromolecules* **2015**, *48*, 6606–6616.
(68) Virgili, J. M.; Tao, Y.; Kortright, J. B.; Balsara, N. P.; Segalman, R. A. *Macromolecules* **2007**, *40*, 2092–2099.
(69) Sunday, D. F.; Hammond, M. R.; Wang, C.; Wu, W.-l.; Delongchamp, D. M.; Tjio, M.; Cheng, J. Y.; Pitera, J. W.; Kline, R. J. *ACS Nano* **2014**, *8*, 8426–8437.
(70) Ferron, T.; Pope, M.; Collins, B. A. *Phys. Rev. Lett.* **2017**, *119*, 167801.
(71) Chang, A. B.; Bates, C. M.; Lee, B.; Garland, C. M.; Jones, S. C.; Spencer, R. K. W.; Matsen, M. W.; Grubbs, R. H. *Proc. Natl. Acad. Sci. U.S.A.* **2017**, *114*, 6462–6467.
(72) Kawamoto, K.; Zhong, M.; Gadelrab, K. R.; Cheng, L.-C.; Ross, C. A.; Alexander-Katz, A.; Johnson, J. A. *J. Am. Chem. Soc.* **2016**, *138*, 11501–11504.
(73) Cowie, B. C. C.; Tadich, A.; Thomsen, L. *AIP Conf. Proc.* **2010**, *1234*, 307–310.
(74) Gann, E.; McNeill, C. R.; Tadich, A.; Cowie, B. C. C.; Thomsen, L. *J. Synchrotron Radiat.* **2016**, *23*, 374–380.
(75) Dura, J. A.; Richter, C. A.; Majkrzak, C. F.; Nguyen, N. V. *Appl. Phys. Lett.* **1998**, *73*, 2131–2133.

Chapter 5

Consequences of Low-χ Block Polymer Design: Phase Behavior, Equilibrium, and Crystallization

ABSTRACT

The preceding chapter describes our discovery of an unusual partially mixed lamellar morphology (LAM$_\mathrm{P}$) in LSO brush triblock terpolymers featuring grafted poly(D,L-lactide) (L), polystyrene (S), and poly(ethylene oxide) (O) side chains. Partial mixing emerges as a consequence of low-χ interactions between the end blocks. This chapter will describe other physical consequences associated with the molecular architecture and low-χ design. We will first discuss the ternary phase diagram for LSO brush triblock terpolymers, representing variations in both the relative backbone degrees of polymerization and the side chain molecular weights (Section 5-1). The influence of the brush architecture will be highlighted across >100 unique samples. Section 5-2 will address potential non-equilibrium effects in brush LSO, which may affect comparisons with theory. Variable-temperature X-ray scattering experiments indicate that LAM$_\mathrm{P}$ is thermally stable: consistent with other reports of fully grafted bottlebrush polymers, no order-disorder transition is observed below the onset of decomposition. Lastly, Section 5-3 will discuss the crystallization of PEO in LSO brush triblock terpolymers, in particular highlighting trends in the crystal orientation with O block backbone length. The potential contributions of screening and confinement effects will be described. Collectively, these studies of the phase behavior of brush LSO and brush LS + X (where X = L, S, or O) provide key insights into the roles of the brush polymer architecture, chain connectivity, and molecular interactions. Understanding the complex interplay of these structural and chemical parameters introduces new guidelines for low-χ block polymer design.

Table of Contents

5-1 Ternary Phase Behavior

5-1.1 LSO Brush Triblock Terpolymers

Bottlebrush polymers adopt extended conformations compared to their linear analogues.[1-4] Steric interactions between the densely grafted side chains impart a certain bending rigidity to the backbone, which manifests in the strong scaling of domain sizes with total backbone length (Chapter 3-3), ultrahigh entanglement molecular weights (Chapter 3-4), and other physical phenomena. These architecture effects offer many advantages in the context of block polymer self-assembly, enabling the fabrication of structures with large domain sizes[5-7] and large grain sizes.[8] However, the relative bending rigidity also introduces one potential limitation: in general, densely grafted block polymers resist the interfacial curvature required to access non-lamellar morphologies. Brush diblock polymers with symmetric side chains exclusively self-assemble to 1D lamellar structures,[6,9] even at highly asymmetric compositions where analogous *linear* diblock polymers form 2D or 3D morphologies.[10-11]

Varying the molecular architecture can enable brush-like polymers to access non-lamellar morphologies: for example, cylinder, sphere, and gyroid phases have been recently identified for graft block polymers with asymmetric side chain lengths[9,12-15] or A-*branch*-B "Janus" architectures.[16] This section will describe another approach to modifying the chain connectivity: synthesizing **ABC** brush triblock terpolymers. Compared to AB diblock polymers, ABC triblock terpolymers vastly expand the parameter space for materials design. Whereas the phase behavior of AB diblock polymers can be captured by *three* independent parameters (the total degree of polymerization, N; the volume fraction of block A, $f_A = 1 - f_B$;

and the free-energy penalty to mixing blocks, χ_{AB}) the phase behavior of ABC triblock terpolymers requires *six* parameters for complete description: $N, f_A, f_B, \chi_{AB}, \chi_{BC}$, and χ_{AC}.[11,17] A rich phase space emerges. Figure 5.1 provides select examples of the variety of morphologies identified for linear ABC triblock terpolymers.

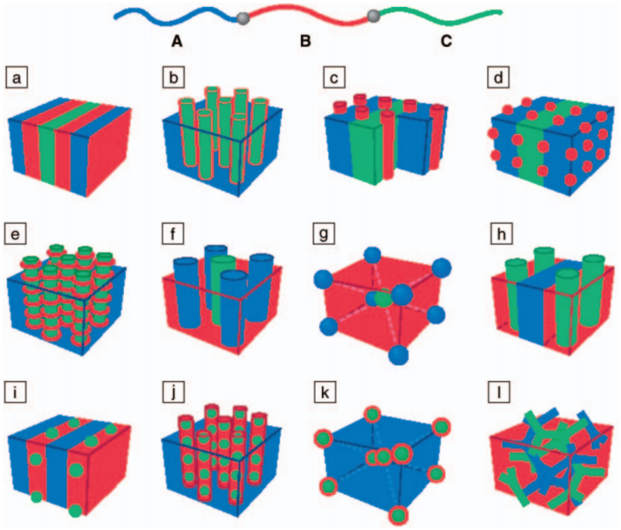

Figure 5.1: Schematic illustrations of the diverse morphologies identified for linear ABC triblock terpolymers. Variations in the block sequence and block volume fractions create an enormous parameter space for materials design. Reproduced with permission from Refs. 11 and 17.

The phase behavior of *linear* ABC triblock terpolymers has been extensively investigated through both theory[17-22] and experiments.[23-28] However, the phase behavior of *brush* ABC triblocks has not been systematically studied, in large part due to long-standing challenges associated with synthesizing well-defined materials. In this section, we present our work to close this gap. Bottlebrush triblock terpolymers with grafted poly(D,L-lactide) (L), polystyrene (S), and poly(ethylene oxide) (O) side chains were synthesized by living ring-opening metathesis polymerization (ROMP). (Further synthetic information can be found in Appendix C-2.) Sequential ROMP provides a robust, modular strategy to tune key elements of the molecular architecture (Scheme 5.1): (1) the block sequence (LSO, LOS, or LSO, via the order of addition), (2) the backbone degrees of polymerization (N_A, N_B, and N_C, via the equivalents of each macromonomer to the catalyst), and (3) the side chain degrees of polymerization (*x, y*, and *z*, via the macromonomer molecular weights). This extensive synthetic tunability enables systematic studies of influence of molecular architecture on ABC brush triblock terpolymer self-assembly.

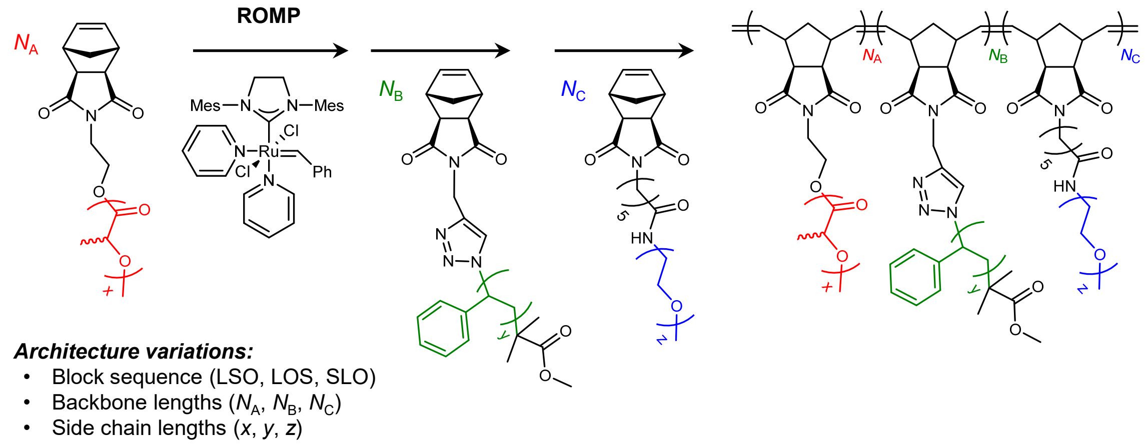

Architecture variations:
- Block sequence (LSO, LOS, SLO)
- Backbone lengths (N_A, N_B, N_C)
- Side chain lengths (x, y, z)

Scheme 5.1: Synthesis of LSO brush triblock terpolymers by ring-opening metathesis polymerization (ROMP). The block sequence, backbone lengths, and side chain lengths can be readily varied.

Scheme 5.1 presents the synthesis of brush LSO. The relative values of the three binary interaction parameters impose $\chi_{AB} > \chi_{BC} > \chi_{AC}$ (where $\chi_{AB} \equiv \chi_{LS}$, $\chi_{BC} \equiv \chi_{SO}$, and $\chi_{AC} \equiv \chi_{LO}$). This choice of block chemistry and sequence introduces morphological frustration. In this frustrated system, the highest-χ interactions occur between adjacent blocks (A/B and B/C). Chain connectivity requires adjacent blocks to share domain interfaces, but the large enthalpic penalties to mixing A/B and B/C segments instead favor the formation of A/C interfaces. Because the A and C blocks are not directly connected, accommodating A/C interfaces while minimizing A/B and B/C contacts favors the formation of 2D and 3D morphologies. Figure 5.2 presents the ternary phase diagram for reported *linear* ABC triblock terpolymers that experience the same type of morphological frustration as brush LSO. (Data were compiled for linear polystyrene-*b*-polybutadiene-*b*-poly(methyl methacrylate) (SBM)[24,29-32] and polystyrene-*b*-poly(ethylene-*co*-butadiene)-*b*-poly(methyl methacrylate [S(EB)M][23-24,32-34]). A rich variety of exotic morphologies emerge as a consequence of frustration, such as helices on spheres, core-shell cylinders, and knitting patterns.

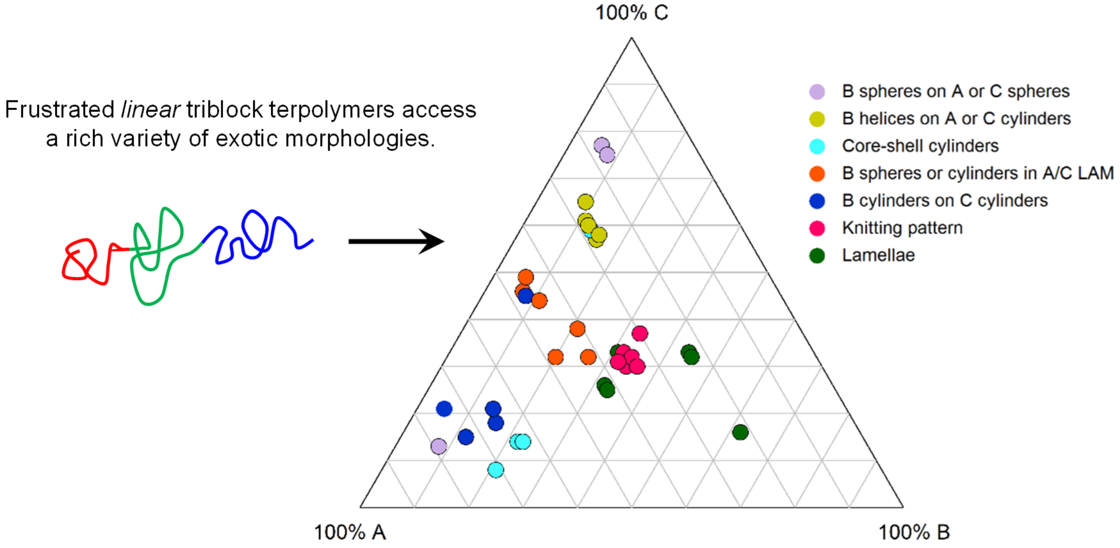

Figure 5.2: Ternary phase diagram for reported *linear* ABC triblock terpolymers with similar frustration (Type II) as LSO. The vertices each represent 100% pure A, B, or C by volume; moving away from a vertex in any direction represents decreasing the volume fraction of the corresponding component. The examples include linear PS-*b*-PB-*b*-PMMA and PS-*b*-P(E-*co*-B)-*b*-PMMA triblocks, compiled from Refs. 23–24 and 29–34.

Can densely grafted bottlebrush triblock terpolymers access similar morphologies? Previous work suggests that the increased bending rigidity of bottlebrush polymers relative to linear analogues strongly disfavors the interfacial curvature required by non-lamellar morphologies. In this context, potential conflicts between the molecular architecture and morphological frustration arise in LSO brush triblock terpolymers.

We synthesized >100 unique LSO brush triblock terpolymers via living ROMP (Scheme 5.1). The total backbone degree of polymerization was fixed ($N_{\mathrm{bb}} = 80$), and the block volume fractions ($f_{\mathrm{A}}, f_{\mathrm{B}}$) were varied across the entire composition space. Unlike linear block polymers, brush block polymers feature two independent handles to tune the composition (*i.e.*, the backbone block lengths and side chain lengths). The brush LSO samples comprised five variations in the side chain molecular weights: [2-2-2], [2-2-3], [2-2-5], [5-2-2], and [5-2-3], where each [M_{L}, M_{S}, M_{O}] indicates the side chain molecular weight in kg/mol. All samples were annealed at 140 °C under modest applied pressure, and the ordered structures that developed were identified by synchrotron small-angle X-ray scattering (SAXS). (See Appendix C-6 for further SAXS information.)

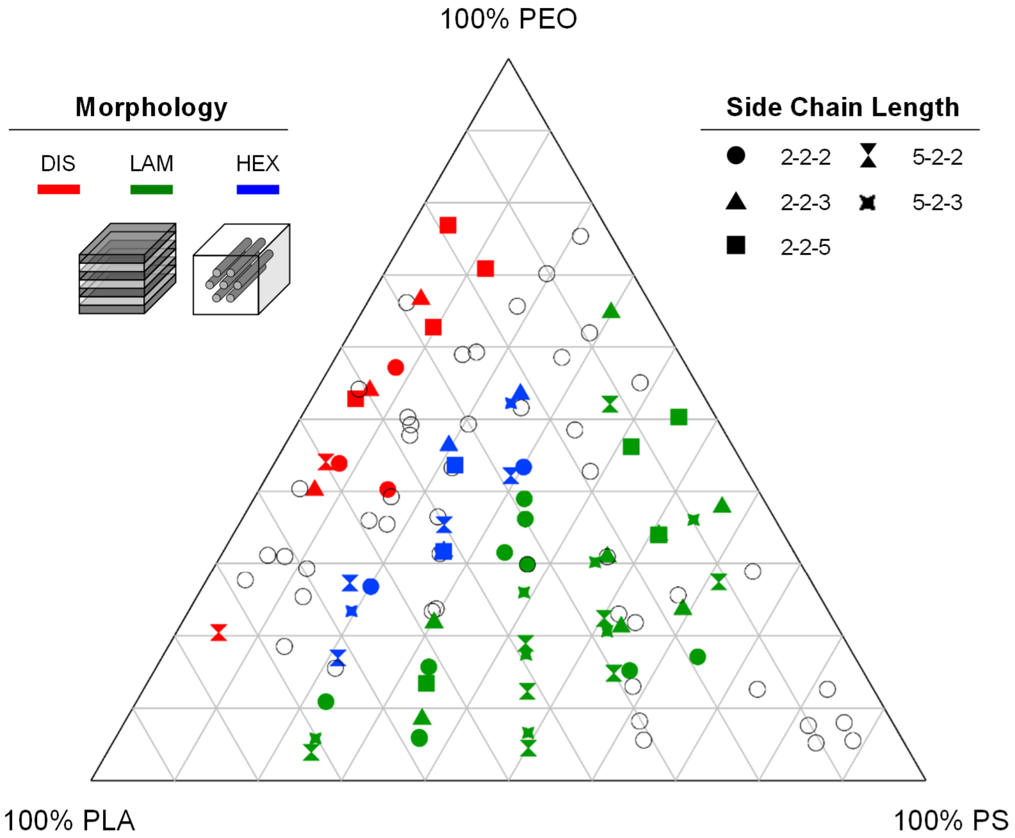

Figure 5.3: Ternary phase diagram for LSO brush triblock terpolymers. The vertices each represent 100% pure PLA (L), PS (S), or PEO (O) by volume. Each symbol represents a brush LSO triblock synthesized, annealed, and studied by SAXS. The colors indicate different morphologies: (*red*) disordered, (*green*) lamellar, (*blue*) hexagonally packed cylinders. The shapes indicate different side chain lengths: in the legend on the right, each triplet indicates [M_L, M_S, and M_O], where M_i is the number-average molecular weight (in kg/mol) of each side chain *i*. Unfilled symbols indicate samples that could not be unambiguously assigned by SAXS.

Figure 5.3 presents the ternary phase diagram for LSO brush triblock terpolymers. Colored symbols represent the different morphologies identified by SAXS, while unfilled symbols indicate samples that could not be unambiguously assigned. Different shapes indicate different combinations of side chain molecular weights. The assigned structures correlate with the composition, leading to narrow regions of disordered materials (DIS, $f_{PS} \approx 0$) and hexagonally packed cylinders (HEX, $f_{PS} \approx 0.25$) as well as a wide swath of lamellae (LAM, $f_{PS} > 0.25$).The phase behavior does not appear to be influenced by the way in which the composition is varied: that is, despite potential differences in the relative backbone lengths and/or side chain lengths, LSO brush triblock terpolymers with similar block volume fractions assemble to the same morphology. This observation is perhaps surprising, since side chain length asymmetry strongly influences the phase behavior of brush *diblock* polymers.[9,12-15] Further increasing the side chain asymmetry may produce similar effects in brush LSO.

In contrast to linear ABC triblock terpolymers, for which a rich variety of morphologies are observed (Figures 5.1–5.2), the brush LSO triblock terpolymers studied herein only assemble to HEX or LAM. The bottlebrush architecture appears to disfavor non-lamellar morphologies, in spite of frustration favoring curved interfaces (*i.e.*, minimal A/B and B/C contacts). Chapter 4 reported our discovery of a unique partially mixed lamellar morphology ($\mathrm{LAM_P}$) in select LSO triblocks. Partial mixing may allow compromises between the demands of the bottlebrush architecture and the enthalpic preference for A/C contacts. Transmission electron microscopy (TEM), self-consistent field theory (SCFT), and the unusual trend in the lamellar period with total molecular weight all provide compelling evidence that the reported LSO-N_C ($52 \leq N_\mathrm{bb} \leq 70$) triblocks all assemble to $\mathrm{LAM_P}$. We note however that the LSO-N_C series is not representative of all LAM materials in Figure 5.3. First, N_bb is shorter among the LSO-N_C series; second, whereas the composition window for LSO-N_C is narrow ($0.5 < f_\mathrm{PLA} < 0.6$, $0.3 < f_\mathrm{PS} < 0.4$), the LAM region spans a very wide range of compositions ($0.05 < f_\mathrm{PLA} < 0.7$, $0.3 < f_\mathrm{PS} < 0.7$). Whether all or merely some of the LAM materials identified in Figure 5.3 are $\mathrm{LAM_P}$ (rather than conventional unmixed $\mathrm{LAM_2}$ or $\mathrm{LAM_3}$) must be confirmed by TEM or additional X-ray scattering experiments.

Narrow regions of DIS and HEX appear in the ternary phase diagram as the volume fraction of PS decreases. HEX emerges when $f_\mathrm{PS} \approx 0.25$. Partial mixing is likely, featuring minority PS cylinders in a matrix of PLA/PEO. When $f_\mathrm{PS} \approx 0$ (*i.e.*, LSO resembles LO), the materials are disordered. This is consistent with the extremely low — potentially even negative — value of χ_LO. Actual literature estimates for χ_LO range from 0.0038 to −0.161 depending on end groups and measurement techniques.[35-36] In the previous chapter, we proposed that the magnitude of χ_LO, beyond simple frustration effects, drives the formation of $\mathrm{LAM_P}$ (Chapter 4-2 and 4-6). The consequences of low-χ design clearly also emerge in the full brush LSO phase diagram.

5-1.2 SLO and LOS Brush Triblock Terpolymers

In addition to brush LSO, we also synthesized and studied brush SLO and brush LOS triblock terpolymers. Changing the block sequence changes the type of morphological frustration imposed by the relative binary interaction parameters (Figure 5.4).[25] LSO features the lowest-χ interactions between the end blocks (χ_{LO}) and therefore Type II frustration. Switching the order of the first two blocks produces SLO triblock terpolymers with Type I frustration ($\chi_{\mathrm{AB}} > \chi_{\mathrm{AC}} > \chi_{\mathrm{BC}}$), which favors end-block contacts over some but not all contacts between adjacent blocks. Lastly, the third unique permutation produces LOS triblock terpolymers that do not experience morphological frustration ($\chi_{\mathrm{AC}} > \chi_{\mathrm{BC}} > \chi_{\mathrm{AB}}$).

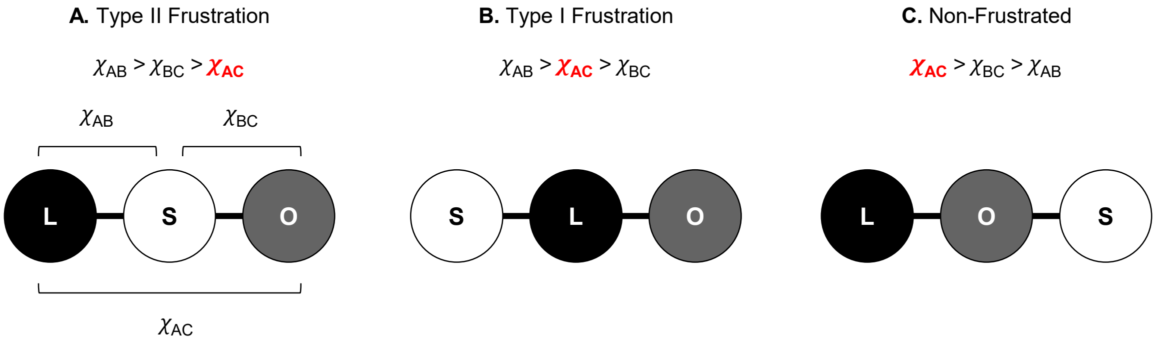

Figure 5.4: ABC triblock terpolymers can be classified according to the relative magnitude of χ_{AC}. (*A–C*) Each circle above represents a block, connected A-B-C from left to right. The contrast between circles represents the relative magnitude of χ; that is, black and white is the highest-contrast pair and therefore represents the highest-χ interaction in the system. (*A*) If χ_{AC} is the smallest interaction parameter, the system experiences Type II frustration. (*B*) If χ_{AC} is larger than one of, but not both, χ_{BC} and χ_{AB}, the system experiences Type I frustration. (*C*) If χ_{AC} is the largest interaction parameter, the system is non-frustrated.

SLO and LOS brush triblocks were synthesized by living ROMP. The total backbone degree of polymerization ($N_{\mathrm{bb}} = 80$) and the side chain molecular weights were fixed, while the compositions were varied via the relative backbone lengths. All samples were thermally annealed and characterized by SAXS. The resulting ternary phase diagrams for brush SLO and brush LOS are provided in Figure 5.5A and 5.5 B, respectively. As for brush LSO, only HEX and LAM morphologies are observed, likely as a consequence of the extended bottlebrush architecture. However, because the PLA and PEO blocks are adjacent in SLO and LOS, partial PLA/PEO mixing (if any) may play a different role than in LSO.

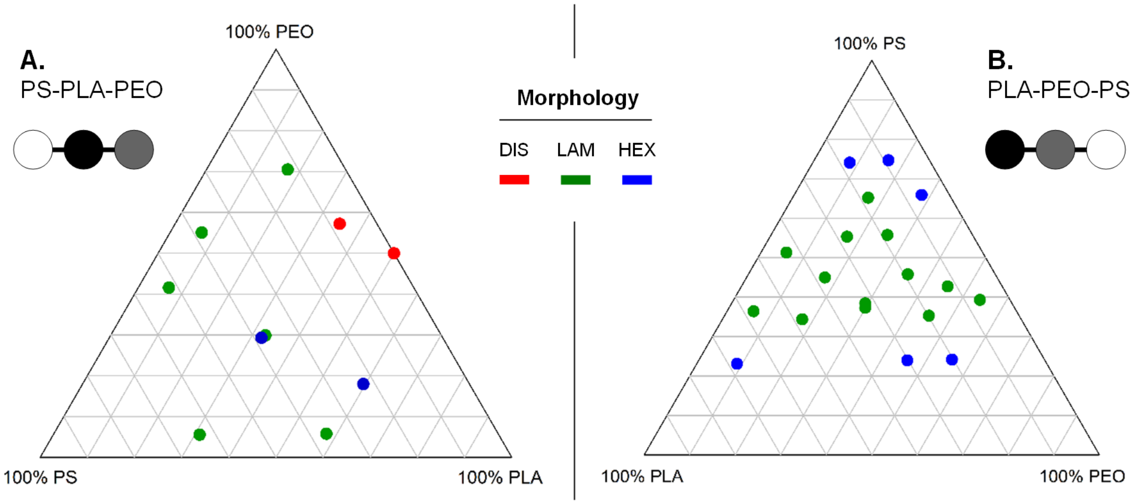

Figure 5.5: Ternary phase diagrams for (*A*) brush SLO and (*B*) brush LOS triblock terpolymers. The colors indicate different morphologies: (*red*) disordered, (*green*) lamellar, (*blue*) hexagonally packed cylinders.

Collectively, these studies of LSO, SOL, and LOS brush triblock terpolymers provide insights into the roles of molecular architecture and morphological frustration in block polymer self-assembly. Consistent with previous reports of related brush diblock polymers, the bottlebrush architecture appears to strongly favor lamellar morphologies: LAM is observed across wide swaths of the composition space (Figures 5.3 and 5.5), even at highly asymmetric compositions where analogous linear block polymers would assemble to 2D or 3D morphologies (Figures 5.1–5.2). This result reinforces a recurring theme of this thesis: namely, densely grafted brush polymers adopt rigid, extended conformations relative to their linear analogues. However, brush polymers should not be considered rigid rods: although the bending rigidity of the backbone appears to largely resist interfacial curvature in brush LSO, SOL, and LOS, exceptions emerge in the formation of HEX morphologies. Future work will perform complementary SAXS, TEM, and SCFT studies to expand our understanding of the dialogue between architecture and frustration in these materials.

5-2 Potential Non-Equilibrium Behavior

The preceding discussion assumes that equilibrium morphologies are attained for brush triblock terpolymers. Although SCFT calculations suggest that LAM_P is at equilibrium with experimentally relevant values of χ and f, experimental proof is currently limited by our inability to access the order-disorder transition temperature (T_{ODT}). SAXS data obtained upon heating a LAM$_P$ sample (LSO with $N_A = 25$, $N_B = 22$, $N_C = 5$) from 25 to 200 °C indicate that LAM$_P$ is thermally stable throughout the entire experimentally accessible temperature range (Figure 5.6). Consistent with other reports of high-molar-mass bottlebrush polymers,[5,37] no T_{ODT} is observed below the onset of decomposition, preventing careful annealing and quench studies originating from the disordered state.

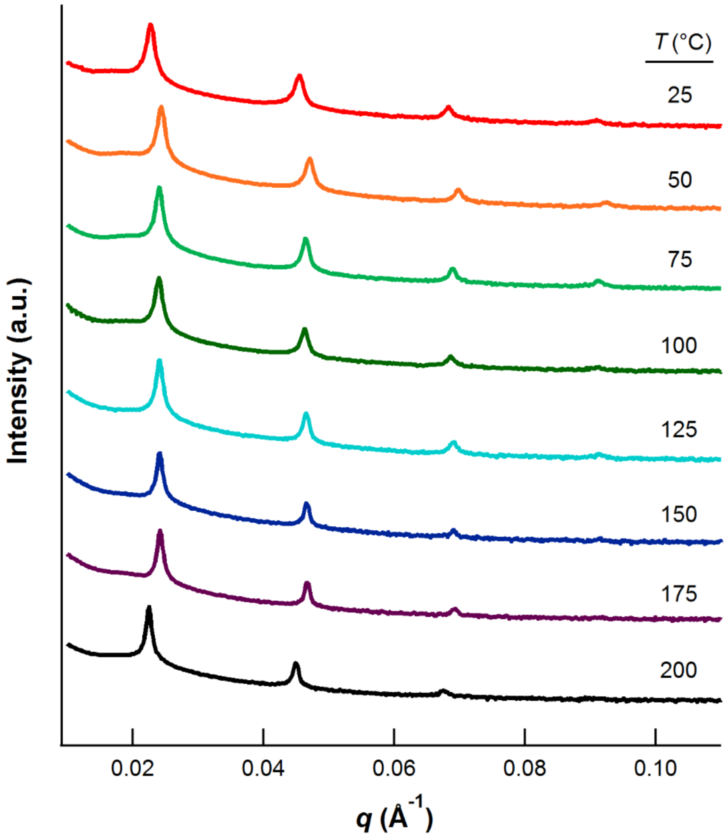

Figure 5.6: SAXS data for an LSO brush triblock terpolymer ($N_A = 25$, $N_B = 22$, $N_C = 5$) obtained upon heating from 25 to 200 °C at 1 °C/min. The lamellar morphology (LAM$_P$) is stable throughout the entire experimentally accessible temperature range. d^* varies slightly (<5%) over this range. No order-disorder transition is observed at any temperature below the onset of decomposition.

All LSO samples exhibit similar behavior, although low-molecular-weight samples suggest that non-equilibrium effects may in fact exist. When N_{C} is large (*e.g.*, LSO-14, Figure 5.7A), no significant changes are observed throughout the heating and cooling cycle. However, when N_{C} is short, additional peaks appear upon cooling that suggest minor higher-symmetry contributions (*e.g.*, LSO-4, Figure 5.7B). These N_{C}-dependent observations are consistent with at least some LSO samples exhibiting persistent metastability close to a phase boundary rather than true equilibrium.[38] Since SCFT is an equilibrium theory, such deviations from equilibrium would affect the agreement between experimentally measured results and predicted behavior.

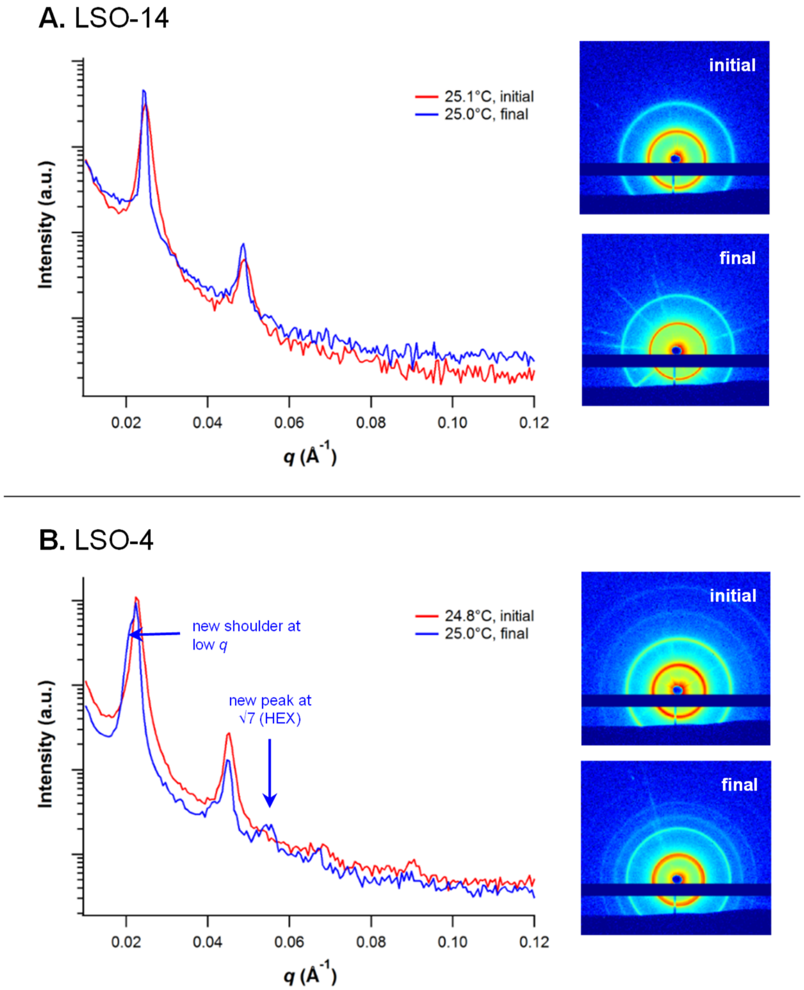

Figure 5.7: Variable-temperature SAXS measurements for (*A*) LSO-14 and (*B*) LSO-4. Samples were heated without pressure at 2 °C/min from 25 to 200 °C, then cooled back to 25 °C at 2 °C/min. Red and blue traces correspond to measurements before and after heating, respectively. (*A*) When N_{C} is long, the peaks become sharper on heating, but otherwise no changes are observed with temperature. (*B*) When N_{C} is short, features consistent with HEX emerge on heating.

To further examine potential non-equilibrium effects, because morphologies for multiblock polymers can be highly sensitive to processing conditions,[39-40] an LSO brush triblock terpolymer ($N_A = 25$, $N_B = 22$, $N_C = 5$) was annealed in four different ways: thermal annealing under pressure, thermal annealing without pressure, drop casting, and channel die alignment. All approaches afforded self-assembled morphologies with virtually identical LAM$_P$ geometry and periodicity (± 0.5 nm) (Figure 5.8). These results are reported while acknowledging studies of linear multiblock polymers that highlight the potential influence of processing path on the formation of kinetically trapped structures,[38,41] which may be mistaken for equilibrium. Previously, ABC block polymer morphologies containing partially mixed regions have indeed been predicted[20] and observed[42] as metastable defect states kinetically trapped upon casting from preferential solvents, but these examples were easily annihilated during the type of extended thermal treatments performed herein to anneal LSO. Equilibrium or not, the morphological attributes of LAM$_P$ are long-lived, in contrast to and notably distinct from prior materials.

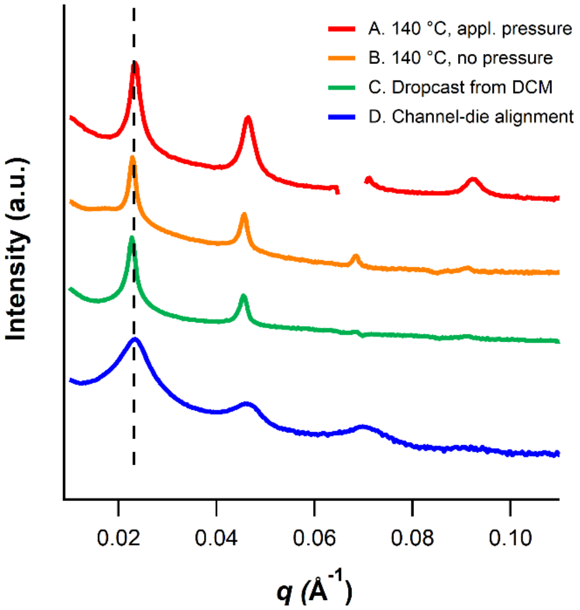

Figure 5.8: Azimuthally integrated 1D SAXS data for an LSO triblock terpolymer ($N_A = 25$, $N_B = 22$, $N_C = 5$) annealed in four different ways: (*A*) Thermally annealed at 140 °C between Kapton under modest applied pressure; (*B*) thermally annealed at 140 °C in a DSC pan with no applied pressure; (*C*) dropcast from DCM onto a glass cover slip; and (*D*) channel-die alignment at 140 °C. SAXS data corresponding to all methods indicate the same morphology (LAM) and period (± 0.5 nm). Note that the discontinuity at $q \approx 0.065$ Å^{-1} in (*A*) is due to a mask applied when averaging the raw 2D data.

5-3 Crystallization

5-3.1 Crystallization and Domain Spacing Trends

In the preceding chapter, we identified the screening of unfavorable PLA/PS contacts as the primary motivation for the unusual domain spacing trend observed in LSO-N_C brush triblock terpolymers. Due to preferential localization of PEO at the PLA/PS interface, when increasing backbone block lengths of PEO are installed from a parent LS diblock, the domain spacing *decreases* even though the total molecular weight increases. Chain pull-out due to molecular asymmetry is another potential factor (Chapter 4-7), but complementary resonant soft X-ray reflectivity (RSoXR) measurements and self-consistent field theory (SCFT) suggest that any chain pull-out effect is minor (Chapter 4-10). A third potential explanation for the unusual trend is crystallization, which we address in this section through wide-angle X-ray scattering (WAXS) measurements.

Little evidence of PEO crystallization is observed on the timescale of sample preparation and analysis. All characterization by SAXS was performed within three days of annealing. Variable-temperature WAXS measurements indicate that all LSO LAM$_P$ samples contain low crystalline weight fractions (<10 wt%) (Figure 5.9). (Further information about WAXS experiments can be found in Appendix C-10.) Densification upon PEO crystallization and concomitant domain contraction is therefore unlikely. The higher-molecular-weight O blocks in linear poly(isoprene-*b*-styrene-*b*-ethylene oxide) (ISO) and poly(styrene-*b*-isoprene-*b*-ethylene oxide) (SIO) triblock terpolymers would presumably accentuate this effect, yet both ISO and SIO show strong increases in d^* with N_C (Chapter 4-5).[43-45] Comparing LSO and LSL' provides further evidence that crystallization is not responsible for the unusual trend in d^*: while both LSO and LSL' exhibit decreasing d^* with increasing end block lengths, LSL' has no crystallizable components.

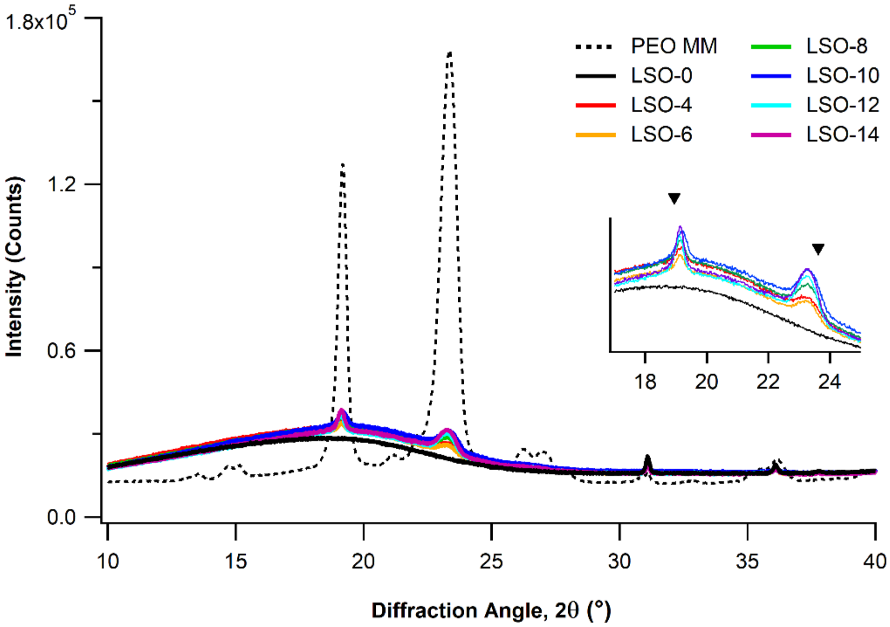

Figure 5.9: Wide-angle X-ray scattering (WAXS) data for the PEO macromonomer (MM, *i.e.,* linear PEO), brush PLA-PS parent diblock (LSO-0), and 6 selected LSO-N_C triblock terpolymers that self-assemble to LAM$_P$. (These data were obtained at 25°C; variable-temperature WAXS data is provided in Figure C.15.) Reflections at $2\theta = 19.1°$ and 23.2° for LSO-N_C (▼, inset) and PEO MM match the (120) and (032) reflections from a monoclinic PEO lattice.[46] The parent diblock (LSO-0), which contains no PEO, is amorphous as expected. Crystallization is suppressed in the LSO brush triblock terpolymers compared to neat PEO. (Note: Minor peaks at 31.1° and 36.1° are artifacts present in every sample due to the geometry of the stage.)

5-3.2 Crystallization Kinetics

Although little evidence of crystallization was observed three days after annealing, we note that the kinetics of crystallization are typically arrested in densely grafted brush polymers.[47-48] In order to assess the possibility that crystallization occurs over time, we performed synchrotron-source SAXS and WAXS measurements on the same LSO-N_C samples one year after the original measurements ($2 \leq N_C \leq 30$). The samples were stored at room temperature. The SAXS data collected both 3 days and 365 days after annealing are provided in Figure 5.10. WAXS data collected 365 days after annealing are also provided in Figure 5.10; however, since no evidence of crystallization was observed in any of the samples 3 days after annealing, the corresponding WAXS data are not included.

Figure 5.1 (Part 1/4): Raw 2D SAXS (*left, middle*) and WAXS (*right*) data for LSO-N_C brush triblock terpolymers. The same set of samples was measured either (*left*) 3 days after annealing or (*middle, right*) 365 days after annealing. N_C = (*A*) 2, (*B*) 4, (*C*) 6.

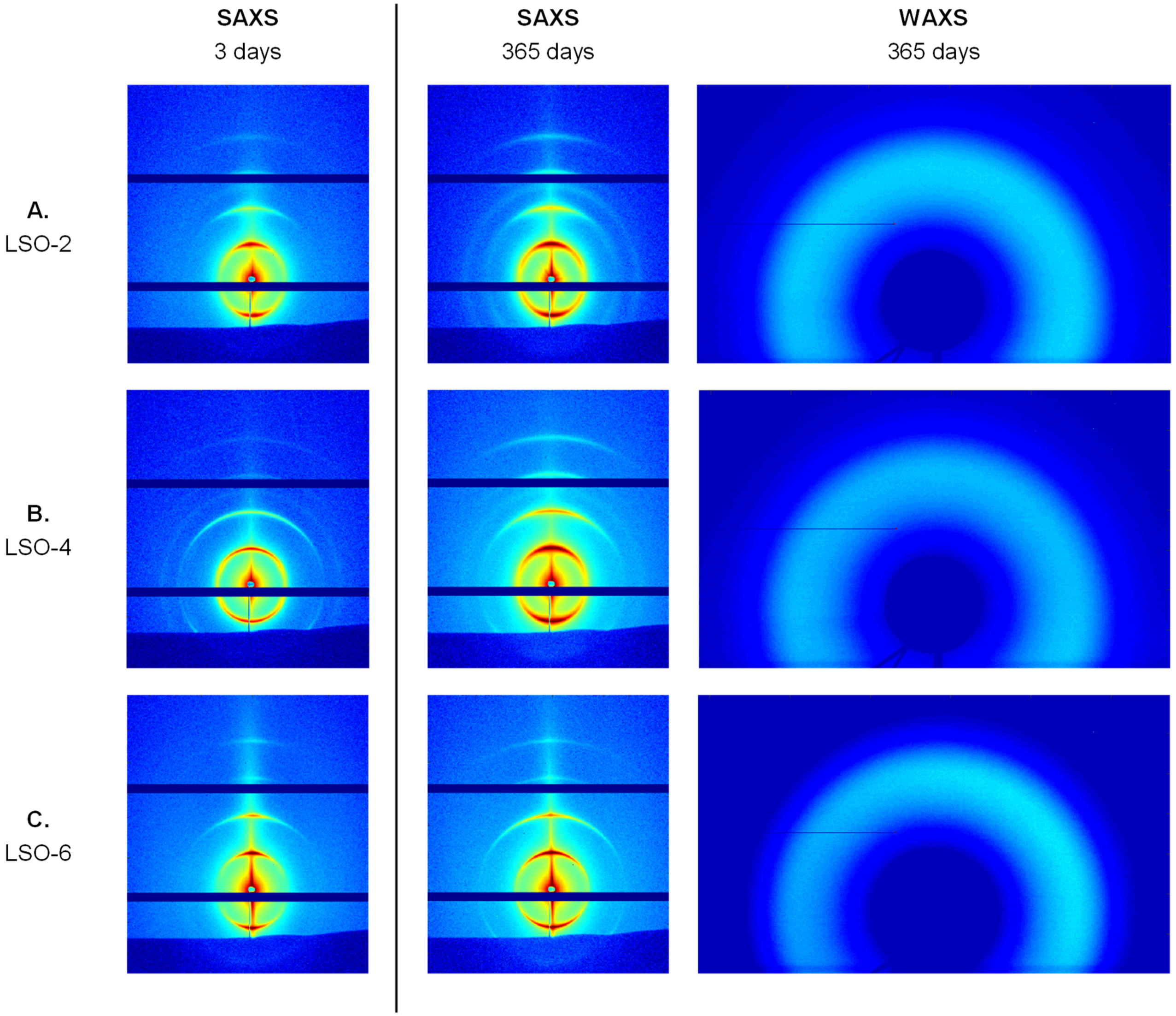

Figure 5.10 (Part 2/4): Raw 2D SAXS (*left, middle*) and WAXS (*right*) data for LSO-N_C brush triblock terpolymers. The same set of samples was measured either (*left*) 3 days after annealing or (*middle, right*) 365 days after annealing. N_C = (*D*) 8, (*E*) 10, (*F*) 12.

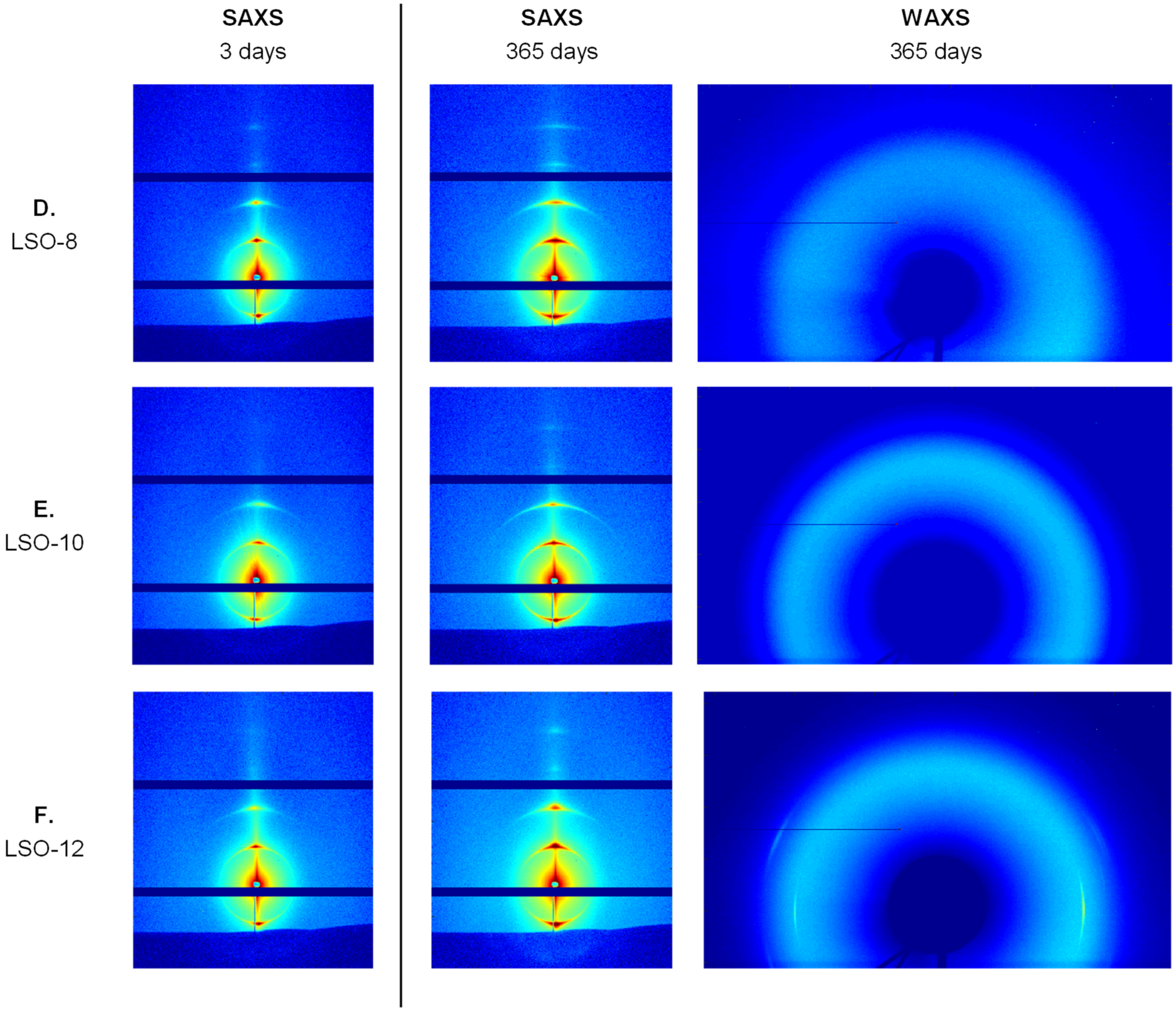

Figure 5.10 (Part 3/4): Raw 2D SAXS (*left, middle*) and WAXS (*right*) data for LSO-N_C brush triblock terpolymers. The same set of samples was measured either (*left*) 3 days after annealing or (*middle, right*) 365 days after annealing. N_C = (*G*) 14, (*H*) 16, (*I*) 20.

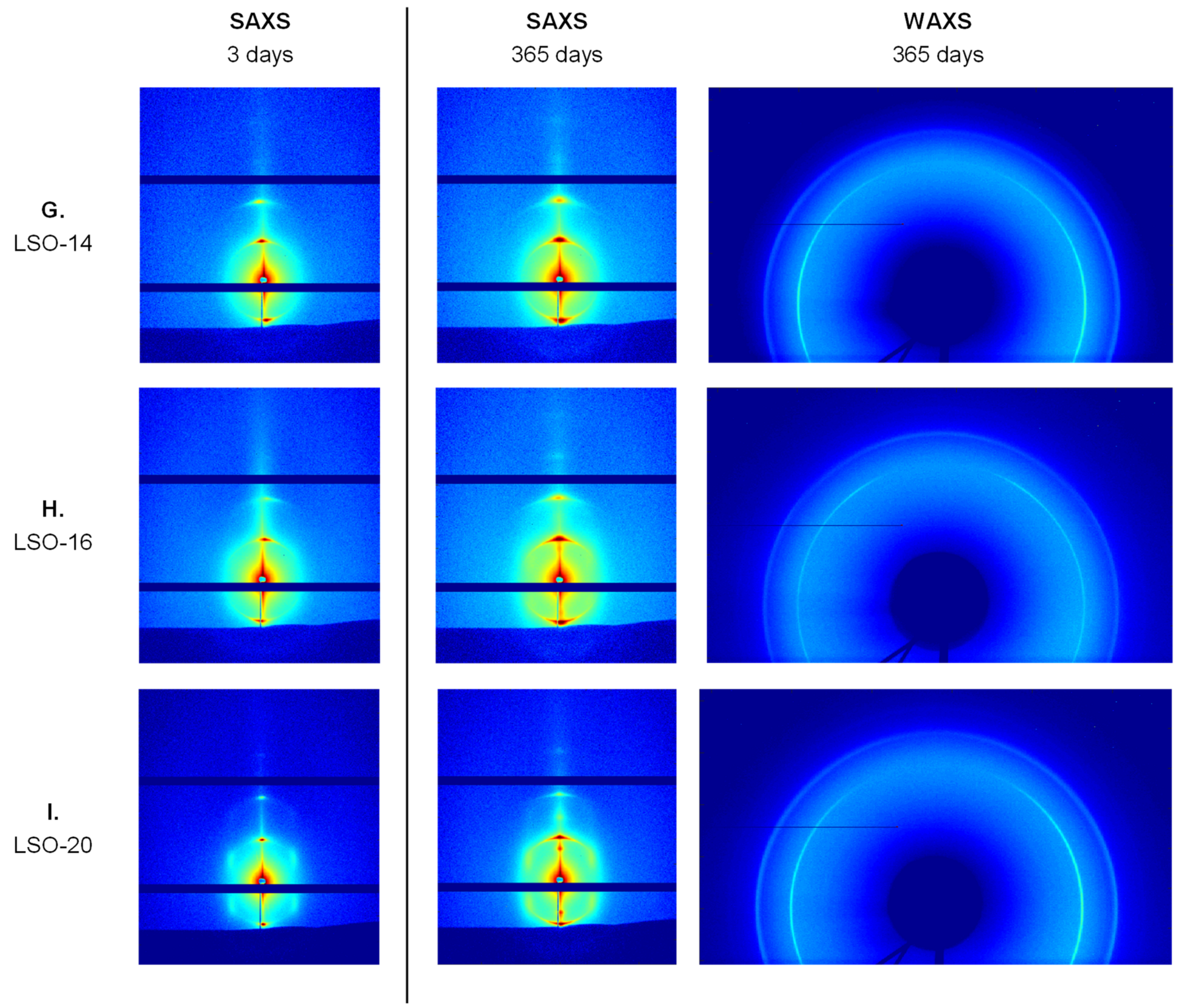

Figure 5.10 (Part 4/4): Raw 2D SAXS (*left, middle*) and WAXS (*right*) data for LSO-N_C brush triblock terpolymers. The same set of samples was measured either (*left*) 3 days after annealing or (*middle, right*) 365 days after annealing. N_C = (*J*) 24, (*K*) 26, (*L*) 30.

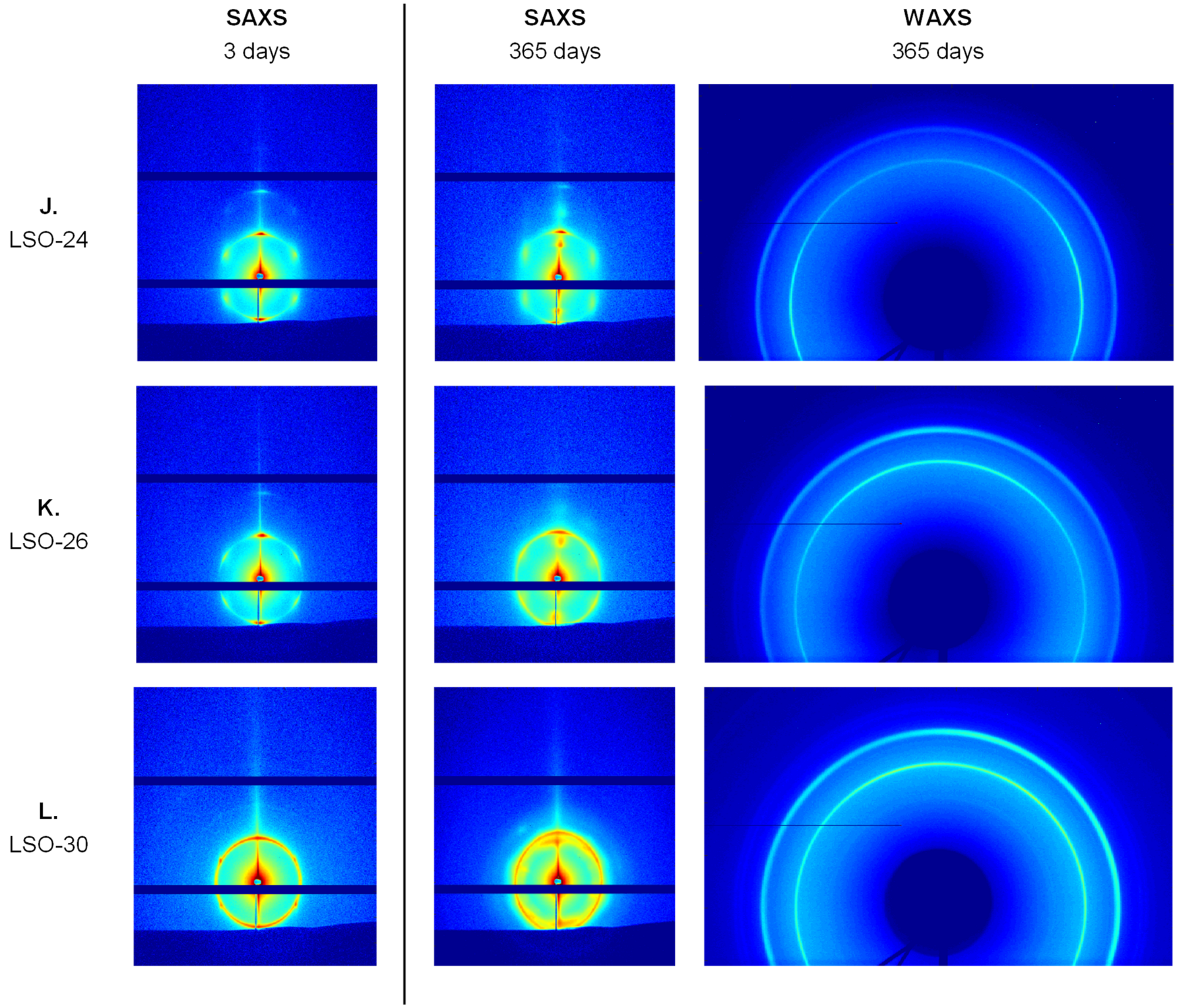

In the discussion of the SAXS and WAXS data presented in Figure 5.10, we will first discuss changes in the observed morphology over time, then comment on the onset of crystallization. We will then discuss potential confinement effects on the kinetics of crystallization. Lastly, we will interpret the orientation of PEO crystals in terms of confinement and the backbone orientation.

The SAXS data in Figure 5.10 indicate that, after aging for one year, each LSO-N_C sample generally retained its initial geometry: that is, $\mathrm{LAM_P}$ samples were still lamellar ($2 \leq N_C \leq 16$, Figure 5.10A–H), and samples that had HEX character ($20 \leq N_C \leq 30$, Figure 5.10I–L) still display HEX features. (We note that a new low-q peak appears for these HEX samples. TEM and additional X-ray scattering experiments are underway to confirm the morphology.) However, for samples with relatively long backbone lengths of the PEO block ($N_C \geq 14$), the domain spacing monotonically *decreases* as N_C increases. The values of d^* after one year, normalized to their values measured 3 days after annealing, are provided in Figure 5.11. We emphasize that this behavior is distinct from the unusual domain spacing trend identified in Chapter 4, since it manifests long after the initial data collection and analysis.

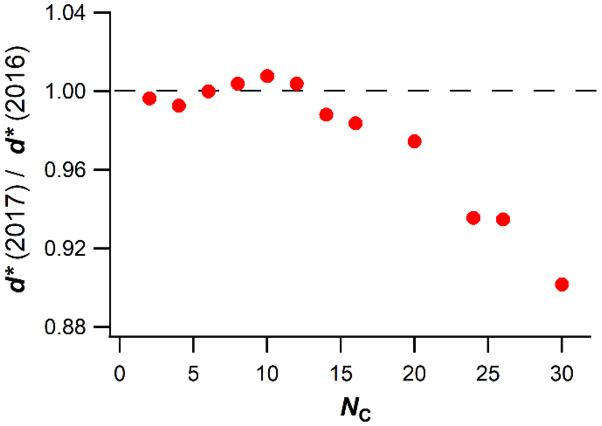

Figure 5.11: Changes in d^* over one year (2016–2017). $d^*(2017) / d^*(2016)$ is the ratio of d^* measured by SAXS 365 days after annealing and d^* measured 3 days after annealing. When the backbone length of the PEO block is short ($N_C \leq 12$), no significant change in d^* is observed over time. However, when N_C is long ($N_C \geq 14$), d^* decreases, concomitant with crystallization of the O blocks observed by WAXS.

The WAXS data indicate that the decrease in d^* is concomitant with the crystallization of PEO blocks. The azimuthally averaged WAXS data are provided in Figure 5.12. Peaks consistent with the (120) and ($\bar{1}32, 032, \bar{2}12, 112$) reflections of PEO crystals are observed for all LSO samples with $N_C \geq 14$ (at q = 1.36 and 1.67 Å^{-1}, respectively). These peaks can also be observed in the 2D WAXS data for LSO-12 (Figure 5.10F) but cannot be clearly distinguished in the 1D reduction because the peaks are relatively low-intensity compared to the amorphous scattering.

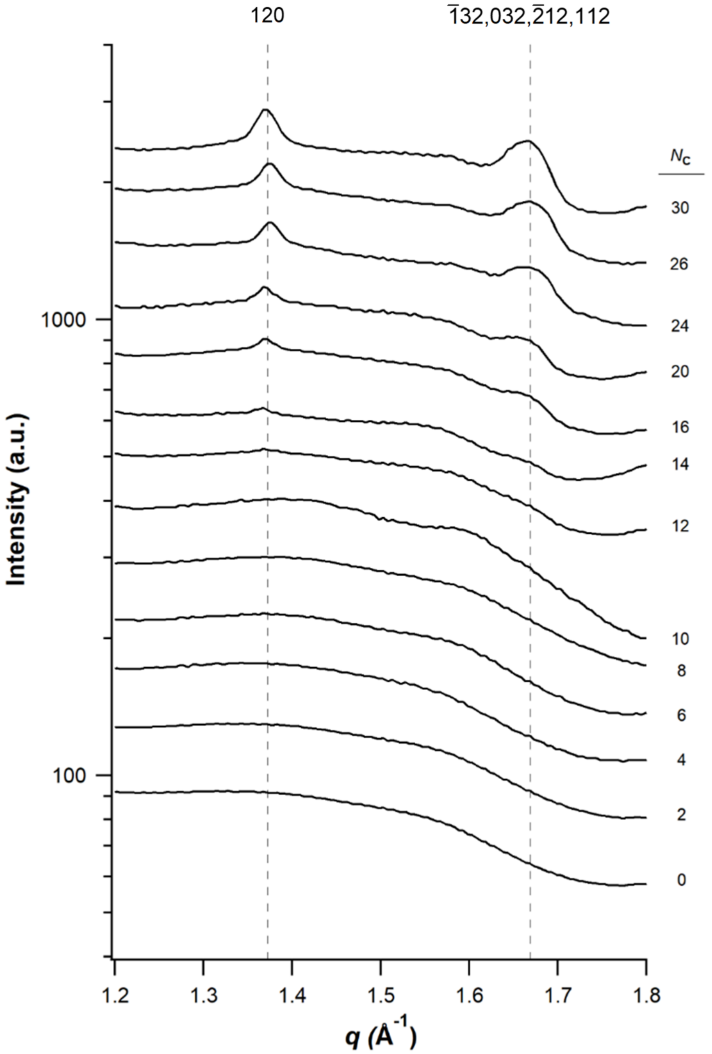

Figure 5.12: Azimuthally averaged 1D WAXS data for LSO-N_C, measured 365 days after annealing. Reflections consistent with PEO crystals are observed for $N_C \geq 14$ (120 at q = 1.36 Å^{-1}; $\bar{1}32, 032, \bar{2}12, 112$ at q = 1.67 Å^{-1}). Traces have been shifted vertically for clarity.

There are three potential factors influencing the slow kinetics of crystallization in brush LSO: the bottlebrush architecture, PLA/PEO mixing, and confinement. First, densely grafted brushes generally exhibit arrested crystallization kinetics. This influence will be discussed further in Chapter 6-2 in the context of PEO-containing electrolyte materials. Second, in the LAM$_\mathrm{P}$ morphology, the PLA and PEO end blocks are partially mixed. In order to form crystals, PEO blocks must be expelled from the mixed PLA/PEO phase. Depending on N_C, the mixed phase may be glassy at room temperature. The glass transition temperature (T_g) of the mixed phase monotonically decreases with increasing N_C, from 53 °C ($N_\mathrm{C} = 2$) to 3 °C ($N_\mathrm{C} = 30$). The observed onset of crystallization at $N_\mathrm{C} = 12$ after one year may be influenced by the value of T_g near room temperature ($T_\mathrm{g} = 30$ °C); for samples with $T_\mathrm{g} > 30$ °C, the kinetic barrier to demixing PEO from the PLA/PEO phase may prevent crystallization. Confined crystallization is a third important factor to consider.

5-3.3 Confined Crystallization and Chain Orientation

Three competing events determine the final morphology in amorphous-semicrystalline block polymers: microphase separation in the melt (T_ODT), crystallization of the crystallizable block (T_c), and vitrification of the amorphous block (T_g).[49-51] The values of T_ODT, T_c, and T_g determine the type of confinement: (1) hard confinement ($T_\mathrm{ODT} > T_\mathrm{g} > T_\mathrm{c}$); (2) soft confinement ($T_\mathrm{ODT} > T_\mathrm{c} > T_\mathrm{g}$); and (3) crystallization-induced microphase separation ($T_\mathrm{ODT} < T_\mathrm{c}$, $T_\mathrm{g} < T_\mathrm{c}$) (Figure 5.13).

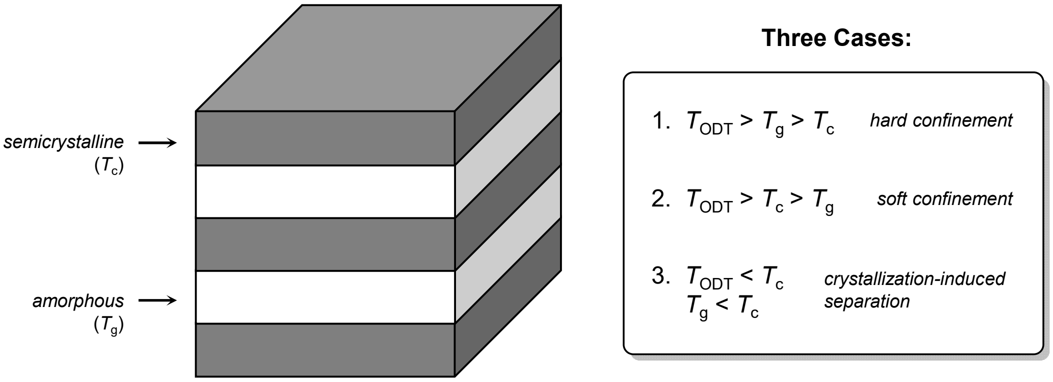

Figure 5.13: Potential types of confined crystallization in the self-assembly of block polymers with one amorphous block and one semicrystalline block. The glass transition temperature (T_g) of the amorphous block, together with the crystallization temperature (T_c) of the crystallizable block, determine three cases for confinement (*right*): hard, soft, and crystallization-induced microphase separation.

In the LSO system, T_{ODT} is thermally inaccessible but is at least greater than 200 °C (Figure 5.6). The T_{g} values of both amorphous blocks are high ($T_{\mathrm{g,PLA}} = 55$ °C, $T_{\mathrm{g,PS}} = 100$ °C) compared to the T_{c} of the crystallizable block (PEO, $T_{\mathrm{c}} = 20$ °C). This combination of relevant parameters indicates that crystallization of PEO in LSO triblock terpolymers occurs under hard confinement, strictly bounded by glassy PS domains. For similar reported PEO-containing block polymers, PEO crystallization is significantly slower under hard confinement than under soft confinement or in the absence of confinement.[52] In addition to the brush architecture and barrier to PLA/PEO demixing, confinement effects potentially contribute to the slow crystallization kinetics of brush LSO.

Depending on the bulk geometry and the domain sizes, confinement can also influence the orientation of crystals.[51,53] The lamellar morphology is the simplest confining geometry (Figure 5.14A). The 2D WAXS pattern for LSO-12 indicates that the PEO crystals are remarkably oriented (Figure 5.10F). In fact, the data closely resembles the *fiber* diffraction pattern for PEO crystals (Figure 5.12B).[51] Comparison of the 2D WAXS patterns for all LSO-N_{C} samples indicates that the orientation of the crystals changes as N_{C} increases.

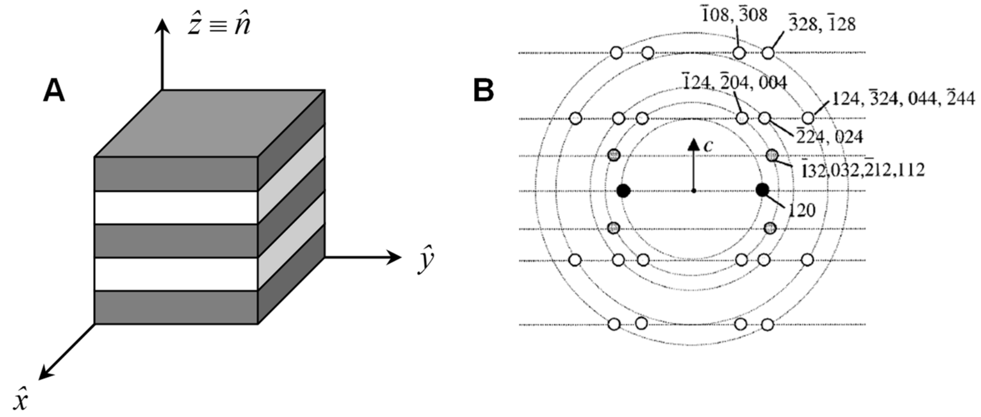

Figure 5.14: (*A*) Geometry of the wide-angle X-ray scattering stage. The lamellar normal $\hat{n}$ is parallel to $\hat{z}$ and perpendicular to the $\hat{x} - \hat{y}$ plane. Samples were measured with the X-ray beam along $\hat{x}$. (*B*) Fiber pattern of PEO crystals, constructed by rotating the reciprocal lattice along the *c*-axis. Adapted from Ref. 51 with permission from the American Chemical Society.

For confined crystallization in a lamellar geometry, two extremes of chain orientations exist with respect to the lamellar normal ($\hat{n}$). The chain direction (typically the crystal *c*-axis) can be oriented either parallel (homeotropic, Figure 5.15A) or perpendicular (homogeneous, Figure 5.15B) to $\hat{n}$. In the absence of confinement, the crystals typically exhibit no preferential orientation (Figure 5.15C). The homeotropic PEO crystal orientation has been proposed to be the most thermodynamically stable configuration, and it has been identified in various PEO-containing linear block polymers crystallized from dilute solution, including PEO-*b*-PS,[54] PEO-*b*-polyisoprene (PI),[55] and PEO-*b*-poly(butylene oxide) (PBO).[56] In contrast, the homogeneous crystal orientation is rare; most observations have been made for shear-aligned polyethylene-containing block polymers.[57-59]

The 2D WAXS pattern for LSO-12 is consistent with a homeotropic crystal orientation. This chain orientation for the PEO side chains strongly suggests that the brush backbone is oriented perpendicular to $\hat{n}$; that is, the PEO crystal orientation suggests that the backbone is highly oriented *parallel* to the PLA/PS domain interface (Figure 5.16A). The 2D WAXS images in Figure 5.10 indicate that, as the PEO backbone length increases to N_C = 24, the extent of orientation decreases but the PEO crystals generally remain homeotropically oriented. However, when $N_C = 26$, WAXS data suggests that the orientation switches, such that PEO crystals favor the homogeneous orientation and the brush backbones are aligned *perpendicular* to the PLA/PS domain interface (Figure 5.16B). Upon increasing to $N_C = 30$, the crystal orientation is isotropic, consistent with the observation of a HEX morphology by SAXS (Figure 5.16C).

The WAXS data suggests that the PEO block backbone in LSO-12 is strongly oriented *parallel* to the domain interface, introducing extreme bending at the block-block junction (Figure 5.16A). This observation is at first surprising, especially in the context of the discussion in Chapter 5-1, which indicates that the bottlebrush architecture generally disfavors to interfacial curvature. However, we note that significant backbone bending in brush LSO has been confirmed via the existence of looping PS midblocks (Chapter 4-10). Screening — the underlying physical motivation for backbone bending to form PS loops — likely also motivates the backbone bending inferred in crystalline LSO-12. Orienting the PEO block backbone parallel to the PLA/PS interface maximizes the number of PLA/PEO and PS/PEO contacts. The onset of crystallization would “lock in” this backbone orientation, resulting in a homeotropic crystal orientation. In turn, the homeotropic crystal orientation is thermodynamically favorable since it permits the growth of crystals parallel to the domain interface and therefore maximizes the possible crystallite size. However, as N_C increases, the entropic penalty to aligning the brush backbone along the interface may overwhelm the enthalpic screening advantages, resulting in the gradual loss of the homeotropic crystal orientation and eventually a transition to the homogeneous crystal orientation (Figure 5.16B).

A. *homeotropic: c-axis // $\hat{n}$*

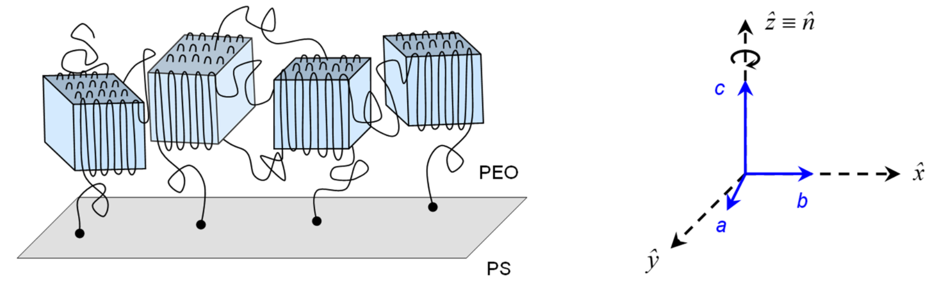

B. *homogeneous: c-axis ⊥ $\hat{n}$*

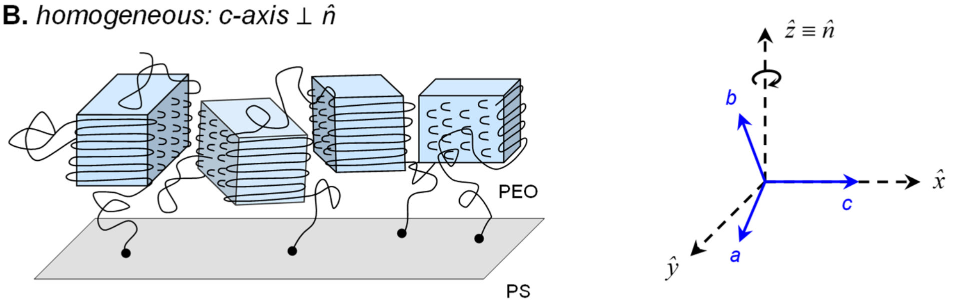

C. *random: isotropic*

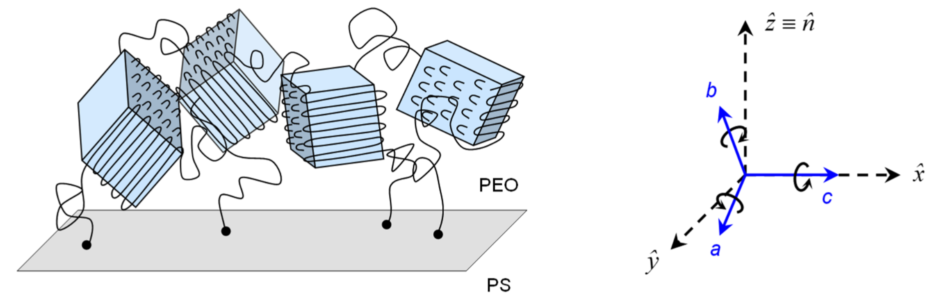

Figure 5.15: Schematic illustrations of orientations of PEO crystallites with respect to the lamellar normal, $\hat{n}$. The X-ray beam is along $\hat{x}$, and the gray planes represent the interface between PLA/PEO and PS domains. (*A*) Homeotropic alignment: the *c*-axis of the crystals is parallel to $\hat{n}$. (*B*) Homogeneous alignment: the *c*-axis is perpendicular to $\hat{n}$. (*C*) Random: no preferred orientation is observed.

Figure 5.16: Comparison of the (*left*) 2D WAXS data along $\hat{x}$, (*middle*) PEO crystal orientation, and (*right*) inferred brush backbone orientation. (*A*) $N_C = 12$: homeotropic alignment is observed. $c \parallel \hat{n}$ suggests that the PEO block backbone is orthogonal to $\hat{n}$. (*B*) $N_C = 26$: homogeneous alignment is observed. $c \perp \hat{n}$ suggests that the PEO block backbone is parallel to $\hat{n}$. (*C*) $N_C = 30$: random orientations are observed, consistent with the HEX morphology identified by SAXS.

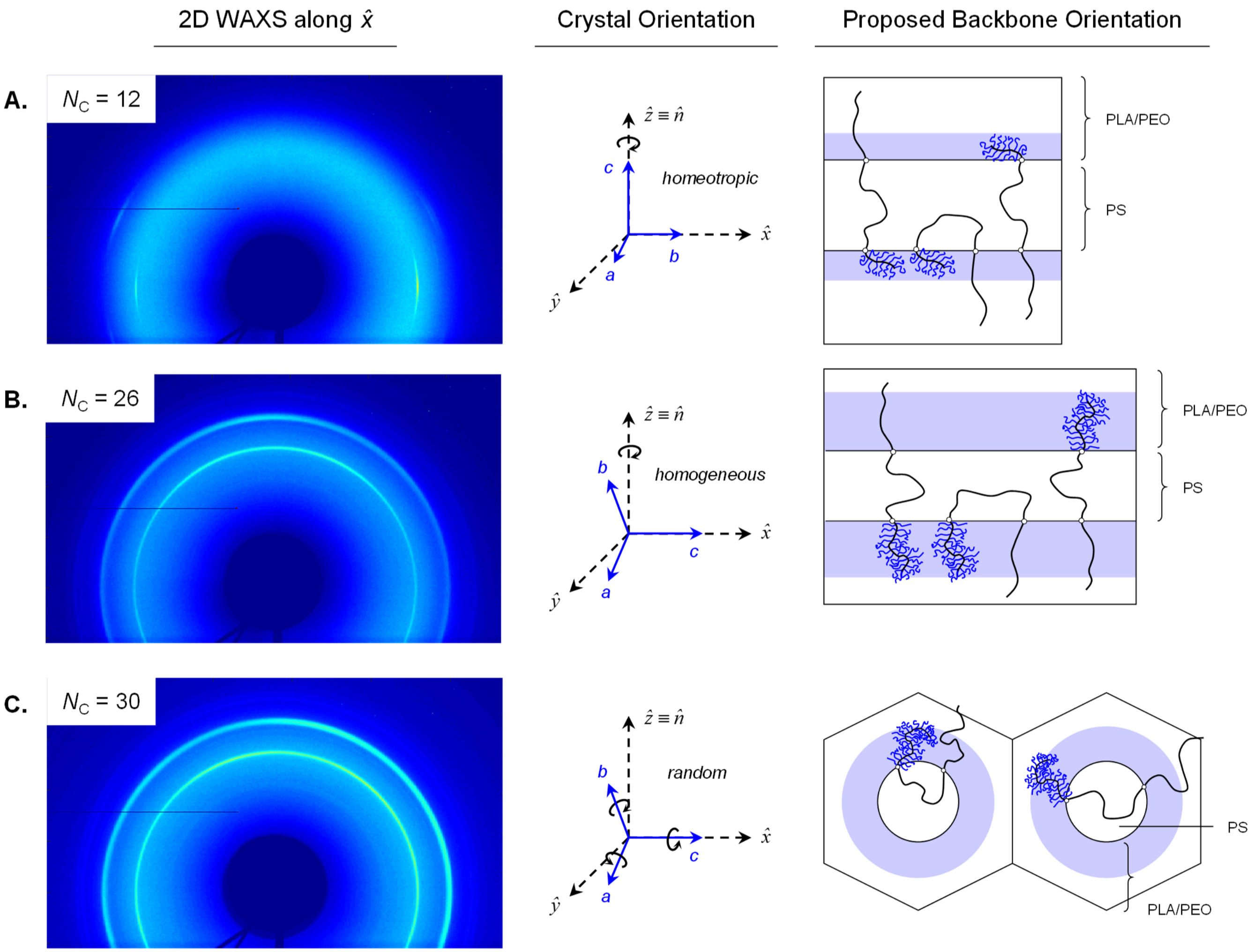

The crystallization of PEO in brush LSO triblock terpolymers reveals rich connections between the polymer dynamics, low-χ interactions, and chain orientation. Little evidence of crystallization was observed within several days of annealing, but after aging the samples at room temperature for one year, crystallization was observed for certain samples ($N_{\mathrm{C}} \geq 12$). The arrested crystallization kinetics in brush LSO reflect the interplay of the bottlebrush architecture, PLA/PEO demixing, and hard confinement effects. Confinement leads to orientation of the PEO crystals — and therefore the brush backbone — with respect to the lamellar geometry. To initial surprise, the crystal orientation suggests extreme backbone bending for short N_{C}. As described herein and in Chapter 4, low-χ interactions drive this unusual behavior, thereby overcoming the bending rigidity introduced by the bottlebrush architecture.

5-4 References

(1) Kikuchi, M.; Nakano, R.; Jinbo, Y.; Saito, Y.; Ohno, S.; Togashi, D.; Enomoto, K.; Narumi, A.; Haba, O.; Kawaguchi, S. *Macromolecules* **2015**, *48*, 5878–5886.
(2) Liang, H.; Cao, Z.; Wang, Z.; Sheiko, S. S.; Dobrynin, A. V. *Macromolecules* **2017**, *50*, 3430–3437.
(3) Paturej, J.; Sheiko, S. S.; Panyukov, S.; Rubinstein, M. *Sci. Adv.* **2016**, *2*, e1601478.
(4) Rathgeber, S.; Pakula, T.; Wilk, A.; Matyjaszewski, K.; Beers, K. L. *J. Chem. Phys.* **2005**, *122*, 124904.
(5) Xia, Y.; Olsen, B. D.; Kornfield, J. A.; Grubbs, R. H. *J. Am. Chem. Soc.* **2009**, *131*, 18525–18532.
(6) Rzayev, J. *Macromolecules* **2009**, *42*, 2135–2141.
(7) Sveinbjörnsson, B. R.; Weitekamp, R. A.; Miyake, G. M.; Xia, Y.; Atwater, H. A.; Grubbs, R. H. *Proc. Natl. Acad. Sci. U.S.A.* **2012**, *109*, 14332–14336.
(8) Song, D.-P.; Li, C.; Colella, N. S.; Xie, W.; Li, S.; Lu, X.; Gido, S.; Lee, J.-H.; Watkins, J. J. *J. Am. Chem. Soc.* **2015**, *137*, 12510–12513.
(9) Sveinbjörnsson, B. R. Self-Assembly of Brush Polymers. California Institute of Technology, 2014.
(10) Bates, F. S.; Fredrickson, G. H. *Annu. Rev. Phys. Chem.* **1990**, *41*, 525–557.
(11) Bates, F. S.; Fredrickson, G. H. *Phys. Today* **1999**, *52*, 32–38.
(12) Bolton, J.; Rzayev, J. *Macromolecules* **2014**, *47*, 2864–2874.
(13) Gai, Y.; Song, D.-P.; Yavitt, B. M.; Watkins, J. J. *Macromolecules* **2017**, *50*, 1503–1511.
(14) Runge, M. B.; Bowden, N. B. *J. Am. Chem. Soc.* **2007**, *129*, 10551–10560.
(15) Runge, M. B.; Lipscomb, C. E.; Ditzler, L. R.; Mahanthappa, M. K.; Tivanski, A. V.; Bowden, N. B. *Macromolecules* **2008**, *41*, 7687–7694.

(16) Kawamoto, K.; Zhong, M.; Gadelrab, K. R.; Cheng, L.-C.; Ross, C. A.; Alexander-Katz, A.; Johnson, J. A. *J. Am. Chem. Soc.* **2016**, *138*, 11501–11504.

(17) Zheng, W.; Wang, Z.-G. *Macromolecules* **1995**, *28*, 7215–7223.

(18) Kane, L.; Spontak, R. J. *Macromolecules* **1994**, *27*, 1267–1273.

(19) Bohbot-Raviv, Y.; Wang, Z.-G. *Phys. Rev. Lett.* **2000**, *85*, 3428–3431.

(20) Xia, J.; Sun, M.; Qiu, F.; Zhang, H.; Yang, Y. *Macromolecules* **2005**, *38*, 9324–9332.

(21) Tyler, C. A.; Qin, J.; Bates, F. S.; Morse, D. C. *Macromolecules* **2007**, *40*, 4654–4668.

(22) Liu, M.; Li, W.; Qiu, F.; Shi, A.-C. *Macromolecules* **2012**, *45*, 9522–9530.

(23) Auschra, C.; Stadler, R. *Macromolecules* **1993**, *26*, 2171–2174.

(24) Stadler, R.; Auschra, C.; Beckmann, J.; Krappe, U.; Voight-Martin, I.; Leibler, L. *Macromolecules* **1995**, *28*, 3080–3097.

(25) Bailey, T. S. Morphological behavior spanning the symmetric AB and ABC block copolymer states. University of Minnesota, 2001.

(26) Epps, T. H.; Cochran, E. W.; Bailey, T. S.; Waletzko, R. S.; Hardy, C. M.; Bates, F. S. *Macromolecules* **2004**, *37*, 8325–8341.

(27) Radlauer, M. R.; Sinturel, C.; Asai, Y.; Arora, A.; Bates, F. S.; Dorfman, K. D.; Hillmyer, M. A. *Macromolecules* **2016**, *50*, 446–458.

(28) Kumar, R.; Sides, S. W.; Goswami, M.; Sumpter, B. G.; Hong, K.; Wu, X.; Russell, T. P.; Gido, S. P.; Misichronis, K.; Rangou, S.; Avgeropoulos, A.; Tsoukatos, T.; Hadjichristidis, N.; Beyer, F. L.; Mays, J. W. *Langmuir* **2013**, *29*, 1995–2006.

(29) Krappe, U.; Stadler, R.; Voigt-Martin, I. *Macromolecules* **1995**, *28*, 4558–4561.

(30) Breiner, U.; Krappe, U.; Jakob, T.; Abetz, V.; Stadler, R. *Polym. Bull.* **1998**, *40*, 219–226.

(31) Brinkmann, S.; Stadler, R.; Thomas, E. L. *Macromolecules* **1998**, *31*, 6566–6572.

(32) Breiner, U.; Krappe, U.; Thomas, E. L.; Stadler, R. *Macromolecules* **1998**, *31*, 135–141.

(33) Breiner, U.; Krappe, U.; Stadler, R. *Macromol. Rapid Commun.* **1996**, *17*, 567–575.

(34) Ott, H.; Abetz, V.; Altstädt, V. *Macromolecules* **2001**, *34*, 2121–2128.

(35) Mao, H.; Hillmyer, M. A. *Macromol. Chem. Phys.* **2008**, *209*, 1647–1656.

(36) Lai, W.-C.; Liau, W.-B.; Lin, T.-T. *Polymer* **2004**, *45*, 3073–3080.

(37) Dalsin, S. J.; Rions-Maehren, T. G.; Beam, M. D.; Bates, F. S.; Hillmyer, M. A.; Matsen, M. W. *ACS Nano* **2015**, *9*, 12233–12245.

(38) Lipic, P. M.; Bates, F. S.; Matsen, M. W. *J. Polym. Sci., Part B: Polym. Phys.* **1999**, *37*, 2229–2238.

(39) Mori, K.; Hasegawa, H.; Hashimoto, T. *Polymer* **1990**, *31*, 2368–2376.

(40) Lodge, T. P.; Pudil, B.; Hanley, K. J. *Macromolecules* **2002**, *35*, 4707–4717.

(41) Chanpuriya, S.; Kim, K.; Zhang, J.; Lee, S.; Arora, A.; Dorfman, K. D.; Delaney, K. T.; Fredrickson, G. H.; Bates, F. S. *ACS Nano* **2016**, *10*, 4961–4972.

(42) Corté, L.; Yamauchi, K.; Court, F.; Cloître, M.; Hashimoto, T.; Leibler, L. *Macromolecules* **2003**, *36*, 7695–7706.

(43) Bailey, T. S.; Hardy, C. M.; Epps, T. H.; Bates, F. S. *Macromolecules* **2002**, *35*, 7007–7017.

(44) Meuler, A. J.; Ellison, C. J.; Qin, J.; Evans, C. M.; Hillmyer, M. A.; Bates, F. S. *J. Chem. Phys.* **2009**, *130*, 234903.

(45) Bailey, T. S.; Pham, H. D.; Bates, F. S. *Macromolecules* **2001**, *34*, 6994–7008.

(46) Takahashi, Y.; Tadokoro, H. *Macromolecules* **1973**, *6*, 672–675.

(47) Zhao, C.; Wu, D.; Huang, N.; Zhao, H. *J. Polym. Sci., Part B: Polym. Phys.* **2008**, *46*, 589–598.

(48) Bates, C. M.; Chang, A. B.; Momčilović, N.; Jones, S. C.; Grubbs, R. H. *Macromolecules* **2015**, *48*, 4967–4973.

(49) Loo, Y.-L.; Register, R. A.; Ryan, A. J. *Macromolecules* **2002**, *35*, 2365–2374.

(50) Schmalz, H.; Knoll, A.; Müller, A. J.; Abetz, V. *Macromolecules* **2002**, *35*, 10004–10013.

(51) Zhu, L.; Cheng, S. Z. D.; Calhoun, B. H.; Ge, Q.; Quirk, R. P.; Thomas, E. L.; Hsiao, B. S.; Yeh, F.; Lotz, B. *J. Am. Chem. Soc.* **2000**, *122*, 5957–5967.

(52) Zhu, L.; Mimnaugh, B. R.; Ge, Q.; Quirk, R. P.; Cheng, S. Z. D.; Thomas, E. L.; Lotz, B.; Hsiao, B. S.; Yeh, F.; Liu, L. *Polymer* **2001**, *42*, 9121–9131.

(53) Huang, P.; Zhu, L.; Guo, Y.; Ge, Q.; Jing, A. J.; Chen, W. Y.; Quirk, R. P.; Cheng, S. Z. D.; Thomas, E. L.; Lotz, B.; Hsiao, B. S.; Avila-Orta, C. A.; Sics, I. *Macromolecules* **2004**, *37*, 3689–3698.

(54) Lotz, B.; Kovacs, A. J.; Bassett, G. A.; Keller, A. *Kolloid-Z.u.Z.Polymere* **1966**, *209*, 115–128.

(55) Hirata, E.; Ijitsu, T.; Soen, T.; Hashimoto, T.; Kawai, H. *Polymer* **1975**, *16*, 249–260.

(56) Yang, Y.-W.; Tanodekaew, S.; Mai, S.-M.; Booth, C.; Ryan, A. J.; Bras, W.; Viras, K. *Macromolecules* **1995**, *28*, 6029–6041.

(57) Cohen, R. E.; Bellare, A.; Drzewinski, M. A. *Macromolecules* **1994**, *27*, 2321–2323.

(58) Hamley, I. W.; Patrick, J.; Fairclough, A.; Ryan, A. J.; Bates, F. S.; Towns-Andrews, E. *Polymer* **1996**, *37*, 4425–4429.

(59) Hamley, I. W.; Fairclough, J. P. A.; Terrill, N. J.; Ryan, A. J.; Lipic, P. M.; Bates, F. S.; Towns-Andrews, E. *Macromolecules* **1996**, *29*, 8835–8843.

Chapter 6

Applications of Bottlebrush Polymers in Functional Materials

1. Macfarlane, R. J.; Kim, B.; Lee, B.; Weitekamp, R. A.; Bates, C. M.; Lee, S. F.; Chang, A. B.; Delaney, K. T.; Fredrickson, G. H.; Atwater, H. A.; Grubbs, R. H. Improving Brush Polymer Infrared One-Dimensional Photonic Crystals via Linear Polymer Additives. *J. Am. Chem. Soc.* **2014**, *136*, 17374–17377.

2. Bates, C. M.; Chang, A. B.; Momčilović, N.; Jones, S. C.; Grubbs, R. H. ABA Triblock Brush Polymers: Synthesis, Self-Assembly, Conductivity, and Rheological Properties. *Macromolecules* **2015**, *48*, 4967–4973.

3. Bates, C. M.; Chang, A. B.; Schulze, M. W.; Momčilović, N.; Jones, S. C.; Grubbs, R. H. Brush Polymer Ion Gels. *J. Polym. Sci., Part B* **2016**, *54*, 292–300.

4. McNicholas, B. J.; Blakemore, J. D.; Chang, A. B.; Bates, C. M.; Kramer, W. W.; Grubbs, R. H.; Gray, H. B. Electrocatalysis of CO_2 Reduction in Brush Polymer Ion Gels. *J. Am. Chem. Soc.* **2016**, *138*, 11160–11163.

ABSTRACT

In the preceding chapters, we have discussed the design, synthesis, and self-assembly of graft block polymers. Robust synthetic methods have enabled the preparation of graft polymers toward a wide variety of applications in photonics,[1-3] drug delivery,[4-6] transport,[7-8] and thermoplastics.[9-10] This chapter will focus on applications of fully grafted bottlebrush block polymers as photonic crystals (Section 6-1) and solid polymer electrolytes (Section 6-2). Our work demonstrates the impacts of molecular architecture on the macroscopic properties of these materials, including the reflectivity, conductivity, and modulus. Key results have been rewritten and summarized here in order to support the central themes of this thesis: (1) ring-opening metathesis polymerization is a powerful strategy to synthesize well-defined graft polymers; (2) bottlebrush polymers have unique physical properties; and (3) these unique properties enable the design of new functional materials.

Table of Contents

6-1 Photonic Crystals

6-1.1 Introduction

Photonic crystals are ordered nanostructures that feature a periodic arrangement of domains with different refractive indices.[11-12] The spatial periodicity of the crystal determines the photonic band gap, which spans the range of frequencies in which light cannot propagate through the material. The simplest example of a photonic crystal is the one-dimensional multilayer stack. In a multilayer stack, each interface between layers reflects a certain amplitude and phase of incident light, and constructive interference results in resonant reflectivity. Traditionally, photonic crystals have been fabricated by complex top-down approaches, such as layer-by-layer deposition or co-extrusion, which require expensive equipment and limit applications to flat surfaces. The bottom-up self-assembly of bottlebrush block polymers provides an attractive alternative.

Polymer-based photonic crystals offer many advantages: they can be prepared from inexpensive materials, painted on any geometric surface, and designed to tune desired properties.[13-15] One key property of interest is the wavelength of reflection, λ. For a one-dimensional, two-component crystal, λ is determined by Bragg's law:

$$\lambda = 2(n_1 d_1 + n_2 d_2) \quad \text{Eq. 6-1}$$

where n_i and d_i are the refractive index and thickness, respectively, of domain i.[16] Most all-organic polymers have similar $n \approx 1.5$, such that $\lambda \approx 3d^*$ (where $d^* = d_1 + d_2$ is the lamellar period). In other words, the wavelength of reflected light increases linearly with d^*. In turn, d^* is controlled by the total polymer molecular weight (M, Figure 6.1):

$$\lambda \sim d^* \sim M^\alpha \qquad \text{Eq. 6-2}$$

The scaling exponent α is typically between 1/2 and 2/3 for symmetric linear block polymers, which represent the majority of systems developed as polymer photonic crystals. In comparison, α is significantly larger for bottlebrush block polymers ($\alpha \approx 0.9$). Steric repulsion between the densely grafted side chains causes the brush backbones to adopt extended conformations;[17] further discussion of the effects of grafting density on block polymer self-assembly can be found in Chapter 3-3.

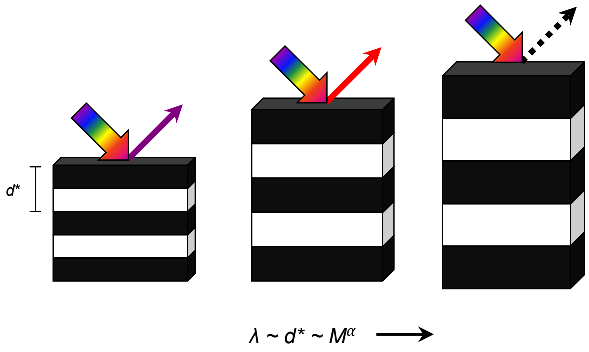

Figure 6.1: The wavelength of reflection (λ) increases linearly with the lamellar period (d^*), which in turn scales with the total block polymer molecular weight (M).

The stronger scaling of λ with M for bottlebrush polymers compared to linear polymers presents significant advantages in the context of photonic crystals. For most applications, the reflection of light at least in the visible spectrum is desired ($\lambda > 380$ nm). This requirement imposes a domain size minimum that is difficult to achieve via the synthesis and self-assembly of linear block polymers. For example, a photonic crystal that reflects blue light ($\lambda = 460$ nm) would require a linear block polymer with ultrahigh $M >$ 1 MDa.[15] The controlled synthesis of such ultrahigh-M linear block polymers is challenging, and chain entanglement presents a prohibitively high barrier to self-assembly. The unique architecture of brush polymers overcomes these challenges: λ increases strongly with M, and the extremely high entanglement molecular weights result in low viscosities[18-20] and rapid ordering kinetics.[21-22] Chapter 3-4 provides further discussion of the linear rheology of graft polymers.

Recent advances have reported the synthesis of well-defined, ultrahigh-M brush block polymers and their self-assembly to lamellar structures with unprecedentedly large domain sizes and grain sizes.[22-24] Brush block polymers can access sufficiently large d^* to reflect light throughout the visible spectrum and even into the near-infrared.[1,3,25-26] One ultimate goal is to prepare brush block polymer photonic crystals that reflect *infrared* radiation ($\lambda > 1200$ nm). These materials could be developed as heat-reflecting transparent coatings for energy-inefficient windows in buildings and other infrastructure. Reflecting infrared radiation would combat the urban heat island effect and dramatically reduce the costs and emissions associated with cooling.[27]

Despite the advantages of brush block polymers, several factors prevent potential applications from being realized in commercial settings:

1. The macromonomers required are expensive and challenging to synthesize.
2. Only short-range order is typically achieved.
3. The process does not allow post-synthetic modification to improve durability, reflectivity, and other film properties.

We have explored several design strategies to address these limitations. Three approaches will be summarized in this chapter. First, opportunities to tune d^* via the grafting density (z) will be described (Section 6-1.2). The scaling exponents α for graft block polymers with $0 \ll z < 1$ are typically similar to the exponent for fully grafted bottlebrush block polymers ($z = 1$); by decreasing z, less of the expensive macromonomer can be used to access similar d^*. Second, the self-assembly of polynorbornene block polymers with discrete monomers that exploit noncovalent interactions will described (Section 6-1.3). Lastly, blending graft block polymers and linear homopolymers will be described as a route to improve the optical properties of polymeric photonic crystals (Section 6-1.4).

6-1.2 Grafting Density

We recently reported the efficient synthesis of graft polymers with controlled grafting density (z), defined as the average number of polymer side chains per backbone repeat unit (Chapter 2). The scaling of d^* with the total backbone degree of polymerization depends on z, such that $d^* \sim N_{\mathrm{bb}}^{\alpha(z)}$ and $\alpha \sim z$ (Chapter 3-3).[17] The scaling of the zero-shear viscosity (η_0, strongly influenced by the onset of entanglements at the entanglement molecular weight, M_{e}) also affects self-assembly: ultrahigh viscosity, typical for linear polymers, leads to slower ordering kinetics and trapped metastable states. For the graft homopolymers described in Chapter 3-4, given similar N_{bb} and $M < M_{\mathrm{e}}$, the polymers have similar η_0 *regardless of grafting density.* In other words, η_0 closely tracks N_{bb}, not the number of side chains (zN_{bb}).

Combining these insights into the statics and dynamics of graft polymers guides the design of graft block polymers. Figure 6.2 provides an example. The scaling of d^* with N_{bb} for symmetric graft polymers with poly(D,L-lactide) (PLA) and polystyrene (PS) side chains was studied for $0 \leq z \leq 1$. (Further discussion can be found in Chapter 3-3.) For fully grafted bottlebrushes ($z = 1.0$), the scaling exponent α is large: $d^* \sim 1.033N_{\mathrm{bb}}^{0.858}$. As an illustrative example, given $N_{\mathrm{bb}} = 100$, d^* is predicted to be 54 nm (Figure 6.2A). The large domain sizes required for photonic properties can be accessed by increasing N_{bb}, but the dispersity typically increases and more of the expensive macromonomers is required. Instead of increasing N_{bb} at fixed $z = 1.0$, we can decrease the grafting density while largely retaining the advantages of the bottlebrush architecture. For example, for $z = 0.5$, α is only slightly smaller ($d^* \sim 0.926N_{\mathrm{bb}}^{0.815}$) and η_0 is only slightly higher. For a 50% grafted block polymer with the same side chain chemistry (PLA and PS) and same number of side chains ($zN_{\mathrm{bb}} = 100$) as the fully grafted example in Figure 6.2A, d^* is significantly larger: $d^* = 70$ nm. In other words, by using the same amount of the expensive macromonomer but decreasing z from 1.0 to 0.5, the total molecular weight M increases by only 7% but d^* increases by **30%**. This ability to increase d^* by decreasing z (using similar amounts of the expensive building blocks) introduces an attractive strategy for preparing polymeric photonic crystals.

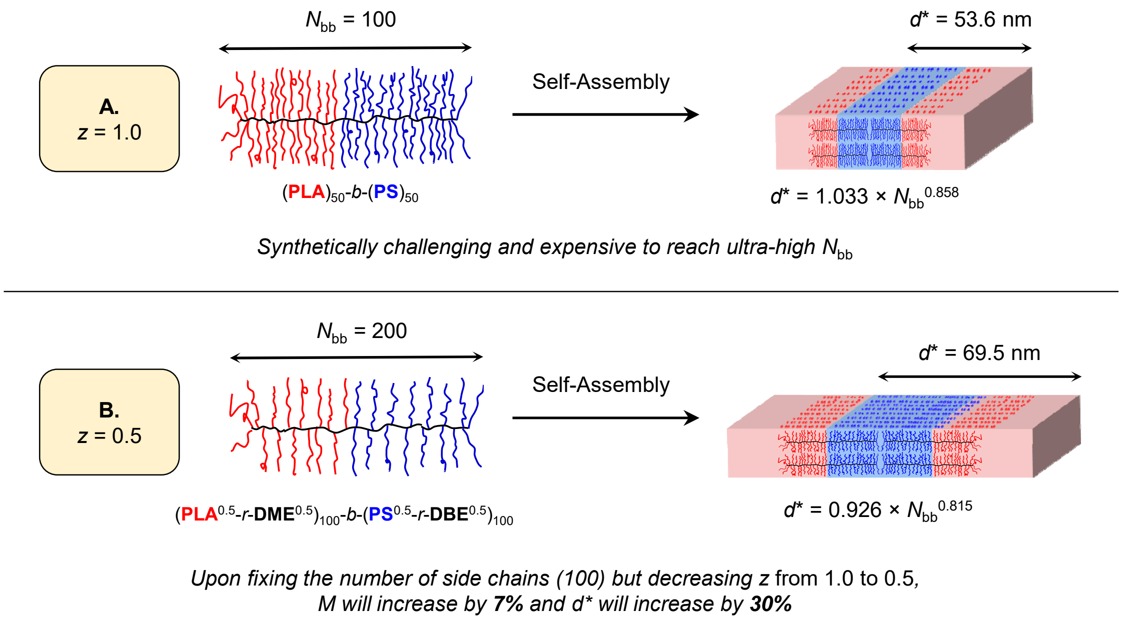

Synthetically challenging and expensive to reach ultra-high N_{bb}

Upon fixing the number of side chains (100) but decreasing z from 1.0 to 0.5,
*M will increase by **7%** and d* will increase by **30%***

Figure 6.2: Predicted lamellar periods (d^*) for (*A*) z = 1.0 and (*B*) z = 0.5 block polymers with the same number of side chains (zN_{bb} = 100). Comparing *A* and *B* indicates that decreasing z from 1.0 to 0.5 but maintaining the same number of side chains increases d^* by 30%.

6-1.3 Discrete Monomers

The multi-step syntheses and associated high costs of the macromonomers employed in previous approaches motivate the development of alternative building blocks. One strategy toward this goal is to design discrete monomers that promote self-assembly by templating local interactions. We synthesized three *exo*-norbornene monomers, each via a one-step amidation from commercially available starting materials. Each monomer was linked to either an octadecyl chain (C18), biphenyl group (BP), or polyhedral oligomeric silsequioxane cage (POSS). Octadecyl and biphenyl groups experience aliphatic and π-stacking interactions, respectively. POSS cages are nanosize structures with the general formula $(RSiO_{1.5})_8$. The R groups offer handles to incorporate a wide variety of functionalities,[28-29] and crystallization of the cages introduces opportunities for hierarchical organization.[30] The bulky groups of the C18, BP, and POSS monomers were proposed to template domain formation in block polymers. Local interactions could potentially eliminate the need for grafted architectures in order to access long-range-ordered, large-d^* nanostructures.

Several series of POSS-*b*-C18 and C18-*b*-BP block polymers were synthesized by sequential ROMP (Scheme 6.1) The livingness, stability, and functional group tolerance of ROMP enable the synthesis of block polymers with ultrahigh total molecular weights and low dispersity. The total degree of polymerization ($N = x + y$) and the relative volume fraction of each block ($\phi_{\mathrm{C18}} \sim y / x$) can be easily tuned; data for a representative series of POSS-*b*-C18 block polymers is provided in Table 6.1. This series targeted $x = 800$ for the first block and systematically varied the incorporation of C18, the second block. ϕ_{C18} was varied between 0.15 to 0.85, sweeping the ratios at which *linear* diblock polymers access different morphologies (including spheres, cylinders, and lamellae).

Scheme 6.1: Synthesis of block polymers with polyhedral oligomeric silsequioxane (POSS) and octadecyl (C18) side chains by sequential ROMP.

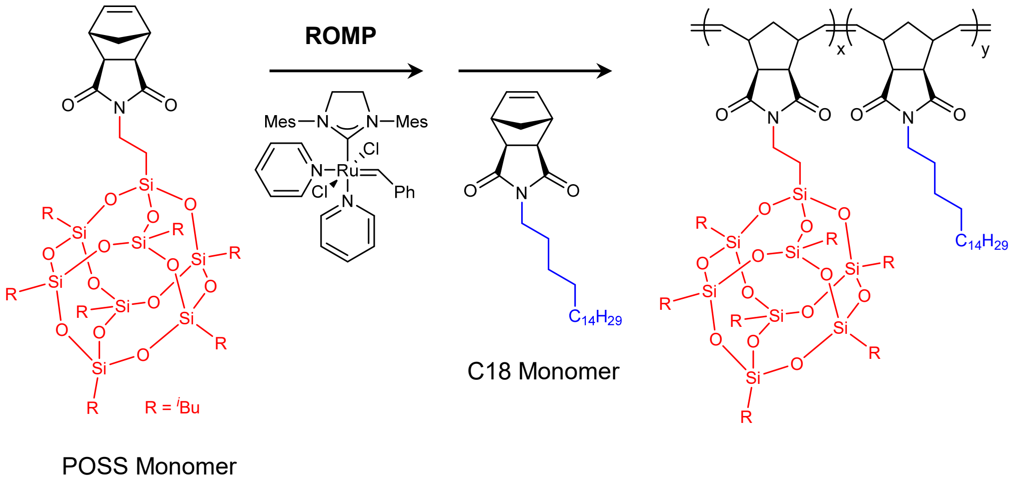

Table 6.1: Characterization data for POSS-*b*-C18 block polymers with target $x = 800$. M_w is the weight-average molecular weight, $Đ = M_w/M_n$ is the dispersity, and λ is the peak wavelength of reflected light. The morphologies were identified by scanning electron microscopy (SEM).

Entry	ϕ_{C18}	M_w (MDa)	$Đ$	λ (nm)	Morphology
1	0.14	1.80	1.28	—	DIS
2	0.24	2.30	1.28	670	LAM
3	0.32	2.42	1.31	590	LAM
4	0.48	3.40	1.50	510	DIS
5	0.67	2.97	1.36	—	DIS
6	0.74	2.72	1.26	—	DIS
7	0.86	2.34	1.21	—	DIS

Films of each block polymer were prepared by controlled evaporation from dichloromethane solutions. Three of the films reflected visible light: entries 2, 3, and 4 reflected orange, green, and violet light, respectively. Scanning electron micrographs (SEM) reveal lamellar morphologies (Figure 6.3). Compared to other linear block polymers, the domain sizes were large (*d** > 200 nm); however, compared to block polymers with polymeric or dendritic side chains,[31] the grain sizes were small. The lack of long-range order is supported by diffuse reflectance UV-vis spectrometry, which indicate very low percent reflectances for all films (<5%).

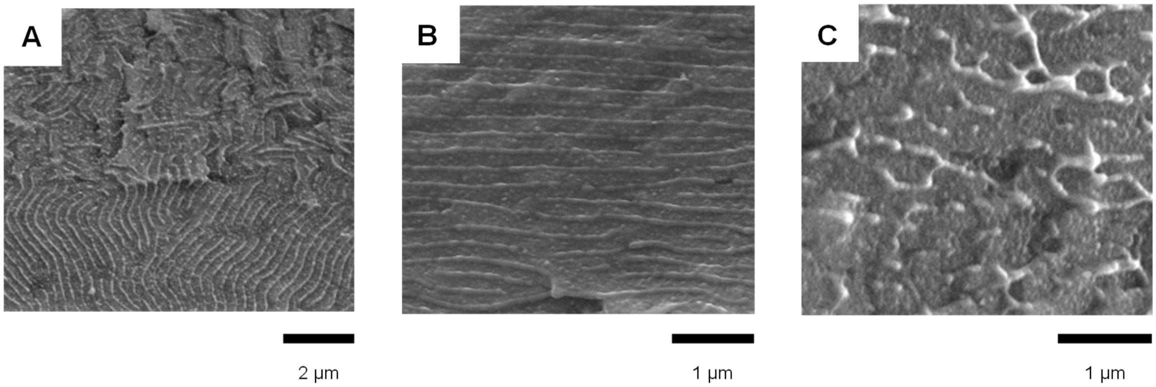

Figure 6.3: Scanning electron micrographs of cross-sections of POSS-*b*-C18 films. See Table 6.1: (*A*) Entry 2, (*B*) Entry 3, and (*C*) Entry 4. Ruthenium tetroxide (RuO_4) was used to preferentially stain POSS domains.

Like the POSS-*b*-C18 block polymers, C18-*b*-BP also lacked long-range order. These data suggest that the discrete side chains studied (and any nonspecific interactions between them) are not sufficient to promote block polymer self-assembly to photonic crystals with large *d**. We expect that these discrete groups do not to impose sufficient steric demands to extend the main chain and reduce chain entanglement. As a result, these polymers cannot achieve both the large domain sizes and long-range order displayed by graft block polymers with similar backbone lengths. Brush or brush-like building blocks may in fact be required for the rapid self-assembly of block polymers to photonic crystals that reflect light in the visible or infrared regimes.

6-1.4 Blends with Linear Homopolymers

In the preceding sections, we have discussed strategies to increase domain sizes by manipulating the polymer architecture (*i.e.*, by increasing N_{bb}, increasing z, or introducing potential templating interactions within domains). Another promising strategy to reduce the cost and improve the properties of polymeric photonic crystals is to blend graft block polymers with linear homopolymers.[32-33] Blending introduces a facile route to post-synthetically tune d^*. In addition, blending reduces the amount of expensive, architecturally complex block polymer required to reach the desired d^*. In fact, for many photonic block polymers the corresponding homopolymers are cheap commodity plastics (for example, PLA and PS), further reducing fabrication costs.

The swelling of *linear* diblock polymers with homopolymers has been extensively investigated through both theory and experiment.[34-37] We studied the swelling of *brush* diblock polymers with homopolymers (Figure 6.4).[38] Fully grafted brush block polymers with PLA (3.1 kDa) and PS (3.5 kDa) side chains were synthesized by sequential ROMP, then blended with symmetric equivalents of low-molecular-weight linear PLA and PS (M_{HP} ≈ 3 kDa).

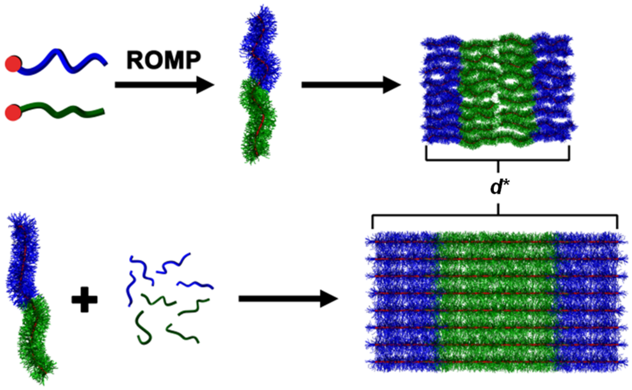

Figure 6.4: Brush block polymers self-assemble to lamellar arrays with large periods (d^*). Blending with low-molecular-weight linear homopolymers (identical to the side chains of the brush polymer) swells the structures, increasing d^*.

Blends were annealed by heating between glass slides in air for <1 minute using a heat gun (≈ 200 °C). The films were subsequently characterized by UV-visible spectrometry, scanning electron microscopy (SEM), and small-angle X-ray scattering (SAXS). Representative SEM images and plain-view photographs for a series of blends are shown in Figure 6.5A. The blends assembled to long-range ordered lamellar morphologies up to extremely high total homopolymer weight fractions ($\phi_{HP} > 0.70$), and the lamellar period d^* increased monotonically with increasing ϕ_{HP} (Figure 6.5B). For a fully grafted bottlebrush with $N_{bb} = 300$, blending increased d^* by up to 160% ($\phi_{HP} = 0.68$), corresponding to an increase in the wavelength of reflected light from 400 nm (blue) to 530 nm (orange). Higher-molecular-weight bottlebrushes could tolerate higher ϕ_{HP}: for example, a bottlebrush with the same side chain molecular weights but $N_{bb} = 530$ assembled to lamellae with $\phi_{HP} = 0.73$, corresponding to a **180%** increase in d^* and λ. Above these values of ϕ_{HP}, λ decreased while reflectance peak widths increased, suggesting the onset of macrophase separation. Self-consistent field theory (SCFT) calculations indicate that each homopolymer distributes uniformly throughout domains of the same composition (*i.e.*, PLA/PLA and PS/PS), with a slight increase in relative concentrations at the centers of domains (Figure 6.5C), consistent with the behavior of linear block polymer / homopolymer blends.[34-37]

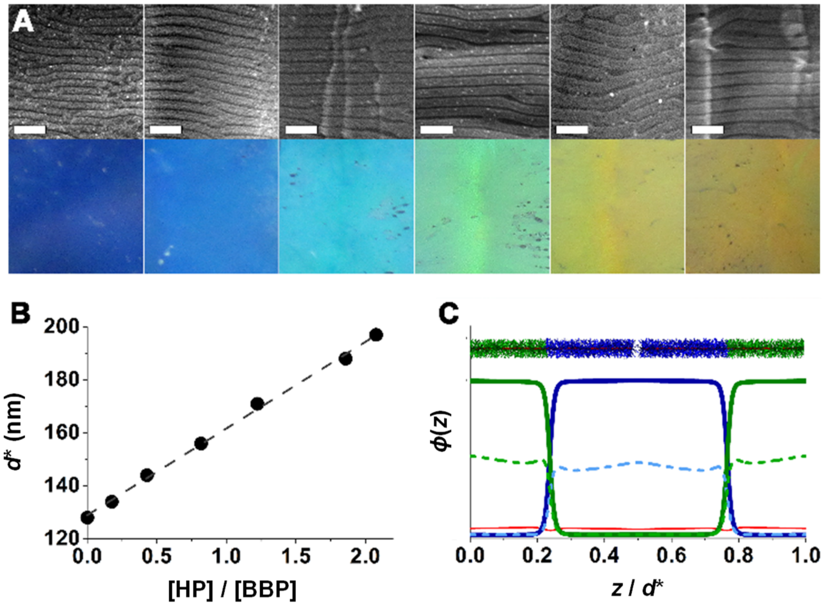

Figure 6.5: (*A*) Scanning electron micrographs of cross-sections of $(\mathbf{PLA})_{143}$-*b*-$(\mathbf{PS})_{155}$ brush block polymer films with $\phi_{HP} = 0, 0.30, 0.45, 0.55, 0.65$, and 0.68 (*left to right*). Below each image is a plain-view photograph showing increasing λ with increasing ϕ_{HP}. Scale bars are 500 nm. (*B*) d^* increases with added homopolymer (HP). d^* values were obtained by SAXS and correspond to the films in *A*. (*C*) SCFT composition profile showing the relative concentrations [$\phi(z)$] of brush block polymer and HP segments within one normalized lamellar period (z / d^*). The profile corresponds to the $\phi_{HP} = 0.45$ sample in *A*–*B*. *Blue:* PS brushes and HP; *green:* PLA brushes and HPr; *red:* polynorbornene backbone. Solid lines correspond to the brush polymer, and dashed lines correspond to HPs.

The preceding discussion has described the effects of blending linear homopolymers with fully grafted bottlebrush block polymers ($z = 1$). We have recently extended this work by studying blends of linear homopolymers with *graft* block polymers, where $z < 1$. The advantages of blending (this section) can be combined with the advantages of lowering the grafting density (Chapter 6-1.2) toward the large-scale fabrication of polymeric photonic crystals.

The self-assembly of graft block polymers with PLA and PS side chains was discussed in Chapter 3-3 of this thesis. Briefly: to vary z, the first block was synthesized by copolymerizing a **PLA** macromonomer ($M_n = 3230$ g/mol) with a discrete co-monomer, **DME** (*endo*,*exo*-norbornenyl dimethyl ester, $M_n = 210$ g/mol). After both co-monomers were fully consumed, a mixture of a **PS** macromonomer ($M_n = 3990$ g/mol) and another discrete diluent, **DBE** (*endo*,*exo*-norbornenyl di-*n*-butyl ester, $M_n = 294$ g/mol), was introduced as the second block. The **PS**/**DBE** feed ratio was the same as the **PLA**/**DME** feed ratio in the first block, and the reactivity ratios indicated that the copolymerization was statistically random. These $(\mathbf{PLA}^{z}\text{-}r\text{-}\mathbf{DME}^{1-z})_{n}\text{-}b\text{-}(\mathbf{PS}^{z}\text{-}r\text{-}\mathbf{DBE}^{1-z})_{n}$ graft block polymers self-assembled to lamellae, where $d^* \sim N_{bb}^{\alpha(z)}$ and $\alpha \sim z$.

We blended three series of graft block polymers with symmetric equivalents of linear PLA and PS homopolymers (*i.e.*, the **PLA** and **PS** macromonomers). These series — $z = 0.75$, 0.50, and 0.25 — correspond to entries B1–B4, C1–C4, and E1–E7 in Table 3.1. N_{bb} and d^* for the neat graft block polymers are reported in Table 6.2 for convenience; the fully grafted block polymers ($z = 1.00$, A1–A5) are included for comparison. In order to directly compare all blends, z was interpreted in terms of the backbone weight fraction (ϕ_{bb}). ϕ_{rel} indicates the backbone fraction for each series relative to $\phi_{bb}\,(z = 1.00)$.

Table 6.2: Graft block polymers with PLA (3230 g/mol) and PS (3990 g/mol) side chains, to be blended with linear homopolymers. The data also appear in Table 3.1.

z	ϕ_{bb}	ϕ_{rel}	**ID**	N_{bb}	d^* **(nm)**
1.00	0.028	1.0	A1	44	27.5
			A2	84	46.0
			A3	129	65.8
			A4	165	82.0
			A5	199	97.5
0.75	0.036	1.3	B1	84	40.3
			B2	130	58.2
			B3	168	72.5
			B4	219	89.5
0.50	0.052	1.9	C1	86	35.0
			C2	126	47.6
			C3	163	58.7
			C4	207	71.5
0.25	0.092	3.3	E1	90	27.9
			E2	134	36.7
			E3	153	41.5
			E4	183	47.0
			E5	197	51.5
			E6	223	55.5
			E7	262	63.5

Block polymers in each series were blended with the appropriate amounts of linear PLA and PS to match ϕ_{rel} for series with higher z. For example, polymers with $z = 0.50$ ($\phi_{\mathrm{rel}} = 1.9$) or $z = 0.75$ ($\phi_{\mathrm{rel}} = 1.3$) were blended with sufficient amounts of linear homopolymers to dilute the backbone concentration to $\phi_{\mathrm{rel}} = 1.0$ (analogous to $z = 1.00$). Figure 6.6 shows the corresponding changes in d^*. Consistent with previous work on symmetric blends of fully grafted brush block polymers, d^* increases with increasing ϕ_{HP} (equivalently, *decreasing* ϕ_{rel}).

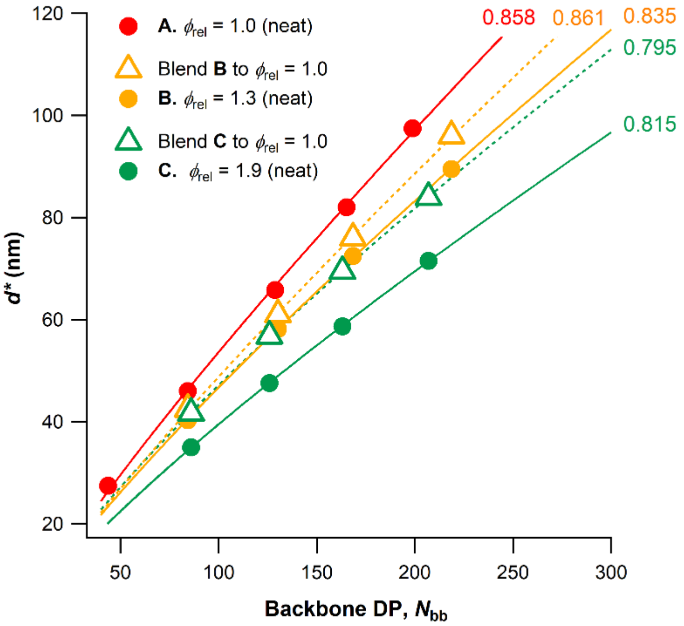

Figure 6.6: Plots of d^* versus N_{bb} for graft block polymers and blends with symmetric equivalents of linear homopolymers. ϕ_{rel} is the relative backbone concentration. **A** (*red circles*) represents neat $z = 1.00$ block polymers ($\phi_{rel} = 1.0$, A1–A5); **B** (*yellow circles*) represents neat $z = 0.75$ block polymers ($\phi_{rel} = 1.3$, B1–B4); and **C** (*green circles*) represents neat $z = 0.50$ block polymers ($\phi_{rel} = 1.9$, C1–C4). **B** and **C** were each blended with sufficient amounts of homopolymer to dilute ϕ_{rel} to 1.0 (*unfilled triangles*). Each series was fit to a power law ($d^* \sim N_{bb}{}^{\alpha}$), and the scaling exponents α are provided in the upper right corner.

Figure 6.7 compares data for blends of 25% and 50% grafted block polymers to ϕ_{rel} = 1.3 (analogous to $z = 0.75$). The data for each blend were fitted to a power law: $d^*_{blend} \sim N_{bb}{}^{\alpha}$. For each z, α decreases monotonically with ϕ_{rel}: for example, neat $z = 0.25$ ($\phi_{rel} = 3.3$) block polymers exhibit $\alpha = 0.788$; upon blending with sufficient amounts of linear homopolymers to reach $\phi_{rel} = 1.9$ or 1.3, α decreases to 0.714 or 0.666, respectively (Figure 6.7). We note that blending from $\phi_{rel} = 3.3$ to $\phi_{rel} = 1.0$ (equivalent to $\phi_{HP} = 0.72$) results in disordered materials rather than lamellar morphologies. However, the observation that blending $\phi_{rel} = 3.3$ to $\phi_{rel} = 1.9$ (equivalent to $\phi_{HP} = 0.62$) *does* produce lamellar morphologies suggests that low-z block polymers can tolerate large amounts of incorporated homopolymers. Fully grafted ($z = 1.00$) bottlebrushes with identical side chain chemistries (PLA, PS) and molecular weights (≈ 3 kDa) also disorder when $\phi_{HP} > 0.70$.[38] These trends expand previous insights into the impact of grafting density on block polymer self-assembly. Ongoing work aims to further understand how the molecular architecture affects the ordering kinetics and scaling of d^* in blends.

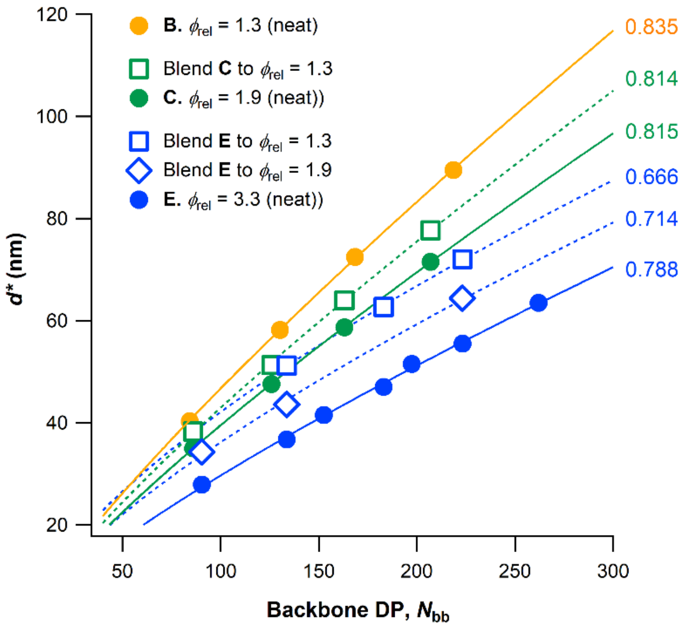

Figure 6.7: Plots of d^* versus N_{bb} for graft block polymers and blends with symmetric equivalents of linear homopolymers. ϕ_{rel} is the relative backbone concentration. **B** (*yellow circles*) represents neat $z = 0.75$ block polymers ($\phi_{rel} = 1.3$, B1–B4); **C** (*green circles*) represents neat $z = 0.50$ block polymers ($\phi_{rel} = 1.9$, C1–C4); and **E** (*blue circles*) represents neat $z = 0.25$ block polymers ($\phi_{rel} = 3.3$, E1–E7). **C** and **E** were each blended with sufficient amounts of homopolymer to dilute ϕ_{rel} to 1.3 (*unfilled squares*); **E** was also blended to reach $\phi_{rel} = 1.9$ (*unfilled diamonds*). Each series was fit to a power law ($d^* \sim N_{bb}^{\alpha}$), and the scaling exponents α are provided on the right.

6-2 Solid Polymer Electrolytes

6-2.1 Introduction

Batteries require electrolytes that facilitate the reversible movement of charges and physically separate the anode and cathode. Lithium ion batteries typically contain highly conductive liquid electrolytes that suffer from potential safety issues due to lithium dendrite grown and the use of flammable small molecule solvents. Solid polymer electrolytes (SPEs) are promising alternatives to conventional liquid electrolytes.[39-40] The ideal SPE exhibits both high ionic conductivity and a high modulus: the key challenge is to achieve high mechanical and thermal performance without sacrificing ionic conductivity. By far the most widely used conductive component is amorphous poly(ethylene oxide) (PEO), which dissolves lithium salts and enables the movement of lithium cations by cooperative polymer segmental relaxation.[41] Unfortunately, rubbery materials such as amorphous PEO lack the mechanical integrity necessary for application in polymer electrolyte membranes (PEMs), and as a consequence, many strategies have been explored to improve PEM stiffness (typically by copolymerization and/or crosslinking). With few exceptions,[42] conductivity and modulus are generally inversely related: highly conductive materials are structurally weak (*e.g.*, fluids), while stiff materials are typically non-conductive (*e.g.*, polymer glasses).

Block polymers provide successful strategies to decouple these properties. AB diblock and ABA triblock copolymers — in which block A is a glassy, rigid insulator and block B is a rubbery conductor — allow the mechanical properties and conductivity to be independently tuned. Many polymer architectures have been studied to date.[43-44] The most prevalent of these materials is linear poly(styrene-*block*-ethylene oxide), PS-*b*-PEO, which generally offers modest conductivity ($\leq 10^{-3}$ S/cm at 90 °C) and promising elastic moduli approaching 10^8 Pa.[45-46]

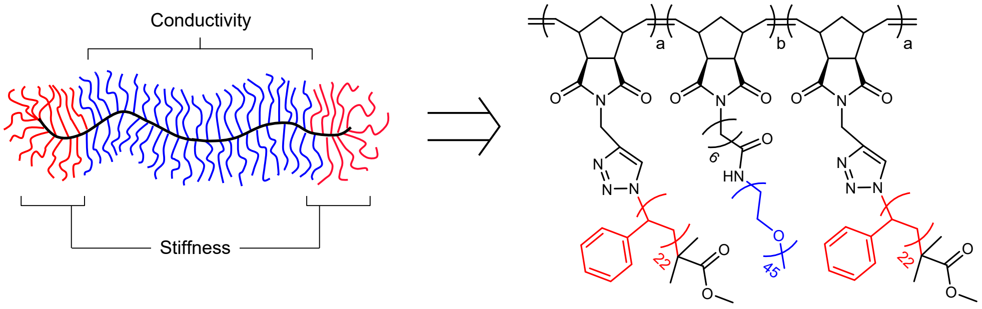

Figure 6.8: (*left*) Schematic illustration and (*right*) chemical structure of *g*PS-*g*PEO-*g*PS (SOS) brush triblock copolymers.

In this chapter, we describe the synthesis, characterization, and initial SPE applications of well-defined bottlebrush triblock copolymers, designated *g*PS-*g*PEO-*g*PS (SOS) (Figure 6.8). Section 6-2.2 will discuss the properties of blends of SOS brush triblock copolymers with lithium salt. The normalized conductivity improves but the modulus decreases relative to linear PS-*b*-PEO-*b*-PS and PS-*b*-PEO analogues. Section 6-

2.3 will discuss blends of SOS with ionic liquids, forming physically crosslinked ion gels, as well as applications of these materials as solid supports for electrocatalysis. Reflecting the themes of this thesis, we will highlight the impact of the brush architecture on the self-assembly and properties of these materials.

6-2.2 Blends with Lithium Salt

Brush *g*PS-*g*PEO-*g*PS triblock copolymers were synthesized by sequential ring-opening metathesis polymerization (ROMP) (PS: M_n = 2.5 kDa; PEO: M_n = 2.0 kDa). Four triblocks with different absolute and relative backbone degrees of polymerization for the PS and PEO blocks were synthesized (Table 6.3).

Table 6.3: Characterization data for $g\mathrm{PS}_a$-$g\mathrm{PEO}_b$-$g\mathrm{PS}_a$ brush triblock copolymers.

Sample	$N_{\mathrm{bb},i}$[a]	M_n[b] (kDa)	$Đ$[b]	ϕ_{PS}[c]
$g\mathrm{PS}_3$-$g\mathrm{PEO}_{85}$-$g\mathrm{PS}_3$	3-85-3	208	1.05	0.077
$g\mathrm{PS}_6$-$g\mathrm{PEO}_{87}$-$g\mathrm{PS}_5$	6-87-5	225	1.12	0.12
$g\mathrm{PS}_{11}$-$g\mathrm{PEO}_{78}$-$g\mathrm{PS}_{11}$	11-78-11	234	1.17	0.24
$g\mathrm{PS}_{15}$-$g\mathrm{PEO}_{119}$-$g\mathrm{PS}_{15}$	15-119-15	348	1.08	0.22

[a] Backbone degrees of polymerization for each block *i*.
[b] Determined by size-exclusion chromatography in tetrahydrofuran with 1 vol% trimethylamine.
[c] PS volume fraction calculated using ρ_{PS} = 1.05 g/cm^3 and ρ_{PEO} = 1.06 g/cm^3.

Blends of these brush block polymers and lithium bis(trifluoromethylsulfonyl)imide (LiTFSI) were subsequently prepared with different [EO]:[Li$^+$] ratios, calculated as the average total number of ethylene oxide repeat units per chain relative to moles of LiTFSI. Differential scanning calorimetry (DSC) reveals a monotonic increase in the glass transition temperature (T_g) of PEO with increasing LiTFSI concentration (*i.e.*, *decreasing* [EO]:[Li$^+$]) (Figure 6.9). The observed increase in T_g with increasing salt concentration reflects the reduction in chain mobility due to polymer-ion interactions and transient crosslinking. Under the DSC conditions (ramp rates of 5, 10, and 20 °C/min), PEO crystallization was suppressed for [EO]:[Li$^+$] = 2:1, 5:1, and 10:1 for both $g\mathrm{PS}_{11}$-$g\mathrm{PEO}_{78}$-$g\mathrm{PS}_{11}$ and $g\mathrm{PS}_{15}$-$g\mathrm{PEO}_{119}$-$g\mathrm{PS}_{15}$. For the former (lower N_{bb}), crystallization suppression was additionally observed for [EO]:[Li$^+$] = 15:1. Although no evidence of crystallization was observed on the timescales of the DSC measurements, both $g\mathrm{PS}_{11}$-$g\mathrm{PEO}_{78}$-$g\mathrm{PS}_{11}$/LiTFSI (15:1) and $g\mathrm{PS}_{15}$-$g\mathrm{PEO}_{119}$-$g\mathrm{PS}_{15}$/LiTFSI (10:1) blends exhibited clear melting transitions after aging for two months at room temperature, indicating arrested crystallization kinetics. All other samples remained unchanged.

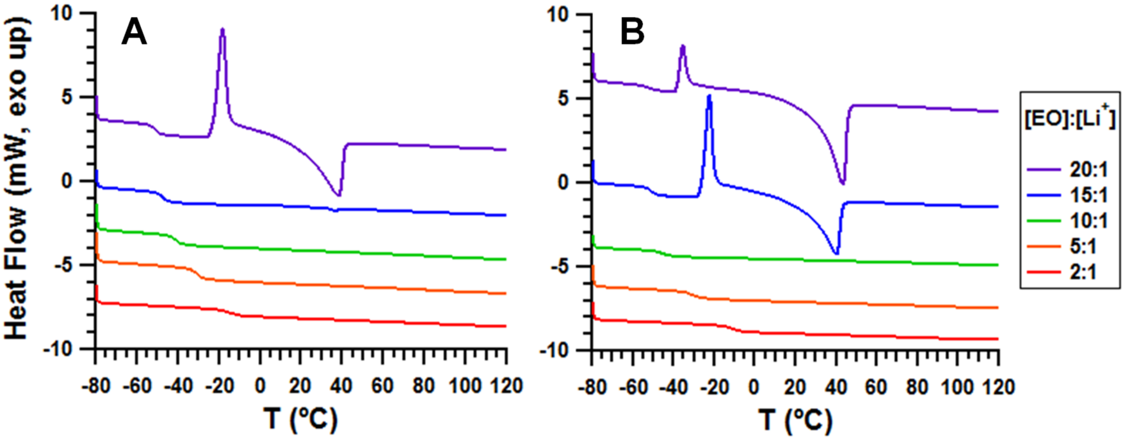

Figure 6.9: Differential scanning calorimetry data for SOS brush triblock copolymers as functions of LiTFSI loading: (*A*) $g\mathrm{PS}_{11}$-$g\mathrm{PEO}_{78}$-$g\mathrm{PS}_{11}$ and (*B*) $g\mathrm{PS}_{15}$-$g\mathrm{PEO}_{119}$-$g\mathrm{PS}_{15}$. Traces are shown for a 5 °C/min ramp rate on heating and are shifted vertically for clarity.

Since Li^+ diffusion usually occurs exclusively in amorphous PEO (*i.e.*, not in crystalline domains), preventing crystallization is crucial for PEM applications. Various strategies have addressed this issue, including using lithium salt mixtures[47] and (meth)acrylates functionalized with low-molecular-weight oligo-PEO side chains.[48-51] Our brush SOS/LiTFSI blends ($N_{\mathrm{PEO}} = 45$) demonstrate a surprising tendency to avoid crystallization considering oligo-PEO acrylate derivatives with side chain degrees of polymerization $N_{\mathrm{PEO}} \geq 7$ typically show incipient crystallization.[49] In addition, blends of linear PEO homopolymer ($N_{\mathrm{PEO}} \approx 90$) with LiTFSI display relatively small crystallinity gaps ($6 < [\mathrm{EO}]:[\mathrm{Li}^+] < 12$)[52] compared to brush SOS/LiTFSI blends (see Figure 6.9A, $2 < [\mathrm{EO}][\mathrm{Li}^+] < 15$). DSC measurements performed for blends of the PEO macromonomer ($N_{\mathrm{PEO}} = 45$) and LiTFSI are consistent with the crystallinity gap reported for brush SOS; in other words, the side chains in the *g*PEO brush behaves in the same way as a linear PEO homopolymer with the same molecular weight. The suppression of crystallization over this range of lithium salt concentrations highlights one advantage of the brush architecture:

high-molecular-weight brush polymers (large *a*, *b*) bearing low-molecular-weight grafted PEO side chains (N_{PEO}) appear to minimize crystallization, since crystallinity generally increases with N_{PEO} and evidently not the backbone degree of polymerization (*b*).

The polymer architecture may also affect the kinetics of brush polymer crystallization. Previous reports of the crystallization of brush poly(L-lactide) (PLLA) homopolymers reveal an Avrami exponent (*n*) approaching 2, in contrast to linear PLLA ($n \approx 4$). The lower exponent observed for brush PLLA suggests considerably slower crystallization kinetics and lower equilibrium melting temperatures (*i.e.*, more crystal defects).[53] Combining the graft and block architectures therefore combines the advantages of crystallization suppression with the potential to decouple conductive and mechanical properties.

AC impedance spectroscopy was used to measure conductivity (σ) as a function of [EO]:[Li$^+$]. Because LiTFSI is highly hygroscopic, all sample preparation was performed in a dry room to eliminate moisture contamination. Conductivity increases with [EO]:[Li$^+$] up to moderate blend ratios (10:1–20:1), since the number of charge carriers increases with salt concentration. However, conductivity decreases upon further increasing the salt concentration, consistent with saturating EO binding motifs and reducing chain mobility. Figure 6.10 plots the normalized conductivity ($\sigma/\sigma_{\text{max}}$) versus temperature for [EO]:[Li$^+$] = 2:1, 5:1, and 10:1. σ_{max} corresponds to the conductivity of a linear 300 kDa PEO homopolymer and is defined, analogous to previous reports,[45] as the measured conductivity of homo-PEO (σ_{PEO}) moderated by the volume fraction of PEO in the block polymer (ϕ_{PEO}) and a morphology factor ($0 \leq f \leq 1$) related to the continuity of the conducting phase:

$$\sigma_{\text{max}} = f\sigma_{\text{PEO}}\phi_{\text{PEO}} \qquad \text{Eq. 6-3}$$

SAXS measurements identified hexagonally packed cylindrical morphologies for all blends, dictating continuous PEO domains ($f = 1$).[41] The normalized conductivities in Figure 6.10 are remarkably large for 2 kDa PEO chains. (Normalization with literature-reported σ values for 4 kDa linear PEO[52] reduces $\sigma/\sigma_{\text{max}}$ by 50% but reaches the same conclusion.) For comparable *linear* PS-*b*-PEO, $\sigma/\sigma_{\text{max}} < 0.1$ [46,54] and reaches 0.3 only when $M_{\text{PEO}} \approx 40$ kDa.[45] Instead, the values for brush SOS more closely resemble those for ultralow-M_{PEO} disordered PS-*b*-PEO.[55] $\sigma/\sigma_{\text{max}} \approx 1$ suggests differences between the graft and linear block polymer architectures involving Li^+ diffusion, wherein the graft block polymers more closely mimic PEO homopolymers.

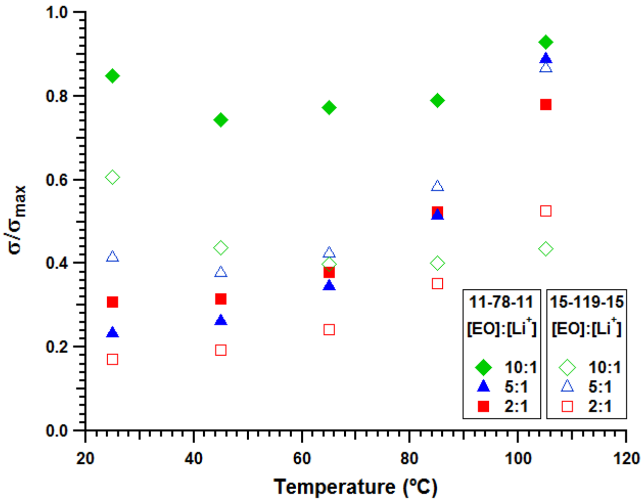

Figure 6.10: Normalized ionic conductivity (σ/σ_{max}) for gPS$_{11}$-gPEO$_7$-gPS$_{11}$/LiTFSI and gPS$_{15}$-gPEO$_{119}$-gPS$_{15}$/LiTFSI blends, relative to linear PEO (M_n = 300 kDa).

The SOS brush triblock copolymers display similar or moderately higher conductivity than linear PEO-containing block polymers (*e.g.*, PS-*b*-PEO,[46] PS-*b*-PEO-*b*-PS,[56] and PP-*b*-PEO-*b*-PP[57]). The comparable conductivity is perhaps surprising, since the brush architecture dilutes the volume fraction of the conducting PEO domain with the polynorbornene backbone (by ≈ 10% for gPS$_{11}$-gPEO$_{78}$-gPS$_{11}$), previously assumed to *decrease* conductivity.[43] Other architecture effects may compensate for dilution by the backbone, such as low melt viscosity,[18-20] altered lithium ion distribution in brush PEO domains,[58] chain end effects,[59] ionic interactions,[60] and/or conductive domain grain sizes.[61] We also note that the conductivity of these SOS brush triblock copolymers appears to decrease with b, the backbone degree of polymerization of the gPEO block; in stark contrast, the conductivity of linear PEO-containing block polymers dramatically *increases* with increasing N_{PEO}.[45-46] Ongoing work aims to elucidate the physical mechanisms underlying the relationships between conductivity and polymer architecture.

Frequency-dependent melt rheology data are reported in Figure 6.11 for gPS$_{11}$-gPEO$_{78}$-gPS$_{11}$. Between 0.01 and 100 rad/s, at temperatures 45–105 °C, the storage modulus (G') is on the order of 10^4 Pa and is always larger than the loss modulus (G'').

Time-temperature superposition of the relaxation spectra fails; the data are therefore reported as isothermal frequency sweeps. *g*PS$_{11}$-*b*-*g*PEO$_{78}$-*b*-*g*PS$_{11}$ is a viscoelastic solid and considerably softer than linear PS-*b*-PEO ($G' \sim 10^7$ Pa at 90 °C for $\phi_{\mathrm{PEO}} = 0.38$).[45] Based on reports of linear PS-*b*-PEO,[45] the brush SOS/Li$^+$ blends should be more elastic (perhaps by an order of magnitude), but the relative softness is likely an inevitable limitation of the brush architecture.[51,62]

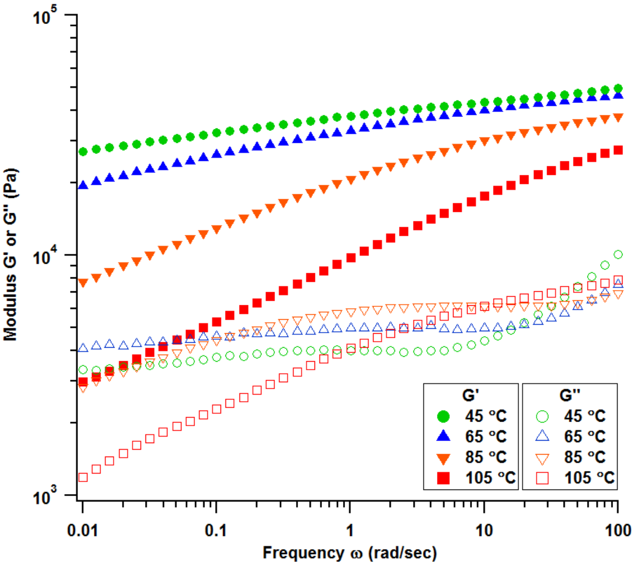

Figure 6.11: Dynamic mechanical analysis of neat *g*PS$_{11}$-*g*PEO$_{78}$-*g*PS$_{11}$, presenting the storage (G') and loss (G'') moduli as functions of temperature and frequency (ω).

Table 6.4 compares ABA linear and bottlebrush polymer architectures in terms of the conductivity and modulus, two key properties of solid polymer electrolytes. The normalized conductivity ($\sigma / \sigma_{\mathrm{max}}$) is typically higher for brush polymers, while the storage modulus (G') is typically higher for linear polymers. Further advances are required in order to maximize both the conductivity and modulus. Combining the brush block polymer architecture with techniques such as polymerization-induced phase separation[42] may provide routes towards stiffer materials while retaining the advantages of higher normalized conductivities.

Table 6.4: Comparison of linear and brush polymer architectures in terms of the normalized conductivity ($\sigma / \sigma_{\max}$) and storage modulus (G').

	 **ABA Linear Polymer**	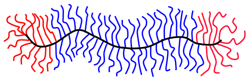 **ABA Brush Polymer**
Conductivity (σ/σ_{max})	≤ 0.3	≤ 0.9
Modulus (G', Pa)	~ 10^7	~ 10^4

6-2.3 Brush Polymer Ion Gels

In addition to blends of brush SOS triblock copolymers with LiTFSI, we have also studied blends of brush SOS with ionic liquids (IL).[8] Block polymers containing IL have emerged as promising alternative electrolytes for lithium batteries.[63-65] ILs are room-temperature molten salts composed mostly of organic ions. Their unique combination of properties — including reduced flammability, low vapor pressure, exceptional thermal and electrochemical stability, low toxicity, and high ionic conductivity — make them attractive materials for battery applications.[66-67] Toward integration in devices, providing ILs with mechanical integrity without sacrificing ionic conductivity is desired. Ion gels (*i.e.*, SPEs incorporating ILs) are advantageous due to their high ionic conductivity (~10^{-3} S/cm at 25 °C)[68] compared to conventional lithium salt SPEs such as PEO/$LiClO_4$ (~10^{-5} S/cm at 25 °C).[69]

The network structure of the ion gel can be formed either by chemically reacting monomers with functional crosslinkers or by creating physically associated crosslinks. The physical crosslinking of block polymers is a particularly versatile strategy due to the synthetic ease of tuning the gel structure and properties via block lengths and sequences. In the presence of IL, an ABA triblock copolymer with *ionophobic* A blocks and an *ionophilic* B block self-assembles to a network in which micelles of A are bridged by B blocks and dispersed in a continuous B/IL phase.[45,70] We have exploited this phenomenon to fabricate brush polymer ion gels (Figure 6.12A). The *g*PS-*g*PEO-*g*PS brush triblock copolymers described in Section 6-2.2 (Table 6.3) were gelled in 1-butyl-3-

methylimidazolium bis(trifluoromethylsulfonyl)imide ([BMI][TFSI]) at polymer concentrations spanning $0.05 < \phi_{\mathrm{SOS}} < 0.5$. SAXS measurements of the ion gels confirms a disordered micellar structure (Figure 6.12B).

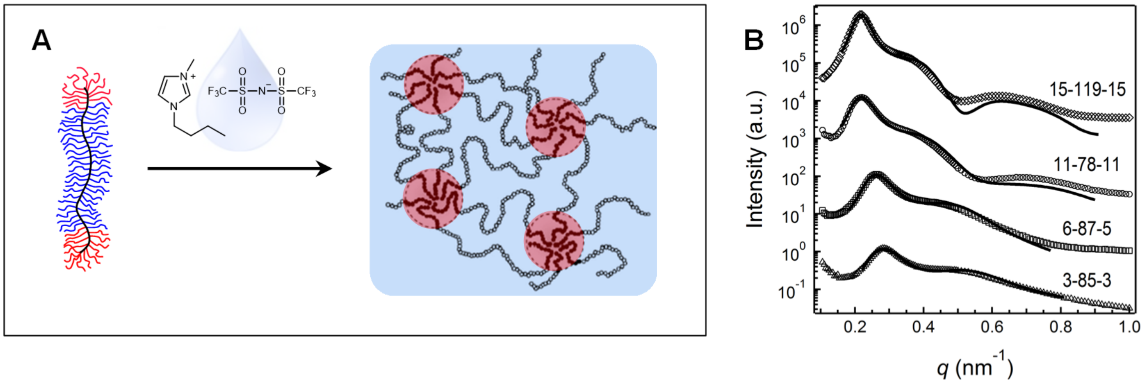

Figure 6.12: (*A*) Brush polymer ion gels were prepared by blending *g*PS-*g*PEO-*g*PS brush triblock copolymers with an ionic liquid, [BMI][TFSI]. Disordered micelles of *g*PS in a continuous matrix of *g*PEO and [BMI][TFSI] result. (*B*) Azimuthally averaged small-angle X-ray scattering data from four different *g*PS-*g*PEO-*g*PS brush block polymers at polymer concentrations $\phi_{\mathrm{SOS}} = 0.33$. The backbone degrees of polymerization for each block are provided. Solid block lines represent fits to a model using a hard sphere form factor and Percus-Yevick structure factor. Traces are shifted vertically for clarity.

As in our study of polymer/Li^{+} blends, we aim to (1) study the conductivity and rheological properties of these materials and (2) understand the impact of the brush polymer architecture. Frequency-dependent rheology data are provided in Figure 6.13 for ion gels containing $\phi_{\mathrm{SOS}} = 0.16$ $g\mathrm{PS}_{3}$-$g\mathrm{PEO}_{85}$-$g\mathrm{PS}_{3}$ or $g\mathrm{PS}_{15}$-$g\mathrm{PEO}_{119}$-$g\mathrm{PS}_{15}$ in [BMI][TFSI]. The two samples display markedly different viscoelastic behavior, which we attribute primarily to the different *g*PS backbone lengths. For $g\mathrm{PS}_{15}$-$g\mathrm{PEO}_{119}$-$g\mathrm{PS}_{15}$ ($\phi_{g\mathrm{PS}} = 0.22$), the storage modulus ($G'$) remains constant ($\approx 10^{3}$ Pa) at frequencies 0.01–100 rad/sec and temperatures 25–85 °C. In contrast, $g\mathrm{PS}_{3}$-$g\mathrm{PEO}_{85}$-$g\mathrm{PS}_{3}$ ($\phi_{g\mathrm{PS}} = 0.077$) transitions from a solid-like ($G' > G''$) to liquid-like ($G' < G''$) response at 25°C on the order of 10^{2} sec, which decreases by at least four orders of magnitude as the temperature increases to 85 °C (data not shown). The strong dependence of modulus and relaxation time on end-block length, polymer composition, and/or temperature is also observed with linear ABA block copolymer gels.[71] The energetic penalty for chain pullout (a stress relaxation mechanism) is controlled by the interaction parameter $\chi_{g\mathrm{PS/IL}}$, characterizing the unfavorable interactions between the *g*PS end blocks and IL. Typical mixtures exhibit upper critical solution behavior ($\chi \sim T^{-1}$), such that the components become more miscible as the temperature increases. In contrast, increasing the *g*PS molecular weight (M_A) should disfavor mixing since the ideal combinatorial entropy of mixing scales as $\Delta S_{\mathrm{mix}} \sim M_A^{-1}$. Midblock entanglements also significantly influence the modulus and relaxation of ABA triblock copolymers and their corresponding gels. Although the grafted PEO side-chains are slightly longer than their entanglement molar mass (M_e = 1.6 kDa),[72] the brush architecture suppresses entanglements,[73] decreasing the elastic modulus of bulk brush polymers relative to linear analogues.[19,62,74] This trend also holds for gels; a linear PS-*b*-PEO-*b*-PS ion gel ($\phi_{PS} \approx 0.07$) exhibits frequency-dependent elastic moduli approximately 10^1–10^2 Pa larger than the similar *g*PS$_3$-*g*PEO$_{85}$-*g*PS$_3$ brush block polymers reported herein.[75]

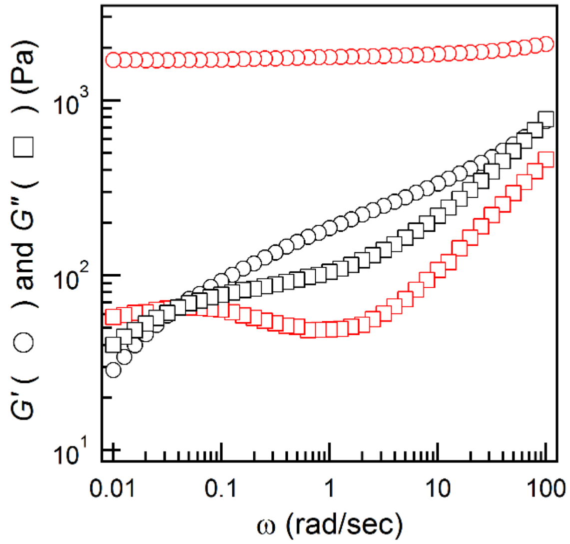

Figure 6.13: Dynamic mechanical analysis of ϕ_{SOS} = 0.16 ion gels containing *g*PS$_{15}$-*g*PEO$_{119}$-*g*PS$_{15}$ (*red*) or *g*PS$_3$-*g*PEO$_{85}$-*g*PS$_3$ (*black*) at 25 °C, presenting the storage (G') and loss (G'') moduli as functions of frequency (ω).

The ionic conductivity (σ) of the brush polymer ion gels was probed using AC impedance spectroscopy over the temperature range 25–95°C. Conductivities (~1 mS/cm at 25°C) are comparable to ion gels derived from linear triblock copolymers[75] and represent a considerable increase relative to dry linear[45] and brush[7] electrolytes. Conductivity generally decreases as polymer concentration increases due to an increase in T_g and concomitant decrease in ion mobility, a trend also found with both chemically[76] and physically[77] cross-linked linear polymer gels. Normalized conductivities (σ/σ_{max}, relative to neat [BMI][TFSI]) are provided in Figure 6.14 for *g*PS$_3$-*g*PEO$_{85}$-*g*PS$_3$ and *g*PS$_{15}$-*g*PEO$_{119}$-*g*PS$_{15}$ gels. The relatively high conductivities ($0.2 < \sigma/\sigma_{max} < 0.8$) highlight the liquid-like order in the gel phase, consistent with measurements obtained for linear analogues. The conductivity decreases with increasing *a*:*b* backbone block ratios and polymer concentration but generally remains near neat [BMI][TFSI].

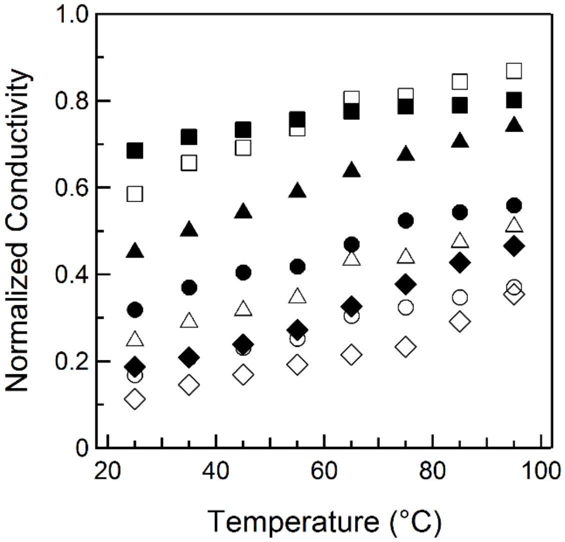

Figure 6.14: Ionic conductivities for brush polymer ion gels, normalized to neat [BMI][TFSI]. Closed and open symbols represent *g*PS$_3$-*g*PEO$_{85}$-*g*PS$_3$ and *g*PS$_{15}$-*g*PEO$_{119}$-*g*PS$_{15}$ samples, respectively. Polymer concentrations are 9 (□ and ■), 16 (△ and ▲), 23 (○ and ●), and 29 wt% (◊ and ♦).

In addition to studying the conductivity and rheological properties of ion gels, we have recently demonstrated that ion gels are attractive solid supports for electrocatalysis.[78] *g*PS$_{15}$-*g*PEO$_{119}$-*g*PS$_{15}$ in [BMI][TFSI] was mixed with some combination of ferrocene (Fc), cobaltocenium ($CoCp_2^+$), and $Re(bpy)(CO)_3Cl$ (Figure 6.15). The physically crosslinked polymer networks decouple the molecular interactions providing macroscopic solid-like mechanical properties from the electrochemical activity of the homogenous small-molecule catalysts. This design captures the benefits of a solid support without requiring catalyst redesign and/or surface attachment. The electroactive small molecules dissolved in the *g*PEO / [BMI][TFSI] matrix domain are capable of undergoing redox reactions due to the high ionic conductivity and polarizability of the IL medium. Incorporating Re(bpy)(CO)$_3$Cl, a well-established CO$_2$ reduction catalyst,[79-81] enables useful electrochemical reactions with homogenous catalysts exhibiting macroscopic solid-like properties.

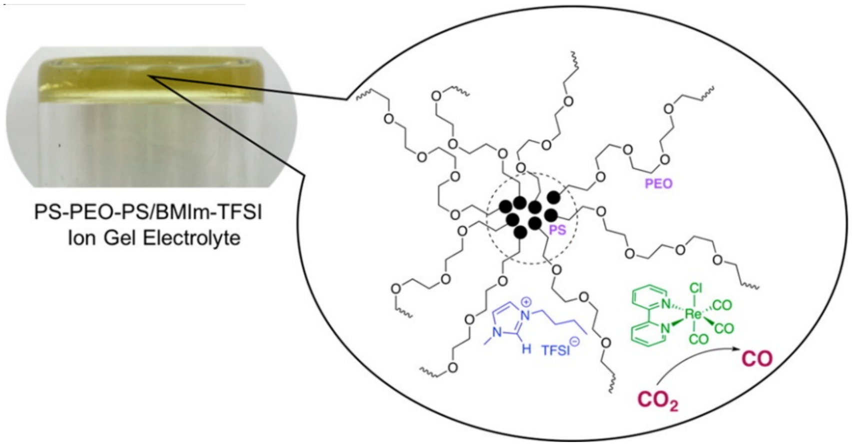

Figure 6.15: Electrocatalytic reduction of CO$_2$ to CO in *g*PS-*g*PEO-*g*PS brush polymer ion gels. The catalyst, Re(bpy)(CO)$_3$Cl, dissolves in the continuous *g*PEO / [BMI][TFSI] matrix.

The brush polymer ion gels exhibited diffusion-controlled redox processes with diffusion coefficients approximately one-fifth of those observed in neat [BMI][TFSI]. In gels containing Fc, Re(bpy)(CO)$_3$Cl, and 1 atm CO$_2$, a catalytic wave was observed (Figure 6.16). The catalytic wave exhibits a sizeable, positive shift compared to analogous non-aqueous solvents with a reduction potential 500 mV positive of onset and 90% Faradaic efficiency.

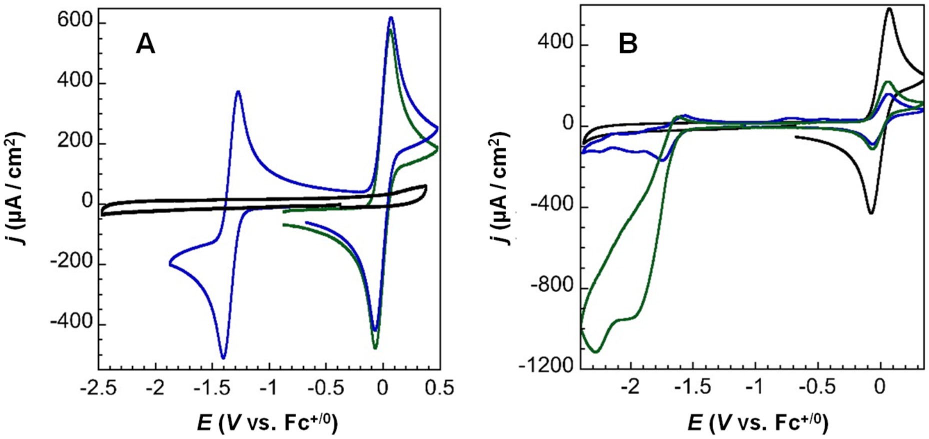

Figure 6.16: Cyclic voltammetric scans of brush polymer ion gels comprising gPS$_{15}$-gPEO$_{119}$-gPS$_{15}$, [BMI][TFSI]. (*A*) Ion gels containing no additives (*black*); 14.3 mM Fc (*green*); or 14.3 mM Fc and 15.3 mM $CoCp_2^+$ (*blue*). (*B*) Ion gels containing 14.3 mM Fc and 1 atm CO_2 (*black*); 5 mM Fc and 10 mM Re(bpy)$(CO)_3$Cl (*blue*); or 7.1 mM Fc, 14.3 mM Re(bpy)$(CO)_3$Cl, and 1 atm CO_2 (*green*).

Brush polymer ion gels represent valuable platforms that bridge the gap between homogenous, solution-state catalysis and heterogeneous, solid-state catalysis. This new class of materials is capable of electrocatalytically reducing CO_2 with a well-defined, small-molecule catalyst typically used in homogenous solutions. The catalytic enhancement and high CO_2 solubility imparted by the ionic liquid results in a significant decrease in CO_2 reduction potential compared to other non-aqueous electrolytes. Since physical crosslinks imbue mechanical properties, reversible gelation is thermally accessible. Extraction of electrochemical reaction products, macroscopic shape adjustment, and repeated recycling should therefore be possible. These advances are all crucially enabled by the graft polymer molecular architecture.

6-3 References

(1) Liberman-Martin, A. L.; Chu, C. K.; Grubbs, R. H. *Macromol. Rapid Commun.* **2017**, *38*, 1700058.

(2) Runge, M. B.; Bowden, N. B. *J. Am. Chem. Soc.* **2007**, *129*, 10551–10560.

(3) Sveinbjörnsson, B. R.; Weitekamp, R. A.; Miyake, G. M.; Xia, Y.; Atwater, H. A.; Grubbs, R. H. *Proc. Natl. Acad. Sci. U.S.A.* **2012**, *109*, 14332–14336.

(4) Qiu, L. Y.; Bae, Y. H. *Biomaterials* **2007**, *28*, 4132–4142.

(5) Johnson, J. A.; Lu, Y. Y.; Burts, A. O.; Lim, Y.-H.; Finn, M. G.; Koberstein, J. T.; Turro, N. J.; Tirrell, D. A.; Grubbs, R. H. *J. Am. Chem. Soc.* **2011**, *133*, 559–566.

(6) Bhattarai, N.; Ramay, H. R.; Gunn, J.; Matsen, F. A.; Zhang, M. *J. Control. Release* **2005**, *103*, 609–624.

(7) Bates, C. M.; Chang, A. B.; Momčilović, N.; Jones, S. C.; Grubbs, R. H. *Macromolecules* **2015**, *48*, 4967–4973.

(8) Bates, C. M.; Chang, A. B.; Schulze, M. W.; Momčilović, N.; Jones, S. C.; Grubbs, R. H. *J. Polym. Sci., Part B: Polym. Phys.* **2016**, *54*, 292–300.

(9) Jiang, F.; Wang, Z.; Qiao, Y.; Wang, Z.; Tang, C. *Macromolecules* **2013**, *46*, 4772–4780.

(10) Zhang, J.; Schneiderman, D. K.; Li, T.; Hillmyer, M. A.; Bates, F. S. *Macromolecules* **2016**, *49*, 9108–9118.

(11) Joannopoulos, J. D.; Johnson, S. G.; Winn, J. N.; Meade, R. D. *Photonic Crystals: Molding the Flow of Light*; 2nd ed.; Princeton University Press: Princeton, NJ, 2008.

(12) Yablonovitch, E. *J. Phys.: Condens. Matter* **1993**, *5*, 2443.

(13) Fink, Y.; Urbas, A. M.; Bawendi, M. G.; Joannopoulos, J. D.; Thomas, E. L. *J. Lightwave Technol.* **1999**, *17*, 1963.

(14) Edrington, A. C.; Urbas, A. M.; DeRege, P.; Chen, C. X.; Swager, T. M.; Hadjichristidis, N.; Xenidou, M.; Fetters, L. J.; Joannopoulos, J. D.; Fink, Y.; Thomas, E. L. *Adv. Mater.* **2001**, *13*, 421–425.

(15) Yoon, J.; Lee, W.; Thomas, E. L. *MRS Bulletin* **2005**, *30*, 721–726.

(16) Alfrey, T.; Gurnee, E. F.; Schrenk, W. J. *Polym. Eng. Sci.* **1969**, *9*, 400–404.

(17) Lin, T.-P.; Chang, A. B.; Luo, S.-X.; Chen, H.-Y.; Lee, B.; Grubbs, R. H. *ACS Nano* **2017**, *11*, 11632–11641.

(18) Jeong, S. H.; Kim, J. M.; Baig, C. *Macromolecules* **2017**, *50*, 4491–4500.

(19) Dalsin, S. J.; Hillmyer, M. A.; Bates, F. S. *ACS Macro Lett.* **2014**, *3*, 423–427.

(20) Lohse, D. J.; Milner, S. T.; Fetters, L. J.; Xenidou, M.; Hadjichristidis, N.; Mendelson, R. A.; García-Franco, C. A.; Lyon, M. K. *Macromolecules* **2002**, *35*, 3066–3075.

(21) Gu, W.; Huh, J.; Hong, S. W.; Sveinbjornsson, B. R.; Park, C.; Grubbs, R. H.; Russell, T. P. *ACS Nano* **2013**, *7*, 2551–2558.

(22) Song, D.-P.; Li, C.; Colella, N. S.; Xie, W.; Li, S.; Lu, X.; Gido, S.; Lee, J.-H.; Watkins, J. J. *J. Am. Chem. Soc.* **2015**, *137*, 12510–12513.

(23) Xia, Y.; Kornfield, J. A.; Grubbs, R. H. *Macromolecules* **2009**, *42*, 3761–3766.

(24) Xia, Y.; Olsen, B. D.; Kornfield, J. A.; Grubbs, R. H. *J. Am. Chem. Soc.* **2009**, *131*, 18525–18532.

(25) Miyake, G. M.; Weitekamp, R. A.; Piunova, V. A.; Grubbs, R. H. *J. Am. Chem. Soc.* **2012**, *134*, 14249–14254.

(26) Miyake, G. M.; Piunova, V. A.; Weitekamp, R. A.; Grubbs, R. H. *Angew. Chem., Int. Ed.* **2012**, *51*, 11246–11248.

(27) Rizwan, A. M.; Dennis, L. Y. C.; Liu, C. *J. Environ. Sci.* **2008**, *20*, 120–128.

(28) Li, G.; Wang, L.; Ni, H.; Pittman, C., Jr. *J. Inorg. Organomet. Polym.* **2001**, *11*, 123–154.

(29) Cordes, D. B.; Lickiss, P. D.; Rataboul, F. *Chem. Rev.* **2010**, *110*, 2081–2173.

(30) Chae, C.-G.; Yu, Y.-G.; Seo, H.-B.; Kim, M.-J.; Grubbs, R. H.; Lee, J.-S. *Macromolecules* **2018**, *ASAP*.

(31) Piunova, V. A.; Miyake, G. M.; Daeffler, C. S.; Weitekamp, R. A.; Grubbs, R. H. *J. Am. Chem. Soc.* **2013**, *135*, 15609–15616.

(32) Urbas, A.; Fink, Y.; Thomas, E. L. *Macromolecules* **1999**, *32*, 4748–4750.

(33) Urbas, A.; Sharp, R.; Fink, Y.; Thomas, E. L.; Xenidou, M.; Fetters, L. J. *Adv. Mater.* **2000**, *12*, 812–814.

(34) Tanaka, H.; Hasegawa, H.; Hashimoto, T. *Macromolecules* **1991**, *24*, 240–251.

(35) Hashimoto, T.; Tanaka, H.; Hasegawa, H. *Macromolecules* **1990**, *23*, 4378–4386.

(36) Winey, K. I.; Thomas, E. L.; Fetters, L. J. *Macromolecules* **1991**, *24*, 6182–6188.

(37) Matsen, M. W. *Macromolecules* **1995**, *28*, 5765–5773.

(38) Macfarlane, R. J.; Kim, B.; Lee, B.; Weitekamp, R. A.; Bates, C. M.; Lee, S. F.; Chang, A. B.; Delaney, K. T.; Fredrickson, G. H.; Atwater, H. A.; Grubbs, R. H. *J. Am. Chem. Soc.* **2014**, 17374–17377.

(39) Tarascon, J. M.; Armand, M. *Nature* **2001**, *414*, 359–367.

(40) Goodenough, J. B.; Kim, Y. *Chem. Mater.* **2010**, *22*, 587–603.

(41) Hallinan, D. T.; Balsara, N. P. *Annu. Rev. Mater. Res.* **2013**, *43*, 503–525.

(42) Schulze, M. W.; McIntosh, L. D.; Hillmyer, M. A.; Lodge, T. P. *Nano Lett.* **2013**, *14*, 122–126.

(43) Young, W.-S.; Kuan, W.-F.; Epps, T. H. *J. Polym. Sci., Part B: Polym. Phys.* **2014**, *52*, 1–16.

(44) Agrawal, R. C.; Pandey, G. P. *J. Phys. D: Appl. Phys.* **2008**, *41*, 223001.

(45) Singh, M.; Odusanya, O.; Wilmes, G. M.; Eitouni, H. B.; Gomez, E. D.; Patel, A. J.; Chen, V. L.; Park, M. J.; Fragouli, P.; Iatrou, H.; Hadjichristidis, N.; Cookson, D.; Balsara, N. P. *Macromolecules* **2007**, *40*, 4578–4585.

(46) Panday, A.; Mullin, S.; Gomez, E. D.; Wanakule, N.; Chen, V. L.; Hexemer, A.; Pople, J.; Balsara, N. P. *Macromolecules* **2009**, *42*, 4632–4637.

(47) Young, W.-S.; Albert, J. N. L.; Schantz, A. B.; Epps, T. H. *Macromolecules* **2011**, *44*, 8116–8123.

(48) Sun, J.; Stone, G. M.; Balsara, N. P.; Zuckermann, R. N. *Macromolecules* **2012**, *45*, 5151–5156.

(49) Cowie, J. M. G.; Sadaghianizadeh, K. *Solid State Ionics* **1990**, *42*, 243–249.

(50) Kuan, W.-F.; Remy, R.; Mackay, M. E.; Epps, T. H. *RSC Adv.* **2015**, *5*, 12597–12604.

(51) Zhang, Y.; Costantini, N.; Mierzwa, M.; Pakula, T.; Neugebauer, D.; Matyjaszewski, K. *Polymer* **2004**, *45*, 6333–6339.

(52) Lascaud, S.; Perrier, M.; Vallee, A.; Besner, S.; Prud'homme, J.; Armand, M. *Macromolecules* **1994**, *27*, 7469–7477.

(53) Zhao, C.; Wu, D.; Huang, N.; Zhao, H. *J. Polym. Sci., Part B: Polym. Phys.* **2008**, *46*, 589–598.

(54) Yuan, R.; Teran, A. A.; Gurevitch, I.; Mullin, S. A.; Wanakule, N. S.; Balsara, N. P. *Macromolecules* **2013**, *46*, 914–921.

(55) Teran, A. A.; Mullin, S. A.; Hallinan, D. T.; Balsara, N. P. *ACS Macro Lett.* **2012**, *1*, 305–309.

(56) Bouchet, R.; Phan, T. N. T.; Beaudoin, E.; Devaux, D.; Davidson, P.; Bertin, D.; Denoyel, R. *Macromolecules* **2014**, *47*, 2659–2665.

(57) Young, N. P.; Devaux, D.; Khurana, R.; Coates, G. W.; Balsara, N. P. *Solid State Ionics* **2014**, *263*, 87–94.

(58) Gomez, E. D.; Panday, A.; Feng, E. H.; Chen, V.; Stone, G. M.; Minor, A. M.; Kisielowski, C.; Downing, K. H.; Borodin, O.; Smith, G. D.; Balsara, N. P. *Nano Lett.* **2009**, *9*, 1212–1216.

(59) Ganesan, V.; Pyramitsyn, V.; Bertoni, C.; Shah, M. *ACS Macro Lett.* **2012**, *1*, 513–518.

(60) Hou, W.-H.; Chen, C.-Y.; Wang, C.-C.; Huang, Y.-H. *Electrochim. Acta* **2003**, *48*, 679–690.

(61) Chintapalli, M.; Chen, X. C.; Thelen, J. L.; Teran, A. A.; Wang, X.; Garetz, B. A.; Balsara, N. P. *Macromolecules* **2014**, *47*, 5424–5431.

(62) Pakula, T.; Zhang, Y.; Matyjaszewski, K.; Lee, H.-i.; Boerner, H.; Qin, S.; Berry, G. C. *Polymer* **2006**, *47*, 7198–7206.

(63) Quartarone, E.; Mustarelli, P. *Chem. Soc. Rev.* **2011**, *40*, 2525–2540.

(64) Armand, M.; Endres, F.; MacFarlane, D. R.; Ohno, H.; Scrosati, B. *Nat. Mater.* **2009**, *8*, 621–629.

(65) Ye, Y.-S.; Rick, J.; Hwang, B.-J. *J. Mater. Chem. A* **2013**, *1*, 2719–2743.

(66) Welton, T. *Chem. Rev.* **1999**, *99*, 2071–2084.

(67) Galiński, M.; Lewandowski, A.; Stępniak, I. *Electrochim. Acta* **2006**, *51*, 5567–5580.

(68) Lee, K. H.; Zhang, S.; Lodge, T. P.; Frisbie, C. D. *J. Phys. Chem. B* **2011**, *115*, 3315–3321.

(69) Fullerton-Shirey, S. K.; Maranas, J. K. *Macromolecules* **2009**, *42*, 2142–2156.

(70) He, Y.; Boswell, P. G.; Bühlmann, P.; Lodge, T. P. *J. Phys. Chem. B* **2007**, *111*, 4645–4652.

(71) Seitz, M. E.; Burghardt, W. R.; Faber, K. T.; Shull, K. R. *Macromolecules* **2007**, *40*, 1218–1226.

(72) Heimenz, P. C.; Lodge, T. P. *Polymer Chemistry*; 2nd ed.; CRC Press: Boca Raton, FL, 2007.

(73) Hu, M.; Xia, Y.; McKenna, G. B.; Kornfield, J. A.; Grubbs, R. H. *Macromolecules* **2011**, *44*, 6935–6943.

(74) Dalsin, S. J.; Hillmyer, M. A.; Bates, F. S. *Macromolecules* **2015**, *48*, 4680–4691.

(75) Zhang, S.; Lee, K. H.; Frisbie, C. D.; Lodge, T. P. *Macromolecules* **2011**, *44*, 940–949.

(76) Susan, M. A. B. H.; Kaneko, T.; Noda, A.; Watanabe, M. *J. Am. Chem. Soc.* **2005**, *127*, 4976–4983.

(77) Tang, B.; White, S. P.; Frisbie, C. D.; Lodge, T. P. *Macromolecules* **2015**, *48*, 4942–4950.

(78) McNicholas, B. J.; Blakemore, J. D.; Chang, A. B.; Bates, C. M.; Kramer, W. W.; Grubbs, R. H.; Gray, H. B. *J. Am. Chem. Soc.* **2016**, *138*, 11160–11163.
(79) Hawecker, J.; Lehn, J.-M.; Ziessel, R. *J. Chem. Soc., Chem. Commun.* **1983**, 536–538.
(80) Hawecker, J.; Lehn, J.-M.; Ziessel, R. *J. Chem. Soc., Chem. Commun.* **1984**, 328–330.
(81) Blakemore, J. D.; Gupta, A.; Warren, J. J.; Brunschwig, B. S.; Gray, H. B. *J. Am. Chem. Soc.* **2013**, *135*, 18288–18291.

Appendix A

Appendix to Chapter 2: Control over the Graft Polymer Architecture via Ring-Opening Metathesis Polymerization

1. Lin, T.-P.; Chang, A. B.; Chen, H.-Y.; Liberman-Martin, A. L.; Bates, C. M.; Voegtle, M. J.; Bauer, C. A.; Grubbs, R. H. Control of Grafting Density and Distribution in Graft Polymers by Living Ring-Opening Metathesis Copolymerization. *J. Am. Chem. Soc.* **2017**, *139*, 3896–3903.

2. Chang, A. B.;$^+$ Lin, T.-P.;$^+$ Thompson, N. B.; Luo, S.-X.; Liberman-Martin, A. L.; Chen, H.-Y.; Grubbs, R. H. Design, Synthesis, and Self-Assembly of Polymers with Tailored Graft Distributions. *J. Am. Chem. Soc.* **2017**, *139*, 17683–17693. ($^+$*Equal contributions.*)

Table of Contents

A-1 Instrumentation

Ambient-temperature NMR spectra were recorded on a Varian 400 MHz or 500 MHz NMR spectrometer. Chemical shifts (δ) were given in ppm and referenced against residual solvent signals (^{1}H, ^{13}C). SEC data were collected using two Agilent PLgel MIXED-B 300 × 7.5 mm columns with 10 μm beads, connected to an Agilent 1260 Series pump, a Wyatt 18-angle DAWN HELEOS light scattering detector, and Optilab rEX differential refractive index detector. Online determination of d*n*/d*c* assumed 100% mass elution under the peak of interest. The mobile phase was THF. Thermal profiles of polymer samples were obtained using a Hitachi DSC7020 calorimeter with an aluminum reference pan. Following an initial run to erase thermal history (by heating from 25 °C to 130 °C at a rate of 10 °C/min), sample temperature was maintained at 120 °C in an external oven while the furnace cooled for approximately 20 minutes. Samples were then removed from the oven, cooled for 45 seconds on a thermally conductive surface, then rerun through an identical calorimeter cycle (25–130 °C, 10 °C/min). The reported data were collected on the second heating ramp.

A-2 Macromonomer Synthesis

The work presented in this thesis employs macromonomers featuring poly(D,L-lactide) (**PLA**), polystyrene (**PS**), poly(dimethyl siloxane) (**PDMS**), and poly(ethylene oxide) (**PEO**) side chains. This section describes the synthesis of all macromonomers.

*A-2.1 Synthesis of Poly(D,L-lactide) Macromonomer (**PLA**)[1]*

Scheme A.1: Synthesis of *cis*-5-norbornene-*exo*-dicarboxylic anhydride (**A.1**).

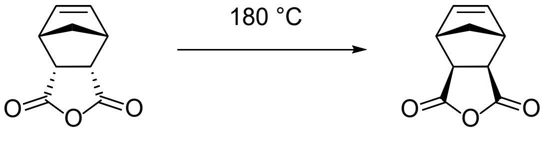

A.1

A 500 mL round bottom flask was half filled with commercially available *cis*-5-norbornene-*endo*-dicarboxylic anhydride (carbic anhydride), fitted with a reflux condenser, and heated neat at 180 °C for 16 hours. The resulting molten yellow solid was slowly cooled to 75 °C and benzene was added before the entire volume crystallized to facilitate dissolution. The resulting mixture was heated to reflux and crystallized at room temperature. The recrystallization in benzene was repeated three additional times to yield a white or slightly off-white crystalline solid (**A.1**, ca. 30 g isolated mass). ^{1}H NMR ($CDCl_3$) δ (ppm): 6.31 (2H, t), 3.43 (2H, s), 2.99 (2H, s), 1.65 (1H, m), 1.42 (1H, m).

Scheme A.2: Synthesis of *N*-hydroxyethyl-*cis*-5-norbornene-*exo*-dicarboximide initiator (**A.2**).

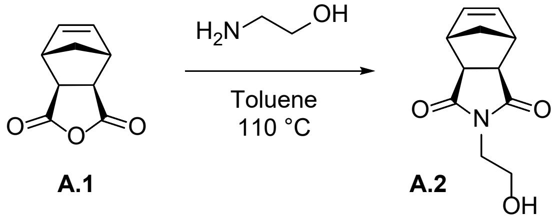

Cis-5-norbornene-*exo*-dicarboxylic anhydride (**A.1**) (1.0 eq., 2.07 g, 12.6 mmol), 2-aminoethanol (1.05 eq., 0.80 mL, 13.2 mmol), triethylamine (0.1 eq., 0.18 mL, 1.3 mmol) and toluene (15 mL) were mixed in a round bottom flask equipped with a Dean-Stark trap. The mixture was heated to reflux for 15 hours. The resulting orange solution was cooled to room temperature, and the toluene was removed *in vacuo*. The crude solid was recrystallized in ethanol to yield **A.2** as a white solid (2.4 g). ^{1}H NMR ($CDCl_3$) δ (ppm): 6.29 (2H, t), 3.78 (2H, m), 3.70 (2H, m) (2H, d), 3.28 (2H, t), 2.71 (2H, d), 1.50 (1H, dt), 1.34 (1H, d).

Scheme A.3: Synthesis of *ω*-norbornenyl poly(D,L-lactide) (**PLA**) macromonomer.

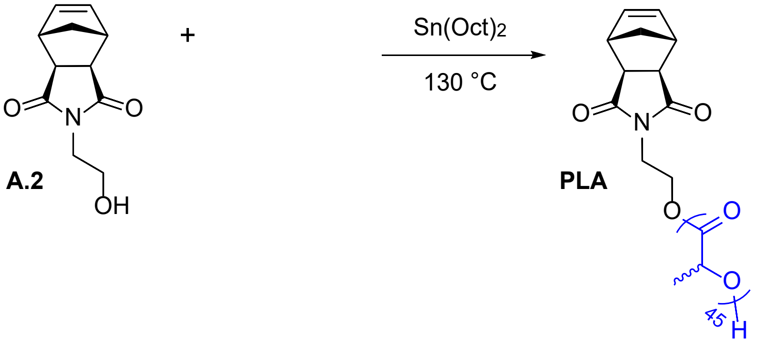

For this representative example, ^{1}H NMR end group analysis indicates M_n = 3450 g/mol. A flame-dried Schlenk flask was charged with a stir bar, initiator **A.2** (2.00 g, 9.65 mmol, 1.00 equiv), and racemic 3,6-dimethyl-1,4-dioxane-2,5-dione (29.2 g, 203 mmol, 21.0 equiv). The flask was subjected to three pump-purge cycles using argon, then transferred to an oil bath heated to 130 °C. Once the contents of the flask had fully melted (approx. 0.5 hr), one drop of the catalyst, tin (II) 2-ethylhexanoate (≈ 5 mg), was added using a 21G needle. The reaction was allowed to stir at 130 °C for 4 hr, then quenched by rapidly cooling in a dry ice bath. The solid was dissolved in dichloromethane, and then the solution was filtered through basic alumina to remove the tin catalyst. The solution was concentrated by rotary evaporation until slightly viscous, then precipitated dropwise to stirring cold (−78 °C) methanol. The solid was isolated by centrifugation and dried under high vacuum to yield the PLA macromonomer as a white crystalline solid. The ^{1}H NMR spectrum in $CDCl_3$ is provided in Figure A.1.

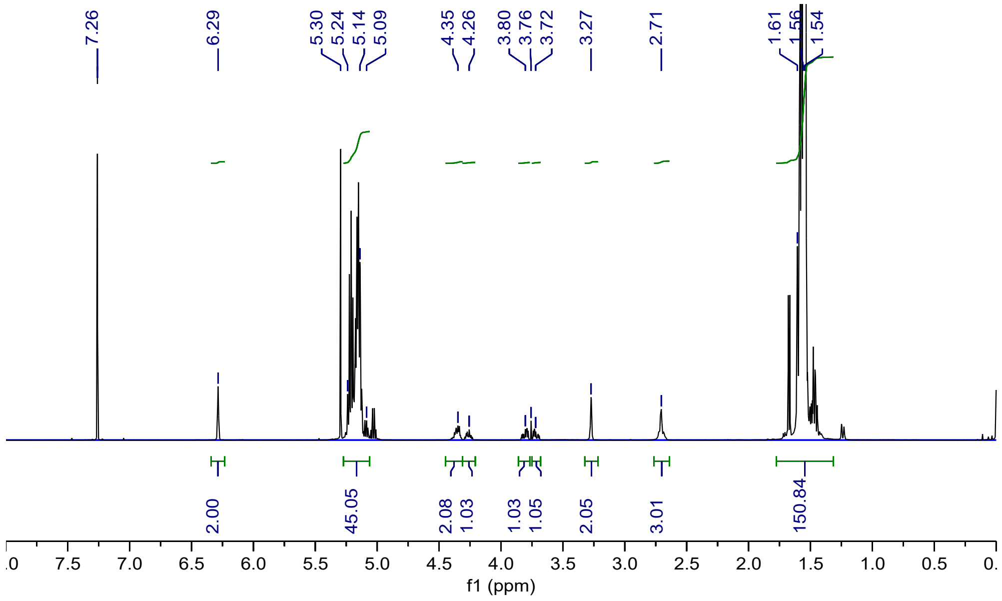

Figure A.1: ^{1}H NMR spectrum of **PLA** macromonomer in $CDCl_3$.

*A-2.2 Synthesis of Polystyrene Macromonomer (**PS**)*[2]

Scheme A.4: Synthesis of *N*-propargyl-*cis*-5-norbornene-*exo*-dicarboximide (**A.3**).

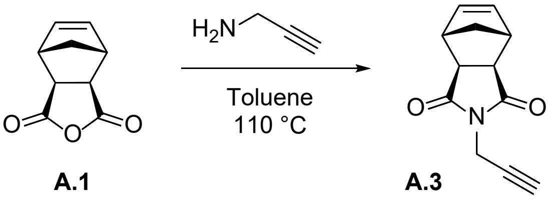

Cis-5-norbornene-*exo*-dicarboxylic anhydride (**A.1**) (1.0 eq., 62.59 g, 381.2 mmol), propargylamine (1.0 eq., 21 g, 381.2 mmol), triethylamine (0.1 eq., 3.86 g, 38.1 mmol) and toluene (300 mL) were mixed in a round bottom flask equipped with a Dean-Stark trap. The mixture was heated to reflux for 15 hours. The resulting orange solution was cooled to room temperature, and the toluene was removed *in vacuo*. The crude solid was recrystallized in ethanol to yield **A.3** as light brown, plate-like crystals (56.25 g). ^{1}H NMR ($CDCl_3$) δ (ppm): 6.28 (2H, m), 4.20 (2H, d), 3.30 (2H, m), 2.70 (2H, d), 2.17 (1H, t), 1.50 (1H, d), 1.25 (1H, d).

Scheme A.5: Synthesis of PS-Br (**A.4**) by atom-transfer radical polymerization (ATRP).

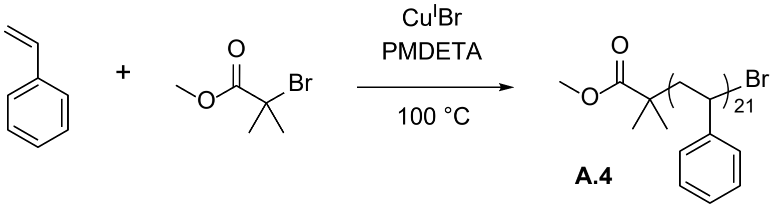

For this representative example, ^{1}H NMR end group analysis indicates M_n = 2390 g/mol. Styrene monomer (500 mL) was stirred with basic alumina for 30 min and filtered to yield a clear liquid. Styrene (50.0 eq., 350 mL, 3.054 mol) was added to a 500 mL Schlenk flask equipped with a stir bar and septum. The flask was charged with ligand *N,N,N',N',N''*-pentamethyldiethylenetriamine (0.3 eq., 3.83 mL, 0.018 mol) and subsequently freeze-pump-thawed three times to remove oxygen. The flask was frozen in liquid nitrogen, placed under an active flow of argon (while still frozen), and Cu^{I}Br (0.3 eq., 2.63 g, 0.018 mol) was quickly added upon removal of the septum. The septum was re-attached, the argon flow stopped, and the flask was evacuated. (Caution: argon condenses at liquid nitrogen temperatures and can cause an explosion upon expansion when thawed.) Three additional pump/purge (argon/vacuum) cycles were performed and the flask was left under dynamic vacuum for at least 5 min. The flask was thawed in warm water and placed under argon. Most, but not all, of the copper dissolved to yield a green solution. (A blue color indicates oxygen contamination; a yellow color indicates insufficient copper dissolution – both result in a failed polymerization.) In a separate flask, methyl α-bromoisobutyrate was freeze-pump-thawed three times. Methyl α-bromoisobutyrate (1.0 eq., 7.90 mL, 0.061 mol) was injected into the Schlenk flask containing styrene and the mixture was heated in an oil bath pre-set to 100 °C. Aliquots were collected every ca. 30 min under a dynamic flow of argon. Conversion was monitored by ^{1}H NMR. The polymerization was quenched in liquid nitrogen after 2 hr 35 min at approximately 38% conversion. The viscous solution was warmed to room temperature, diluted with tetrahydrofuran (100 mL), filtered through basic alumina to remove copper, and precipitated into methanol at -78 °C. The polymer was redissolved in THF, precipitated five more times into methanol at −78 °C, and dried *in vacuo* to yield **A.4** as a white powder.

Scheme A.6: End group conversion: PS-Br to PS-N_3 (**A.5**)

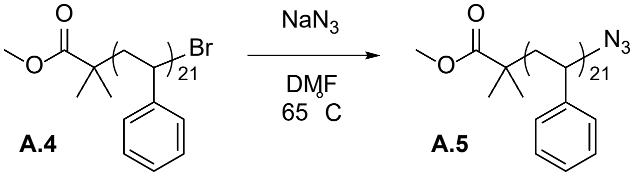

Bromo-terminated polystyrene (**A.4**) (1.0 eq., 73 g, 37.0 mmol), sodium azide (3.0 eq., 7.12 g, 109.5 mmol), and dimethylformamide (350 mL) were mixed in a round bottom flask equipped with a stir bar and reflux condenser. The mixture was heated at 65 °C for 16 hr and then cooled to room temperature. The product was precipitated into methanol at −78 °C then redissolved in THF five times in total. Quantitative conversion of the end group was observed by ^{1}H NMR ($CDCl_3$) δ (ppm): PS-Br 4.6–5.0 ppm, PS-N_3 3.75–4.25.

Scheme A.7: Synthesis of ω-norbornenyl polystyrene macromonomer (**PS**).

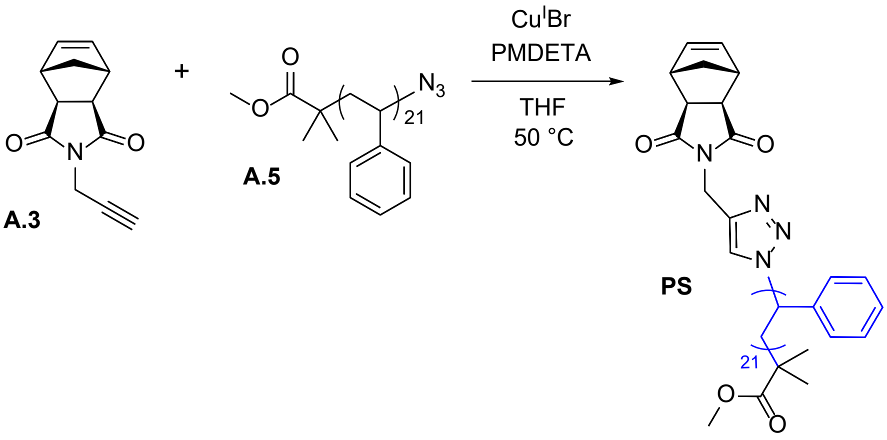

Azide-terminated polystyrene (**A.5**) (1.0 eq., 64.30 g, 30.6 mmol), *N*-propargyl-*cis*-5-norbornene-*exo*-dicarboximide (**A.3**) (1.5 eq., 9.24 g, 45.9 mmol), and Cu^IBr (0.4 eq., 1.76 g, 12.3 mmol) were added to a 500 mL three-neck round bottom flask equipped with a stir bar, reflux condenser, and two septa. The flask was pump/purged with argon three times and placed under argon. Dry tetrahydrofuran (180 mL) was added via syringe, followed by *N,N,N′,N′,N″*-pentamethyldiethylenetriamine (0.4 eq., 2.56 mL, 12.3 mmol), upon which the solution turned light green and clear. The flask was heated at 50 °C for 16 hr and cooled to room temperature. The solution was diluted with tetrahydrofuran (100 mL), filtered through basic alumina to remove the copper, and precipitated into methanol at −78 °C. The precipitation was repeated five additional times to yield a white powder. Quantitative conversion of the end group was observed by ^1H NMR ($CDCl_3$) δ (ppm): PS-N_3 3.75–4.25, PS-norbornene 4.89–5.05 (Figure A.2).

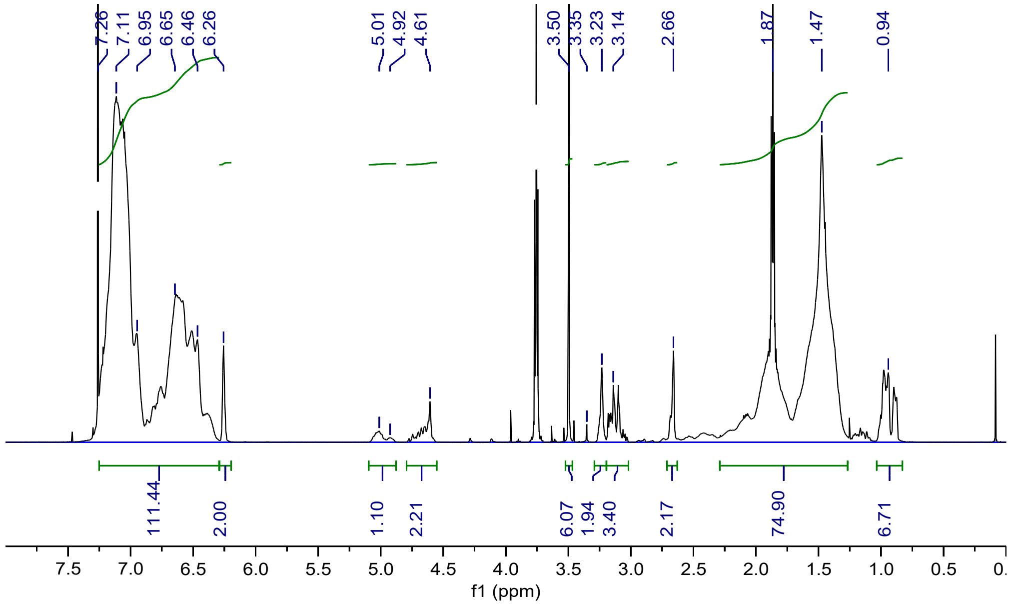

Figure A.2: ^{1}H NMR spectrum of **PS** macromonomer in $CDCl_3$.

*A-2.3 Synthesis of Poly(dimethyl siloxane) Macromonomer (**PDMS**)*[3]

Scheme A.8: Synthesis of *N*-(hexanoic acid)-*cis*-5-norbornene-*exo*-dicarboximide (**A.6**).

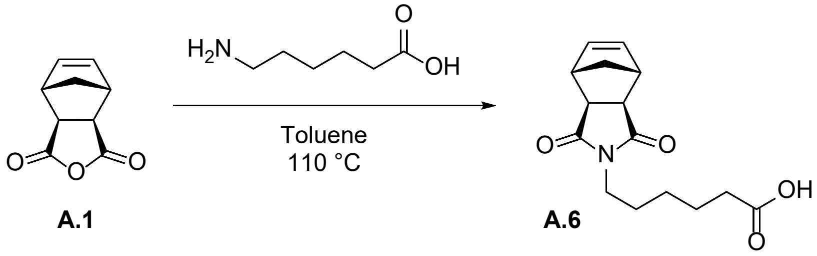

Cis-5-norbornene-*exo*-dicarboxylic anhydride (**A.1**) (1.0 eq., 8.00 g, 48.7 mmol), 6-aminohexanoic acid (1.0 eq., 6.39 g, 48.7 mmol), triethylamine (0.1 eq., 0.679 mL, 4.87 mmol), and toluene (51 mL) were added to a round bottom flask equipped with a stir bar and reflux condenser. The mixture was heated at 110 °C for 19 hr, cooled to room temperature, and the solvent was removed *in vacuo*. The remaining solid was redissolved in dichloromethane, washed with water (x3) then brine (x3), and dried with magnesium sulfate. The solvent was removed *in vacuo* to yield **A.6** as a white solid. ^{1}H NMR ($CDCl_3$) δ (ppm): 6.28 (2H, m), 3.46 (2H, t), 3.27 (2H, m), 2.35 (2H, t), 1.72–1.18 (10H, m).

Scheme A.9: Synthesis of ω-norbornenyl poly(dimethyl siloxane) macromonomer (**PDMS**).

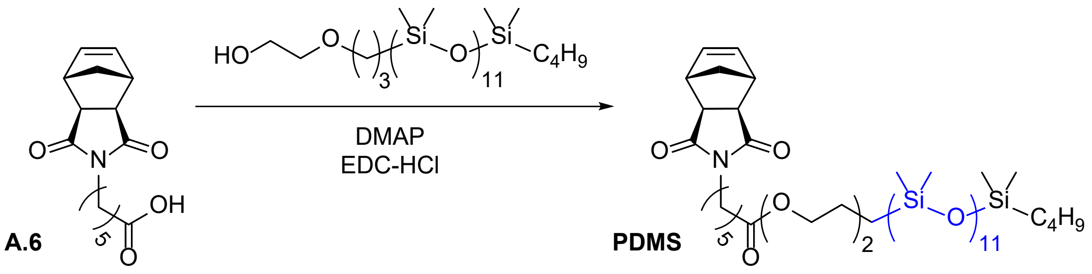

N-(hexanoic acid)-*cis*-5-norbornene-*exo*-dicarboximide (**A.6**) (1.2 eq., 6.00 g, 21.6 mmol), alcohol-terminated PDMS (1.0 eq., 18.1 g, 18.1 mmol, M_n = 1000 g/mol from Gelest), 1-ethyl-3-(3-dimethylaminopropyl)carbodiimide (1.6 eq., 5.52 g, 28.8 mmol), 4-dimethylaminopyridine (0.1 eq., 0.22 g, 1.80 mmol), and dichloromethane (250 mL) were mixed in a 500 mL round bottom flask equipped with a stir bar. The reaction was stirred for 20 hr under air at room temperature. The mixture was washed with 1 M HCl (x3), brine (x3), and deionized water (x3). The organic solution was stirred over anhydrous $MgSO_4$ then filtered, and dichloromethane was removed *in vacuo*. The product was filtered through a plug of silica with dichloromethane (2 L) then dried *in vacuo* to yield **PDMS** as a colorless oil (18.6 g, 82%).

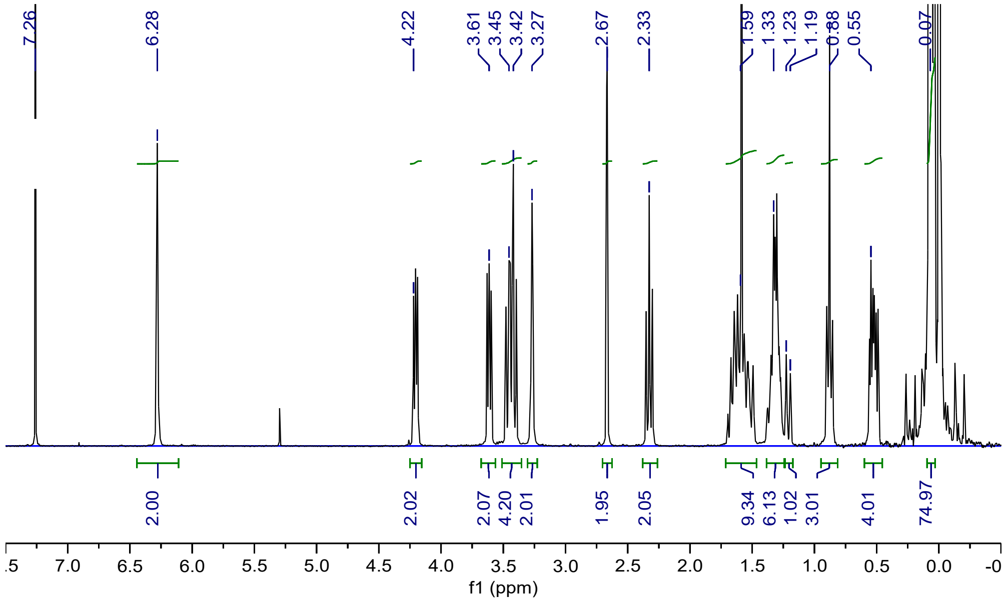

Figure A.3: ^{1}H NMR spectrum of **PDMS** macromonomer in $CDCl_3$.

*A-2.4 Synthesis of Poly(ethylene oxide) Macromonomer (**PEO**)*[2]

Scheme A.10: Synthesis of ω-norbornenyl poly(ethylene oxide) macromonomer (**PEO**).

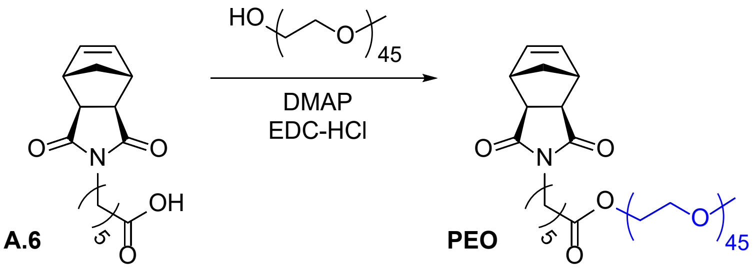

N-(hexanoic acid)-*cis*-5-norbornene-*exo*-dicarboximide (**A.6**) (1.2 eq., 19.74 g, 71.2 mmol), poly(ethylene glycol) methyl ether (1.0 eq., 118.64 g, 59.3 mmol, M_n = 2000 g/mol, 1-ethyl-3-(3-dimethylaminopropyl)carbodiimide (1.6 eq., 18.24 g, 117.5 mmol), 4-dimethylaminopyridine (0.1 eq., 0.73 g, 5.9 mmol), and dichloromethane (790 mL) were mixed in a 1 L round bottom flask equipped with a stir bar. The reaction was stirred for 24 hr, then half of the dichloromethane was removed *in vacuo*. The mixture was washed with 1 M HCl (x3), brine (x1), and dried with sodium sulfate. Most of the solvent was removed *in vacuo* and the remaining solution was precipitated into diethyl ether at −78 °C. The off-white solid was filtered and dried *in vacuo* to yield 123.3 g (93%) of isolated material.

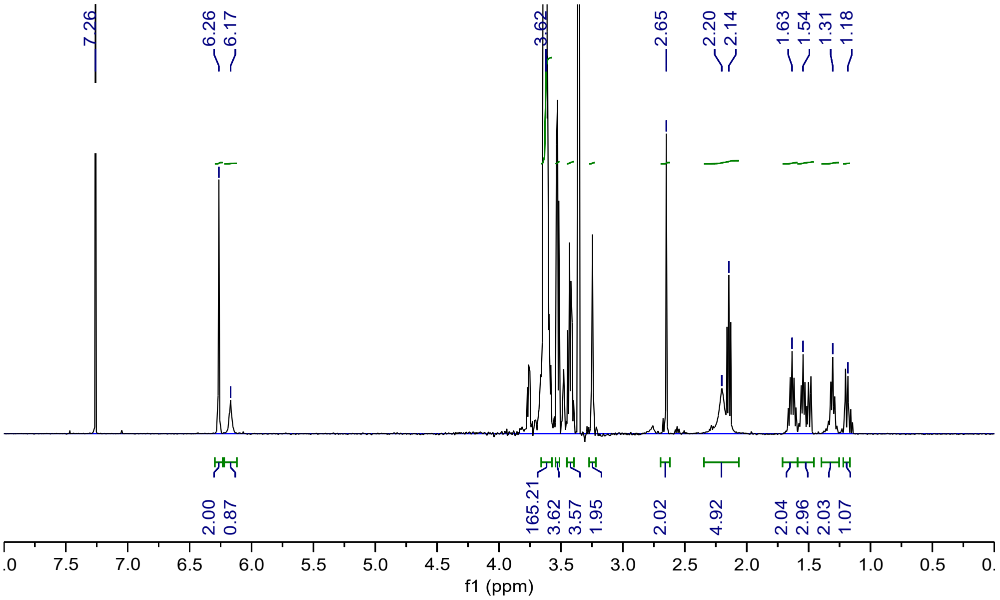

Figure A.4: ^{1}H NMR spectrum of **PEO** macromonomer in $CDCl_3$.

A-3 Diluent Synthesis

Norbornene diluents were prepared according to reported procedures. General synthetic schemes are provided in Schemes A.11−A.16. Diluents are identified as reported in Chapter 2 (**1a**, **1b**, etc.).

Scheme A.11: Synthesis of *endo*,*exo*-norbornenyl diester diluents (**1a**–**1d**).

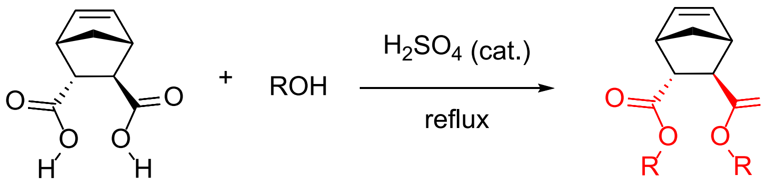

R = Me (**1a**), Et (**1b**),
^{n}Pr (**1c**), ^{n}Bu (**1d**)

Cis-5-norbornene-*endo,exo*-2,3-dicarboxylic acid (5 g, 27.5 mmol) was added to 50 mL of the corresponding anhydrous alcohol. To this mixture was added ~50 mg of conc. H_2SO_4. After stirring at 50 °C for 12 h, an excess of solid $KHCO_3$ was added to quench the reaction. The alcohol was removed under reduced pressure, and 30 mL CH_2Cl_2 was added. The organic solution was washed with brine (20 mL × 3), dried with $MgSO_4$, and filtered to afford a colorless oil. The product was purified by either vacuum distillation or recrystallization from cold *n*-pentane.

Scheme A.12: Synthesis of *endo*,*exo*-norbornenyl diester diluents (**1e**–**1j**).

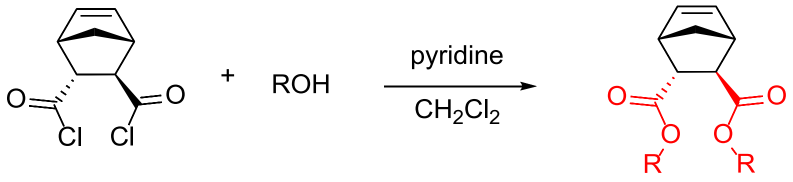

R = ^{i}Pr (**1e**), ^{t}Bu (**1f**), CH_2CF_3 (**1g**),
Ph (**1h**), *p*-CF_3Ph (**1i**), *p*-MeOPh (**1j**)

Cis-5-norbornene-*endo,exo*-2,3-diacyl chloride (3 mL, 18.5 mmol) was dissolved in CH_2Cl_2 (25 mL) and pyridine (4.91 mL, 61.0 mmol). A CH_2Cl_2 solution (5 mL) of the corresponding anhydrous alcohol (42.5 mmol) was slowly added at –78 °C. The mixture was allowed to slowly warm to room temperature over 1 hour and was allowed to stir for 12 h. The pyridinium salt was removed by filtration. The organic solution was washed with brine (20 mL × 3), dried with $MgSO_4$, and filtered to afford a colorless oil. The product was purified by either vacuum distillation or recrystallization from cold *n*-pentane.

Scheme A.13: Synthesis of *endo*,*endo*-norbornenyl diester diluents (**2a**–**2d**).

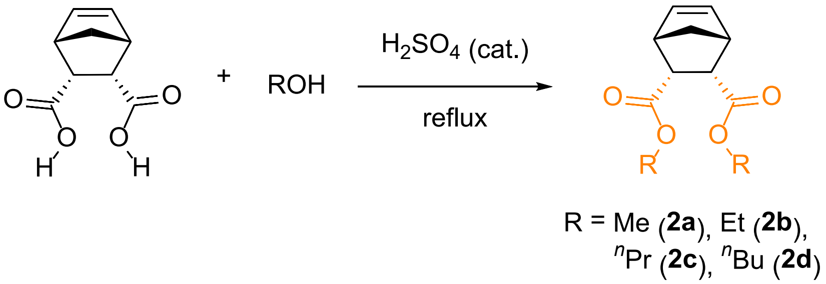

A suspension of *cis*-5-norbornene-*endo,endo*-2,3-dicarboxylic acid (2.0 g, 11 mmol), 4 drops of concentrated sulfuric acid, and 20 mL of the corresponding anhydrous alcohol was stirred under air at 75 °C. After 36 hours, the solution was cooled to room temperature and was concentrated under reduced pressure. The resulting oil was redissolved in 50 mL CH_2Cl_2 and washed with saturated aqueous $NaHCO_3$ (2 × 30 mL) and brine (1 × 30 mL). The organic solution was dried over $MgSO_4$, filtered, and concentrated *in vacuo* to afford an oil. The oil was filtered through a plug of basic alumina, precipitated from cold (–78 °C) hexanes, and dried *in vacuo* to obtain the product as a white crystalline solid (**2a**), pink oil (**2b–2c**) or colorless oil (**2d**).

Scheme A.14: Synthesis of *exo*,*exo*-norbornenyl diester diluents (**3a**–**3d**).

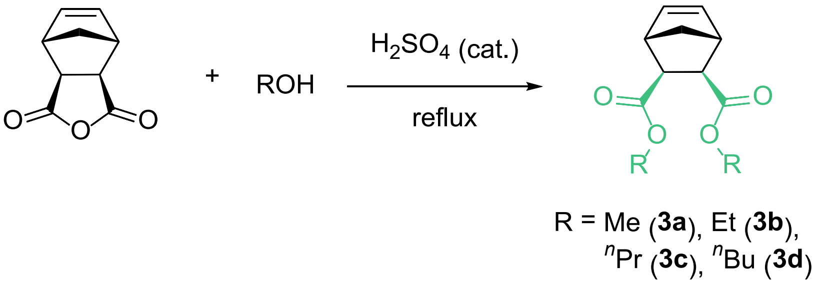

A suspension of *cis*-5-norbornene-*exo*-2,3-dicarboxylic anhydride (2.00 g, 12.2 mmol), 4 drops of concentrated sulfuric acid, and 20 mL of the corresponding anhydrous alcohol was stirred under air at 75 °C. After 20 hours, the colorless solution was cooled to room temperature and was concentrated under reduced pressure. The resulting pale yellow oil was redissolved in 50 mL CH_2Cl_2 and washed with saturated aqueous $NaHCO_3$ (2 × 30 mL) and brine (1 × 30 mL). The organic solution was dried over $MgSO_4$, filtered, and concentrated *in vacuo* to afford a colorless oil. Precipitation from cold (–78 °C) hexanes produced the product as a white crystalline solid (**3a**) or colorless oil (**3b**–**3d**) that was dried *in vacuo.*

Scheme A.15: Synthesis of *endo*-norbornenyl imide diluents (**4a**–**4c**).

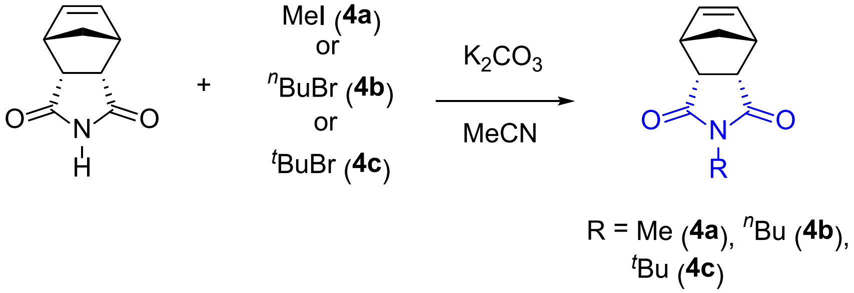

To a 10 mL MeCN solution of *cis*-5-norbornene-*endo*-2,3-diimide (1 g, 6.13 mmol) was added the corresponding alkyl halide (12.3 mmol) and K_2CO_3 (1.69 g, 12.3 mmol). The resulting mixture was allowed to stir at room temperature for 24 h (**4a**) or at 65 °C for 54 h (**4b** and **4c**). The product was purified using column chromatography.

Scheme A.16: Synthesis of *exo*-norbornenyl imide diluents (**5a**–**5c**).

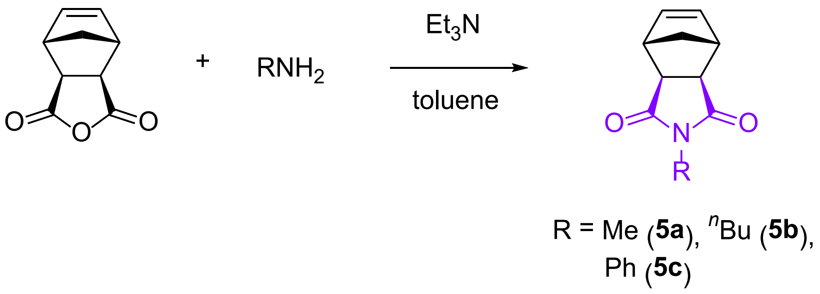

To a 20 mL toluene solution of *cis*-5-norbornene-*exo*-2,3-dicarboxylic anhydride (1 g, 6.09 mmol) was added the corresponding alkyl amine (6.70 mmol) and Et_3N (0.85 mL, 0.609 mmol). The resulting mixture was allowed to stir at 110 °C for 15 h. The product was purified using column chromatography.

A-4 Standard Procedures for Homo- and Copolymerization Kinetics

A-4.1 Standard Procedure for the Determination of Homopolymerization Rate Constants

A 4 mL vial was charged with a flea stir bar and a norbornene monomer (0.025 mmol) in CH_2Cl_2 at 298 K. While stirring vigously, the polymerization was initiated by adding a CH_2Cl_2 solution of **G3** (0.0125 M, 20 µL, 0.25 µmol) to achieve initial conditions of $[\text{norbornene}]_0$ (0.05 M) and $[\mathbf{G3}]_0$ (0.5 mM). During the course of the reaction, aliquots (~20 µL) were extracted at different time points and immediately quenched into a seperate vial containing a large excess of ethyl vinyl ether (~0.2 mL) and silica-bound metal scavenger (SiliaMetS, dimercaptotriazine [DMT]) in THF. The quenched reaction mixtures were subsequentially subjected to SEC and ^{1}H NMR analysis, allowing the determination of $[\text{norbornene}]_t$. For each homopolymerization experiment, the self-propagation rate constant k_{homo} was determined according to Eq. 2-1.

A-4.2 Standard Procedure for the Determination of Copolymerization Reactivity Ratios

A 4 mL vial was charged with a flea stir bar and a CH_2Cl_2 solution of two norbornene monomers (M_1, M_2, each 0.025 mmol) at 298 K. While stirring vigously, the copolymerization was initiated by adding a CH_2Cl_2 solution of **G3** (0.0125 M, 20 µL, 0.25 µmol) to achieve initial conditions of $[M_1]_0$ (0.05 M), $[M_2]_0$ (0.05 M), and $[\mathbf{G3}]_0$ (0.5 mM).

During the course of the reaction, aliquots (~20 µL) were extracted at different time points and immediately quenched in a seperate vial containing a large excess of ethyl vinyl ether (~0.2 mL) and silica-bound metal scavenger (SiliaMetS, dimercaptotriazine [DMT]) in THF. The quenched reaction mixtures were subsequentially subjected to SEC and ^{1}H NMR analysis, allowing the determination of $[M_1]_t$ and $[M_2]_t$. Values of k_{12} and k_{21} were obtained by fitting the experimentally determined kinetic data to the numerical solutions for Eq. 2-2 to 2-5 using a MATLAB non-linear least-square solver (*lsqcurvefit*) in conjunction with non-stiff differential equation solver (*ode45*).[3]

A-5 Characterization of $(\mathbf{PLA}^{z}\text{-}\mathit{ran}\text{-}\mathbf{DME}^{1-z})_n$ Graft Polymers

Table A.1: SEC characterization of ($\mathbf{PLA}^{z}$-*ran*-$\mathbf{DME}^{1-z}$)$_n$ with variable grafting densities *z* and backbone degrees of polymerization *n*.

z	*n*	Expected M_n (kg mol^{-1})	Measured M_n^{a} (kg mol^{-1})	Difference in M_n	$Đ^a$
1.00	167	539	548	1.7%	1.03
	133	431	432	0.1%	1.01
	100	323	335	3.7%	1.01
	67	216	227	5.3%	1.01
	33	108	109	1.0%	1.02
0.75	167	413	404	-2.2%	1.03
	133	330	337	1.9%	1.03
	100	248	250	0.8%	1.03
	67	165	169	2.2%	1.02
	33	82.6	81.1	-1.8%	1.02
0.50	167	287	296	3.3%	1.03
	133	230	234	1.7%	1.02
	100	172	179	3.9%	1.01
	67	115	119	3.4%	1.01
	33	57.4	60.1	4.7%	1.02
0.25	167	161	161	0.2%	1.01
	133	129	126	-2.6%	1.01
	100	96.6	97.4	0.8%	1.01
	67	64.4	66.1	2.6%	1.01
	33	32.2	32.3	0.2%	1.02

[a] Determined by SEC of quenched aliquots of the copolymerization mixtures without further workup.

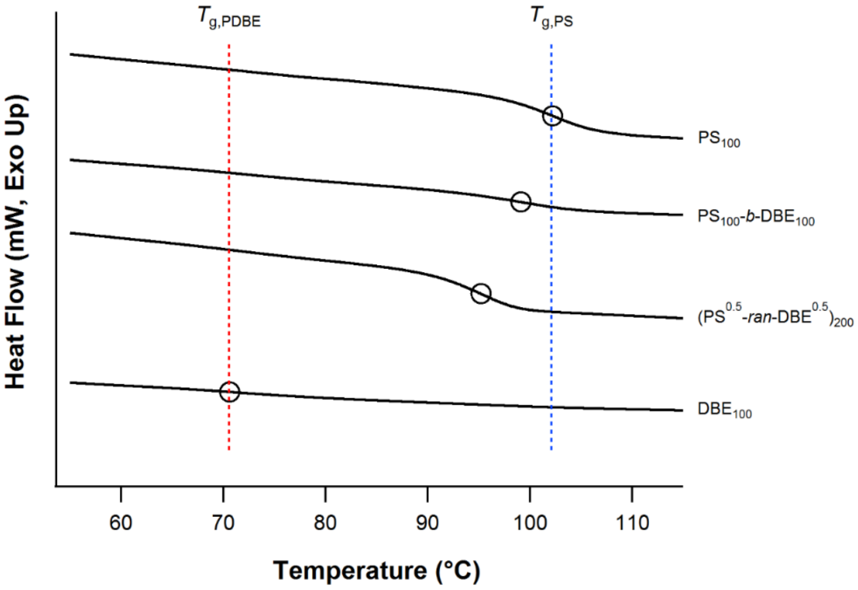

Figure A.5: Differential scanning calorimetry (DSC) data for $\mathbf{PS}_{100}$, $\mathbf{DBE}_{100}$, and two copolymers thereof: ($\mathbf{PS}_{100}$-*b*-$\mathbf{DBE}_{100}$), a block polymer with one fully grafted block and one ungrafted block, synthesized by sequential addition of **PS** and **DBE**; and $(\mathbf{PS}^{0.5}$-*ran*-$\mathbf{DBE}^{0.5})_{200}$, a random bottlebrush copolymer with 50% grafting density, synthesized by copolymerizing **PS** and **DBE** in a 1:1 feed ratio. The data were collected on the second heating cycle using a 10 °C/min ramp rate, and glass transition temperatures (T_g, open circles) were identified from the corresponding derivative curves. Both copolymers exhibit a single T_g between the T_gs of the pure components, indicating successful incorporation of both **PS** and **DBE**. The T_g of $\mathbf{PS}_{100}$-*b*-$\mathbf{DBE}_{100}$ (which has a guaranteed blocky sequence) differs from the T_g of $(\mathbf{PS}^{0.5}$-*ran*-$\mathbf{DBE}^{0.5})_{200}$ in terms of both position and shape, suggesting that $(\mathbf{PS}^{0.5}$-*ran*-$\mathbf{DBE}^{0.5})_{200}$ is at least not blocky and instead likely random as expected.

A-6 Expanding Monomer Scope: Homopolymerization Rate Constants

Table A.2: Structures and homopolymerization rate constants (k_{homo}) for all monomers synthesized and studied herein.

Anchor Group		**ID**	**R**	k_{homo} **(M^{-1} s^{-1})**
endo,exo-diester (*dx*-DE)	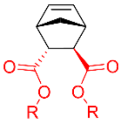	**1a**	Me	18.7
		1b	Et	14.6
		1c	^{n}Pr	10.4
		1d	^{n}Bu	6.90
		1e	^{i}Pr	6.14
		1f	^{t}Bu	5.32
		1g	CH$_2$CF$_3$	10.5
		1h	Ph	8.36
		1i	*p*-CF$_3$Ph	5.14
		1j	*p*-MeOPh	7.76
endo,endo-diester (*dd*-DE)	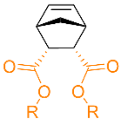	**2a**	Me	2.24
		2b	Et	0.934
		2c	^{n}Pr	0.518
		2d	^{n}Bu	0.362
exo,exo-diester (*xx*-DE)	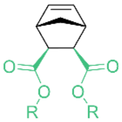	**3a**	Me	30.8
		3b	Et	16.4
		3c	^{n}Pr	11.2
		3d	^{n}Bu	10.4
endo-imide (*d*-I)	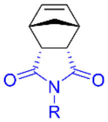	**4a**	Me	0.814
		4b	^{n}Bu	0.930
		4c	^{t}Bu	0.782
exo-imide (*x*-I)	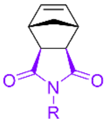	**5a**	Me	82.4
		5b	^{n}Bu	63.2
		5c	Ph	34.8
		PDMS	PDMS (1k)	21.6
		PLA	PLA (3k)	17.2
		PS	PS (4k)	4.18

A-7 Mechanistic Studies

A-7.1 Pyridine Binding

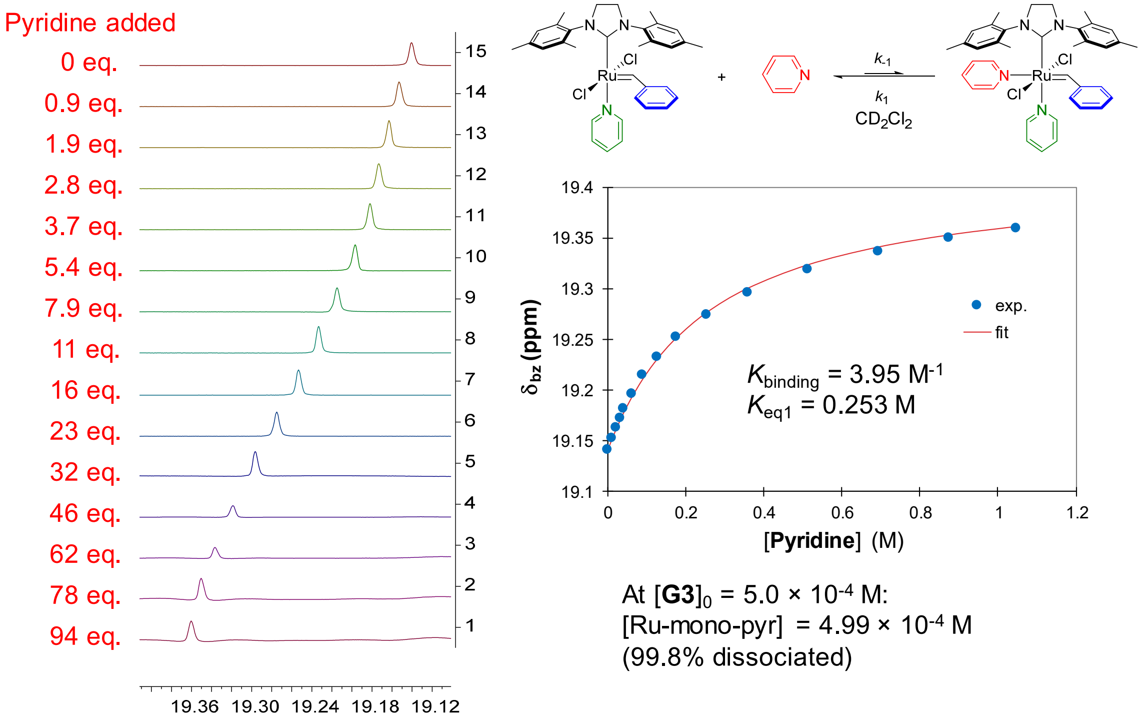

At $[\mathbf{G3}]_0 = 5.0 \times 10^{-4}$ M:
[Ru-mono-pyr] = 4.99×10^{-4} M
(99.8% dissociated)

Figure A.6: Stacked ^{1}H NMR spectra obtained during the pyridine titration experiments. To an NMR tube containing a CD_2Cl_2 solution of the monopyridine complex (11.2 mM) was titrated with a CD_2Cl_2 solution containing both pyridine (1.47 M) and the monopyridine complex (11.2 mM). The concentration of the monopyridine complex remained constant during the titrations. The chemical shifts of the benzylidene ^{1}H resonance was monitored at 298 K and could be employed to fit the pyridine binding constant ($K_{binding} = 1/K_{eq,1}$).

A-7.2 Derivation of Rate Expression (Eq. 2-8)

We derived a simplified rate expression corresponding to the proposed dissociative ROMP mechanism in which olefin coordination is the rate-limiting step:

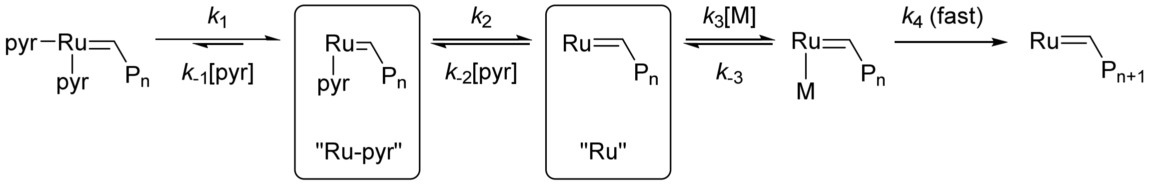

The large value estimated for $K_{eq,1} = k_1/k_{-1}$ indicates that >99.8% of the precatalyst **G3** exists as the monopyridine adduct in solution under the conditions employed in our homo- and copolymerization studies. The initial concentration of **G3** equals the sum of the concentrations of the monopyridine adduct ("Ru-pyr") and the 14-electron vacant species ("Ru"):

$$[\mathbf{G3}]_0 = [\mathrm{Ru-pyr}] + [\mathrm{Ru}] \qquad \text{Eq. A-1}$$

A steady-state approximation can be made for the 14-electron vacant species:

$$-\frac{\mathrm{d[Ru]}}{\mathrm{dt}} = k_2[\mathrm{Ru-pyr}] - k_{-2}[\mathrm{Ru}][\mathrm{pyr}] - k_3[\mathrm{Ru}][\mathrm{M}] = 0 \qquad \text{Eq. A-2}$$

Substituting A-1 in A-2 obtains the following:

$$-\frac{\mathrm{d[Ru]}}{\mathrm{dt}} = k_2[\mathbf{G3}]_0 - k_2[\mathrm{Ru}] - k_{-2}[\mathrm{Ru}][\mathrm{pyr}] - k_3[\mathrm{Ru}][\mathrm{M}] = 0 \qquad \text{Eq. A-3}$$

$$[\mathrm{Ru}] = \frac{k_2[\mathbf{G3}]_0}{k_2 + k_{-2}[\mathrm{pyr}] + k_3[\mathrm{M}]} \qquad \text{Eq. A-4}$$

$$[\mathrm{Ru}] \times \frac{1/k_{-2}}{1/k_{-2}} = \frac{K_{\mathrm{eq},2}[\mathbf{G3}]_0}{K_{\mathrm{eq},2} + [\mathrm{pyr}] + \frac{k_3}{k_{-2}}[\mathrm{M}]} \approx \frac{K_{\mathrm{eq},2}[\mathbf{G3}]_0}{K_{\mathrm{eq},2} + [\mathrm{pyr}]} \qquad \text{Eq. A-5}$$

In Eq. A-5, since $k_3 << k_{-2}$, the third term in the denominator is close to 0. The time-dependent consumption of the monomer ("M") is provided by Eq. A-6 (Eq. 2-8 in Chapter 2):

$$-\frac{\mathrm{d[M]}}{\mathrm{dt}} = k_3[\mathrm{Ru}][\mathrm{M}] = \frac{K_{\mathrm{eq},2}k_3}{K_{\mathrm{eq},2}+[\mathrm{pyr}]}[\mathbf{G3}]_0[\mathrm{M}] \qquad \text{Eq. A-6}$$

A-7.3 Rate Dependence on Catalyst Concentration

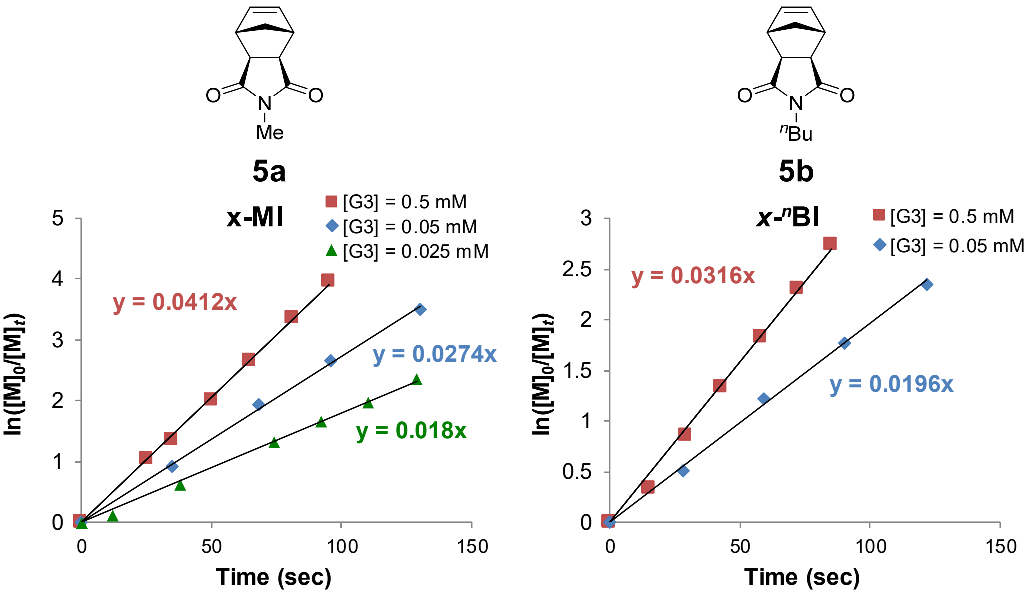

Figure A.7: ROMP of **5a** (left) and **5b** (right) in CH_2Cl_2 at 298 K showing the rate dependence on $[\mathbf{G3}]_0$ (maroon: $[\mathbf{G3}]_0 = 0.5$ mM, blue: $[\mathbf{G3}]_0 = 0.05$ mM, green: $[\mathbf{G3}]_0 = 0.025$ mM). The slope corresponds to the k_{obs} (s^{-1}). These polymerization reactions have the same $[\mathbf{5a}]_0/[\mathbf{G3}]_0$ and $[\mathbf{5b}]_0/[\mathbf{G3}]_0$ ratio of 100. Time-lapse kinetic traces were obtained using our standard homopolymerization procedure.

A-8 Copolymerization Kinetics Data

Table A.3: Compiled SEC data for **PLA** + diluent copolymerizations at full conversion.

ID	Diluent	M_n (kDa)[a]	Đ
2d	*dd*-D^{n}BuE	95.4	1.07
4c	*d*-^{t}BuI	89.9	1.10
4a	*d*-MeI	90.5	1.04
4b	*d*-^{n}BuI	103	1.04
2a	*dd*-DMeE	94.5	1.05
1d	*dx*-D^{n}BuE	101	1.04
3d	*xx*-D^{n}BuE	—[b]	—[b]
3c	*xx*-D^{n}PrE	101	1.08
3b	*xx*-DEtE	99.5	1.06
1a	*dx*-DMeE	108	1.05
3a	*xx*-DMeE	95.4	1.04
5b	*x*-^{n}BuI	95.9	1.02
5a	*x*-MeI	86.4	1.02

[a] Reported relative to polystyrene in THF (d*n*/d*c* = 0.185 mL g^{-1}).

[b] Data is not available for **PLA** + **3d**.

Table A.4: Kinetic data for the copolymerization of **PLA** (M_1, M_n = 3230 g mol^{-1}) with selected diluents (M_2). The self-propagation rate constants k_{22} and k_{11} were determined from homopolymerization experiments, and the cross-propagation rate constants k_{12} and k_{21} were determined by fitting copolymerization data using non-linear least squares regression. The reactivity ratios $r_1 = k_{11}/k_{12}$ and $r_2 = k_{22}/k_{21}$ are also provided.

ID	**Diluent**	k_{22} (M^{-1} s^{-1})	k_{11} (M^{-1} s^{-1})	k_{12} (M^{-1} s^{-1})	k_{21} (M^{-1} s^{-1})	r_1	r_2	r_1r_2	r_1/r_2
2d	*dd*-D^{n}BuE	0.362	17.2	8.03	0.860	2.14	0.421	0.902	5.09
4c	*d*-^{t}BuI	0.782	17.2	11.0	1.72	1.56	0.455	0.708	3.43
4a	*d*-MeI	0.814	17.2	4.55	1.24	3.78	0.656	2.48	5.76
4b	*d*-^{n}BuI	0.930	17.2	8.14	1.08	2.11	0.861	1.82	2.45
2a	*dd*-DMeE	2.24	17.2	8.05	2.71	2.14	0.827	1.77	2.58
1d	*dx*-D^{n}BuE	6.90	17.2	16.4	7.35	1.05	0.939	0.983	1.12
3d	*xx*-D^{n}BuE	10.4	17.2	46.0	8.94	0.374	1.17	0.436	0.320
3c	*xx*-D^{n}PrE	11.2	17.2	47.2	9.38	0.364	1.20	0.436	0.304
3b	*xx*-DEtE	16.4	17.2	48.6	10.1	0.354	1.63	0.577	0.217
1a	*dx*-DMeE	18.7	17.2	18.0	15.7	0.953	1.19	1.13	0.801
3a	*xx*-DMeE	30.8	17.2	49.2	18.3	0.350	1.68	0.588	0.208
5b	*x*-^{n}BuI	63.2	17.2	27.2	21.4	0.633	2.95	1.87	0.214
5a	*x*-MeI	82.4	17.2	28.4	27.1	0.606	3.05	1.85	0.199

Table A.5: Kinetic data for the copolymerization of **PDMS** (M_1, M_n = 1280 mol^{-1}) with selected diluents (M_2). The self-propagation rate constants k_{22} and k_{11} were determined from homopolymerization experiments, and the cross-propagation rate constants k_{12} and k_{21} were determined by fitting copolymerization data using non-linear least squares regression. The reactivity ratios $r_1 = k_{11}/k_{12}$ and $r_2 = k_{22}/k_{21}$ are also provided.

ID	**Diluent**	k_{22} (M^{-1} s^{-1})	k_{11} (M^{-1} s^{-1})	k_{12} (M^{-1} s^{-1})	k_{21} (M^{-1} s^{-1})	r_1	r_2	r_1r_2	r_1/r_2
4a	*d*-MeI	0.814	21.6	3.34	2.44	6.47	0.334	2.16	19.4
4b	*d*-^{n}BuI	0.930	21.6	6.85	2.00	3.15	0.465	1.47	6.78
1d	*dx*-D^{n}BuE	6.90	21.6	19.5	15.9	1.11	0.434	0.481	2.55
3d	*xx*-D^{n}BuE	10.4	21.6	48.2	10.3	0.448	1.02	0.455	0.441
1a	*dx*-DMeE	18.7	21.6	19.9	19.9	1.09	0.940	1.02	1.16
3a	*xx*-DMeE	30.8	21.6	50.4	26.3	0.429	1.17	0.502	0.367

Table A.6: Kinetic data for the copolymerization of **PS** (M_1, M_n = 3990 mol^{-1}) with selected diluents (M_2). The self-propagation rate constants k_{22} and k_{11} were determined from homopolymerization experiments, and the cross-propagation rate constants k_{12} and k_{21} were determined by fitting copolymerization data using non-linear least squares regression. The reactivity ratios $r_1 = k_{11}/k_{12}$ and $r_2 = k_{22}/k_{21}$ are also provided.

ID	Diluent	k_{22} (M^{-1} s^{-1})	k_{11} (M^{-1} s^{-1})	k_{12} (M^{-1} s^{-1})	k_{21} (M^{-1} s^{-1})	r_1	r_2	r_1r_2	r_1/r_2
1d	*dx*-D^{n}BuE	6.90	4.18	5.23	5.66	0.799	1.22	0.974	0.656
3d	*xx*-D^{n}BuE	10.4	4.18	29.9	7.58	0.140	1.38	0.193	0.102
1b	*dx*-DEtE	14.6	4.18	7.77	8.75	0.538	1.67	0.897	0.322
1a	*dx*-DMeE	18.7	4.18	7.74	13.2	0.540	1.42	0.765	0.381
3a	*xx*-DMeE	30.8	4.18	30.8	23.3	0.136	1.32	0.180	0.103
5b	*x*-^{n}BuI	63.2	4.18	30.8	38.9	0.136	1.63	0.221	0.0836
5a	*x*-MeI	82.4	4.18	31.9	63.2	0.131	1.30	0.171	0.100

Table A.7: Compiled SEC data for **PDMS** + diluent copolymerizations at full conversion.

ID	Diluent	M_n (kDa)^a	Đ
4a	*d*-MeI	39.3	1.04
4b	*d*-^{n}BuI	42.7	1.05
1d	*dx*-D^{n}BuE	32.5	1.06
3d	*xx*-D^{n}BuE	39.9	1.09
1a	*dx*-DMeE	32.2	1.04
3a	*xx*-DMeE	37.9	1.03

[a] Reported relative to polystyrene in THF (d*n*/d*c* = 0.185 mL g^{-1}).

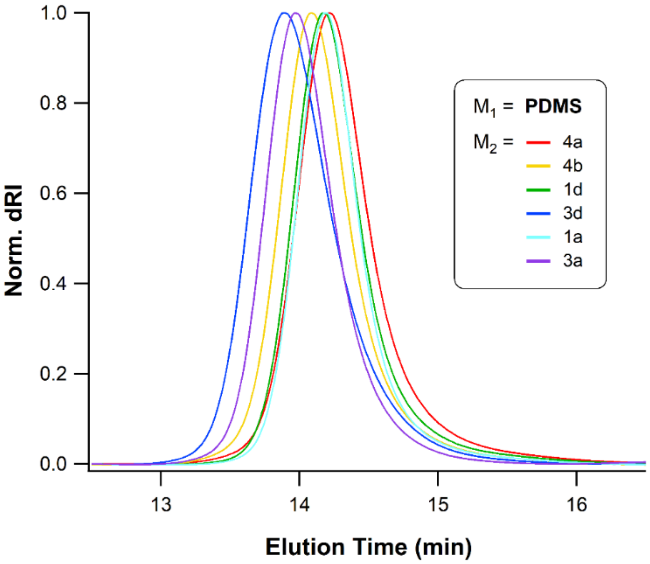

Figure A.8: SEC traces for **PDMS** + diluent copolymerizations at full conversion.

Table A.8: Compiled SEC data for **PS** + diluent copolymerizations at full conversion.

ID	**Diluent**	***M*$_n$ (kDa)**	***Đ***
1d	*dx*-D^{n}BuE	362	1.09
3d	*xx*-D^{n}BuE	379	1.09
1b	*dx*-DEtE	398	1.10
1a	*dx*-DMeE	375	1.04
3a	*xx*-DMeE	376	1.05
5b	*x*-^{n}BuI	386	1.04
5a	*x*-MeI	364	1.06

[a] Reported relative to polystyrene in THF (d*n*/d*c* = 0.185 mL g^{-1}).

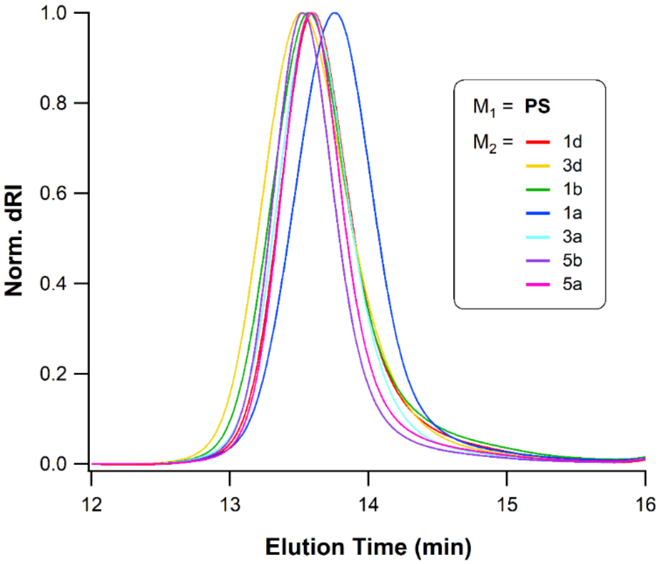

Figure A.9: SEC traces for **PS** + diluent copolymerizations at full conversion.

References

(1) Sveinbjörnsson, B. R.; Weitekamp, R. A.; Miyake, G. M.; Xia, Y.; Atwater, H. A.; Grubbs, R. H. *Proc. Natl. Acad. Sci. U.S.A.* **2012**, *109*, 14332–14336.

(2) Bates, C. M.; Chang, A. B.; Momčilović, N.; Jones, S. C.; Grubbs, R. H. *Macromolecules* **2015**, *48*, 4967–4973.

(3) Lin, T.-P.; Chang, A. B.; Chen, H.-Y.; Liberman-Martin, A. L.; Bates, C. M.; Voegtle, M. J.; Bauer, C. A.; Grubbs, R. H. *J. Am. Chem. Soc.* **2017**, *139*, 3896–3903.

Appendix B

Appendix to Chapter 3: Impacts of the Graft Polymer Architecture on Physical Properties

1. Chang, A. B.;[+] Lin, T.-P.;[+] Thompson, N. B.; Luo, S.-X.; Liberman-Martin, A. L.; Chen, H.-Y.; Grubbs, R. H. Design, Synthesis, and Self-Assembly of Polymers with Tailored Graft Distributions. *J. Am. Chem. Soc.* **2017**, *139*, 17683–17693. ([+]*Equal contributions.*)

2. Lin, T.-P.;[+] Chang, A. B.;[+] Luo, S.-X.; Chen, H.-Y.; Lee, B.; Grubbs, R. H. Effects of Grafting Density on Block Polymer Self-Assembly: From Linear to Bottlebrush. *ACS Nano* **2017**, *11*, 11632–11641. ([+]*Equal contributions.*)

3. Haugan, I. N.; Maher, M. J.; Chang, A. B.; Lin, T.-P.; Grubbs, R. H.; Hillmyer, M. A.; Bates, F. S. Consequences of Grafting Density on the Linear Viscoelastic Behavior of Graft Polymers. *ACS Macro Lett.* **2018**, *7*, 525–530.

Table of Contents

B-1 Characterization

Many aspects of the characterization relevant to this chapter have been discussed in Appendix A, including ^{1}H NMR and SEC instrumentation (Appendix A-1) as well as standard procedures for determining copolymerization reactivity ratios (Appendix A-4). This section will first provide details for other measurements, including small-angle X-ray scattering and rheology, then describe how a combination of ^{1}H NMR and SEC can be used to determine the grafting density and total molecular weight.

B-1.1 *Instrumentation*

Scanning Electron Microscopy

Samples were prepared for SEM by fracturing films supported on glass to expose a cross-section, staining over ruthenium tetroxide vapors for 5 minutes, then coating with 5 nm Pd/Pt. SEM images were taken on a ZEISS 1550 VP Field Emission SEM.

Small-Angle X-ray Scattering (SAXS)

Sections 3-2 to 3-3: SAXS data were collected at Beamline 12-ID-B at Argonne National Laboratory's Advanced Photon Source. All polymers were thermally annealed at 140 °C for 24 hours under modest pressure and between Kapton films. The samples were studied using 12 keV (1.033 Å) X-rays, and the sample-to-detector distance was calibrated using a silver behenate standard. The beam was collimated using two sets of slits and a pinhole was used to remove parasitic scattering. The beamwidth was approximately 200–300 μm horizontally and 50 μm vertically.

Section 3-4: SAXS data were collected at Beamline 5-ID-D at Argonne National Laboratory's Advanced Photon Source. All polymers were dried under vacuum at elevated temperatures (> 100 °C) for several hours to remove any residual solvent, and bulk samples were mounted onto Kapton tape. The samples were studied using 0.729 Å X-rays, and the sample-to-detector distance was calibrated using a silver behenate standard.

Differential Scanning Calorimetry (DSC): Section 3-4

DSC data were collected by our collaborators at the University of Minnesota. Measurements were collected using TA Q1000 instrument equipped with a TA LNCS under dry N_2. All polymers were dried under vacuum at elevated temperatures (> 100 °C) for several hours to remove any residual solvent prior to collecting data, then hermetically sealed at room temperature using Tzero pans. All samples were heated between 0 and 220 °C at a rate of 10 °C/min. The data reported was collected on the second heating cycle.

Linear Rheology: Section 3-4

All rheology data were collected by our collaborators at the University of Minnesota using a Rheometric Scientific Ares 2 rheometer. The temperature was controlled by a forced convection oven. All samples were loaded onto 8 mm parallel plates and measured under dry nitrogen. Dynamic strain sweep analysis at 70 °C and 100 rad/s showed the linear viscoelastic regime persisted to 20% strain for all samples. (One exception: linear poly(DME) samples were measured at 100 °C.) Dynamic frequency sweep analysis was carried out from 70 to 200 °C (100–220 °C for linear DME samples) at a frequency range of 100–0.1 rad/s and a strain lower than the linear viscoelastic threshold. Master curves were prepared by shifting G^* along frequency axis to a reference of $T_{\mathrm{ref}} = T_{\mathrm{g}} + 34$ °C, an arbitrary temperature to compare values of η_0.

B-1.2 *Determination of Grafting Density by ¹H NMR of Co-Monomer Mixtures*

For each sample, an aliquot of the macromonomer/diluent mixture was collected prior to initiating the polymerization. We note that in Sections 3-2 and 3-3, the samples are each block of the graft block polymer [*i.e.,* 3-3: $(\mathbf{PLA}^{z}\text{-}r\text{-}\mathbf{DME}^{1-z})_{\mathrm{n}}$, $(\mathbf{PLA}^{z}\text{-}r\text{-}\mathbf{DBE}^{1-z})_{\mathrm{n}}$, or $(\mathbf{PS}^{z}\text{-}r\text{-}\mathbf{DBE}^{1-z})_{\mathrm{n}}$], whereas in Chapter 3-4, the samples are effectively graft homopolymers [*i.e.*, $(\mathbf{PLA}^{z}\text{-}r\text{-}\mathbf{DME}^{1-z})_{\mathrm{n}}$]. The following discussion will use $(\mathbf{PLA}^{z}\text{-}r\text{-}\mathbf{DME}^{1-z})_{\mathrm{n}}$ graft polymers as examples [M_{n}(**PLA**) = 3450 g/mol].

The grafting density was determined from the relative ^{1}H NMR integrations of the olefin resonances for the PLA macromonomer (6.30–6.25 ppm) and the discrete diluent (6.30–6.25, 6.10–6.05 ppm) in $CDCl_3$. Because the diluent resonances are centrosymmetric (*ddd*), the molar equivalents of the macromonomer and diluent are directly obtained by comparison. In turn, the grafting density is obtained from the mole fraction of the macromonomer. Representative spectra and calculations for the $z = 0.15$ series are provided in Figure B.1 and Table B.1. For all samples, the calculated grafting densities were within 3% of the target values.

Figure B.1: ^{1}H NMR spectra of the co-monomer mixtures for each (**PLA**$^{0.15}$-*r*-**DME**$^{0.85}$)$_n$ sample (Table 3.3) prior to initiation.

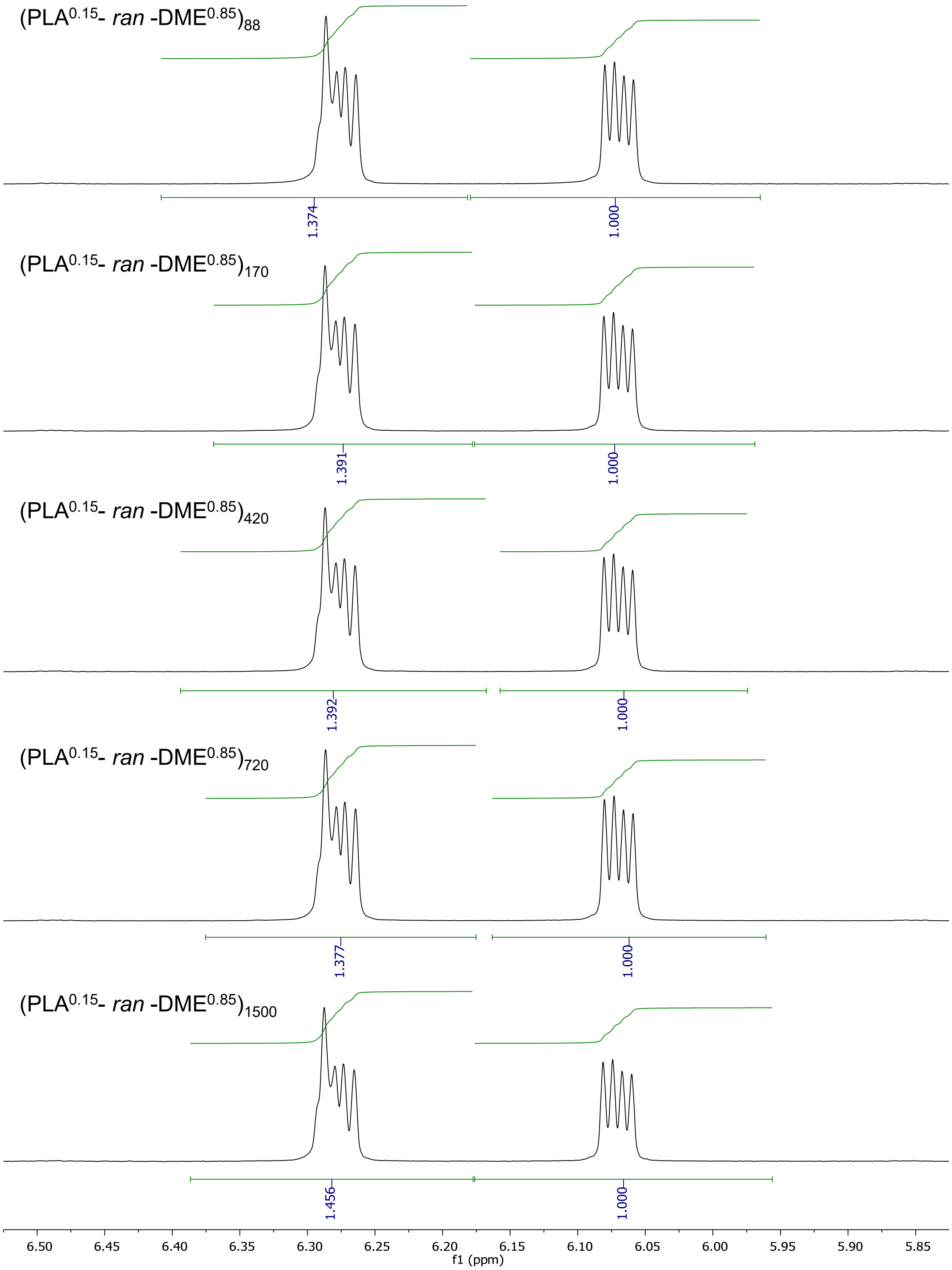

Table B.1: Representative calculations for the grafting density of each $(\mathbf{PLA}^{0.15}\text{-}r\text{-}\mathbf{DME}^{0.85})_n$ sample (Table 3.3) from ^{1}H NMR analysis.

Sample ID	Integration (6.30–6.25 ppm)	Integration (6.10–6.05 ppm)	Equiv. MM	Equiv. DME	*z*
$(\text{PLA}^{0.15}\text{-}ran\text{-DME}^{0.85})_{88}$	1.37	1.00	0.37	2.00	0.158
$(\text{PLA}^{0.15}\text{-}ran\text{-DME}^{0.85})_{170}$	1.39	1.00	0.39	2.00	0.164
$(\text{PLA}^{0.15}\text{-}ran\text{-DME}^{0.85})_{420}$	1.39	1.00	0.39	2.00	0.164
$(\text{PLA}^{0.15}\text{-}ran\text{-DME}^{0.85})_{720}$	1.38	1.00	0.38	2.00	0.159
$(\text{PLA}^{0.15}\text{-}ran\text{-DME}^{0.85})_{1500}$	1.45	1.00	0.45	2.00	0.185

B-1.3 *Determination of N_{bb} by SEC*

For each sample, a solution of known concentration (2 mg/mL) was prepared. The dn/dc values were determined by online measurements assuming 100% mass elution under the peak of interest. For all samples of the same grafting density, the dn/dc values were averaged and used to determine the weight-average total backbone degrees of polymerization, N_{bb}.

N_{bb} is the sum of the weight-average backbone degrees of polymerization of the PLA macromonomer and DME diluent (*i.e.*, $N_{\text{bb}} = N_{\text{PLA}} + N_{\text{DME}}$). The grafting density relates N_{PLA} and N_{DME}:

$$f = \frac{z}{1-z} = \frac{N_{\text{PLA}}}{N_{\text{DME}}} \qquad \text{Eq. B-1}$$

Eq. B-1 can be introduced into an expression for the weight-average total molar mass, M_{w}:

$$M_{\text{w}} = M_{\text{PLA}}\, n_{\text{PLA}} + M_{\text{DME}}\, n_{\text{DME}} = n_{\text{DME}}\left(M_{\text{PLA}}\, f + M_{\text{DME}}\right) \qquad \text{Eq. B-2}$$

where M_{PLA} is the weight-average molar mass of the PLA macromonomer (3.45 kg/mol) and M_{DME} is the molar mass of the diluent (0.21 kg/mol). N_{DME} can be calculated using the M_{w} values determined by SEC:

$$n_{\text{DME}} = \frac{\text{M}_{\text{w}}\,(\text{kDa})}{3.45\,f + 0.21} \qquad \text{Eq. B-3}$$

From Eqs. B-1 and B-3, N_{PLA} and N_{bb} follow.

B-2 Supporting Data: Graft Distribution and Block Polymer Self-Assembly

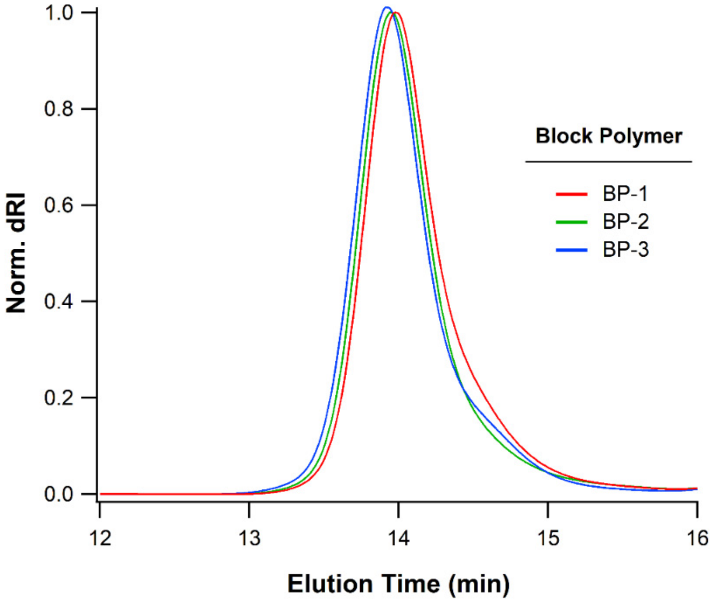

Figure B.2: SEC traces for graft block polymers **BP-1**, **BP-2**, and **BP-3**, indicating essentially identical molecular weights and dispersities.

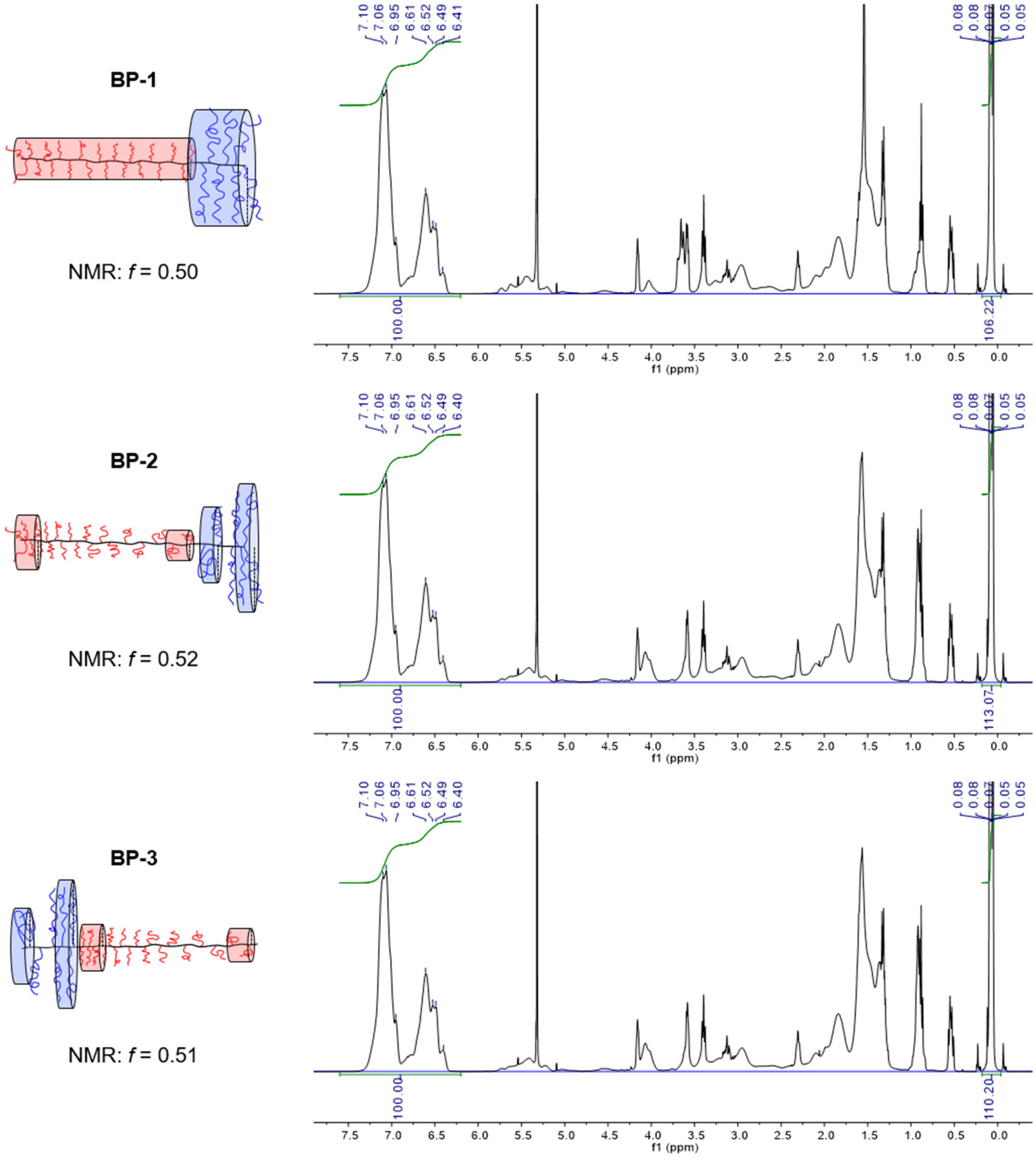

Figure B.3: ^{1}H NMR data for graft block polymers **BP-1**, **BP-2**, and **BP-3**, indicating essentially identical chemical compositions ($f \approx 0.5$).

B-3 Supporting Data: Grafting Density and Block Polymer Self-Assembly

Figure B.4 (Part 1/4): Raw 2D SAXS data for **System I**. Compare sample IDs in Table 3.1.

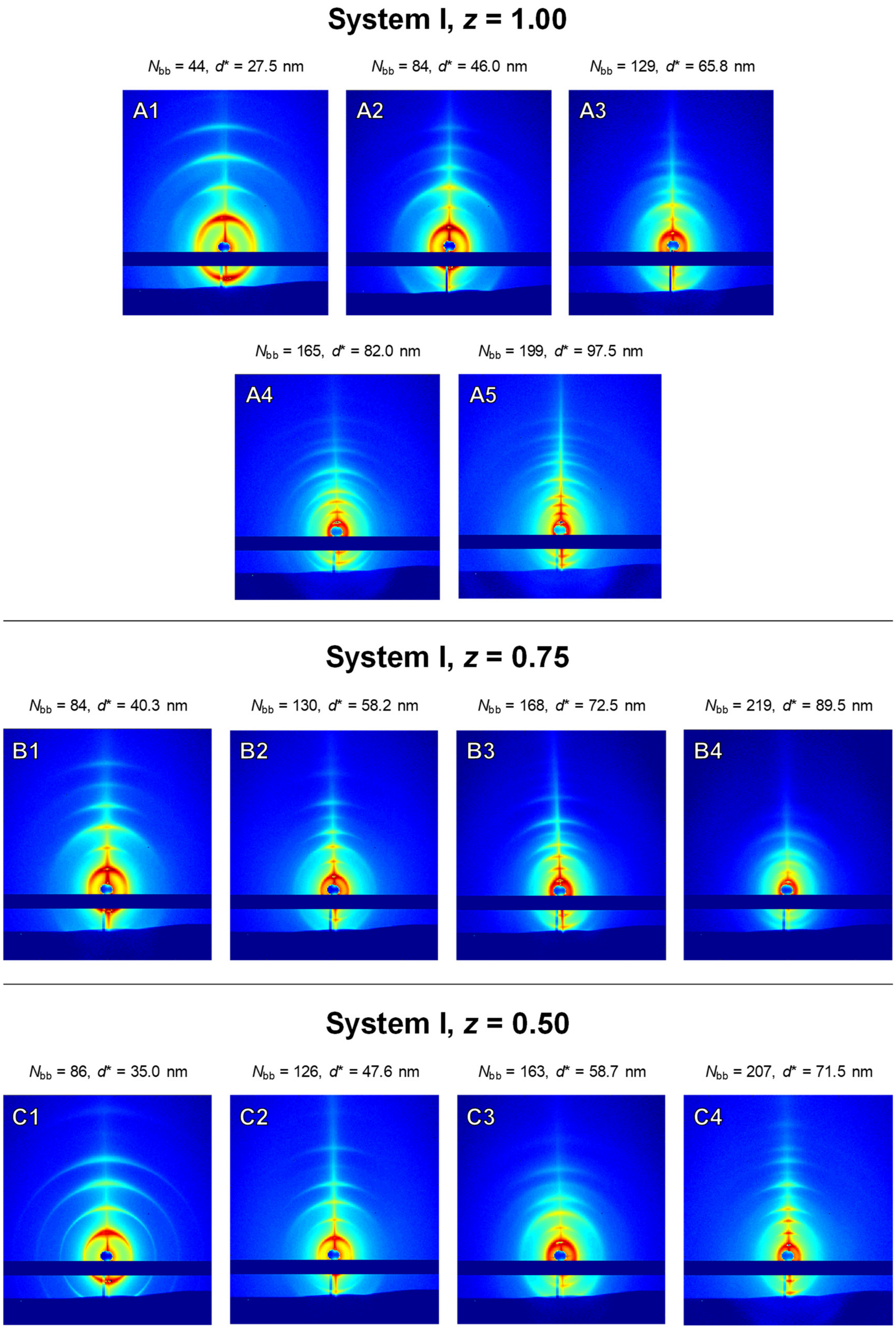

Figure B.4 (Part 2/4): Raw 2D SAXS data for **System I**. Compare sample IDs in Table 3.1.

System I, *z* = 0.35

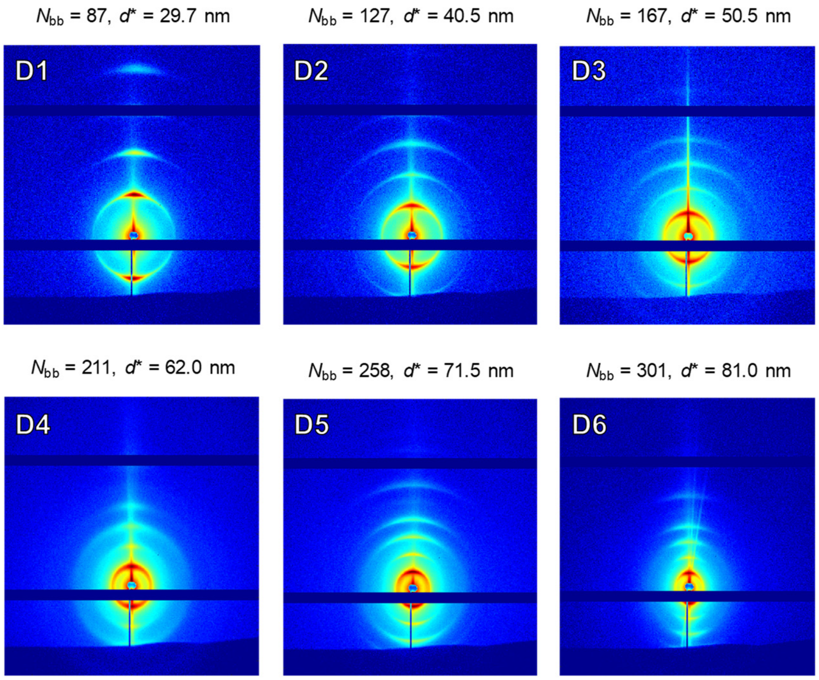

System I, *z* = 0.25

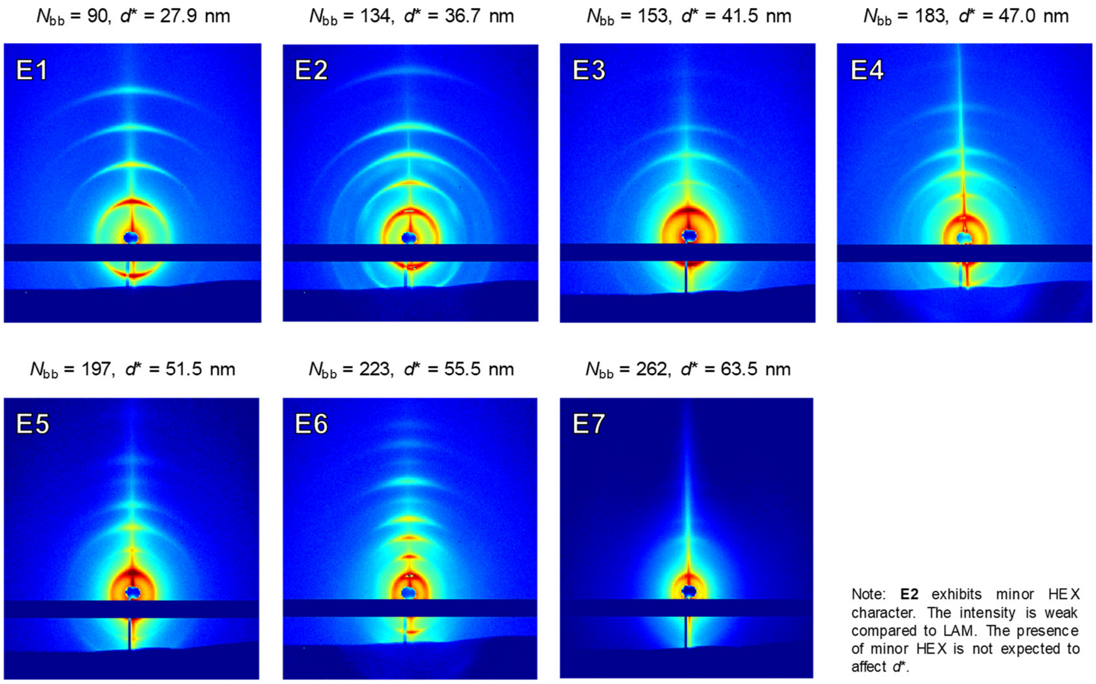

Note: **E2** exhibits minor HEX character. The intensity is weak compared to LAM. The presence of minor HEX is not expected to affect d^*.

Figure B.4 (Part 3/4): Raw 2D SAXS data for **System I**. Compare sample IDs in Table 3.1.

System I, z = 0.20

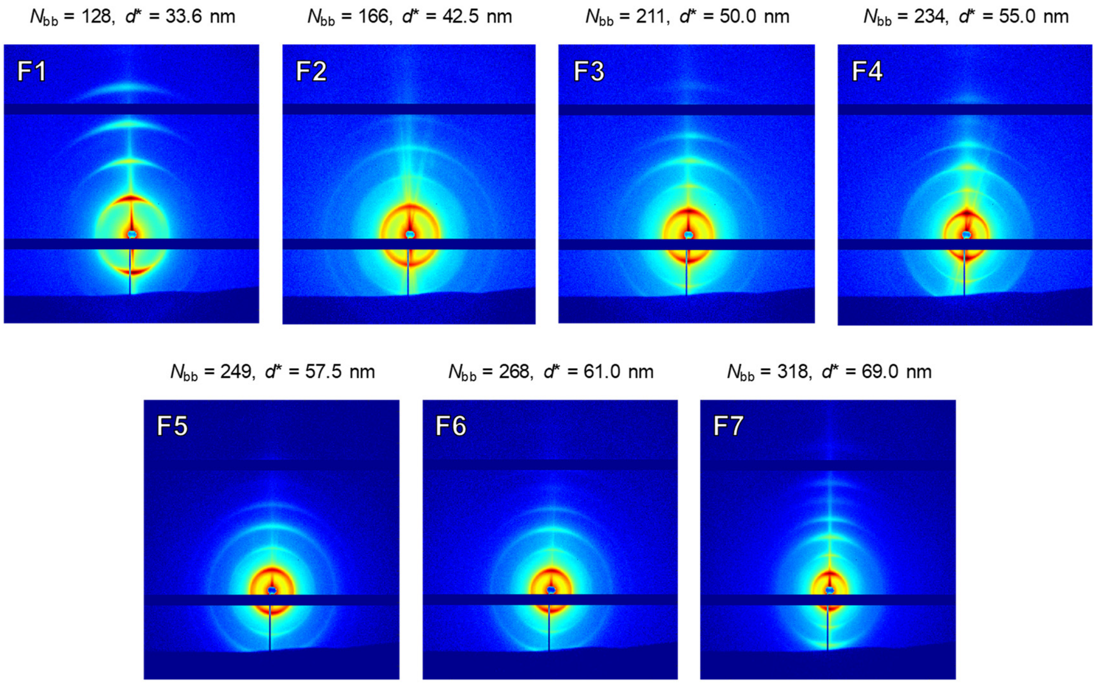

System I, z = 0.15

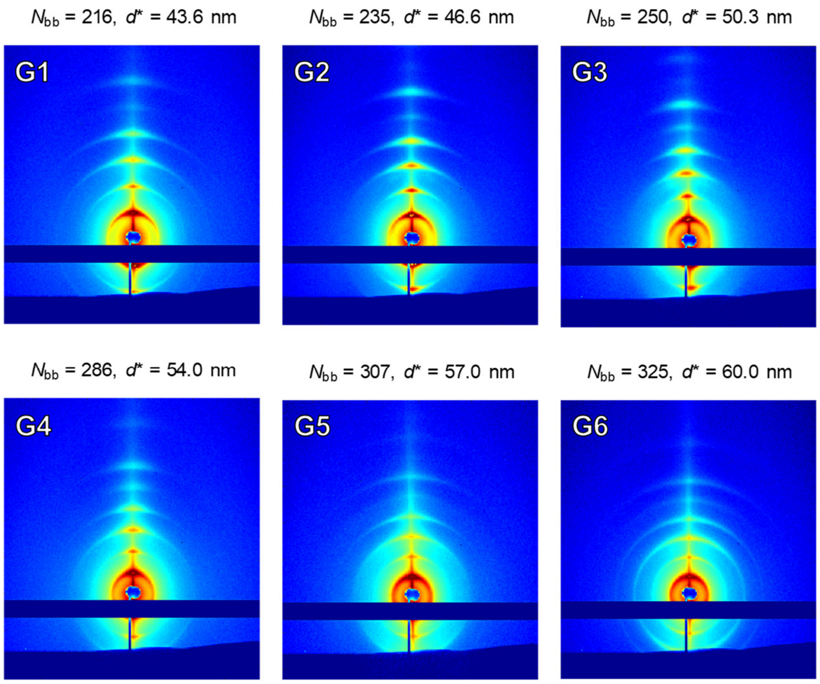

Figure B.4 (Part 4/4): Raw 2D SAXS data for **System I**. Compare sample IDs in Table 3.1.

System I, z = 0.05

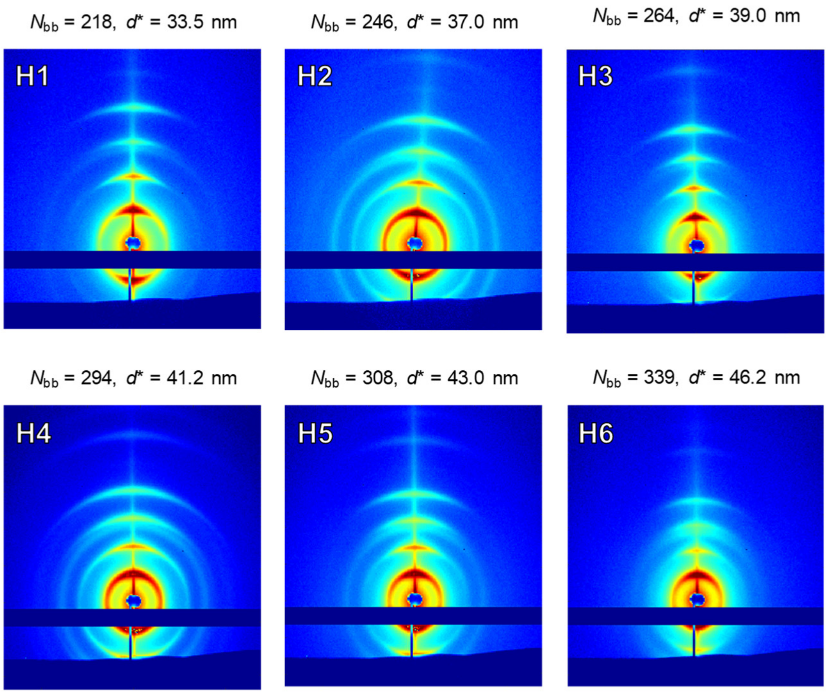

Note: **H** samples exhibit minor HEX character (*i.e.*, weak isotropic √7 peak). The presence of minor HEX is not expected to affect d^*.

System I, z = 0

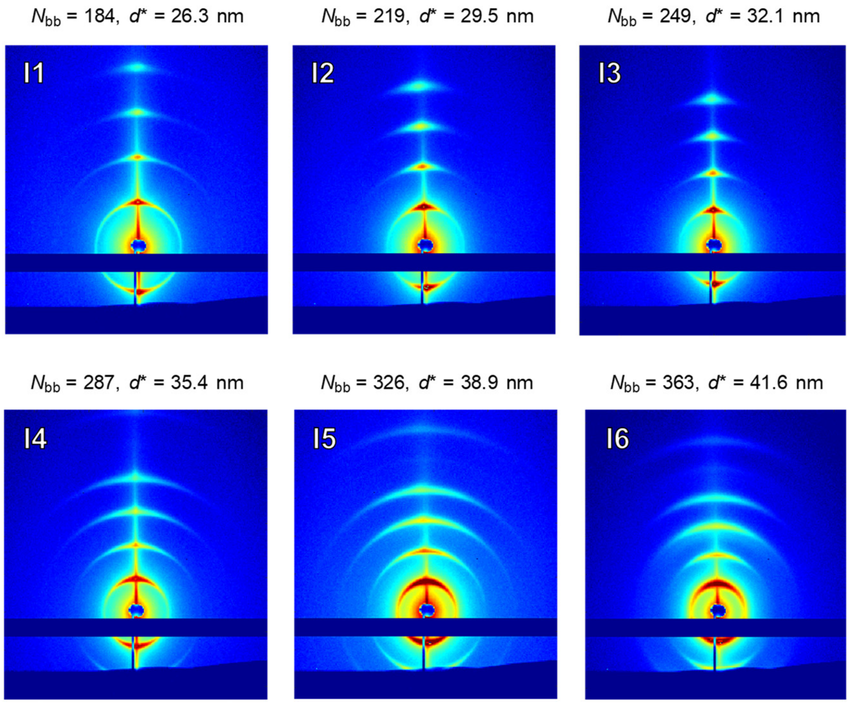

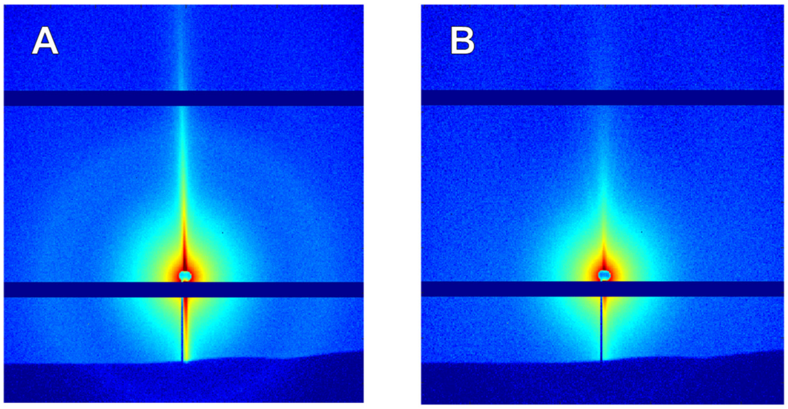

$(\mathbf{PLA}^{0.05}\text{-}r\text{-}\mathbf{DME}^{0.95})_{200}$ $(\mathbf{PS}^{0.05}\text{-}r\text{-}\mathbf{DBE}^{0.95})_{200}$

Figure B.5: Raw 2D SAXS data for z = 0.05 graft polymers: (a) $(\mathbf{PLA}^{0.05}\text{-}r\text{-}\mathbf{DME}^{0.95})_{200}$, (b) $(\mathbf{PS}^{0.05}\text{-}r\text{-}\mathbf{DBE}^{0.95})_{200}$. These polymers correspond to each block of the lowest-grafting-density samples investigated herein. Even at large N_{bb}, no evidence of microphase separation is observed, suggesting that each block is effectively homogeneous. To a first approximation, χ between the backbone and side chains does not appear significant.

Figure B.6 (Part 1/4): Raw 2D SAXS for **System II**. Compare sample IDs in Table 3.2.

System II, *z* = 0.75

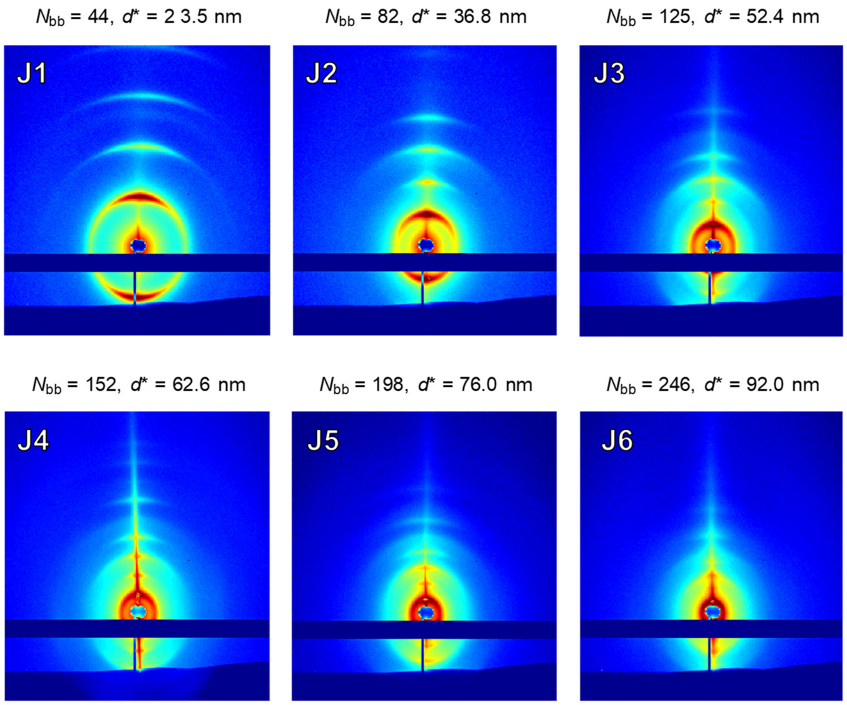

N_{bb} = 44, d^* = 2 3.5 nm

N_{bb} = 82, d^* = 36.8 nm

N_{bb} = 125, d^* = 52.4 nm

N_{bb} = 152, d^* = 62.6 nm

N_{bb} = 198, d^* = 76.0 nm

N_{bb} = 246, d^* = 92.0 nm

System II, *z* = 0.50

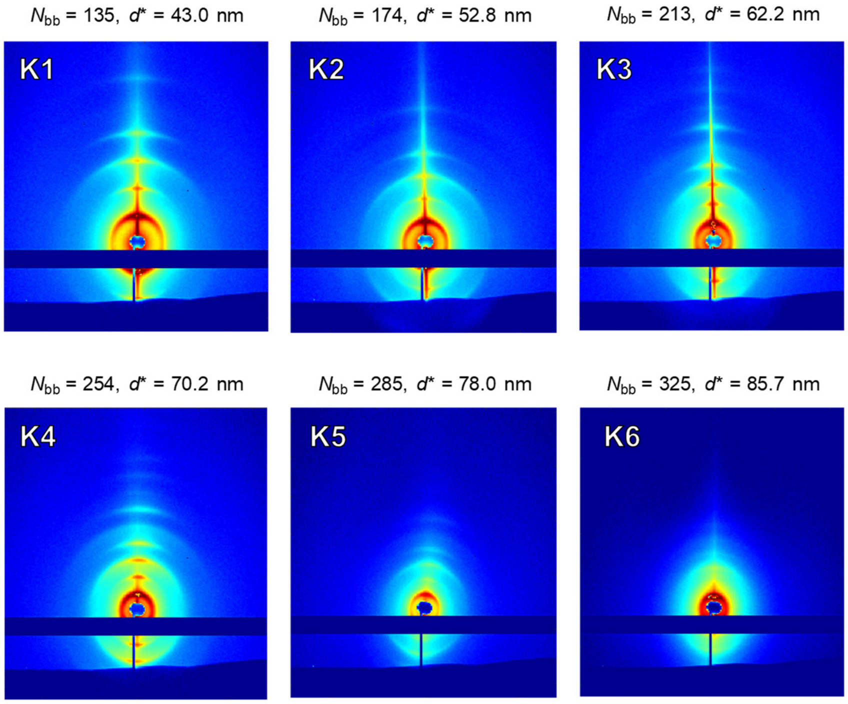

N_{bb} = 135, d^* = 43.0 nm

N_{bb} = 174, d^* = 52.8 nm

N_{bb} = 213, d^* = 62.2 nm

N_{bb} = 254, d^* = 70.2 nm

N_{bb} = 285, d^* = 78.0 nm

N_{bb} = 325, d^* = 85.7 nm

Figure B.6 (Part 2/4): Raw 2D SAXS for **System II**. Compare sample IDs in Table 3.2.

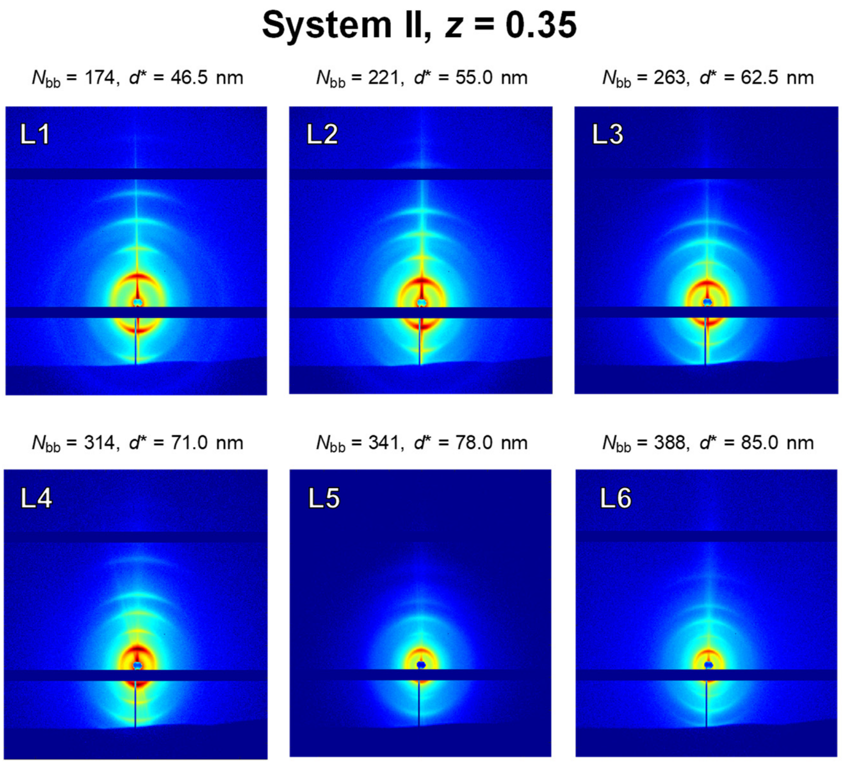

System II, $z = 0.35$

Note: **L1–L2** exhibit minor HEX character (*i.e.*, weak √7 peak). The presence of minor HEX is not expected to affect d^*.

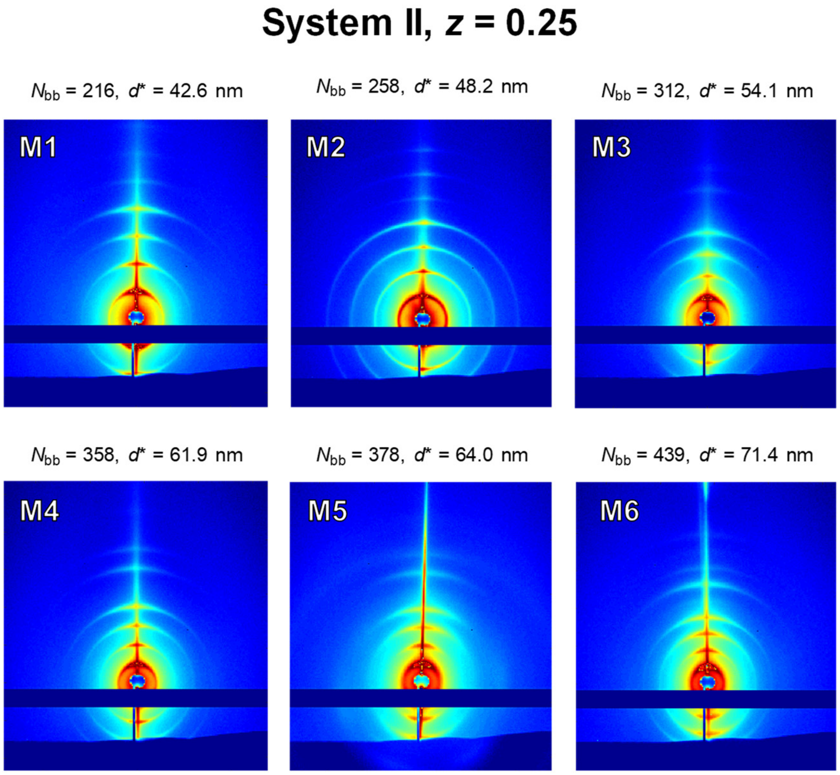

System II, $z = 0.25$

Figure B.6 (Part 3/4): Raw 2D SAXS for **System II**. Compare sample IDs in Table 3.2.

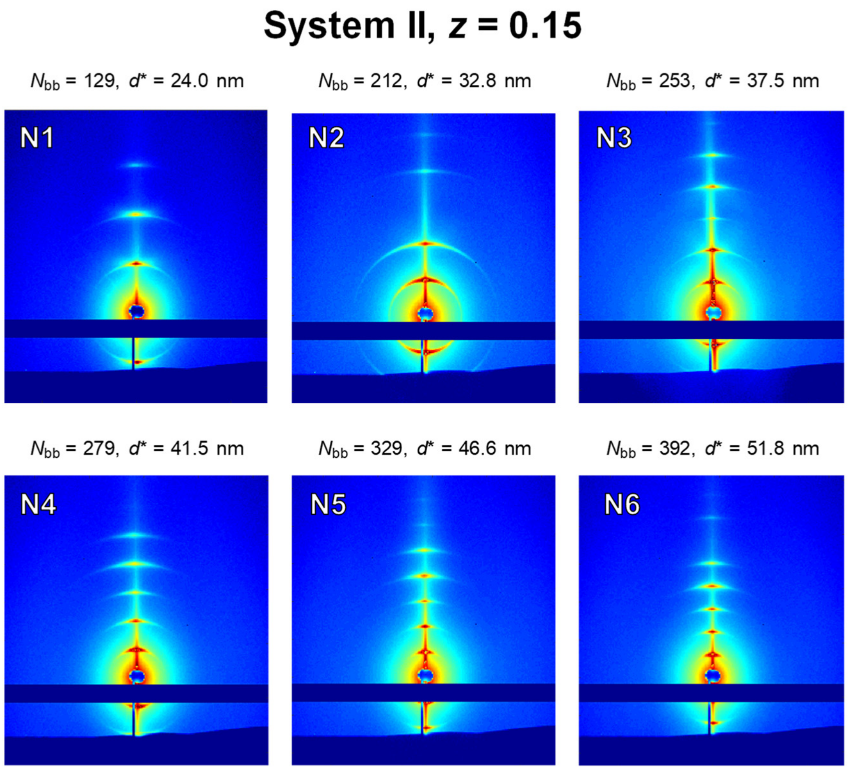

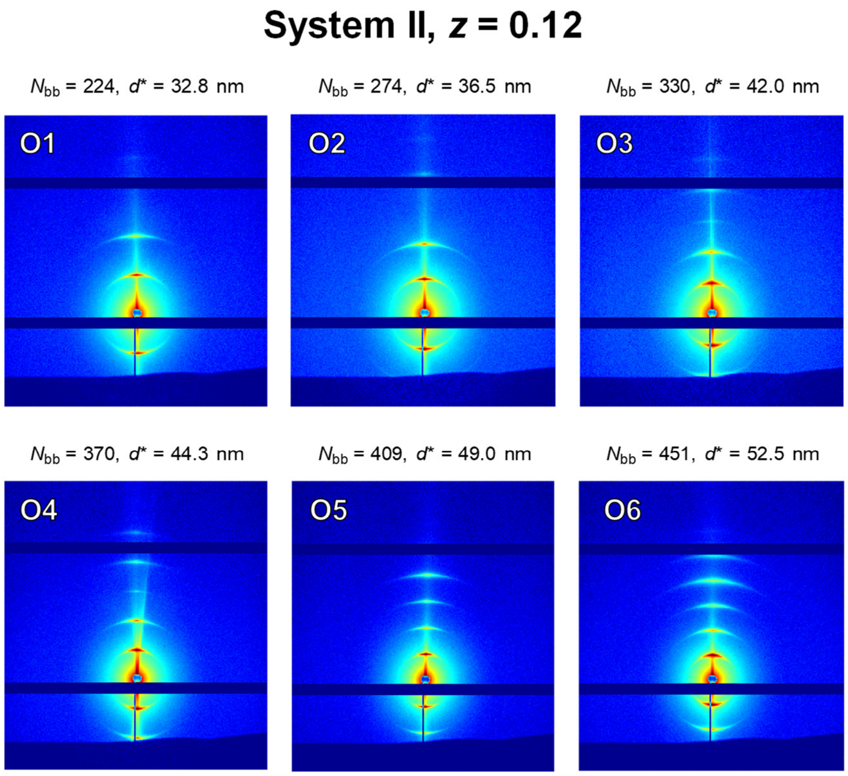

Figure B.6 (Part 4/4): Raw 2D SAXS for **System II**. Compare sample IDs in Table 3.2.

System II, z = 0.06

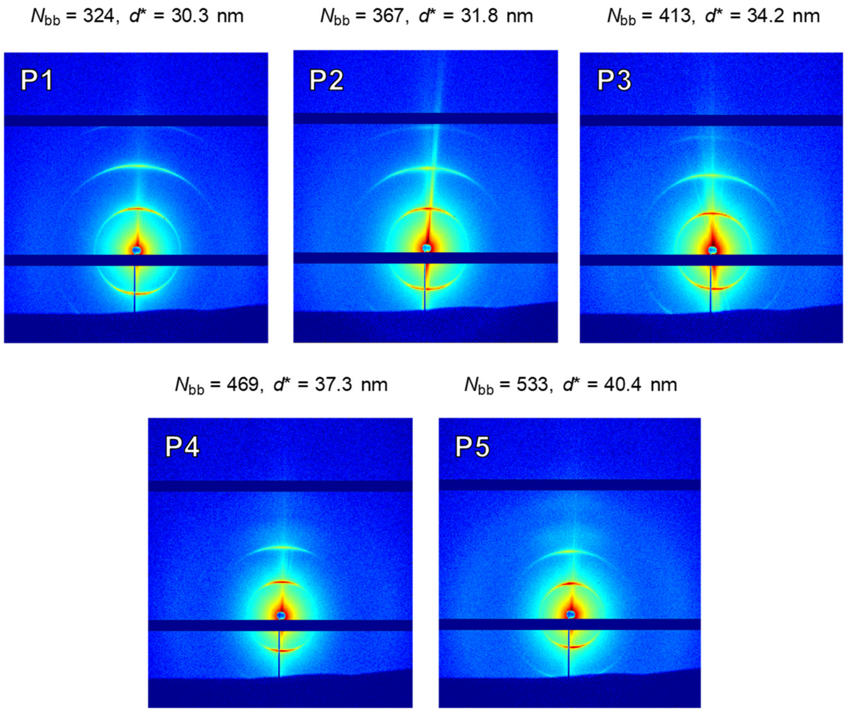

N_{bb} = 324, d^* = 30.3 nm

N_{bb} = 367, d^* = 31.8 nm

N_{bb} = 413, d^* = 34.2 nm

N_{bb} = 469, d^* = 37.3 nm

N_{bb} = 533, d^* = 40.4 nm

System II, z = 0.05

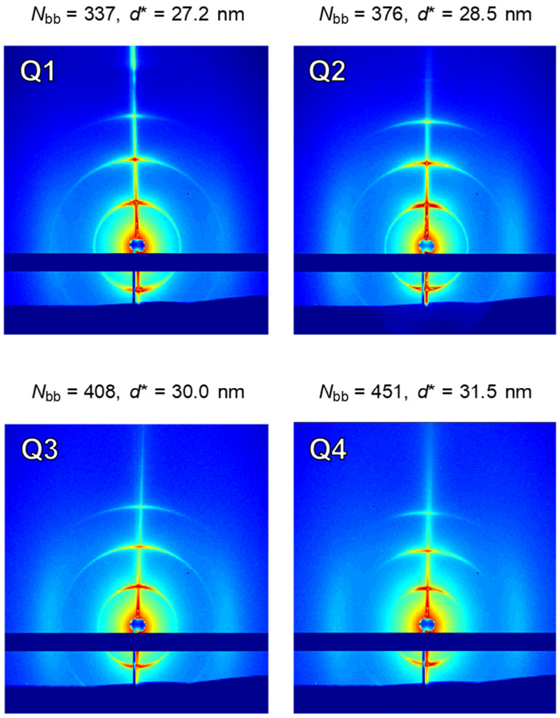

N_{bb} = 337, d^* = 27.2 nm

N_{bb} = 376, d^* = 28.5 nm

N_{bb} = 408, d^* = 30.0 nm

N_{bb} = 451, d^* = 31.5 nm

B-4 Supporting Data: Grafting Density and Linear Rheology

Figure B.7 (Part 1/2): SEC traces for (**PLA**^{z}-*r*-**DME**$^{1-z}$)$_n$ graft polymers, where z = (*A*) 1.00, (*B*) 0.50, (*C*) 0.40, or (*D*) 0.25.

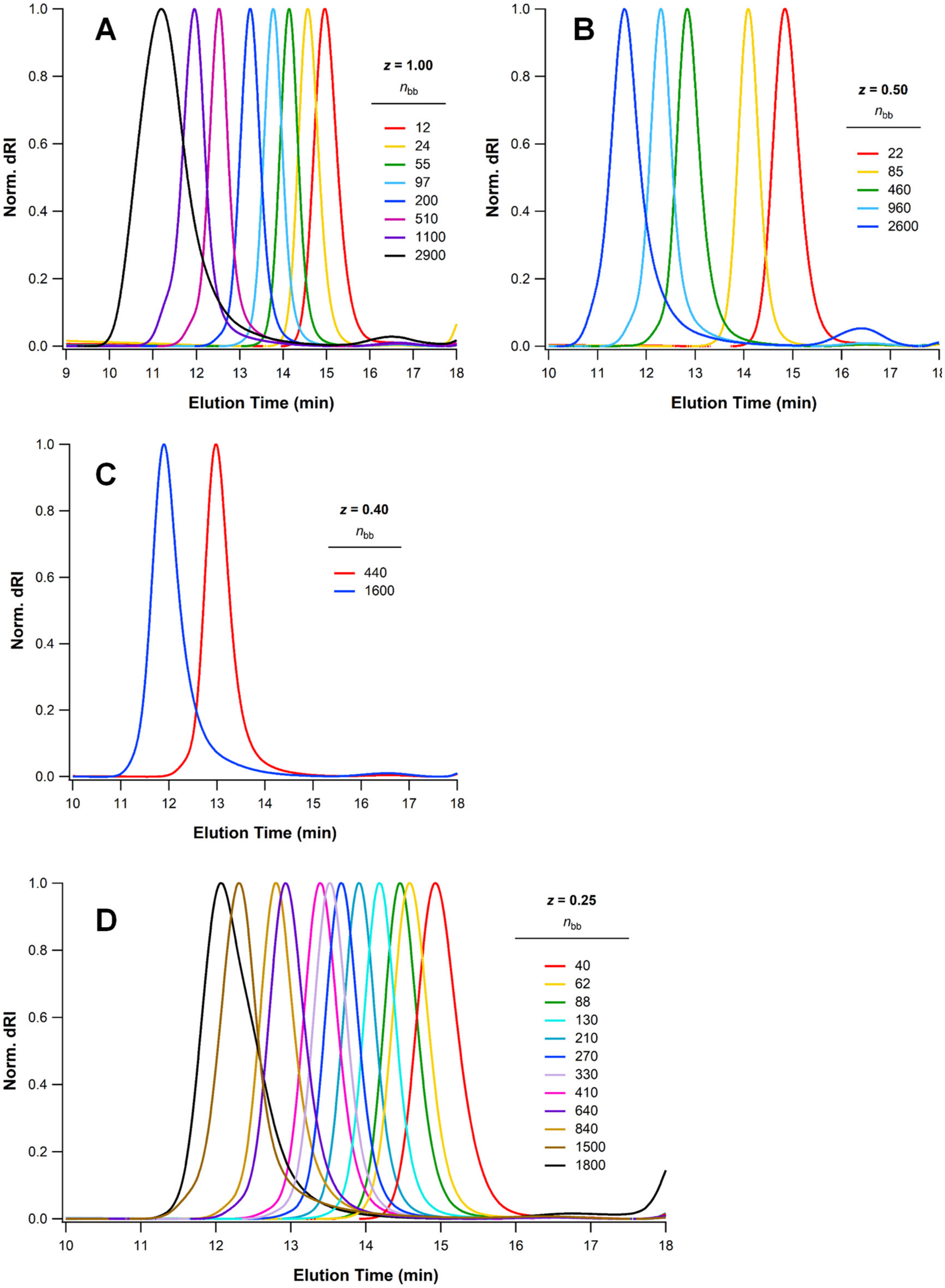

Figure B.7 (Part 2/2): SEC traces for ($\mathbf{PLA}^{z}$-r-$\mathbf{DME}^{1-z}$)$_{n}$ graft polymers, where z = (*E*) 0.20, (*B*) 0.15, (*C*) 0.05, or (*D*) 0.

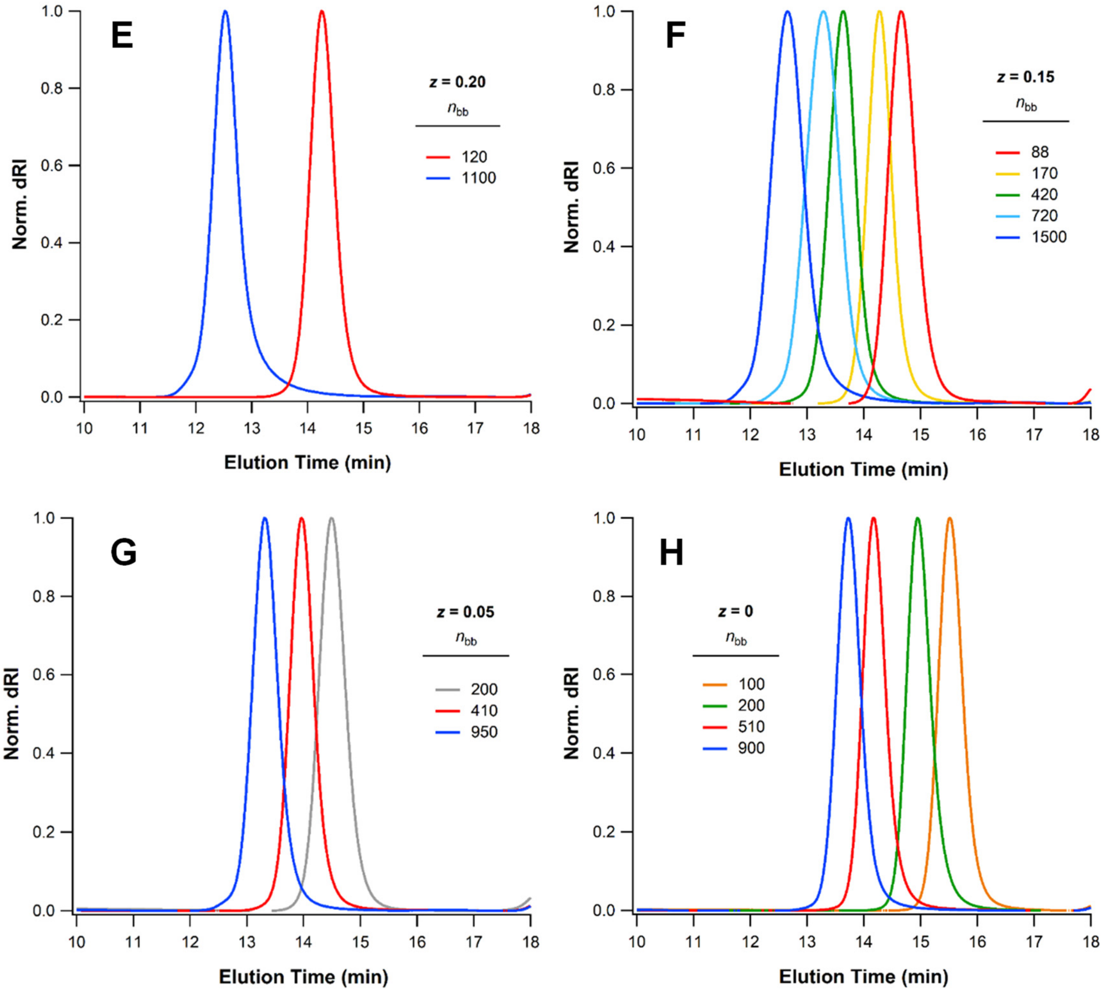

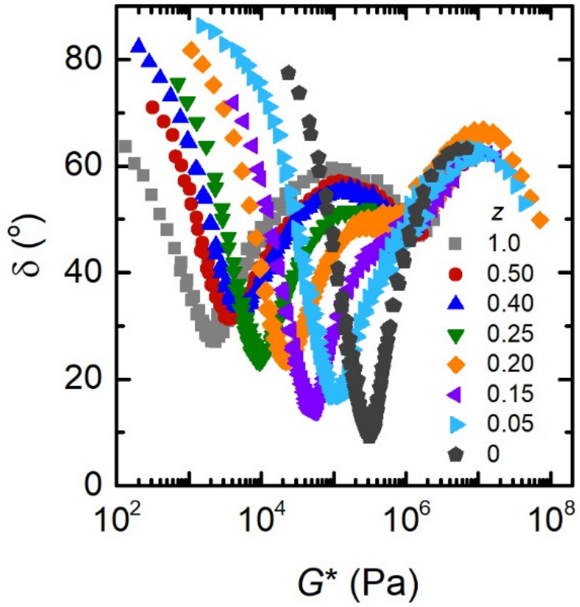

Figure B.8: Van Gurp-Palmen plots of the highest-M_w (*i.e.*, most-entangled) sample for each *z*.

Appendix C

Appendix to Chapter 4: Manipulating the ABCs of Self-Assembly via Low-χ Block Polymer Design

1. Chang, A. B.; Bates, C. M.; Lee, B.; Garland, C. M.; Jones, S. C.; Spencer, R. K.; Matsen, M. W.; Grubbs, R. H. Manipulating the ABCs of Self-Assembly via Low-χ Block Polymer Design. *Proc. Natl. Acad. Sci.* **2017**, *114*, 6462–6467.

2. Sunday, D. F.;* Chang, A. B.;* Liman, C. D.; Gann, E.; DeLongchamp, D. M.; Matsen, M. W.; Grubbs, R. H.; Soles, C. L. Evidence for Backbone Flexibility of Bottlebrush Block Copolymers Driven by Low-χ Assembly. **2018**. *submitted.* (**Corresponding authors.*)

Table of Contents

C-1 Synthesis of LSO and LSL' Brush Triblock Polymers

LSO and LSL' brush triblock polymers were synthesized by the grafting-through ring-opening metathesis polymerization (ROMP) of norbornene-functionalized macromonomers (MMs) (Scheme C.1, Tables 4.1–4.2). The poly(D,L-lactide) (PLA, L) MM ($M_{n,\text{L-MM}}$ = 4410 g/mol, $Đ$ = 1.14); polystyrene (PS, S) MM ($M_{n,\text{S-MM}}$ = 2650 g/mol, $Đ$ = 1.03); and poly(ethylene oxide) (PEO, O) MM ($M_{n,\text{O-MM}}$ = 2280 g/mol, $Đ$ = 1.04) were synthesized as described in Appendix A-2. The same macromonomers were used for all LSO and LSL' syntheses.

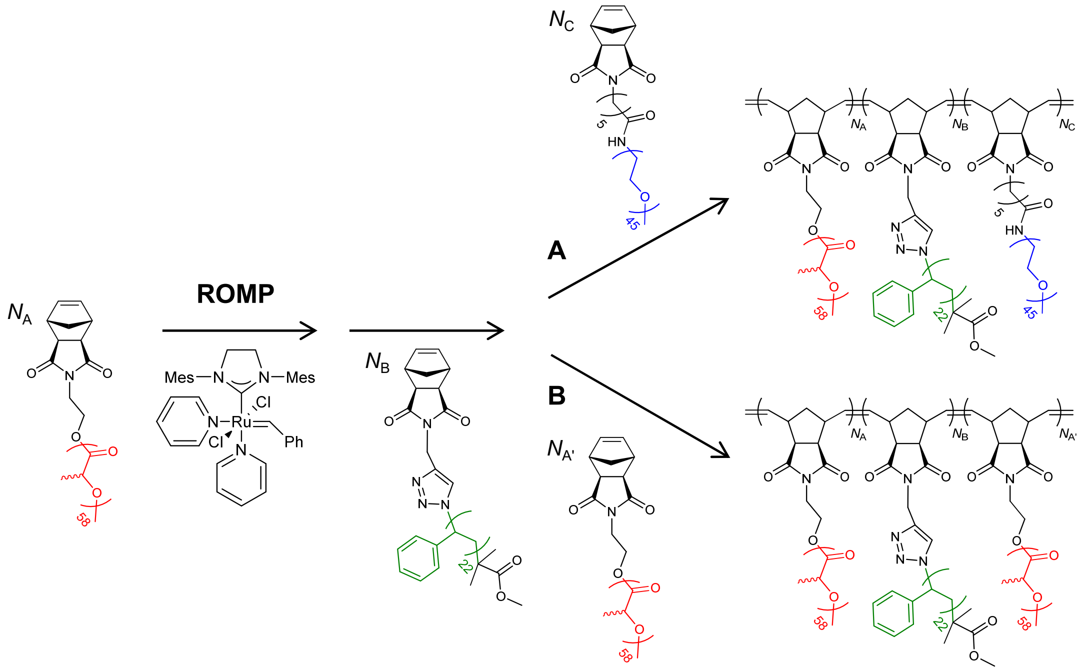

Scheme C.1: Synthesis of brush triblock polymers by ring-opening metathesis polymerization (ROMP): (*A*) LSO, (*B*) LSL'. Red, green, and blue structures represent poly(D,L-lactide) (L), polystyrene (S), and poly(ethylene oxide) (O) side chains, respectively. This color scheme is used in all figures.

In a typical triblock terpolymer synthesis, in a glovebox under inert argon atmosphere, three separate vials were prepared containing stock solutions of each MM in dry DCM. For example, for the synthesis of LSO*, vial A: PLA MM (4.15 g, 31.7 mL); vial B: PS MM (2.46 g, 18.5 mL); vial C: PEO MM (1.18 g, 10.3 mL). A fourth vial was prepared with the ruthenium catalyst (32.6 mg, 0.045 mmol) in 1.30 mL dry DCM (34.6 mM).

To a 4 mL vial equipped with a stir bar, 1.50 mL of the PLA MM stock solution was added (0.0386 mmol, 27 equiv.). The polymerization was initiated by adding 48.4 µL of the catalyst stock solution to the stirring solution (0.00167 mmol, 1.0 equiv.). After 15 minutes, a small aliquot (L, <0.1 mL) was extracted and quenched with ethyl vinyl ether in THF for subsequent analysis by SEC. After the aliquot was collected, 0.83 mL of the PS MM stock solution was added to the reaction vial (0.0416 mmol, 25 equiv.). After an additional 30 minutes, a small aliquot (LS, <0.1 mL) was extracted and quenched with ethyl vinyl ether in THF, and 0.17 mL of the PEO MM stock solution was added to the reaction vial (0.00854 mmol, 5.1 equiv.). After an additional 90 minutes, the vial was removed from the glovebox and quenched with 0.25 mL (10% reaction volume) ethyl vinyl ether. A third aliquot (LSO, <0.1 mL) was collected. After stirring for 30 minutes, the solution was added dropwise to 15 mL cold diethyl ether (−78 °C). The mixture was centrifuged at 10000 rpm for 2 minutes, then the clear supernatant was poured off. The solid was dried *in vacuo* for 24 hours to yield LSO* as an off-white powder (0.27 g, 83%).

This method also enables efficient synthesis of a variety of LSO and LSL' brush triblock terpolymers with varying backbone degrees of polymerization (N_{A}, N_{B}, N_{C} and N_{A}, N_{B}, $N_{\mathrm{A'}}$ respectively), controlled directly by the volume ratios of MM stock solutions. For the series LSO-N_{C}, in which N_{A} and N_{B} are fixed and N_{C} is varied between 0 and 20, the synthetic approach can guarantee fixed N_{A}, N_{B} for all 10 samples in the series. A large batch of the PLA-PS diblock copolymer was synthesized then split to 10 vials, and a different volume of PEO MM stock solution was added to each vial (Table 4.1, Scheme C.2). The same approach was employed to synthesize an analogous series of LSL'-$N_{\mathrm{A'}}$ brush triblock copolymers with fixed N_{A} and N_{B} and variable $N_{\mathrm{A'}}$ (Table 4.2).

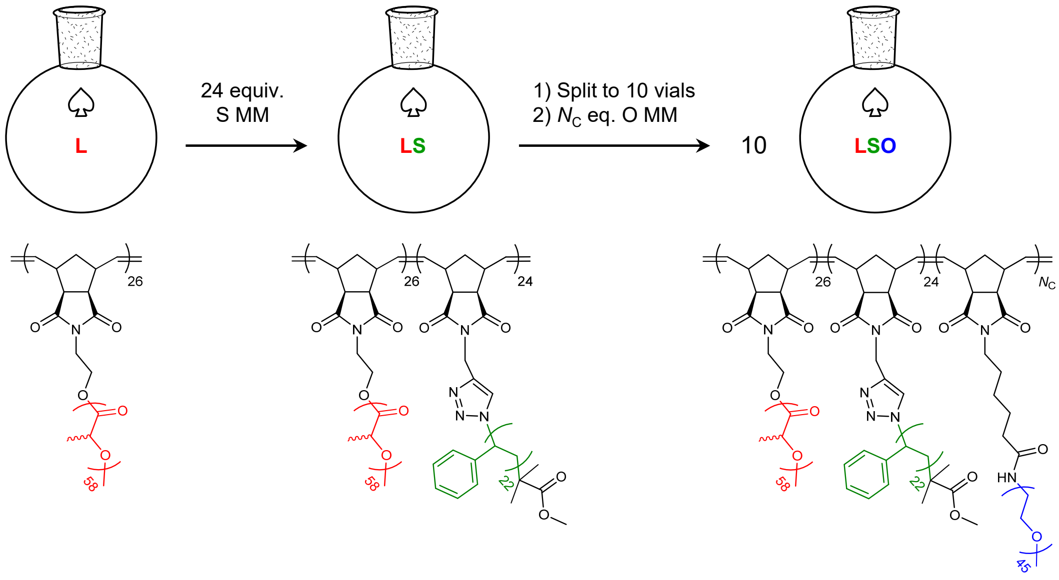

Scheme C.2: Synthesis of LSO-N_{C} brush triblock terpolymers with *guaranteed* fixed N_{A} and N_{B}. A large batch of the PLA macromonomer (L MM) is polymerized by ROMP to the L brush homopolymer. Addition of the PS macromonomer (S MM) to the same flask obtains a parent LS brush diblock copolymer with controlled N_{A} and N_{B}. The solution of LS is split to 10 vials, and an appropriate volume of a stock solution of PEO macromonomer (O MM) is added to each vial. In this way, 10 different LSO brush triblock terpolymers are obtained, each with the same N_{A} and N_{B} and variable N_{C}. LSL' brush triblock copolymers were synthesized in the same way (replacing O MM with L MM in the last step).

C-2 Molecular Characterization

C-2.1 Instrumentation: ^{1}H NMR and SEC

^{1}H NMR spectra were recorded on a Varian Inova 500 MHz instrument. Deuterated chloroform was used as the solvent, and chemical shifts are reported in parts per million (ppm) using residual protonated solvent as an internal standard ($CHCl_3$, ^{1}H 7.26 ppm).

Size-exclusion chromatography (SEC) data was obtained on one of two instruments depending on the composition of the sample. All polymers containing PEO (*i.e.*, the LSO brush triblock terpolymers) were characterized using tetrahydrofuran (THF) with 1 vol% trimethylamine as the mobile phase, which eliminated artificial dragging effects presumably arising from PEO/column interactions in pure THF. The instrument (A) includes an Agilent 1100 Series pump and autosampler and two MZ-Gel SD*plus* 300×8.0 mm columns with 10 μm beads. The columns were connected in series with a Wyatt three-angle miniDAWN TREOS light scattering detector, Optilab rEX differential refractive index detector, and ViscoStar viscometer. Samples were prepared as 2 mg/mL solutions of isolated, dry polymer in THF. For polymers that did not contain PEO, samples were measured on both Instrument A and a second instrument (B), which uses an Agilent 1260 Series pump and autosampler and two Agilent PLgel MIXED-B 300×7.5 mm columns with 10 μm beads. The columns were connected in series with a Wyatt 18-angle DAWN HELEOS light scattering detector and Optilab rEX differential refractive index detector. The mobile phase was pure THF, and the measured molecular weights and dispersities agree within 1%. PEO-containing polymers benefitted from a mobile phase with 1 vol% trimethylamine, but the light scattering detector for Instrument A has fewer angles (3) than Instrument B (18).

C-2.2 Characterization of LSO and LSL' Triblock Polymers

The LSO and LSL' brush triblock polymers were characterized by SEC and ^{1}H NMR. Figures C.1–C.3 show representative SEC traces. Aliquots of the quenched timepoints show complete consumption of the PLA macromonomer (MM), L block, and LS diblock before subsequent blocks are added. For all samples, a single narrow peak is present for all timepoints. The absolute molecular weights of the brush triblock polymers can be determined by a combination of SEC and NMR.

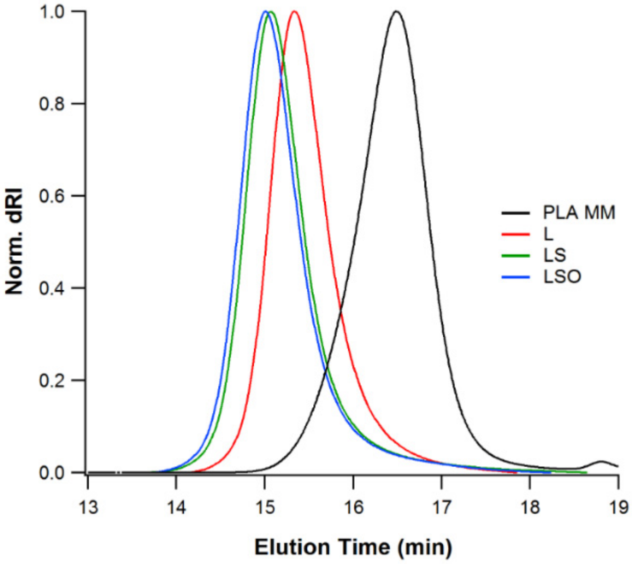

Figure C.1: Size-exclusion chromatogram (SEC) of LSO* (N_A = 28, N_B = 27, N_C = 5). The peaks are unimodal and narrow, indicating low molar mass dispersity. Complete consumption is observed at each stage prior to addition of subsequent blocks.

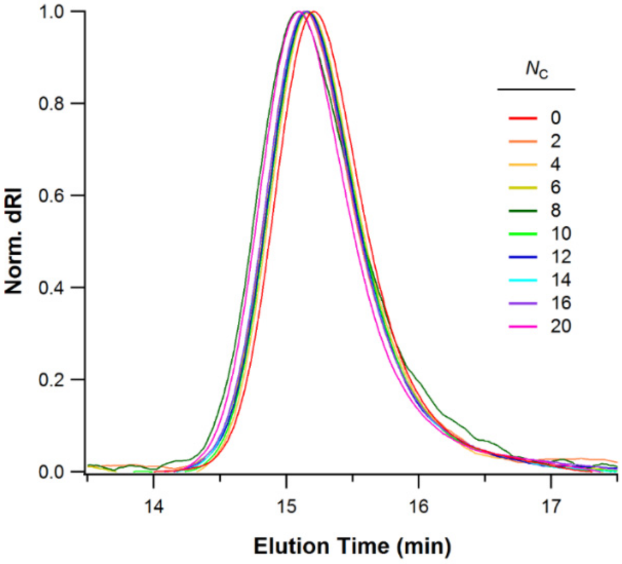

Figure C.2: SEC traces of 10 LSO-N_C triblock terpolymers with fixed N_A and N_B and variable N_C. For these triblocks, N_A = 26, N_B = 24, and $0 \leq N_C \leq 20$ (Table 4.1).

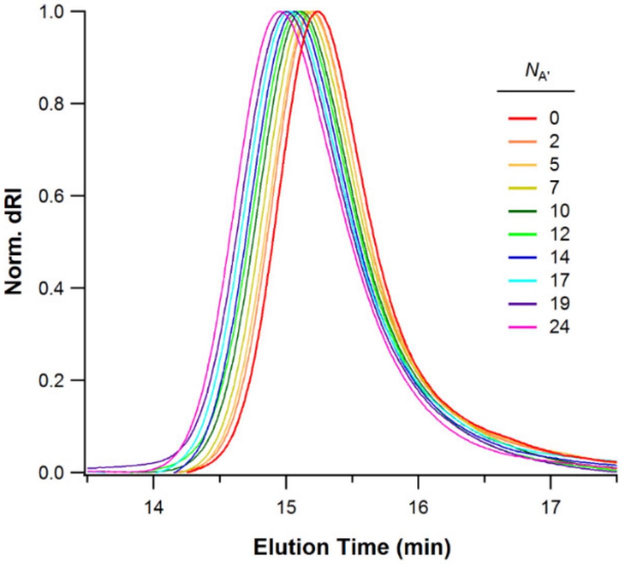

Figure C.3: SEC traces of 10 LSL'-$N_{A'}$ triblock copolymers with fixed N_A and N_B and variable $N_{A'}$. For these triblocks, $N_A = 30$, $N_B = 28$, and $0 \le N_{A'} \le 24$ (Table 4.2).

The following discussion describes the characterization of LSO; characterization of the simpler LSL' systems was performed in the same way. For each triblock, the aliquot of the A block (PLA) collected during synthesis was analyzed by SEC. The dn/dc value used for the PLA brush homopolymer was 0.050 mL/g, determined by assuming 100% mass elution from the columns. This value is consistent with literature reports [1]. SEC enables determination of the absolute weight-average molecular weight of the first block ($M_{w,A}$). Dividing by the dispersity ($Đ < 1.05$ for all samples) obtains the number-average molecular weight of the first block ($M_{n,A}$). In turn, dividing $M_{n,A}$ by the number-average molecular weight of the PLA MM (M_n = 4410 g/mol) obtains the number-average backbone degree of polymerization of the first block (N_A).

The isolated LSO triblock terpolymer was analyzed by SEC and ^{1}H NMR ($CDCl_3$, 500 MHz). For NMR, characteristic peaks for PLA, PS, and PEO were identified: L: 5.30−5.05, S: 7.22−6.32, and O: 3.77−3.60 ppm. Peak integrations (I_L, I_S, I_O) were used to calculate the relative molar fractions of each side chain (X_L, X_S, X_O) (Eqs. C-1−C-3):

$$X_L = \frac{I_L}{1 \times N_{\text{L-MM}}} \qquad \text{Eq. C-1}$$

$$X_{\mathrm{S}} = \frac{I_{\mathrm{S}}}{5 \times N_{\mathrm{S\text{-}MM}}} \qquad \text{Eq. C-2}$$

$$X_{\mathrm{O}} = \frac{I_{\mathrm{O}}}{4 \times N_{\mathrm{O\text{-}MM}}} \qquad \text{Eq. C-3}$$

where $N_{\mathrm{i\text{-}MM}}$ is the degree of polymerization of the side chain (i.e., number of monomers per side chain) and the constant in the denominator is the number of integrated protons per monomer. The ratios $X_{\mathrm{S}}/X_{\mathrm{L}}$ and $X_{\mathrm{O}}/X_{\mathrm{L}}$ represent the relative backbone degrees of polymerization for the PS- and PEO-containing blocks, respectively. Because absolute N_{A} is obtained from the absolute M_{w} of the first block by SEC, the remaining backbone degrees of polymerization N_{B} and N_{C} can be determined using these ratios (Eq. C-4):

$$N_{\mathrm{i}} = \frac{X_{\mathrm{i}}}{X_{\mathrm{L}}} \times N_{\mathrm{A}} \qquad \text{Eq. C-4}$$

From the backbone degrees of polymerization, the total molecular weight of each LSO brush triblock terpolymer can be calculated (M_{n}, Eq. C-5):

$$M_{\mathrm{n}} = N_{\mathrm{A}} M_{\mathrm{n,L\text{-}MM}} + N_{\mathrm{B}} M_{\mathrm{n,S\text{-}MM}} + N_{\mathrm{C}} M_{\mathrm{n,O\text{-}MM}} \qquad \text{Eq. C-5}$$

C-3 Self-Consistent Field Theory (SCFT): Methods

Following the overview of SCFT in Section 4-3, further details and discussion of chain parameters are provided here. For each side chain (PLA, PS, and PEO), data for the statistical segment lengths (a), densities (ρ), monomer molar mass (m_{m}), and number of monomers per reference volume ($V_{\mathrm{ref}} = 118$ Å^3) (n_{v}) are included in Table C.1. Values for PLA,[2] PS,[3] and PEO[3] were obtained from literature reports.

Based on previous work in the literature,[4] the side chains are not expected to extend significantly more than the unperturbed end-to-end distance, $R_0 = aN^{1/2}$ (where a is the statistical segment length and N is the total backbone degree of polymerization) (Figure 4.2). The stretching of cylindrical brushes (*i.e.*, bottlebrush polymers) is far less than the stretching of planar brushes, which itself is typically less than 50% of the unperturbed length.[5] Previous SCFT treatment of bottlebrush polymers has assumed that the side chains stretch approximately 10% more than the unperturbed chain lengths and that the extent of stretching is uniform throughout the brush (*i.e.*, similar at the chain ends and the middle of the brush).[4] In this report, we did not increase the segments of the sidechains as was done previously to account for end effects that become important for small N.

For the backbone, we employ a worm-like chain of fixed contour length (L) with a certain persistence length (ξ_b). The side chains are attached to the backbone with a uniform spacing of $\Delta L = 6.2$ Å equal to the length of one polynorbornene backbone unit, such that the total length of the backbone is $L = N\Delta L$. For LSO*, the contour length is estimated as follows: $L = (N_A + N_B + N_C) \times 0.62$ nm $= (28 + 27 + 5) \times 0.62$ nm $=$ **37 nm**. We set the persistence length to $\xi_b = 5\Delta L$, the same value that successfully modeled the polynorbornene backbone previously.[4] Due to the extreme side chain crowding, we assume that the backbone only experiences interactions with its grafted side chains, which implies that its interaction energy remains constant and thus can be omitted from the Hamiltonian. By also ignoring the volume of the backbone, there is no field whatsoever acting on the backbone, which simplifies the calculation. The remaining fields [$w_L(\mathbf{r})$, $w_S(\mathbf{r})$ and $w_O(\mathbf{r})$], acting on the three different side chain species, were solved for the usual self-consistent conditions of an incompressible melt.

Table C.1: SCFT input parameters for the grafted PLA, PS, and PEO side chains: a is the statistical segment length, ρ is the bulk density, m_m is the monomer molar mass, and n_V is the number of monomers per reference volume ($V_{ref} = 118$ Å^3). All data were obtained from literature sources[2-3] and reported at 140 °C, the annealing temperature.

	PLA	**PS**	**PEO**
Structure	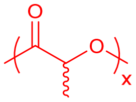	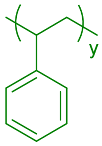	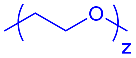
a (Å)	6.4	6.7	6.0
ρ (g cm^{-3})	1.152	0.969	1.064
m_m (g mol^{-1})	72.10	104.15	44.05
n_V	1.135	0.661	1.716

C-4 Transmission Electron Microscopy (TEM)

Transmission electron microscopy (TEM) was performed on an FEI Tecnai F30 instrument operated at 300 keV. A 10 µm objective aperture was used in order to enhance contrast. LSO* was annealed by channel-die alignment at 140 °C. A bulb extruded from the end of the die was trimmed using a double-edged razor blade to expose a face with superficial area under 200 µm × 200 µm. The sample was stained over ruthenium tetroxide (RuO_4) vapors for 4 hr. RuO_4 vapors were generated in situ by mixing 50 mg ruthenium (III) chloride hydrate and 3.0 mL sodium hypochlorite solution in a 20 mL vial. After staining, the samples were microtomed at room temperature and cut speed 1.0 mm/s using a Leica EM UC7 ultramicrotome and Diatome diamond knife. Thin sections (~70 nm thick) were floated off water onto holey carbon-coated copper grids (SPI, 200 mesh). TEM images for LSO* are shown in Figures 4.3A and C.4.

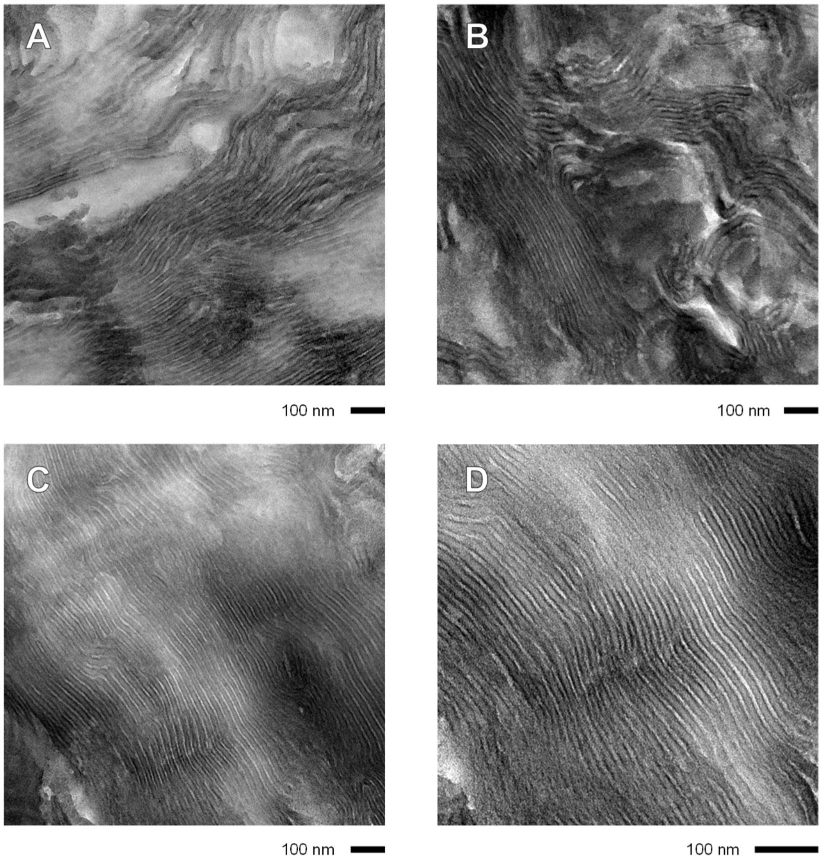

Figure C.4: (*A–C*) TEM images of different sections of LSO*. (*D*) Higher-magnification image of one area in (*C*). All images show a three-color, four-layer lamellar morphology with the same relative domain thicknesses and contrast. Compare Figure 4.3A.

TEM images for LSO-4, -10, and -14 are shown in Figure C.8. The same method was attempted to obtain images of these LSO-N_C samples. However, the channel-die aligned samples were not well-ordered, and sectioning out-of-plane resulted in non-uniform sections. Instead, sections of LSO-N_C were prepared using exactly the same films characterized by SAXS. One piece of Kapton was peeled away from the Kapton-sandwiched sample. The remaining piece, on which the polymer film remained, was stained over RuO_4 vapors for 4 hours. A small amount of EpoKwick epoxy (~10 mL) was prepared in a vial by mixing resin and hardener in a 5:1 ratio by weight. The stained film on Kapton was placed face up in a small plastic weigh boat, and ~1 mL epoxy was poured on top. After curing at room temperature overnight, the Kapton was peeled away, leaving the polymer film embedded on epoxy. The epoxy was trimmed and then embedded in a mold with additional EpoKwick epoxy. After curing at room temperature, the blocks were trimmed using a double-edged razor blade to expose a face with superficial area under 200 μm × 200 μm. The blocks were stained over RuO_4 for 24 hours to harden the material and improve contrast. After staining, the samples were microtomed at room temperature and cut speed 1.0 mm/s using a Leica EM UC7 ultramicrotome and Diatome diamond knife. Thin sections (~70 nm thick) were floated off water onto holey carbon-coated copper grids.

In our hands, it was challenging to consistently generate three-color contrast for all samples. We note that LSO* was annealed and sectioned at the University of Minnesota, whereas the LSO-N_C samples were annealed and sectioned at Caltech, contributing to the challenges associated with reproducing TEM conditions. Samples were prepared in multiple different ways for TEM, spanning variations in annealing methods (channel-die alignment, annealing between glass, annealing between Kapton), microtomy conditions (temperature, section thickness), and staining times (1 minute to 24 hours). Despite these attempts, the three-phase contrast could not be obtained for LSO-N_C samples. Based on images for LSO* and extensive other evidence (including SAXS, DSC, and SCFT) however, we believe that the LSO-N_C samples do in fact form the LAM_P morphology. The TEM images confirm that the structure is well-ordered and lamellar, but the sectioning and staining procedures may not be fully optimized to visualize the expected relative contrast.

C-5 Small-Angle X-ray Scattering (SAXS)

Small-angle X-ray scattering (SAXS) was performed at Beamline 12-ID-B at the Advanced Photon Source (APS) at Argonne National Laboratory. The samples were studied using 14 keV (0.89 Å) X-rays and a sample-to-detector distance of 2.00 m, calibrated using a silver behenate standard. SAXS data for each sample was collected parallel to the plane of the substrate (approximately 2 mm thick in the beam direction). The sample was tilted ϕ = 3° relative to the normal toward the detector in order to improve the signal since the lamellar samples were highly oriented perpendicular to the beam. Exposure times between 0.1 and 1 s were used for all measurements.

All LSO and LSL' brush triblock polymers were prepared for analysis by SAXS as follows: (1) Neat LSO or LSL' triblock powder (approx. 10 mg) was placed between two sheets of 25 μm thick Kapton film. (2) The sample between Kapton was placed between two glass slides. (3) The glass slides were clamped with medium binder clips (Office Depot). (4) The samples were annealed under vacuum at 140 °C for 12 hr. (5) After 12 hr, the samples were allowed to slowly cool to 25 °C under vacuum. (6) Scissors were used to cut a thin strip of the Kapton-sandwiched sample (approx. 10 × 2 × 0.07 mm, length × width × height). (7) SAXS measurements were performed normal to the sample cross-section, through the width of the sample (2 mm).

Applying modest pressure while thermally annealing brush LSO and LSL' orients the self-assembled lamellae, as evident from raw 2D SAXS patterns. For some samples, applied pressure also appears to improve the extent of order. Each dropcast sample was prepared by applying 0.3 mL of a 10 mg/mL solution of polymer in DCM onto a piece of Kapton. The solvent was allowed to evaporate in air at room temperature for 12 hours, and the film was subsequently dried under high vacuum (<50 mTorr) for 24 hours to remove any residual solvent.

C-6 Supporting Data for LSO-N_C Series

Table C.2: Glass transition temperatures (T_g), LAM spacings (d^*, d LAM$_{//}$), and assigned morphologies for LSO-N_C (fixed N_A and N_B and variable N_C). See Table 4.1 for full molecular characterization data and Figures C.6–C.7 for full SAXS analysis.

Sample	f_O [a]	T_g (°C) [b]	d^* LAM$_\perp$ (nm) [c]	d LAM$_{//}$ (nm) [d]	**Morphology**
LSO-0	0.00	55.2	29.0	32.2	LAM$_2$
LSO-2	0.02	53.1	27.9	30.1	LAM$_P$
LSO-4	0.05	50.1	27.0	29.8	LAM$_P$
LSO-6	0.07	47.1	26.8	27.6	LAM$_P$
LSO-8	0.09	42.1	26.5	27.0	LAM$_P$
LSO-10	0.11	35.3	25.8	26.2	LAM$_P$
LSO-12	0.13	30.4	25.2	26.1	LAM$_P$
LSO-14	0.15	30.2	24.6	25.9	LAM$_P$
LSO-16	0.17	29.1	24.5	25.0	LAM$_P$
LSO-20	0.20	21.2	23.6	24.2	LAM$_P$

[a] Volume fraction of the C block (O, PEO).

[b] Determined from DSC derivative curves of the second heating cycle. Only one T_g is observed for each sample.

[c] Lamellar period, $d^* = 2\pi/q^*$, determined by SAXS and reported at 25 °C. Note: d^* is the period of lamellae stacked normal to the beam, identical to $a_\perp$ indexed to the $P1$ space group.

[d] Spacing of lamellae in-plane, Note: d LAM$_{//} = a_{//}$ indexed to $P1$.

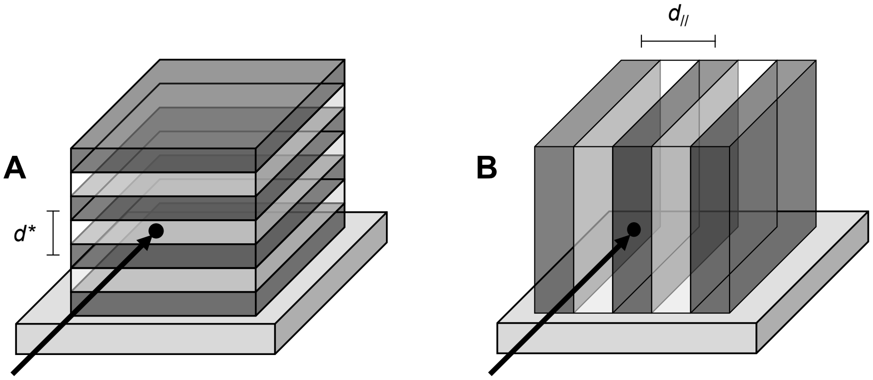

Figure C.5: Structures and relevant domain spacings indexed by SAXS. Black and white layers represent two different domains; for simplicity in visualizing the parameters, only two domains are illustrated for lamellae (whereas LAM$_3$ and LAM$_P$ each have three domains). The substrate is shown at the bottom of each sample, and the arrow indicates the direction of the X-ray beam. (*A*) LAM stacked normal to the beam. The relevant spacing is d^*, the lamellar period discussed in this report. (*B*) LAM stacked in-plane with the beam. The relevant spacing is $d_{//}$.

Figure C.6 (Part 1/3)

Raw 2D SAXS data for LSO-N_C indexed (*left*) to the $P1$ space group along the perpendicular direction, corresponding to lamellae stacked normal to the beam (LAM$_\perp$) and (*right*) to the $P1$ space group along the parallel direction, corresponding to lamellae stacked in-plane with the beam (LAM$_{//}$). The relevant parameters, provided in nanometers, are the lamellar periods $d^* = d$ LAM$_\perp$ and $d_{//} = d$ LAM$_{//}$. Green dots superimposed on the images indicate the expected peak positions. See Table C.2 for an overview of the indexed data.

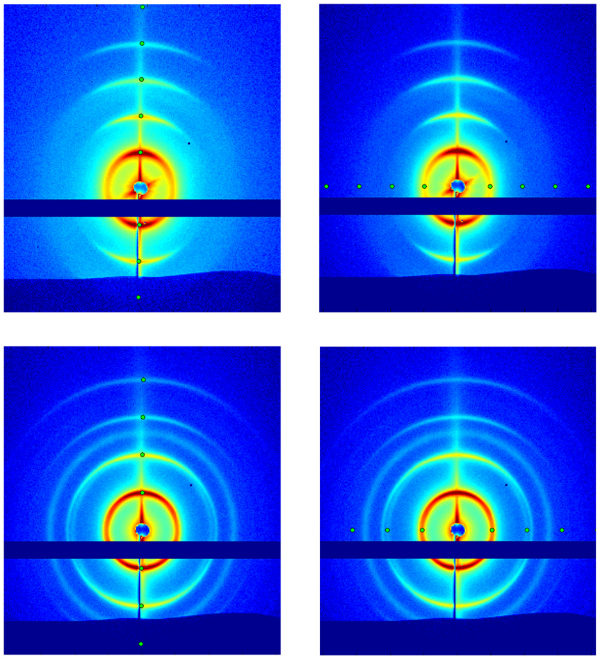

LSO-0
d^* = 29.0
d LAM$_{//}$ = 32.2

LSO-2
d^* = 27.9
d LAM$_{//}$ = 30.1

Figure C.6 (Part 2/3)

Raw 2D SAXS data for LSO-N_C indexed (*left*) to the $P1$ space group along the perpendicular direction, corresponding to lamellae stacked normal to the beam (LAM$_\perp$) and (*right*) to the $P1$ space group along the parallel direction.

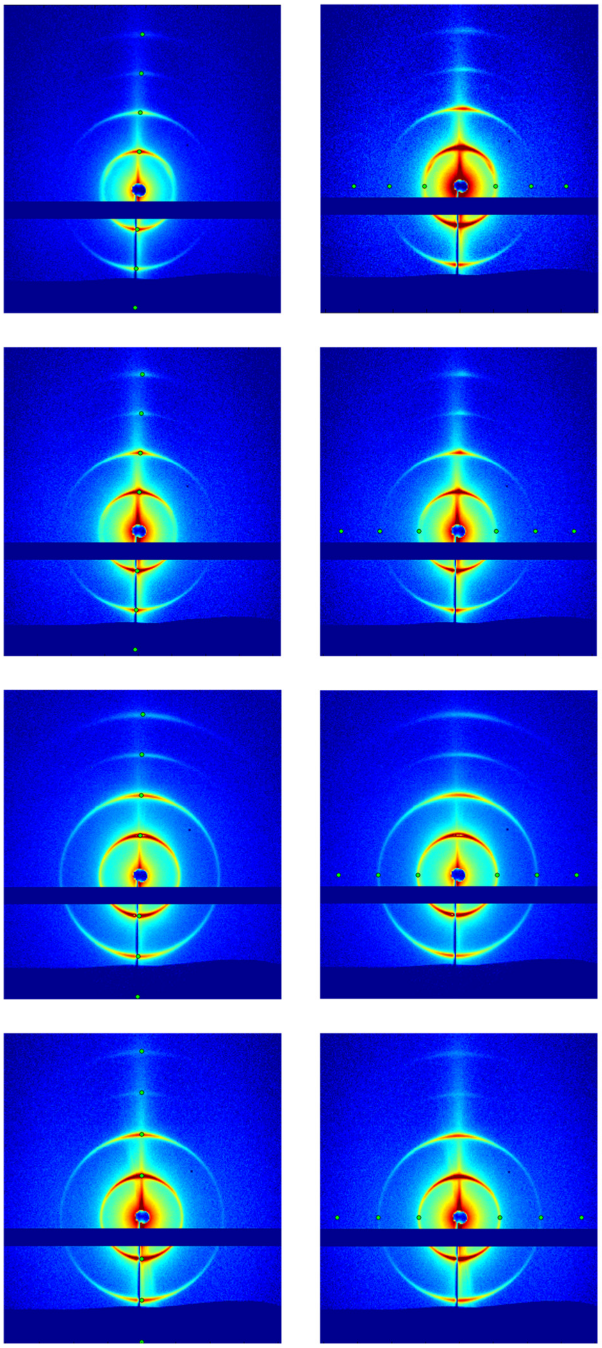

LSO-4
d^* = 27.0
d LAM$_{//}$ = 29.8

LSO-6
d^* = 26.8
d LAM$_{//}$ = 27.6

LSO-8
d^* = 26.5
d LAM$_{//}$ = 27.0

LSO-10
d^* = 25.8
d LAM$_{//}$ = 26.2

Figure C.6 (Part 3/3)

Raw 2D SAXS data for LSO-N_C indexed (*left*) to the *P*1 space group along the perpendicular direction, corresponding to lamellae stacked normal to the beam (LAM$_\perp$) and (*right*) to the *P*1 space group along the parallel direction.

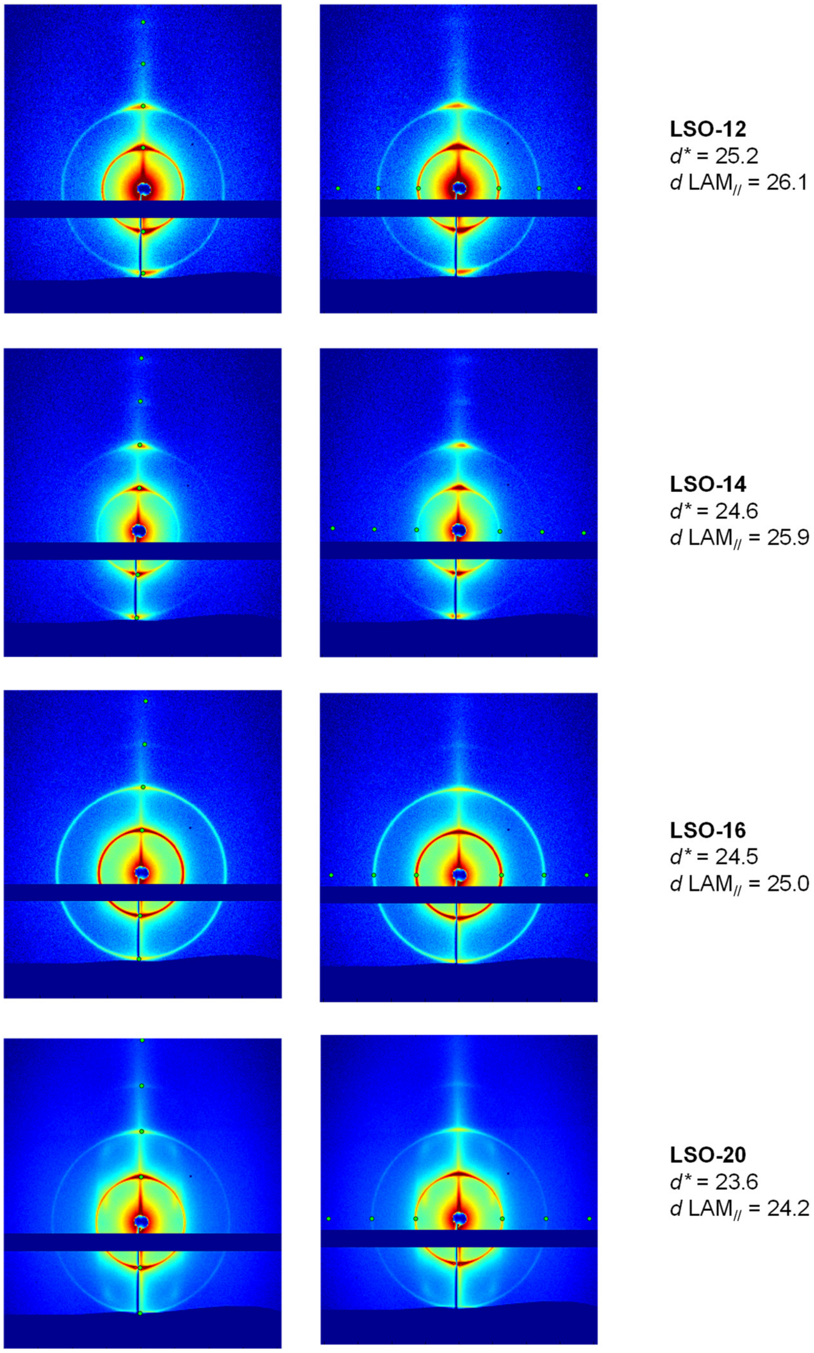

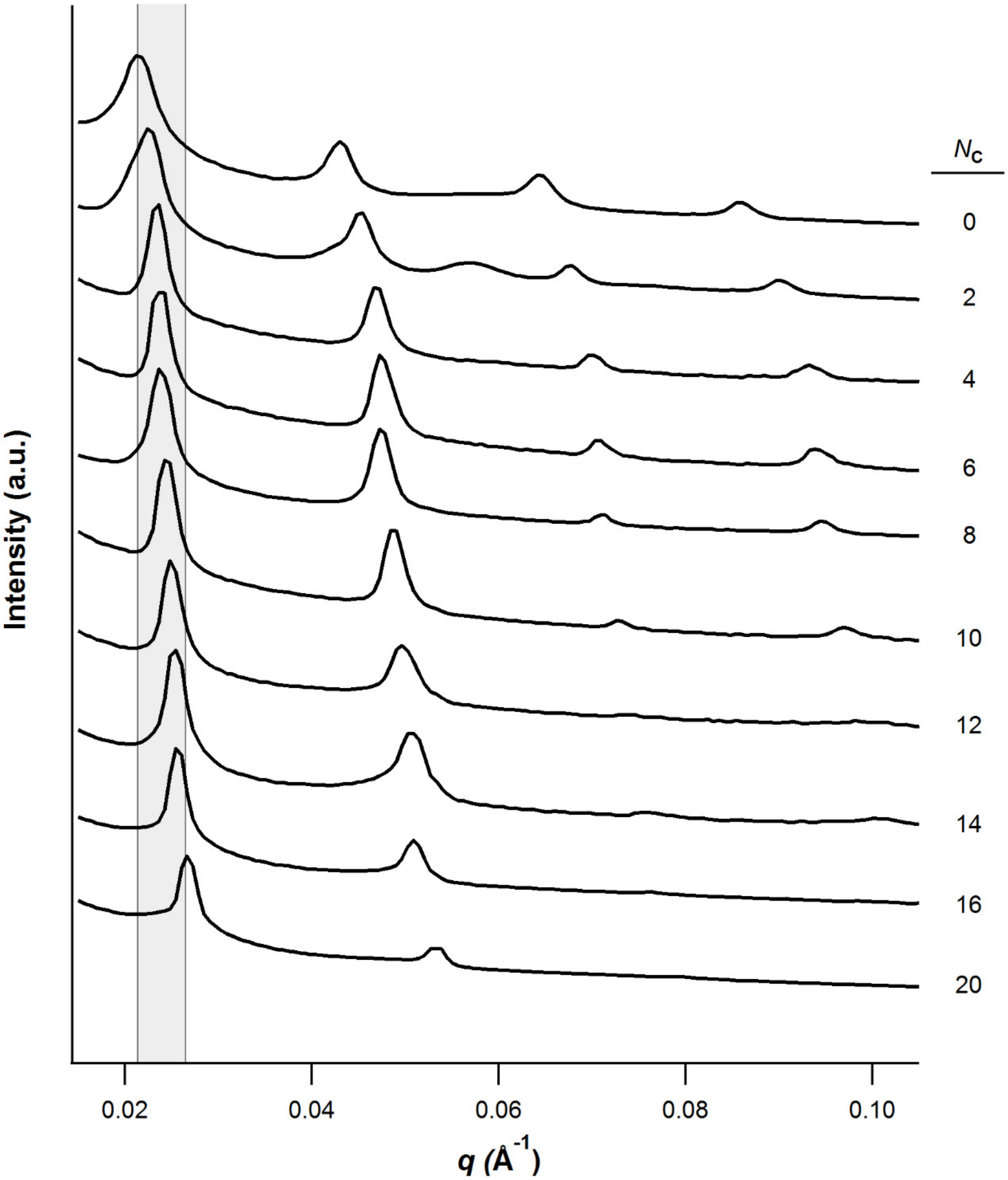

Figure C.7: Azimuthally integrated 1D SAXS patterns for LSO-N_C (fixed N_A, N_B and variable N_C), which obey $d^* \sim M^{-0.87}$. The large change in the position of q^* (and therefore $d^* = 2\pi/q^*$) across the series is emphasized by the gray box. All traces correspond to samples that self-assemble to majority LAM. Compare Fig. C.10 (LSL').

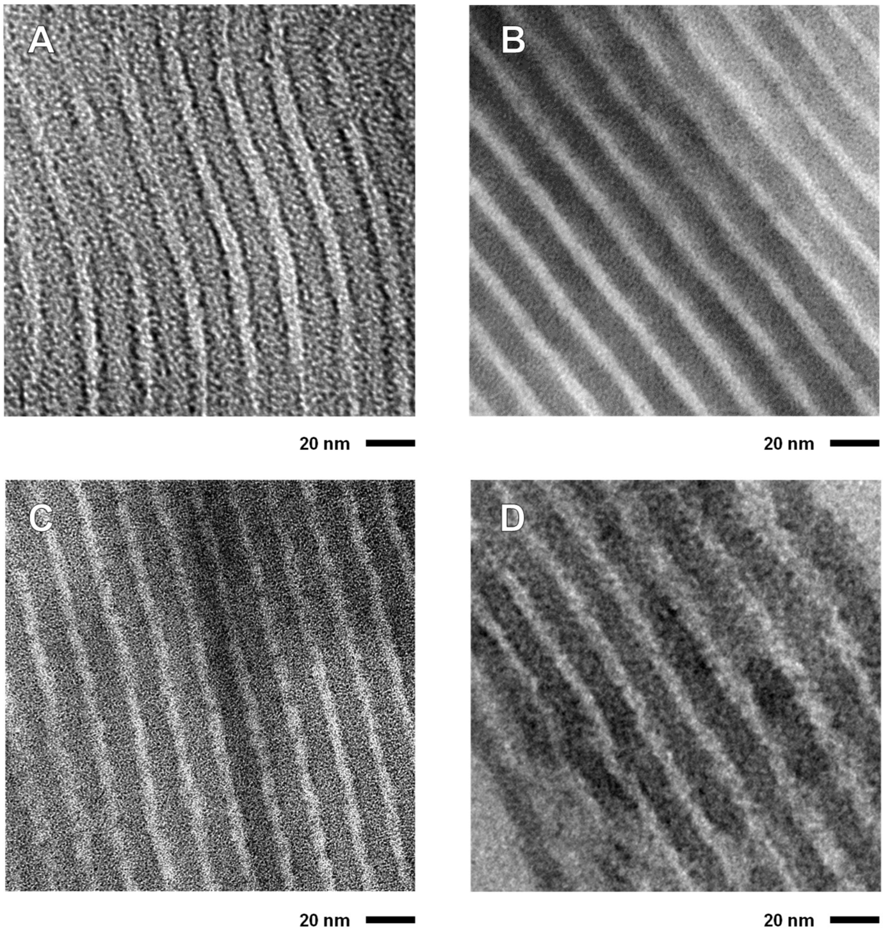

Figure C.8: TEM images of (*A*) LSO*, (*B*) LSO-4, (*C*) LSO-10, and (*D*) LSO-14. All self-assemble to lamellar morphologies, consistent with SAXS. For LSO-N_C, the domain spacings were calculated by averaging over 20 periods, and the same trend is observed by TEM and SAXS. As N_C increases, d^* decreases: d^*(LSO-4) = 19.1 nm, d^*(LSO-10) = 17.8 nm, d^*(LSO-14) = 17.7 nm. The magnitudes of the periods are smaller than those obtained from SAXS, likely due to compression of the sample upon sectioning. The three-phase contrast is clear for LSO* but is challenging to obtain for all images.

C-7 Supporting Data for LSL'-$N_{A'}$ Series

Table C.3: Glass transition temperatures (T_g), LAM spacings (d^*, d LAM$_{//}$), and assigned morphologies for LSL'-$N_{A'}$ (fixed N_A and N_B and variable $N_{A'}$). See Table 4.2 for full molecular characterization data and Figures C.9–C.10 for full SAXS analysis.

Sample	$f_{L'}$ [a]	T_g (°C) [b]	d^* LAM$_\perp$ (nm) [c]	d LAM$_{//}$ (nm) [d]	Morphology
LSL'-0	0.00	57.1	32.9	39.2	LAM$_2$
LSL'-2	0.05	56.3	31.3	36.0	LAM$_2$
LSL'-5	0.09	55.6	29.6	35.8	LAM$_2$
LSL'-7	0.13	56.3	28.6	27.8	LAM$_2$
LSL'-10	0.16	56.1	27.8	28.2	LAM$_2$
LSL'-12	0.20	55.9	27.4	27.9	LAM$_2$
LSL'-14	0.23	56.9	26.7	29.9	LAM$_2$
LSL'-17	0.26	56.2	26.6	28.8	LAM$_2$
LSL'-19	0.28	55.9	26.2	28.5	LAM$_2$
LSL'-24	0.33	56.3	25.7	27.6	LAM$_2$

[a] Volume fraction of the variable-length PLA block (L').

[b] Determined from DSC derivative curves of the second heating cycle.

[c] Lamellar period, $d^* = 2\pi/q^*$, determined by SAXS and reported at 25 °C. Note: d^* is the period of lamellae stacked normal to the beam, identical to $a_\perp$ indexed to the $P1$ space group.

[d] Spacing of lamellae in-plane, Note: d LAM$_{//} = a_{//}$ indexed to $P1$.

Figure C.9 (Part 1/3)

Raw 2D SAXS data for LSL'-$N_{A'}$ indexed (*left*) to the $P1$ space group along the perpendicular direction, corresponding to lamellae stacked normal to the beam (LAM⊥) and (*right*) to the $P1$ space group along the parallel direction, corresponding to lamellae stacked in-plane with the beam (LAM$_{//}$). The relevant parameters, provided in nanometers, are the lamellar periods $d^* = d$ LAM⊥ and $d_{//} = d$ LAM$_{//}$. Green dots superimposed on the images indicate the expected peak positions. See Table C.3 for an overview of the indexed data.

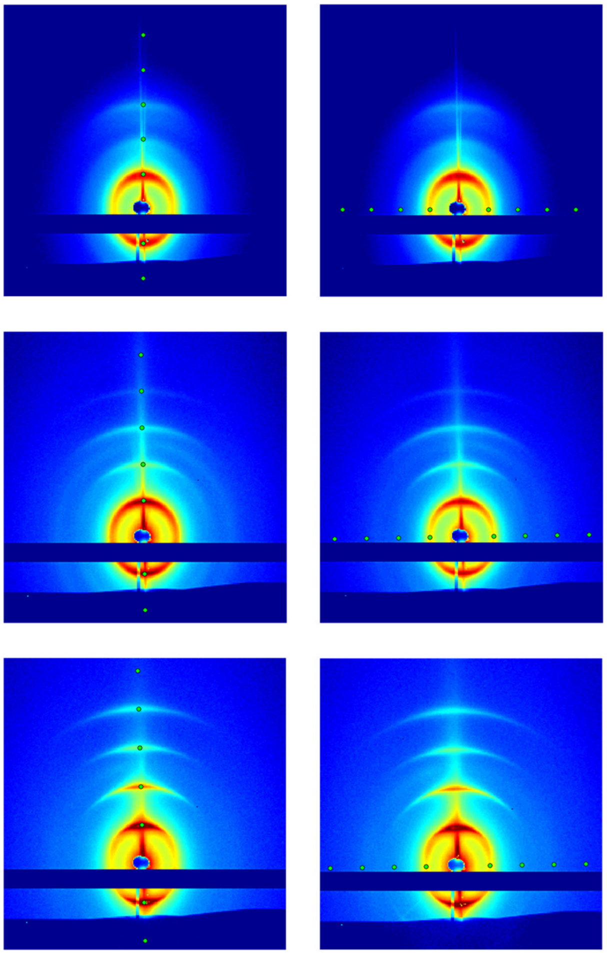

LSL-0
$d^* = 32.9$
d LAM$_{//} = 39.2$

LSL-2
$d^* = 31.3$
d LAM$_{//} = 36.0$

LSL-5
$d^* = 29.6$
d LAM$_{//} = 35.8$

Figure C.9 (Part 2/3)

Raw 2D SAXS data for LSL'-$N_{A'}$ indexed (*left*) to the *P*1 space group along the perpendicular direction, corresponding to lamellae stacked normal to the beam (LAM$_{\perp}$) and (*right*) to the *P*1 space group along the parallel direction.

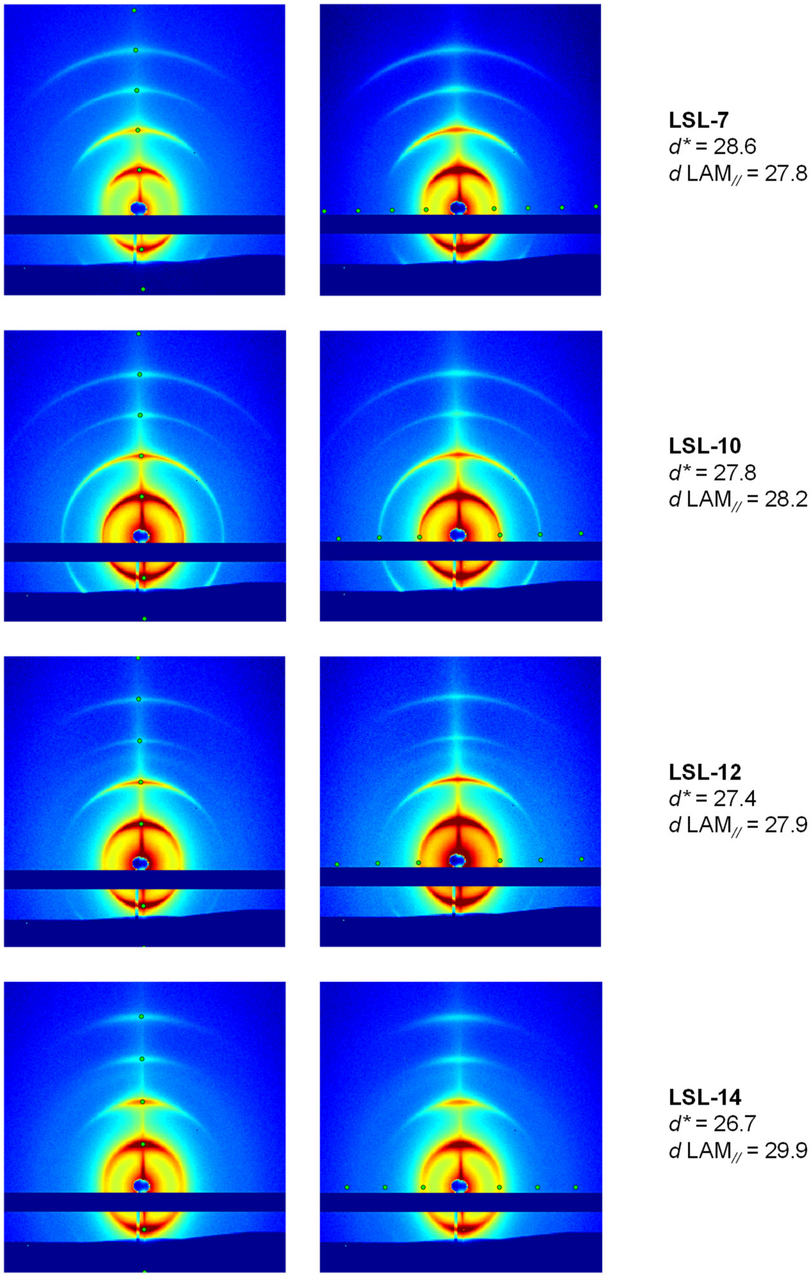

Figure C.9 (Part 3/3)

Raw 2D SAXS data for LSL'-$N_{A'}$ indexed (*left*) to the *P*1 space group along the perpendicular direction, corresponding to lamellae stacked normal to the beam (LAM$_\perp$) and (*right*) to the *P*1 space group along the parallel direction.

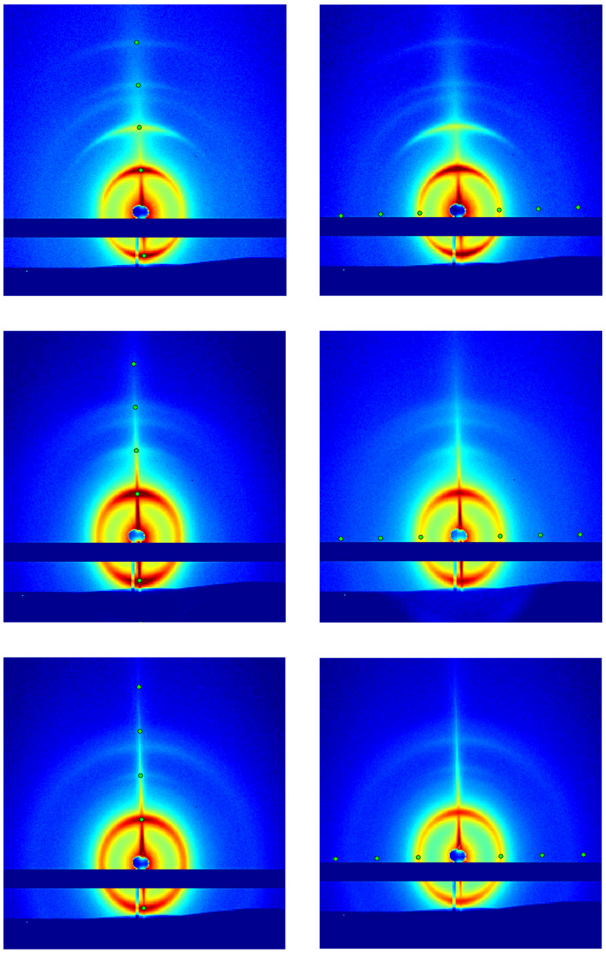

LSL-17
d^* = 26.6
d LAM$_{//}$ = 28.8

LSL-19
d^* = 26.2
d LAM$_{//}$ = 28.5

LSL-24
d^* = 25.7
d LAM$_{//}$ = 27.6

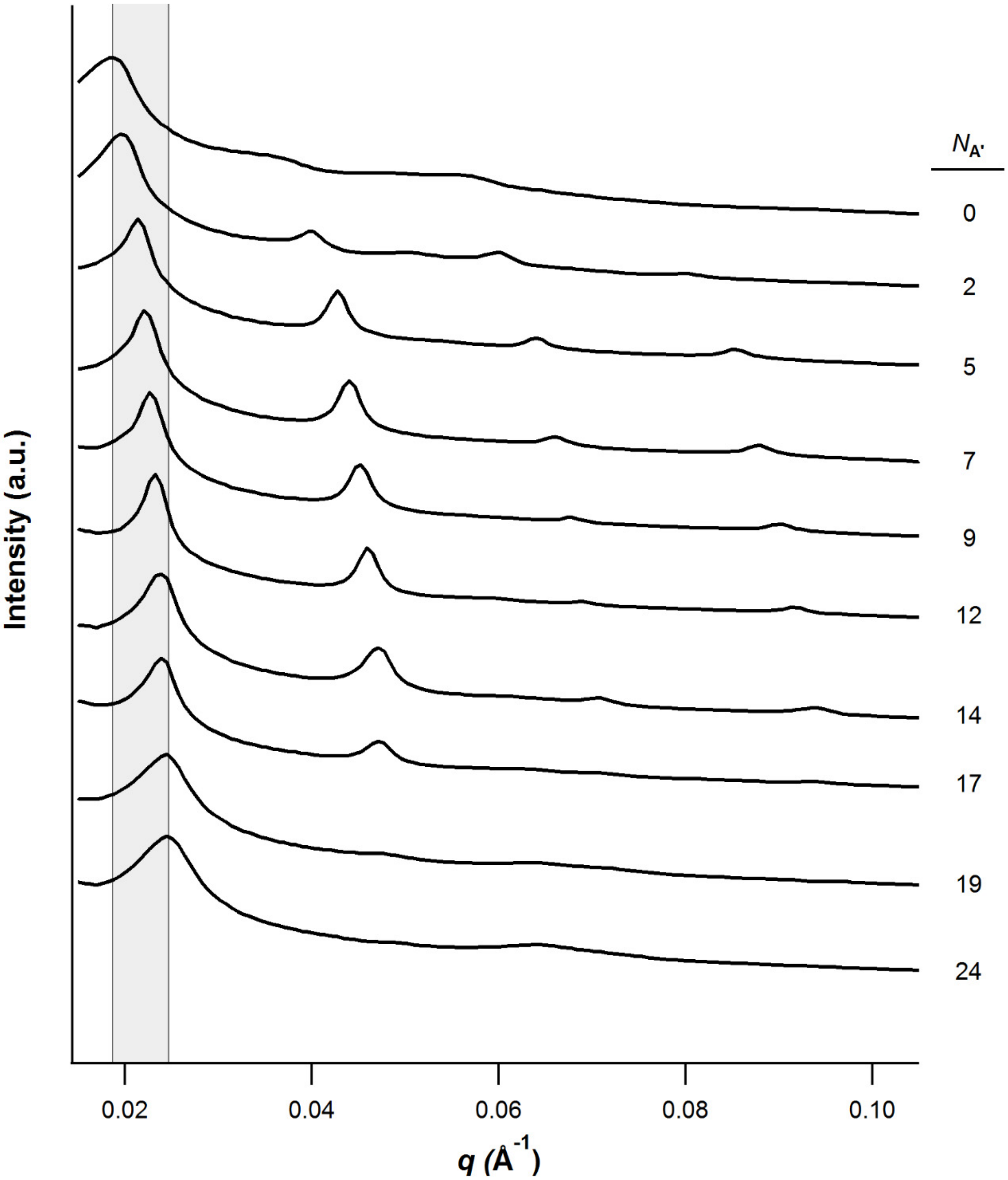

Figure C.10: Azimuthally integrated 1D SAXS patterns for LSL' brush triblock copolymers with fixed N_A and N_B and variable $N_{A'}$. The LSL' series was synthesized from a common parent LS diblock in the same way as LSO with variable N_C. The large change in the position of q^* (and therefore $d^* = 2\pi/q^*$) across the series is emphasized by the gray box. All traces correspond to samples that self-assemble to majority LAM (*i.e.,* LAM$_2$). Compare Figure C.7 (LSO).

C-8 Differential Scanning Calorimetry (DSC)

DSC data was collected on a TA Instruments Q2000 under dry nitrogen atmosphere. The samples were heated and cooled between −85 and 120 °C at 20 °C, 10 °C, and 5 °C/min. The reported values of the glass transition temperatures (T_g) were determined from derivative curves of the second heating cycle (20 °C/min). For each sample, about 10 mg of polymer was hermetically sealed in a Tzero aluminum pan.

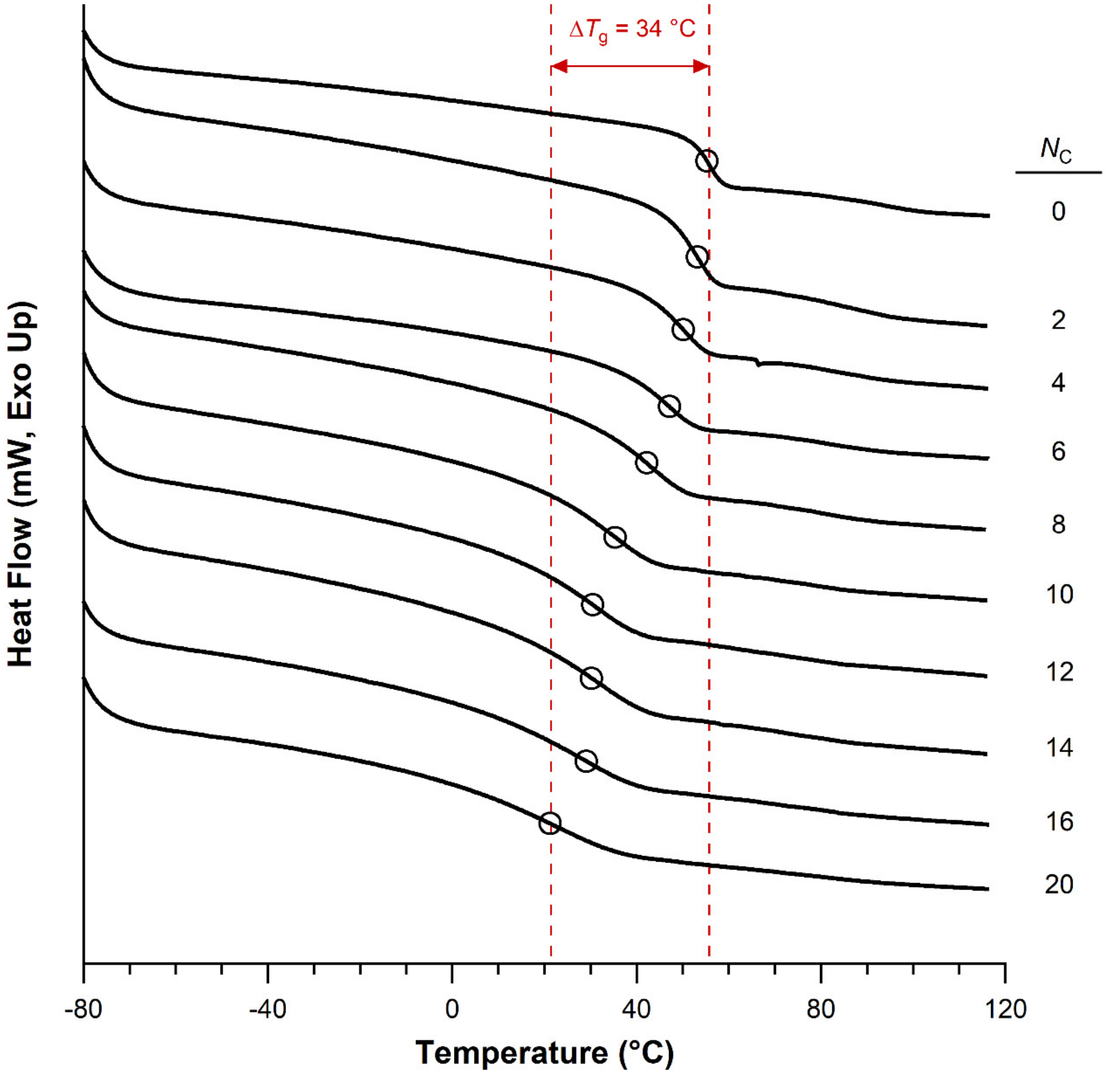

Figure C.11: DSC data for 10 LSO-N_C triblock terpolymers ($0 \leq N_C \leq 20$). Traces correspond to data collected upon heating from −85 °C to 120 °C at 20 °C/min. We note that under these conditions, the glass transitions of pure PLA, PS, and PEO are not observed. Open circles (○) indicate the positions of T_g, determined from the corresponding derivative curves. As N_C (and therefore the PEO content) increases, T_g decreases. Compare Fig. C.12 (LSL').

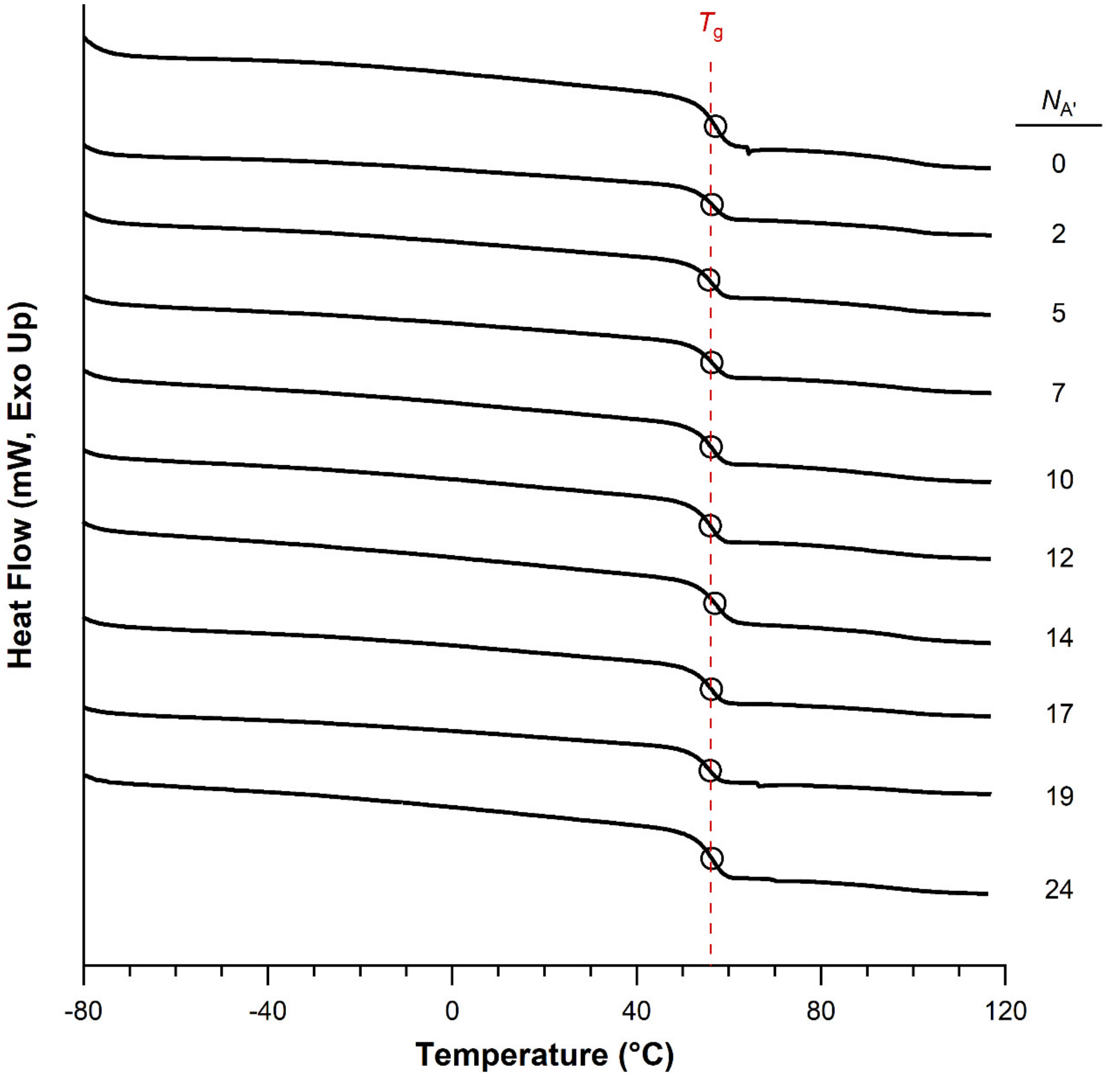

Figure C.12: DSC data for 10 LSL'-$N_{A'}$ triblock terpolymers ($0 \le N_{A'} \le 24$). Traces correspond to data collected upon heating from −85 °C to 120 °C at 20 °C/min. We note that under these conditions, the glass transition of PS is not observed. Open circles (○) indicate the positions of T_g, determined from the corresponding derivative curves. As $N_{A'}$ increases, the T_g remains the same (±1 °C). Compare Figure C.11 (LSO).

C-9 SCFT Calculations: LSO-N_C and LSL'-$N_{A'}$ Series

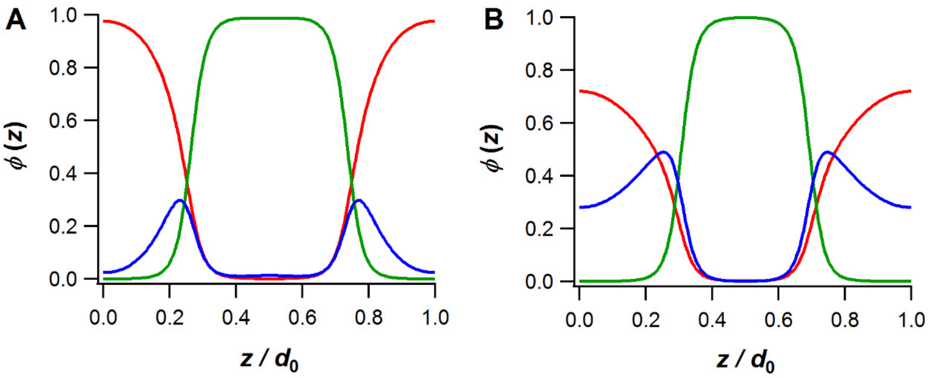

Figure C.13: SCFT composition profiles calculated over one lamellar period for two triblocks that self-assemble to $\mathrm{LAM_P}$: (*A*) LSO-6 and (*B*) LSO-20. The relative segment concentrations $\phi(z)$ of each component are shown (red: PLA, green: PS, blue: PEO). SCFT predicts a small proportion of PEO blocks mixed in PS domains when N_C is small, consistent with the chain pullout model for the unusual *d** trend. Profiles were calculated using $\chi_{LS} = 0.080$, $\chi_{SO} = 0.049$, $\chi_{LO} = -0.010$, and different C block dispersities (Table C.4).

Table C.4: SCFT calculations for the lamellar period for LSO-N_C brush triblock terpolymers, in which N_A, N_B are fixed and N_C is varied. Calculations were performed using $\chi_{LS} = 0.080$, $\chi_{SO} = 0.049$, and $\chi_{LO} = -0.010$. The decrease in *d** can be attributed to the effects of molecular asymmetry and shielding of PLA-PS interactions by the PEO block, which are further enhanced by polydispersity of the PEO block.

Sample	***d** Experiment[a] (nm)**	***d** SCFT, monodisperse[b] (nm)**	***d**, SCFT, polydisperse[c] (nm)**	**$Đ_C$[d]**
LSO-0	29.0	35.3	–[e]	–[e]
LSO-2	27.9	35.0	33.0	1.82
LSO-4	27.0	23.6	26.2	1.67
LSO-6	26.8	23.7	24.9	1.55
LSO-8	26.5	23.9	24.7	1.45
LSO-10	25.8	24.1	24.8	1.37
LSO-12	25.2	24.4	25.0	1.30
LSO-14	24.6	24.7	25.3	1.25
LSO-16	24.5	25.0	25.7	1.20
LSO-20	23.6	25.9	26.3	1.14

[a] Domain spacing, $d^* = 2\pi/q^*$, determined by SAXS and measured at 25 °C.

[b] Doman spacing predicted by SCFT when the polymers are assumed to be monodisperse ($Đ_C = 1.00$).

[c] Domain spacing predicted by SCFT when dispersity in the PEO block ($Đ_C > 1.00$) is introduced, according to the values of $Đ_C$ in the last column.

[d] Dispersity in the backbone length of the C block, calculated using $Đ_C = 1 + \exp(-N_C/10)$.

[e] Because LSO-0 does not have a C end block, polydisperse calculations were not performed.

Table C.5: SCFT calculations for the lamellar period for LSL'-$N_{A'}$ brush triblock terpolymers, in which N_A, N_B are fixed and $N_{A'}$ is varied. Calculations were performed using $\chi_{LS} = 0.080$. The decrease in d^* can be attributed to the effects of molecular asymmetry, which are further enhanced by polydispersity of the second PLA block.

Sample	d^* Experiment[a] (nm)	d^* SCFT, monodisperse[b] (nm)	d^*, SCFT, polydisperse[c] (nm)	$Đ_{A'}$[d]
LSL'-0	32.9	39.7	–[e]	–[e]
LSL'-2	31.3	38.4	35.3	1.82
LSL'-5	29.6	27.0	28.1	1.61
LSL'-7	28.6	27.3	28.1	1.50
LSL'-10	27.8	28.0	28.5	1.37
LSL'-12	27.4	28.5	28.9	1.30
LSL'-14	26.7	28.9	29.4	1.25
LSL'-17	26.6	29.6	30.0	1.18
LSL'-19	26.2	30.1	30.4	1.15
LSL'-24	25.7	31.3	31.7	1.09

[a] Domain spacing, $d^* = 2\pi/q^*$, determined by SAXS and measured at 25 °C.

[b] Doman spacing predicted by SCFT when the polymers are assumed to be monodisperse ($Đ_{A'} = 1.00$).

[c] Domain spacing predicted by SCFT when dispersity in the PEO block ($Đ_{A'} > 1.00$) is introduced, according to the values of $Đ_{A'}$ in the last column.

[d] Dispersity in the backbone length of the A' block, calculated using $Đ_{A'} = 1 + \exp(-N_{A'}/10)$.

[e] Because LSL'-0 does not have an A' end block, polydisperse calculations were not performed.

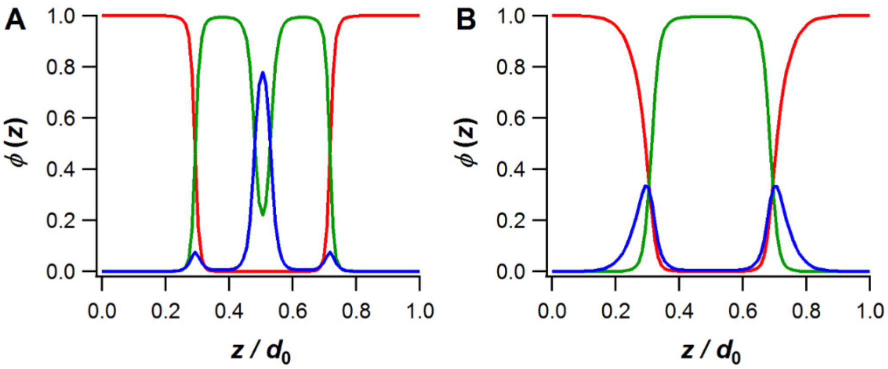

Figure C.14: SCFT composition profiles calculated over one lamellar period for a *linear* LSO triblock terpolymer in which each block has the same molecular weight as the corresponding block in LSO*. The relative segment concentrations $\phi(z)$ of each component are shown (red: PLA, green: PS, blue: PEO). Compare Figure 4.4: both brush and linear LSO triblock terpolymers show a transition from LAM_3 to LAM_P controlled by the magnitude of χ_{LO}. Profiles were calculated using $\chi_{LS} = 0.080$, $\chi_{SO} = 0.049$, and $\chi_{LO} = 0.034 = \chi^C$ (the calculated transition between LAM_3 and LAM_P where each phase is equally stable). (*A*) For large $\chi_{LO} > \chi^C$, SCFT predicts pure domains (LAM_3). (*B*) For small $\chi_{LO} < \chi^C$, SCFT predicts LAM_P.

C-10 Wide-Angle X-ray Scattering (WAXS)

Wide-angle X-ray scattering data was collected using a PANalytical X'Pert Pro. The wavelength of the X-ray beam was 1.54 Å. Samples were analyzed at 25 °C as neat powders, all prepared under the same conditions. Samples were scanned in the range $10° \leq 2\theta \leq 40°$, with step size 0.017°. Due to the geometry of the stage, minor peaks at 31.1° and 36.1° appear as artifacts.

LSO-N_C brush triblock terpolymers, their parent LS diblock (LSO-0), and PEO MM were characterized by WAXS (Figures 5.8, C.15). All samples were measured at room temperature as neat powders, prepared under the same conditions. WAXS data for LSO-4, LSO-14, and PEO MM were additionally collected (1) after heating to 60 °C at 1 °C/min and (2) after cooling to 30 °C at 10 °C/min. The percent crystallinity can be estimated based on such data collected in the molten, completely amorphous state (*i.e.*, above the melting temperature of PEO, T_m = 50 °C) and in the semicrystalline state.

Assuming an isotropic two-phase system comprising crystalline regions and amorphous regions, the scattered intensity I(s) (in sr^{-1}) consists of several contributions:

$$I(s) = \frac{1}{b_e^2}\frac{\mathrm{d}\sigma}{\mathrm{d}\Omega} = I_{\mathrm{cr}}(s) + I_{\mathrm{am}}(s) + I_{\mathrm{inc}}(s) \qquad \text{Eq. C-6}$$

where $s = (2/\lambda)\sin\theta$ is the magnitude of the scattering vector, $\mathrm{d}\sigma/\mathrm{d}\Omega$ is the differential scattering cross section, and b_e is the scattering length of an electron. The intensities $I_{\mathrm{cr}}(s)$ and $I_{\mathrm{am}}(s)$ contain information about the crystalline regions and amorphous regions of the sample, respectively, while the incoherent contribution $I_{\mathrm{inc}}(s)$ contains no structural information. The ratio of $I_{\mathrm{cr}}(s)$ to $I_{\mathrm{am}}(s)$ reflects the weight fraction of crystallinity in a semicrystalline sample. In an approximation developed by Goppel and coworkers,[6] the intensity at a certain scattering vector s_0, chosen between Bragg reflections, is taken as part of $I_{\mathrm{am}}(s)$. $I(s_0)$ is measured both in the semicrystalline sample (scry) and in a molten, completely amorphous sample (molt), and the crystallinity (x_{cr}) follows:

$$\frac{I_{\mathrm{scry}}(s_0)}{I_{\mathrm{molt}}(s_0)} \approx x_{\mathrm{am}} = 1 - x_{\mathrm{cr}} \qquad \text{Eq. C-7}$$

The approach is accurate if the incoherent scattering and diffuse scattering can be neglected or subtracted. In our variable-temperature WAXS experiments, s_0 is chosen to correspond to the maximum in the amorphous halo ($2\theta = 20.2°$), between the reflections at $2\theta = 19.1°$ and 23.3° that correspond to the (120) and (032) reflections, respectively, from the monoclinic PEO lattice.[7] For LSO and PEO MM, $I_{\mathrm{scry}}(s_0)$ was obtained from data collected at 30 °C, and $I_{\mathrm{molt}}(s_0)$ was obtained from data at 60 °C.

LSO-4 and LSO-14 (two samples that self-assemble to LAM$_{\mathrm{P}}$) comprise 6.8 wt% and 20.4 wt% PEO, respectively. From Eq. C-7, the crystalline weight fractions were estimated to be 3% and 6%, respectively. For the PEO MM, measured under the same conditions, the crystalline weight fraction is 50%. Crystallinity appears to be suppressed in the LSO brush triblock terpolymers. Various phenomena may contribute, such as (1) partial mixing of PLA and PEO, (2) the densely grafted bottlebrush architecture,[8] and (3) hard confinement of PEO between glassy PS microdomains.[9] Because the crystalline weight fraction is low throughout the series, we do not expect that crystallinity influences the domain spacing trend observed in LSO-N_{C}. Other work on PEO-containing block copolymers (Chapters 4 and 5) further supports this conclusion.

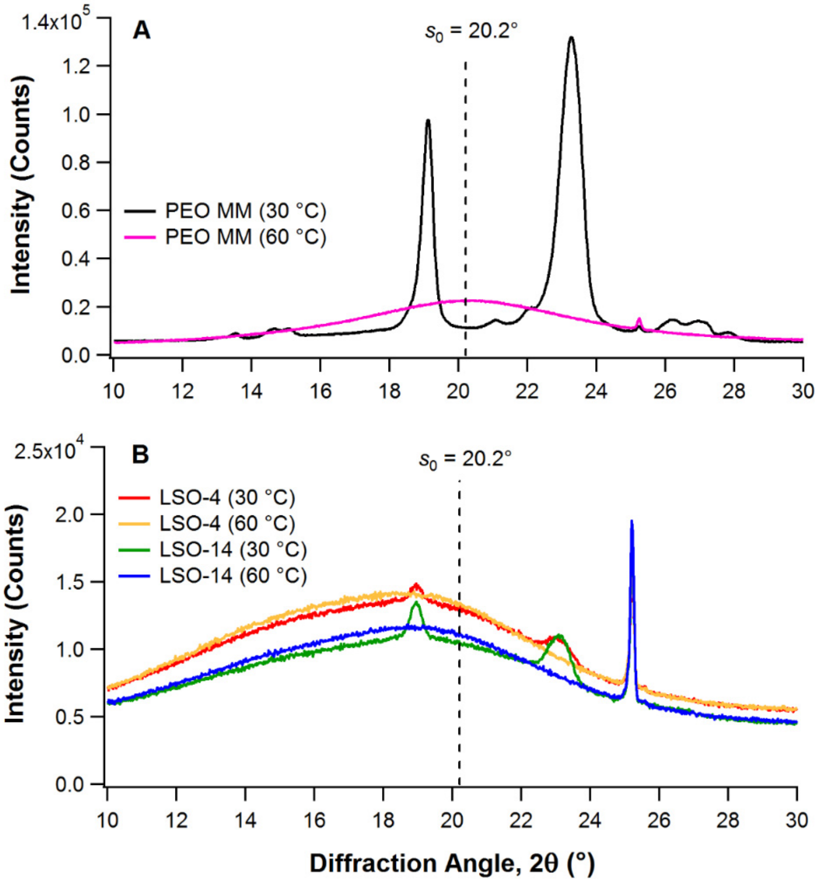

Figure C.15: Variable-temperature WAXS data for (*A*) PEO macromonomer (MM, M_n = 2000 g/mol) and (*B*) brush triblocks LSO-4 and LSO-14. For each sample, the intensity at scattering vector $s_0 = 2\theta = 20.2°$ was determined at 30 °C (before heating) and at 60 °C. At 60 °C, all samples are amorphous; the melting temperature of PEO is approximately 52 °C. The ratio of intensities at s_0 for crystalline and amorphous samples were used to estimate in the crystalline weight fractions (x_{cr}): x_{cr} in PEO MM is 50%, whereas x_{cr} in all LAM$_P$-forming LSO samples is <10%.

References

(1) Sveinbjörnsson, B. R.; Weitekamp, R. A.; Miyake, G. M.; Xia, Y.; Atwater, H. A.; Grubbs, R. H. *Proc. Natl. Acad. Sci. U.S.A.* **2012**, *109*, 14332–14336.

(2) Dorgan, J. R.; Janzen, J.; Knauss, D. M.; Hait, S. B.; Limoges, B. R.; Hutchinson, M. H. *J. Polym. Sci., Part B: Polym. Phys.* **2005**, *43*, 3100–3111.

(3) Fetters, L. J.; Lohse, D. J.; Richter, D.; Witten, T. A.; Zirkel, A. *Macromolecules* **1994**, *27*, 4639–4647.

(4) Dalsin, S. J.; Rions-Maehren, T. G.; Beam, M. D.; Bates, F. S.; Hillmyer, M. A.; Matsen, M. W. *ACS Nano* **2015**, *9*, 12233–12245.

(5) Kim, J. U.; Matsen, M. W. *Macromolecules* **2009**, *42*, 3430–3432.

(6) Goppel, J. M.; Arlman, J. J. *Flow, Turbulence and Combustion* **1949**, *1*, 462–474.

(7) Takahashi, Y.; Tadokoro, H. *Macromolecules* **1973**, *6*, 672–675.

(8) Bates, C. M.; Chang, A. B.; Momčilović, N.; Jones, S. C.; Grubbs, R. H. *Macromolecules* **2015**, *48*, 4967–4973.

(9) Zhu, L.; Cheng, S. Z. D.; Calhoun, B. H.; Ge, Q.; Quirk, R. P.; Thomas, E. L.; Hsiao, B. S.; Yeh, F.; Lotz, B. *Polymer* **2001**, *42*, 5829–5839.